

FRACTURE ANALYSIS

*Proceedings of the
1973 National Symposium
on Fracture Mechanics,
PART II*

 **STP 560**

AMERICAN SOCIETY FOR TESTING AND MATERIALS

Fracture Analysis

Proceedings of the 1973
National Symposium on
Fracture Mechanics, Part II

A symposium sponsored by
Committee E-24 on
Fracture Testing of Metals,
AMERICAN SOCIETY FOR
TESTING AND MATERIALS
University of Maryland,
College Park, Md., 27-29 Aug. 1973

ASTM SPECIAL TECHNICAL PUBLICATION 560
P. C. Paris, chairman of symposium committee
G. R. Irwin, general chairman of symposium

List price \$22.75
04-560000-30



AMERICAN SOCIETY FOR TESTING AND MATERIALS
1916 Race Street, Philadelphia, Pa. 19103

©AMERICAN SOCIETY FOR TESTING AND MATERIALS 1974
Library of Congress Catalog Card Number: 74-81155

NOTE

The Society is not responsible, as a body,
for the statements and opinions
advanced in this publication.

Printed in Lutherville-Timonium, Md.
August 1974

Foreword

The 1973 National Symposium on Fracture Mechanics was held at the University of Maryland Conference Center, College Park, Md., 27–29 Aug. 1973. The symposium was sponsored by the American Society for Testing and Materials through Committee E-24 on Fracture Testing of Metals. Members of the Symposium Subcommittee of Committee E-24 selected papers for the program. Organizational assistance from Don Wisdom and Jane Wheeler at ASTM Headquarters was most helpful. G. R. Irwin, Dept. of Mechanical Engineering, University of Maryland, served as general chairman. Those who served as session chairmen were H. T. Corten, Dept. of Theoretical and Applied Mechanics, University of Illinois; C. M. Carman, Frankford Arsenal; J. R. Rice, Div. of Engineering, Brown University; D. E. McCabe, Research Dept., ARMCO Steel; J. E. Srawley, Fracture Section, Lewis Research Center, NASA; E. T. Wessel, Research and Development Center, Westinghouse Electric Corp.; and E. K. Walker, Lockheed-California Co.

The Proceedings have been divided into two volumes: Part I—*Fracture Toughness and Slow-Stable Cracking* and Part II—*Fracture Analysis*.

Related ASTM Publications

**Stress Analysis and Growth of Cracks, STP 513
(1972), \$27.50 04-513000-30**

**Fracture Toughness, STP 514 (1972), \$18.75
04-514000-30**

**Fracture Toughness Evaluation by R-Curve Methods,
STP 527 (1973), \$9.75 04-527000-30**

**Progress in Flaw Growth and Fracture Toughness
Testing, STP 536 (1973), \$33.25 04-536000-30**

Contents

Introduction	1
Strain Energy Release Rate for a Crack Under Combined Mode I and Mode II— M. A. HUSSAIN, S. L. PU, AND J. UNDERWOOD	2
Mapping Function	5
Reduction of the Problem to Functional Integral Equations	9
Computations of Energy Release Rate	16
Numerical and Experimental Results	21
Fracture Under Combined Modes in 4340 Steel—R. C. SHAH	29
Material and Procedures	31
Test Machine and Instrumentation	34
Test Results and Discussion	36
Conclusions	51
Crack Approaching a Hole—A. S. KOBAYASHI, B. JOHNSON, AND B. G. WADE	53
Experimental Procedure and Results	54
Analytical Background	57
Results	61
Discussion	62
Conclusions	67
Influence of Three-Dimensional Effects on the Stress Intensity Factors of Compact Tension Specimens—M. A. SCHROEDL AND C. W. SMITH	69
Nomenclature	69
Analytical Considerations	70
The Experiments	72
Results	74
Discussion	78
Summary	78
K Calibrations for C-Shaped Specimens of Various Geometries— J. H. UNDERWOOD, R. D. SCANLON, AND D. P. KENDALL	81
Nomenclature	81
Collocation Results	82
Data Analysis Procedures	85
K Calibration Results	86
Discussion	89
A Class of Interface Crack Problems—G. P. SENDECKYJ	92
Basic Equations	93
General Interface Crack Problem	94
Examples	95
Nature of Crack Tip Singularity	98
Crack Tip Stress Intensity Factors	100
Conclusion	103
Stress Analysis of the Compact Specimen Including the Effects of Pin Loading— J. C. NEWMAN, JR.	105
Nomenclature	105
Analysis of the Compact Specimen	107
Results and Discussion	110
Concluding Remarks	120

Some Effects of Experimental Error in Fracture Testing —T. W. ORANGE	122
Analysis	123
Discussion	127
Summary and Conclusions	132
A Combined Analytical-Experimental Fracture Study —P. C. RICCARDELLA	
AND J. L. SWEDLOW	134
Laboratory Experiments	135
Analyses	142
Analytical-Experimental Comparison	150
Recommendations	153
Conclusions	154
An Estimation Model for the Application of the J-Integral —J. A. BEGLEY,	
J. D. LANDES, AND W. K. WILSON	155
The Infinite Plate Problem	156
Crack in a Plastic Zone	159
More Exact Elastic-Plastic Solution for Case of a Hole in a Plate	164
Conclusions	168
Test Results from J-Integral Studies: An Attempt to Establish a J_{Ic} Testing	
Procedure —J. D. LANDES AND J. A. BEGLEY	170
Test Program	171
Size Effect	181
Fracture Toughness Versus Temperature	182
Tentative J_{Ic} Test Method	183
Conclusions	185
Small-Scale Yielding Analysis of Mixed Mode Plane-Strain Crack Problems —	
C. F. SHIH	187
Dominant Singularity Analysis	191
Perfect Plasticity Solutions at Near-Field	196
The Small-Scale Yielding Problem	202
Conclusions	206
Unimod: An Applications Oriented Finite Element Scheme for the Analysis	
of Fracture Mechanics Problems —PRASAD NAIR AND K. L. REIFSNIDER	211
Unimod—The Technique	212
Results Using Unimod	214
Discussion and Conclusions	224
Application of the J-Integral to Obtain Some Similarity Relations —S. J. CHANG	
AND F. J. WITT	226
Some Preliminary Relations	228
The Similarity Conditions	229
Ilyushin's Principle for Rigidly Plastic Material	231
Singular Solution Near the Crack Tip	233
Elastic-Plastic Problems	234
Discussion	238
Fracture Mechanics Evaluation of the Integrity of an Inlet Nozzle of a	
Pressurized Water Reactor Vessel Following a Postulated Loss of	
Coolant —C. B. BUCHALET	240
Method of Analysis	241
Analysis and Results	248
Conclusions	252
Discussion	253

Introduction

The papers grouped in this volume include two which employ photoelastic methods of stress analysis. Stress wave effects from a hole approached by a running crack are of interest in one paper and variations of K through the thickness of a compact tension specimen in the other. Several papers in which the experimental measurements appeared to be supplementary to analysis ideas were included in this volume as illustrated by papers discussing the J-integral and combinations of Mode I and Mode II stress fields. Other topics of special interest are discussed including test specimen calibrations, comparison of J characterization to the "equivalent energy" method, use of characterization in terms of strain intensity factors for a mixed mode plastic zone, and treatment of the nuclear reactor vessel "loss of coolant" problem.

This volume will prove of particular interest to the engineers and scientists concerned with the analysis of the fracture phenomenon as well as designers who must integrate the information available into their plans.

All of the papers in this publication were presented at the 1973 National Symposium on Fracture Mechanics held at the University of Maryland (College Park) 27-29 Aug. 1973.

G. R. Irwin

Dept. of Mechanical Engineering,
University of Maryland,
College Park, Md.

Strain Energy Release Rate for a Crack Under Combined Mode I and Mode II

REFERENCE: Hussain, M. A., Pu, S. L., and Underwood, J., "Strain Energy Release Rate for a Crack Under Combined Mode I and Mode II," *Fracture Analysis*, ASTM STP 560, American Society for Testing and Materials, 1974, pp. 2-28.

ABSTRACT: In this paper we have computed the energy release rate for a crack subjected simultaneously to Mode I and Mode II conditions. The energy was computed by path-independent integrals, using the elastic solution of a deflected crack, having a main branch and a propagation branch. The elasticity solution was obtained from the functional integral equations by the process of iterations. This process leads to a point-wise exact solution in the limit as the propagation branch goes to zero. Interestingly enough, the results indicate that the solution at the tip in the limit as the propagation branch goes to zero is not the same as the solution at the tip with no branch.

Using the Griffith-Irwin criterion, incipient paths of propagation of such a crack were obtained from the maximum value of the energy release rate. To check the validity of the results, an experiment, which gives a pure Mode II condition at the tip of the crack, was devised. The results were in excellent agreement with the theory. The energy release rate, in parametric form, can be used for any crack subjected to Mode I and Mode II loading conditions. To the authors' knowledge, such an expression for the energy release rate does not exist in the literature.

KEY WORDS: fatigue (materials), energy, crack propagation, stresses, fracture properties

The concepts of energy release rate, \mathcal{G} , and the stress intensity factors, K 's, have been widely used in the field of sharp fracture mechanics. Under normal loading conditions (Mode I crack), these concepts are equivalent. The onset of unstable fracture is successfully predicted by the critical value of either the energy release rate \mathcal{G}_c or the stress intensity factor K_{Ic} . The mathematical relationship between \mathcal{G} and K can easily be obtained using Westergaard's near field solution and Irwin's approach [1]²

$$\mathcal{G}_I = \frac{1}{E} K_I^2 \text{ (plane stress)}, \quad \mathcal{G}_I = \frac{1 - \nu^2}{E} K_I^2 \text{ (plane strain)} \quad (1)$$

¹ Mechanical engineer, Applied Math and Mechanics Division; mathematician, Applied Math and Mechanics Division; and Metallurgist, Materials Engineering Division; respectively, Research Directorate, Benet Weapons Laboratory, Watervliet Arsenal, Watervliet, N. Y. 12189.

² The italic numbers in brackets refer to the list of references appended to this paper.

This relation may be obtained from the integral derived more rigorously by Bueckner [2] for the energy release rate and can also be shown by using path-independent integrals to be discussed later.

In the derivation of Eq 1, the crack is assumed to move along its own plane which can be justified from experimental observations under Mode I conditions. Now computing the energy release rate for combined Mode I and Mode II we obtain

$$\mathcal{G} = \frac{1}{E} (K_I^2 + K_{II}^2) \text{ (plane stress)} \quad (2)$$

Equation 2 was obtained on the same assumption as before, that is, the crack under combined loading moves along its own initial plane. Unfortunately, the crack extension is not collinear for a crack subjected to either skew-symmetric loads or combined loads. Hence, Eq 2 has only an academic value unless interpreted properly. An equation which gives the energy release rate for an arbitrary direction of crack propagation is necessary in order to apply the Griffith-Irwin energy release rate criterion to cracks under combined loads. It was first believed that the missing information could be obtained by new path independent integrals found by Knowles and Sternberg [3]. But our initial hopes were not realized (this can be seen from the vanishing of the L and M integrals when the Westergaard near field solution is used). It will become clear that it is necessary first to obtain an elasticity solution for a crack having a main branch and a propagation branch at an arbitrary angle (shown in Fig. 1 and it will be referred to as a deflected crack). Then we compute the energy release rate and obtain its limit as the propagation branch vanishes. The final result in a parametric form is

$$\mathcal{G}(\gamma) = \frac{4}{E} \left(\frac{1}{3 + \cos^2 \gamma} \right)^2 \left(\frac{1 - \gamma/\pi}{1 + \gamma/\pi} \right)^{\gamma/\pi} [(1 + 3 \cos^2 \gamma) K_I^2 + 8 \sin \gamma \cos \gamma K_I K_{II} + (9 - 5 \cos^2 \gamma) K_{II}^2] \quad (3)$$

It is the purpose of this paper to obtain Eq 3 by the process just indicated.

The problem of fracture under combined Mode I and Mode II loading has been of interest to many investigators. Hitherto, in the absence of Eq 3, investigators have had to apply other criteria. The most notable one among them is "maximum normal stress," first proposed by Yoffe [5] for dynamic problems and by Erdogan and Sih [6] for static problems. A similar hypothesis exists in papers by Stroh [7]. Though some experimental results in Ref 6 were in good agreement with their criterion, the authors themselves have indicated certain shortcomings of such an approach: that is, the normal stress is singular at the tip of a crack in all directions and, hence, the concepts of stress may not have a physical meaning. In addition, the criterion requires the crack to extend in a radial direction.

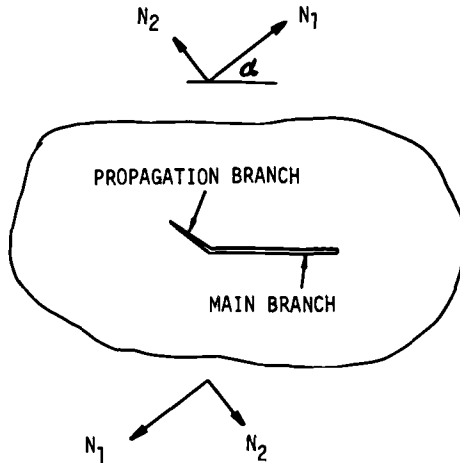


FIG. 1—A deflected crack under general plane loading.

However, they conjectured that if the Griffith-Irwin criterion is valid, then, “The crack will grow in the direction along which the elastic energy release per unit crack extension will be maximum and the crack will start to grow when this energy (release rate) reaches to a critical value.” This “rate of energy release being a controlling factor” is also indicated by Williams [8]. If this indeed is the case then Eq 3 should give us the direction of incipient propagation as well as the energy release rate, and we may boldly extend the hypothesis in the form of the following corollary: “if K_{Ic} is considered as a material property, K_{IIc} is related to K_{Ic} . Hence, it is not necessary to define two independent material properties.” This corollary is derived on a simplified assumption that the critical energy release rate under combined loading is the same as that of Mode I crack for that material. This assumption may not be valid for cracks with considerable plastic or nonlinear zones.

Recently Sih [9] proposed a criterion based on strain energy density which is inversely proportional to the radial distance r measured from the crack tip and is also singular at the crack tip. There exist many such good criteria of fracture. Most of them complement each other in the case of Mode I conditions and deviate from each other for cracks under combined modes. More experimental programs for mixed mode cracks are needed to clarify some of the uncertainties.

To solve the elasticity problem of the deflected crack, Fig. 1, a mapping function which maps a star-shaped crack into a unit circle is used. In the next section, properties of the mapping functions are discussed. In the third section we reduce the problem to a functional integral equation, and after checking its validity we set up an iteration scheme. The asymptotic solution of the first iteration as the propagation branch goes to zero

immediately leads to a recurrence relation for any order of iteration leading thereby to the point-wise exact solution. It should be noted that the solution in the limit as the propagation branch goes to zero is not the same as the solution with zero branch. The energy rate is obtained in the fourth section via the use of path independent integrals. The stress intensity factors at the tip of the propagation branch are also derived. In the final section numerical results are compared with some experimental data and some new experiments are suggested.

Mapping Function

The deflected crack shown in Fig. 1 is a special case of a star-shaped contour consisting of n discrete rays emanating from the origin in the z -plane, Fig. 2. The latter contour can be mapped onto a unit circle in the ζ -plane by the transform

$$z = \omega(\zeta) = A\zeta^{-1}(\zeta - e^{i\alpha_1})^{\lambda_1}(\zeta - e^{i\alpha_2})^{\lambda_2} \dots (\zeta - e^{i\alpha_n})^{\lambda_n} \tag{4}$$

where A , λ_k , and α_k are real constants and

$$0 < \alpha_1 < \alpha_2 < \dots < \alpha_k < \dots < \alpha_n < 2\pi \tag{5}$$

This mapping function was first devised by Sir Darwin [10] and used by H. Andersson [11] in his attempt to obtain an elasticity solution for a star-shaped crack. Unfortunately, Ref 11 contains an error [12] which will be pointed out later. The mapping function has multiple branches with branch points at $\zeta = \exp(i\alpha_k)$. To ensure that $z = \infty$ maps into $\zeta = \infty$, in a one to one fashion, it is required that

$$\sum_{k=1}^n \lambda_k = 2 \tag{6}$$

The image in z -plane of a unit circle, $\zeta = e^{i\theta}$, in ζ -plane is

$$z = 4A \exp \left[i \left\{ \frac{1}{2} \sum_{k=1}^n \alpha_k \lambda_k \pm (2m + 1) \pi \right\} \right] \prod_{k=1}^n \left\{ \sin \left(\frac{\alpha_k - \theta}{2} \right) \right\}^{\lambda_k} \tag{7}$$

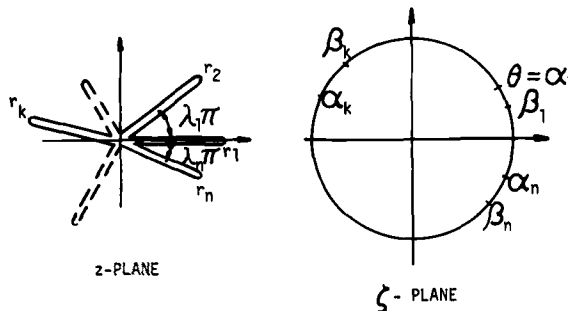


FIG. 2—The mapping of a star-shaped contour in the z -plane into a unit circle in the ζ -plane.

We fix the branch by selecting $\arg(z) = 0$ for $\theta = 0$;³ this gives from Eqs 7 and 5

$$\frac{1}{2} \sum_{k=1}^n \alpha_k \lambda_k \pm (2m + 1) \pi = 0 \quad (8)$$

Taking $\lambda_k > 0$, $m = 0$ and the negative sign, Eq 8 becomes

$$\sum_{k=1}^n \alpha_k \lambda_k = 2\pi \quad (9)$$

From Eqs 9 and 7 the image of a point $\zeta = e^{i\theta}$, $\alpha_{l-1} < \theta < \alpha_l$ where $l = 2, 3, \dots$, is given by

$$z = 4A \exp\left\{i\pi \sum_{k=1}^{l-1} \lambda_k\right\} \prod_{k=1}^n \left| \sin\left(\frac{\alpha_k - \theta}{2}\right) \right|^{\lambda_k} \quad (10)$$

From Eq 10 we see that in the range $\alpha_{l-1} < \theta < \alpha_l$, z traces a ray in the direction $(\lambda_1 + \lambda_2 + \dots + \lambda_{l-1})\pi$, vanishes at $\theta = \alpha_{l-1}$, and $\theta = \alpha_l$, and has a maximum in between. Thus, there are n rays of various lengths at successive angles $\pi\lambda_1, \pi\lambda_2, \dots, \pi\lambda_n$, to one another as shown in Fig. 2. By suitable choice of the λ_k and α_k , Eq 4 transforms any star-shaped contour onto a unit circle. The points $\gamma_l = e^{i\beta_l}$ on the unit circle in the ζ -plane at which z attains its local maxima can be obtained from

$$\sum_{k=1}^n \lambda_k \cot\left(\frac{\alpha_k - \beta_l}{2}\right) = 0, \quad l = 1, 2, \dots, n \quad (11)$$

The lengths of the rays are given by

$$|r_l| = 4A \prod_{k=1}^n \left| \sin\left(\frac{\beta_l - \alpha_k}{2}\right) \right|^{\lambda_k} \quad (12)$$

Once the α_k , β_k , λ_k , and A are determined from Eqs 6, 9, 11, and 12, the conformal transformation of the exterior of the star-shaped crack onto the exterior of the unit circle is completely defined.

Branches and Derivatives of $\omega(\zeta)$

As mentioned, $\omega(\zeta)$ has multiple branches, and we have selected a particular branch. In application it is convenient to locate the branch cut. There are a number of ways this can be accomplished. The simplest way is to locate the branch cut along the unit circle as shown in Fig. 3. This permits us to have a common branch for functions analytically continued from the outside to the inside of the unit circle, that is, $\bar{\omega}(1/\zeta) = \omega(\zeta)$.

³ This corresponds to selecting the first ray to be on the positive x -axis.

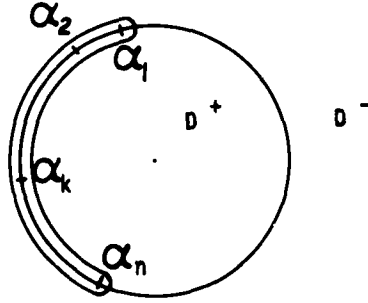


FIG. 3—The branch cut and plus and minus regions in the ζ -plane.

Let us divide the ζ -plane into D^+ and D^- as shown and use σ to denote a boundary point on the unit circle. It is clear that

$$\begin{aligned} \omega^+(\sigma) &= \omega^-(\sigma) \quad \text{for } 0 < \theta < \alpha_1 \quad \text{or} \quad \alpha_n < \theta < 2\pi \\ \omega^+(\sigma) &= \omega^-(\sigma) \exp \left\{ -2\pi i \sum_{k=1}^{l-1} \lambda_k \right\} \quad \text{for } \alpha_{l-1} < \theta < \alpha_l \end{aligned} \tag{13}$$

Equation 13 is the consequence of the irrational function of Eq 4 and leads to the difficulties in obtaining solutions which are discussed, for example, by Bowie [13].

For the elasticity solution we need derivatives of $\omega(\zeta)$ on the boundary. By logarithmic differentiation we have

$$\frac{\omega'(\zeta)}{\omega(\zeta)} = -\frac{1}{\zeta} + \sum_{k=1}^n \frac{\lambda_k}{\zeta - e^{i\alpha_k}} \tag{14}$$

The right hand side of Eq 14 is a proper fraction whose numerator is a polynomial of order n in ζ . The numerator has n roots at $\zeta = \exp(i\beta_k)$, $k = 1, 2, \dots, n$, corresponding to the n crack tips. Hence, Eq 14 may be written in the form [11]

$$\omega'(\zeta)/\omega(\zeta) = [\zeta g(\zeta)]^{-1} \tag{15}$$

where

$$[g(\zeta)]^{-1} = \prod_{k=1}^n \left(\frac{\zeta - e^{i\beta_k}}{\zeta - e^{i\alpha_k}} \right) \tag{16}$$

From Eqs 14 and 16 it is obvious $g(0) = -1$ and $\bar{g}(1/\zeta) = -g(\zeta)$. As expected, $\omega'(\zeta)$ has n zeroes of order one at the tips of the rays. The branches of $\omega'(\zeta)$ are fixed as soon as those of $\omega(\zeta)$ are fixed since $g(\zeta)$ is holomorphic.

In virtue of Eq 13, it is obvious for $\sigma = e^{i\theta}$,

$$\omega'^+(\sigma) = \omega'^-(\sigma) = \frac{1}{\sigma g(\sigma)} \omega^-(\sigma), \quad 0 < \theta < \alpha_1 \quad \text{or} \quad \alpha_n < \theta < 2\pi \quad (17)$$

$$\omega'^+(\sigma) = \frac{1}{\sigma g(\sigma)} \omega^+(\sigma) = \frac{1}{\sigma g(\sigma)} \omega^-(\sigma) \exp \left[-2\pi i \sum_{k=1}^{l-1} \lambda_k \right] \quad \text{for} \quad \alpha_{l-1} < \theta < \alpha_l$$

Taking the complex conjugate and using $\bar{g}(1/\zeta) = -g(\zeta)$, $\bar{\omega}(1/\zeta) = \omega(\zeta)$, we have

$$\frac{\omega^-(\sigma)}{\omega'^-(\sigma)} = \begin{cases} -\frac{1}{\sigma} g(\sigma) & \text{for } 0 < \theta < \alpha_1, \quad \alpha_n < \theta < 2\pi \\ -\frac{1}{\sigma} g(\sigma) \exp \left[2\pi i \sum_{k=1}^{l-1} \lambda_k \right] & \text{for } \alpha_{l-1} < \theta < \alpha_l \end{cases} \quad (18)$$

It was the lack of the study of these branches that led to the fundamental error in Ref 11.

Case of Two Branches and the Asymptotic Scheme

For the deflected crack, shown in Fig. 4 together with its image, the mapping function and its derivatives are

$$\omega(\zeta) = A\zeta^{-1}(\zeta - e^{i\alpha_1})^{1-\gamma/\pi}(\zeta - e^{i\alpha_2})^{1+\gamma/\pi}, \quad 0 < \alpha_1 < \alpha_2 < 2\pi \quad (19)$$

$$\omega'(\zeta) = [\zeta g(\zeta)]^{-1} \omega(\zeta), \quad \omega''(\gamma_2) = \omega(\gamma_2) \frac{(\gamma_2 - \gamma_1)}{\gamma_2(\gamma_2 - e^{i\alpha_1})(\gamma_2 - e^{i\alpha_2})} \quad (20)$$

$$g(\zeta) = \frac{(\zeta - e^{i\alpha_1})(\zeta - e^{i\alpha_2})}{(\zeta - \gamma_1)(\zeta - \gamma_2)}, \quad \gamma_i = e^{i\beta_i} \quad (21)$$

In Eq 21, β_1 and β_2 are determined from

$$\sin\left(\frac{\alpha_1 + \alpha_2}{2} - \beta_1\right) = \frac{\gamma}{\pi} \sin\left(\frac{\alpha_2 - \alpha_1}{2}\right) \quad (22)$$

$$(\alpha_1 + \alpha_2) - (\beta_1 + \beta_2) = \pi$$

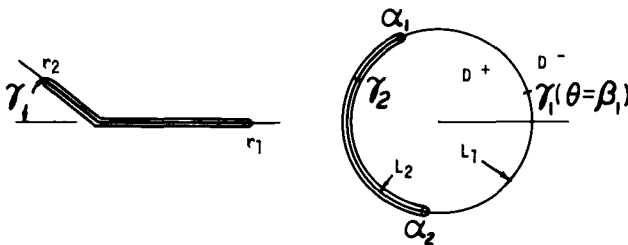


FIG. 4—The deflected crack and its image.

The lengths of the main and propagation branches of the crack are given by Eq 12. In our final solution we shall need the limiting case when the propagation branch approaches zero, that is, $\alpha_1 \rightarrow \pi$, $\alpha_2 \rightarrow \pi$, for fixed γ . In this case it is convenient to choose $\epsilon = \alpha_2 - \alpha_1$, as a parameter for the asymptotic expansion as $|r_2| \rightarrow 0$. In terms of ϵ , the α 's and β 's can be expressed exactly using Eq 22:

$$\begin{aligned} \alpha_1 &= \pi - (\epsilon/2) (1 + \gamma/\pi), & \alpha_2 &= \pi + (\epsilon/2) (1 - \gamma/\pi) \\ \beta_1 &= (m - \epsilon)\gamma/2\pi, & \beta_2 &= \pi - (m + \epsilon)\gamma/2\pi \end{aligned} \quad (23)$$

where

$$m = (2\pi/\gamma) \sin^{-1} \{(\gamma/\pi) \sin(\epsilon/2)\} \quad (24)$$

when $\epsilon \rightarrow 0$ the transform reduces to the classical case of a crack of length $4A$ lying on the positive x -axis, (see Muskhelishvili [14]). The lengths of the main crack and the propagation crack, respectively, are

$$\begin{aligned} \frac{|r_1|}{4A} &= \frac{1}{2} \left| \cos\left(\frac{m\gamma}{2\pi}\right) + \cos\frac{\epsilon}{2} \right| \left| \cos\left(\frac{m\gamma}{4\pi} - \frac{\epsilon}{4}\right) / \cos\left(\frac{m\gamma}{4\pi} + \frac{\epsilon}{4}\right) \right|^{\gamma/\pi} \\ \frac{|r_2|}{4A} &= \left| \sin\left(\frac{m\gamma}{4\pi} - \frac{\epsilon}{4}\right) \right|^{1-\gamma/\pi} \left| \sin\left(\frac{m\gamma}{4\pi} + \frac{\epsilon}{4}\right) \right|^{1+\gamma/\pi} \end{aligned} \quad (25)$$

It is clear from Eq 25 that $|r_2| \rightarrow 0$ and $|r_1| \rightarrow 4A$ as $\epsilon \rightarrow 0$. Boundary values of the derivatives obtained from Eq 18 reduce to

$$\frac{\omega^-(\sigma)}{\omega'^-(\sigma)} = \begin{cases} -\frac{1}{\sigma} g(\sigma), & 0 < \theta < \alpha_1 \text{ or } \alpha_2 < \theta < 2\pi \\ -\frac{1}{\sigma} g(\sigma)e^{-2i\gamma}, & \alpha_1 < \theta < \alpha_2 \end{cases} \quad (26)$$

Certain expansions containing only the first few terms of some pertinent quantities are given in the Appendix.

Reduction of the Problem to Functional Integral Equations

Relevant formulae of the plane problem of elasticity are given in Muskhelishvili [14]:

$$\begin{aligned} z &= \omega(\zeta) \\ \sigma_x + \sigma_y &= 4Re\{\varphi'(\zeta)/\omega'(\zeta)\} \\ \sigma_y - \sigma_x + 2i\tau_{xy} &= 2\{[\bar{\omega}(\zeta)/\omega'(\zeta)] [\varphi'(\zeta)/\omega'(\zeta)]' + [\psi'(\zeta)/\omega'(\zeta)]\} \\ \varphi(\zeta) + [\omega(\zeta)/\omega'(\zeta)] \overline{\varphi'(\zeta)} + \overline{\psi(\zeta)} &= i \int_{AB} (x_n + iy_n) ds + \text{const} \end{aligned} \quad (27)$$

The complex stress functions $\varphi(\zeta)$ and $\psi(\zeta)$ are sectionally holomorphic in D^- (Figs. 3 and 4) and their asymptotic values as $z = A\zeta$, $\zeta \rightarrow \infty$ for

arbitrary uniform loads at infinity, shown in Fig. 1, are given by (assuming no traction on the crack)

$$\begin{aligned}\varphi(\zeta) &= \Gamma A\zeta + \varphi_0(\zeta) \\ \psi(\zeta) &= \Gamma' A\zeta + \psi_0(\zeta)\end{aligned}\tag{28}$$

where $\varphi_0(\zeta)$ and $\psi_0(\zeta)$ are holomorphic functions including infinity and Γ, Γ' in terms of stresses N_1, N_2 at infinity are

$$\begin{aligned}\Gamma &= (N_1 + N_2)/4 + i2\mu\epsilon_\infty/(1 + \kappa) \\ \Gamma' &= -(N_1 - N_2)e^{-2i\alpha}/2\end{aligned}$$

For our problem, taking $\varphi_0(\infty) = \psi_0(\infty) = 0$ Eqs 28 become

$$\varphi(\zeta) = \Gamma A\zeta, \quad \psi(\zeta) = \Gamma' A\zeta \quad \text{as } \zeta \rightarrow \infty\tag{29}$$

This indicates a pole of order one for $\varphi(\zeta)$ and $\psi(\zeta)$ at infinity. In terms of φ and ψ the traction free boundary condition over the unit circle ρ in the ζ -plane may be written in the form

$$\varphi^-(\sigma) + \frac{\omega^-(\sigma)}{\omega'^-(\sigma)} \overline{\varphi'^-(\sigma)} + \overline{\psi^-(\sigma)} = \text{constant}, \quad \sigma \text{ on } \rho\tag{30}$$

The unknown functions $\varphi(\zeta)$ and $\psi(\zeta)$ can be determined to within an arbitrary constant from Eq 30. Furthermore, the constant on the right side of Eq 30 must have the same value for all σ on ρ . To obtain φ and ψ , we get from Eq 30

$$\frac{1}{2\pi i} \oint_{\rho} \frac{\varphi^-(\sigma) d\sigma}{\sigma - \zeta} + \frac{1}{2\pi i} \oint_{\rho} \frac{\omega^-(\sigma)}{\omega'^-(\sigma)} \frac{\overline{\varphi'^-(\sigma)}}{\sigma - \zeta} d\sigma + \frac{1}{2\pi i} \oint_{\rho} \frac{\overline{\psi^-(\sigma)}}{\sigma - \zeta} d\sigma = 0\tag{31}$$

Wherever it is necessary, the integrals in Eq 31 should be understood as Cauchy principal values. Dividing ρ into L_1 and L_2 as shown in Fig. 4 and substituting Eq 26 into Eq 31, we obtain

$$\begin{aligned}\frac{1}{2\pi i} \oint_{\rho} \frac{\varphi^-(\sigma) d\sigma}{\sigma - \zeta} + \frac{1}{2\pi i} \oint_{\rho} \left\{ \psi^-(\sigma) - \frac{g(\sigma)}{\sigma} \overline{\varphi'^-(\sigma)} \right\} \frac{d\sigma}{\sigma - \zeta} \\ + \frac{(1 - e^{-2i\gamma})}{2\pi i} \int_{L_2} \frac{g(\sigma) \overline{\varphi'^-(\sigma)}}{\sigma \sigma - \zeta} d\sigma = 0\end{aligned}\tag{32}$$

In view of Eq 20, some of the integrals in Eq 32 have poles on ρ .⁴ As can be seen from Eq 30 that $\{\psi^-(\sigma) - \sigma^{-1}g(\sigma) \overline{\varphi'^-(\sigma)}\}$ ⁵ has removable poles on L_1 . Denoting L'_2 as an indented contour, Fig. 5, using Cauchy's integral

⁴ Muskhelishvili [14] avoids these poles by solving the problem of an elliptical hole, that is, $m = 1$. Then a straight crack is considered as the limiting case with $m = 1$.

⁵ In fact, there is no pole at γ_2 as $\epsilon \rightarrow 0$ and the pole at γ_1 is indeed removable.

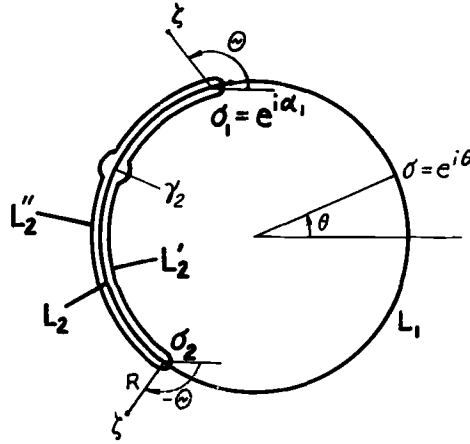


FIG. 5—The branch cut L_2 and the indented contours L_2' and L_2'' .

formula and using properties of analytic function $\bar{\varphi}(1/\zeta)$, $\bar{\psi}(1/\zeta)$ in D^+ with their asymptotic values known from Eq 29, we have

$$\begin{aligned} \varphi(\zeta) = & \Gamma A \zeta - \frac{A}{\zeta} (\bar{\Gamma}' + \bar{\Gamma}) \\ & + (1 - e^{-2i\gamma}) \frac{1}{2\pi i} \int_{L_2'} \frac{1}{\sigma} g(\sigma) \frac{\overline{\varphi'(\sigma)}}{\sigma - \zeta} d\sigma, \zeta \text{ in } D^- \end{aligned} \quad (33)$$

This is the functional integral equation for $\varphi(\zeta)$. Taking the complex conjugate of Eq 30 and following a similar procedure as just indicated, we get the equation for the determination of $\psi(\zeta)$:

$$\begin{aligned} \psi(\zeta) = & -\bar{\Gamma} A \zeta^{-1} + A \zeta (\Gamma' + \Gamma) - \zeta g(\zeta) \varphi'(\zeta) \\ & - \frac{(1 - e^{2i\gamma})}{2\pi i} \int_{L_2''} \frac{\sigma g(\sigma) \varphi'(\sigma)}{\sigma - \zeta} d\sigma, \zeta \text{ in } D^+ \end{aligned} \quad (34)$$

The integral in Eq 34 is taken over the contour L_2'' indented from outside, Fig. 5.

Plemelj Formula for the Integrals

To check the validity of Eqs 33 and 34, we need boundary values of the integrals appearing in Eqs 33 and 34. Denote

$$\Omega_1(\zeta) = \frac{1}{2\pi i} \int_{L_2'} \frac{1}{t} g(t) \frac{\overline{\varphi'(t)}}{t - \zeta} dt \quad (35)$$

$$\Omega_2(\zeta) = \frac{1}{2\pi i} \int_{L_2''} t g(t) \frac{\varphi'(t)}{t - \zeta} dt \quad (36)$$

We obtain from Eq 36, Eq 35

$$\overline{\Omega_2}(1/\zeta) = -D_0 + \Omega_1(\zeta), \quad \zeta \text{ in } D^+ \quad (37)$$

Where D_0 is an unknown constant given by

$$D_0 = \frac{1}{2\pi i} \int_{L_2'} \frac{1}{t^2} g(t) \overline{\varphi'^-(t)} dt = \text{constant} \quad (38)$$

On the boundary, Eq 37 gives

$$\overline{\Omega_2^-(\sigma)} = -D_0 + \Omega_1^+(\sigma) \quad \text{for } \sigma \text{ on } \rho = L_1 + L_2 \quad (39)$$

Now using Plemelj formula for $\Omega_1(\zeta)$, we have

$$\Omega_1^+(\sigma) - \Omega_1^-(\sigma) = \begin{cases} \frac{1}{\sigma} g(\sigma) \overline{\varphi'^-(\sigma)}, & \text{for } \sigma \text{ on } L_2' \\ 0, & \text{for } \sigma \text{ on } L_1 \end{cases} \quad (40)$$

It is obvious that

$$\Omega_1^-(\sigma) - \overline{\Omega_2^-(\sigma)} = \begin{cases} D_0 - \frac{1}{\sigma} g(\sigma) \overline{\varphi'^-(\sigma)}, & \text{for } \sigma \text{ on } L_2' \\ D_0, & \text{for } \sigma \text{ on } L_1 \end{cases} \quad (41)$$

Equation 41 is the Plemelj formula for the integrals Ω_1 and Ω_2 . With Eqs 41, 33, and 34, it is easily seen that Eq 30 is satisfied with the same constant on L_1 and L_2 .

The Iteration Procedure

The functional integral Eqs 33 and 34, in general, are not amenable to a closed form solution. We use the time-honored iteration procedure. The first iteration is carried out exactly. The asymptotic solution of the first iteration as $\epsilon \rightarrow 0$ (that is, the propagation branch approaches zero) immediately indicates the procedure to obtain the solution for any higher order iteration. This gives us the recurrence relation for the derivatives of φ and ψ at a point. This recursion formula leads to the point-wise exact solution at the tip of the crack.

Let

$$\varphi_0(\zeta) = \Gamma A \zeta - \zeta^{-1} A (\overline{\Gamma}' + \overline{\Gamma}) \quad (42)$$

then

$$\varphi_1(\zeta) = \varphi_0(\zeta) + (1 - e^{-2i\gamma}) \Omega_{1,0}(\zeta) \quad (43)$$

$$\varphi_n(\zeta) = \varphi_0(\zeta) + (1 - e^{-2i\gamma}) \Omega_{1,n-1}(\zeta)$$

where

$$\Omega_{1,n}(\zeta) = \frac{1}{2\pi i} \int_{L_2'} \frac{1}{t} g(t) \frac{\overline{\varphi_n'^-(t)}}{t - \zeta} dt \quad (44)$$

Carrying out the integration for the first order iteration, we have

$$\varphi_1(\zeta) = \Gamma A \zeta - \zeta^{-1} A (\bar{\Gamma}' + \bar{\Gamma}) + \frac{A(1 - e^{-2i\gamma})}{2\pi i} [\bar{\Gamma} I_3 + (\Gamma' + \Gamma) I_4] \quad (45)$$

where

$$I_3 = \frac{g(\zeta)}{\zeta} \log\left(\frac{\zeta - e^{i\alpha_2}}{\zeta - e^{i\alpha_1}}\right) - \frac{i(\alpha_1 - \alpha_2)}{\zeta} + \frac{A_1}{\zeta - \gamma_1} \log a + \frac{A_2}{\zeta - \gamma_2} \log b \quad (46)$$

$$I_4 = (e^{i\alpha_2} - e^{i\alpha_1}) + \zeta g(\zeta) \log\left(\frac{\zeta - e^{i\alpha_2}}{\zeta - e^{i\alpha_1}}\right) - A_1 \gamma_1 \left(1 - \frac{\zeta}{\zeta - \gamma_1}\right) \log a - A_2 \gamma_2 \left(1 - \frac{\zeta}{\zeta - \gamma_2}\right) \log b \quad (47)$$

In Eq 44, the function g is written in the form

$$\frac{1}{\zeta} g(\zeta) = -\frac{1}{\zeta} + \frac{A_1}{\zeta - \gamma_1} + \frac{A_2}{\zeta - \gamma_2} \quad (48)$$

where

$$A_1 = \lim_{\zeta \rightarrow \gamma_1} (\zeta - \gamma_1) g(\zeta) \zeta^{-1} = \frac{(\gamma_1 - e^{i\alpha_1})(\gamma_1 - e^{i\alpha_2})}{\gamma_1(\gamma_1 - \gamma_2)} \quad (49)$$

$$A_2 = \lim_{\zeta \rightarrow \gamma_2} (\zeta - \gamma_2) g(\zeta) \zeta^{-1} = \frac{(\gamma_2 - e^{i\alpha_1})(\gamma_2 - e^{i\alpha_2})}{\gamma_2(\gamma_2 - \gamma_1)} \quad (50)$$

In Eqs 46 and 47 the constants a and b are

$$a = \frac{\gamma_1 - e^{i\alpha_1}}{\gamma_1 - e^{i\alpha_2}}, \quad b = \frac{\gamma_2 - e^{i\alpha_1}}{\gamma_2 - e^{i\alpha_2}} \quad (51)$$

Similarly,

$$\psi_0(\zeta) = -\bar{\Gamma} A \zeta^{-1} + (\Gamma' + \Gamma) A \zeta - \zeta g(\zeta) \varphi_0'(\zeta) \quad (52)$$

$$\psi_1(\zeta) = \psi_0(\zeta) - (1 - e^{-2i\gamma}) \zeta g(\zeta) \Omega_{1,0}'(\zeta) - (1 - e^{2i\gamma}) \Omega_{2,0}(\zeta) \quad (53)$$

$$\psi_n(\zeta) = \psi_0(\zeta) - (1 - e^{-2i\gamma}) \zeta g(\zeta) \Omega_{1,n-1}'(\zeta) - (1 - e^{2i\gamma}) \Omega_{2,n-1}(\zeta) \quad (54)$$

where

$$\Omega_{2,n}(\zeta) = \frac{1}{2\pi i} \int_{L_2''} t g(t) \frac{\varphi_n'-(t)}{t - \zeta} dt \quad (55)$$

The first order iteration of $\psi(\zeta)$ is

$$\begin{aligned} \psi_1(\zeta) = & \psi_0(\zeta) - \zeta g(\zeta) (1 - e^{-2i\gamma}) \frac{A}{2\pi i} [\bar{\Gamma} I_3'(\zeta) + (\Gamma' + \Gamma) I_4'(\zeta)] \\ & + (1 - e^{2i\gamma}) \frac{A_2 A}{\zeta - \gamma_2} (\gamma_2^2 \Gamma + \bar{\Gamma}' + \bar{\Gamma}) - (1 - e^{2i\gamma}) \frac{A}{2\pi i} \\ & \times [\Gamma I_4 + (\bar{\Gamma}' + \bar{\Gamma}) I_3] \end{aligned} \quad (56)$$

It should be noted from the zeroes of $g(\zeta)$ and from Eq 51 that the function $\varphi_1(\zeta)$ in Eq 45 has neither the logarithmic singularities at $e^{i\alpha_1}$, $e^{i\alpha_2}$ nor the poles at γ_1 , γ_2 . On the other hand, there exist poles in $\psi(\zeta)$ at γ_1 and γ_2 . It can also be seen from Eqs 45 to 53 that in the limit as $\epsilon \rightarrow 0$ (namely, $\alpha_2 \rightarrow \alpha_1$), $\Omega_{1,0}(\zeta) \rightarrow 0$, $\Omega_{2,0}(\zeta) \rightarrow 0$, and $\varphi_1(\zeta) \rightarrow \varphi_0(\zeta)$. It will become clear in the sequel that the derivatives of $\Omega_{1,0}$, $\Omega_{1,1}$, etc. at the tip of the propagation branch ($\zeta \rightarrow \gamma_2$) does not vanish. It is necessary now to study the branches of the logarithmic terms that appeared in Eqs 46 and 47.

Branches of a Function with Logarithmic Singularity on a Unit Circle

Let

$$f(\zeta) = \log\left(\frac{\zeta - e^{i\alpha_2}}{\zeta - e^{i\alpha_1}}\right) \tag{57}$$

$f(\zeta)$ has branch points at $e^{i\alpha_1}$ and $e^{i\alpha_2}$ on the unit circle $\rho = L_1 + L_2$. Select a branch, analytic in D^- such that $f(\zeta) \rightarrow 0$ as $\zeta \rightarrow \infty$. The branch cut can be chosen in many ways. One such cut is shown in Fig. 5⁶ and we write Eq 57 in the form

$$f(\zeta) = \log\left|\frac{\zeta - e^{i\alpha_2}}{\zeta - e^{i\alpha_1}}\right| + i \arg(\zeta - e^{i\alpha_2}) - i \arg(\zeta - e^{i\alpha_1}) \tag{58}$$

Let

$$\zeta - e^{i\alpha_2} = R_2 e^{i\theta_2}, \quad \zeta - e^{i\alpha_1} = R_1 e^{i\theta_1} \tag{59}$$

where θ_1 and θ_2 in terms of θ , α_1 and α_2 are

$$\theta_1 = \begin{cases} (\pi/2) + (\theta + \alpha_1)/2 & \text{for } \zeta \text{ on } L_2 \\ -(\pi/2) + (\theta + \alpha_1)/2 & \text{for } \zeta \text{ on } L_1 \end{cases} \tag{60}$$

$$\theta_2 = -(\pi/2) + (\theta + \alpha_2)/2 \quad \text{for } \zeta \text{ on } L_1 + L_2$$

Hence, on the boundary $\sigma = e^{i\theta}$, we have

$$f^-(\sigma) = \begin{cases} -i\pi + \log\left|\frac{\sigma - e^{i\alpha_2}}{\sigma - e^{i\alpha_1}}\right| + \frac{i}{2}(\alpha_2 - \alpha_1), & \sigma \text{ on } L_2 \\ \log\left|\frac{\sigma - e^{i\alpha_2}}{\sigma - e^{i\alpha_1}}\right| + \frac{i}{2}(\alpha_2 - \alpha_1), & \sigma \text{ on } L_1 \end{cases} \tag{61}$$

In the limit as $\alpha_2 \rightarrow \alpha_1$, Eq 61 reduces to

$$f^-(\gamma_2) = \begin{cases} -i\pi & \text{on } L_2 \\ 0 & \text{on } L_1 \end{cases} \quad (L_2 \text{ degenerated to a point } \gamma_2) \tag{62}$$

It is precisely this property of the logarithmic function which leads (as

⁶ Such branches were studied by Gakhov [15] in connection with Schwartz problem.

will be seen later) to the result that the solution in the limit as $\epsilon \rightarrow 0$ is not the same as the solution without the propagation branch.

Simultaneous Expansion and the Point-Wise Exact Solution

As will be seen in the next section, the computation of the energy release rate requires the expansion of $\varphi'(\zeta)$ and $\psi'(\zeta)$ etc. around the crack tip $\zeta = \gamma_2$. Such computations were carried out for zero and first order iterations. It became clear that the only contribution to energy release rate came from the values of $\varphi'(\gamma_2), \psi'(\gamma_2)$ in the limit as $\zeta \rightarrow \gamma_2$ and $\epsilon \rightarrow 0$, simultaneously. In this section we present such limits and the process which will immediately lead to the point-wise exact solution.

With the help of the Appendix, we have

$$\frac{1}{\zeta} g(\zeta) = \frac{i\gamma\epsilon}{2\pi} + (\zeta - \gamma_2) \left(\frac{1}{2} + \frac{3}{2} \frac{i\gamma\epsilon}{\pi} \right) + O(\zeta - \gamma_2)^2 + O(\epsilon^2) \quad (63)$$

Substituting Eq 63 and the similar expansion for $\varphi_1'(\zeta)$ into Eq 44 and making use of Eq 62, we have

$$\lim_{\substack{\zeta \rightarrow 0 \\ \zeta \rightarrow \gamma_2}} \begin{cases} \Omega_{1,0}(\gamma_2) = 0 \\ \Omega_{1,0}'(\gamma_2) = -\frac{1}{4} \overline{\varphi_0'(\gamma_2)} \end{cases} \quad (64)$$

The validity of Eq 64 can be seen from the exact value of $\Omega_{1,0}(\zeta)$ which is implicitly given by Eq 45. After some manipulation, the second and higher order iterations were carried out and the following results are obtained:

$$\Omega_{1,1}'(\gamma_2) = -\frac{1}{4} \overline{\varphi_1'(\gamma_2)}, \quad \Omega_{1,n}'(\gamma_2) = -\frac{1}{4} \overline{\varphi_n'(\gamma_2)} \quad (65)$$

This leads to the recurrence relation

$$\varphi_n'(\gamma_2) = \varphi_0'(\gamma_2) - \frac{1}{4} (1 - e^{-2i\gamma}) \overline{\varphi_{n-1}'(\gamma_2)} \quad (66)$$

for any order of iteration. In the limit as $n \rightarrow \infty$, $\varphi_n'(\gamma_2) \rightarrow \varphi'(\gamma_2)$ where $\varphi'(\gamma_2)$ is the exact value. Hence

$$\varphi'(\gamma_2) = \varphi_0'(\gamma_2) - \frac{1}{4} (1 - e^{-2i\gamma}) \overline{\varphi'(\gamma_2)} \quad (67)$$

Taking the complex conjugate of Eq 67 and putting $\overline{\varphi'(\gamma_2)}$ into the right-hand side of Eq 67 we have

$$\varphi'(\gamma_2) \left\{ 1 - \frac{(1 - e^{-2i\gamma})(1 - e^{2i\gamma})}{4} \right\} = \varphi_0'(\gamma_2) - \frac{(1 - e^{-2i\gamma})}{4} \overline{\varphi_0'(\gamma_2)} \quad (68)$$

Using Eq 42, this equation becomes (with $\Gamma = \bar{\Gamma}$)

$$\varphi'(\gamma_2) = \frac{4A}{3 + \cos^2 \gamma} \left\{ (2\Gamma + \bar{\Gamma}') - \frac{1 - e^{-2i\gamma}}{4} (2\Gamma + \Gamma') \right\} \quad (69)$$

This is the point-wise exact solution of φ' , and it clearly shows that φ' at the crack tip is different from that of a straight crack (no propagation branch). By a similar procedure we have

$$\Omega_{2,n'}(\gamma_2) = -\frac{1}{4} \varphi_n'(\gamma_2) \quad (70)$$

For $n \rightarrow \infty$ and $\Gamma = \bar{\Gamma}$, the following result is obtained with the help of Eq 63:

$$\psi'(\gamma_2) = A(2\Gamma + \Gamma') - \frac{1}{4}(1 + e^{2i\gamma})\varphi'(\gamma_2) \quad (71)$$

where $\varphi'(\gamma_2)$ is given by Eq 69.

Computations of Energy Release Rate

As was pointed out in the introduction, the propagation path of a crack subjected to combined loads is not collinear to its original plane. The integrals involved in Irwin's [1] and Bueckner's [2] approaches to obtain the energy release rate cannot be applied directly to the present case due to the discontinuity introduced by the deflected crack extension. However, the basic conservation laws, also known as path independent integrals, do not require such "virtual" motion of the crack. These conservation laws have achieved a place of prominence in the field of fracture mechanics, Rice [16], Budiansky and Rice [17], Knowles and Sternberg [3], Sanders [18], etc. There are basically four such integrals [17,3]. For two dimensions these are

$$J_1 = \oint_C \left(W dy - \bar{\tau} \cdot \frac{d\bar{u}}{dx} dl \right) = \oint_C (W n_1 - \tau_i u_{i,1}) dl \quad (72)$$

$$J_2 = - \oint_C \left(W dx + \bar{\tau} \cdot \frac{d\bar{u}}{dy} dl \right) = \oint_C (W n_2 - \tau_i u_{i,2}) dl \quad (73)$$

$$L = \oint_C \epsilon_{3ij} (W x_j n_i + \tau_i u_j - \tau_k u_{k,i} x_j) dl \quad (74)$$

$$M = \oint_C (W x_i n_i - \tau_k u_{k,i} x_i) dl \quad (75)$$

Where C is a contour in x - y plane ($x_1 = x$, $x_2 = y$) around a crack tip, W is the energy density, $\bar{\tau}$ is the traction vector on C having unit outward normal \bar{n} , \bar{u} is the displacement vector, ϵ_{3ij} is the rotation tensor. The path independence can easily be shown by the use of Green's formula and the equations of equilibrium [16].

It has been shown [17] that J_1, J_2 give the energy release rate per unit crack tip extension in the x - and y -directions, respectively, and L, M the energy release rate per unit crack rotation and expansion, respectively. In our case both L and M vanish in the limit as the propagation branch vanishes, and J_1, J_2 give us the required energy release rate. For application

to our problem it is convenient to use J_1, J_2 in terms of complex potentials which have been derived in Ref 17.

$$J_1 + iJ_2 = -\frac{2}{E} i \left\{ \int_A^B [\varphi'(z)]^2 dz - 2 \int_A^B \overline{\varphi'(z)} \psi'(z) dz - \left[z \overline{\varphi'(z)^2} \right]_A^B \right\} \quad (76)$$

By the mapping transformation $z = \omega(\zeta)$, the Eq 76 in the ζ -plane can be written in the form:

$$J_1 + iJ_2 = -\frac{2}{E} i \left\{ \int_l^u \frac{\varphi'^2(\zeta)}{\omega'(\zeta)} d\zeta - 2 \int_l^u \frac{\overline{\varphi'(\zeta)} \psi'(\zeta)}{\omega'(\zeta)} d\zeta - \left[\omega(\zeta) \overline{\left(\frac{\varphi'(\zeta)}{\omega'(\zeta)} \right)^2} \right]_l^u \right\} \quad (77)$$

Where l and u are points in the ζ -plane corresponding to A and B in the z -plane, respectively. It is required to compute the energy release rate in an arbitrary direction for a crack tip located near the origin; we need to know the expression of $J_1 + iJ_2$ under the translation and rotation of the coordinate system.

Using the superscript ⁽¹⁾ to refer to the new coordinate system, we have for translation, p. 135 [14]

$$\begin{aligned} z &= z^{(1)} + z_0 \\ \Phi^{(1)}(z^{(1)}) &= \Phi(z) = \Phi(z^{(1)} + z_0) \\ \Psi^{(1)}(z^{(1)}) &= \Psi(z) + \bar{z}_0 \Phi^{(1)'}(z^{(1)}) \end{aligned} \quad (78)$$

where $\Phi(z) = \varphi'(z)$, $\Psi(z) = \psi'(z)$. Writing $A^{(1)} = A - z_0$, $B^{(1)} = B - z_0$, and substituting Eq 78 into Eq 76, we obtain

$$J_1^{(1)} + iJ_2^{(1)} = J_1 + iJ_2 \quad (79)$$

This shows that $J_1 + iJ_2$ is invariant for the translation of coordinates. Similarly if the coordinate system rotates counter-clockwise, through an angle λ_0 we have the following results

$$\left. \begin{aligned} z &= z^{(1)} e^{i\lambda_0} \\ \Phi^{(1)}(z^{(1)}) &= \Phi(z) = \Phi(z^{(1)} e^{i\lambda_0}) \\ \Psi^{(1)}(z^{(1)}) &= e^{2i\lambda_0} \Psi(z^{(1)} e^{i\lambda_0}) \end{aligned} \right\} \quad (80)$$

$$J_1^{(1)} + iJ_2^{(1)} = e^{-i\lambda_0} (J_1 + iJ_2) \quad (81)$$

Taking $\lambda_0 = \pi - \gamma$ in Eq 81, we get the energy release rate $\mathcal{G}(\gamma)$ in an arbitrary direction γ (Fig. 1):

$$\mathcal{G}(\gamma) = -(\cos \gamma)J_1 + (\sin \gamma)J_2 \quad (82)$$

Integration Path in the ζ -Plane

For convenience, we choose the path as shown in Fig. 6. In the limit as $R \rightarrow 0$ the path of integration in the ζ -plane corresponds to the integration around the crack tip in the z -plane. After the integration is completed, we first take the limit as $R \rightarrow 0$ and then let the propagation branch vanish (that is, $\alpha_2 - \alpha_1 = \epsilon \rightarrow 0$). Expansions of pertinent quantities around $\zeta = \gamma_2$ (where $\omega'(\gamma_2) = 0$) are given by

$$\omega(\zeta) = \omega(\gamma_2) + \frac{1}{2}(\zeta - \gamma_2)^2 \omega''(\gamma_2) + \frac{1}{6}(\zeta - \gamma_2)^3 \omega'''(\gamma_2) + \dots \quad (83)$$

$$\frac{1}{\omega'(\zeta)} = \frac{1}{\omega''(\gamma_2)(\zeta - \gamma_2)} \{1 + C_1(\zeta - \gamma_2) + C_2(\zeta - \gamma_2)^2 + C_3(\zeta - \gamma_2)^3 + \dots\} \quad (84)$$

$$\left(\frac{1}{\omega'(\zeta)}\right)^2 = \left(\frac{1}{\omega''(\gamma_2)}\right)^2 \frac{1}{(\zeta - \gamma_2)^2} \{1 + 2C_1(\zeta - \gamma_2) + C_2'(\zeta - \gamma_2)^2 + C_3'(\zeta - \gamma_2)^3 + \dots\} \quad (85)$$

where

$$\begin{aligned} C_1 &= -\frac{1}{2} \frac{\omega'''(\gamma_2)}{\omega''(\gamma_2)}, \\ C_2 &= -\frac{1}{6} \frac{\omega^{IV}(\gamma_2)}{\omega''(\gamma_2)} + \frac{1}{4} \left(\frac{\omega'''(\gamma_2)}{\omega''(\gamma_2)}\right)^2, \\ C_2' &= -\frac{1}{3} \frac{\omega^{IV}(\gamma_2)}{\omega''(\gamma_2)} + \frac{3}{4} \left(\frac{\omega'''(\gamma_2)}{\omega''(\gamma_2)}\right)^2, \text{ etc.} \end{aligned} \quad (86)$$

Let $\zeta - \gamma_2 = Re^{i\theta}$ and in view of Eqs 23 and 48 through 50, the following integrals can be evaluated

$$\begin{aligned} \int_l^u \frac{d\zeta}{(\zeta - \gamma_2)} &= \pi i, & \int_l^u \frac{d\zeta}{(\zeta - \gamma_2)^2} &= -\frac{2i}{R} \exp\left[\frac{i\gamma}{2\pi}(m + \epsilon)\right] \\ \int_l^u \frac{d\zeta}{(\zeta - \gamma_2)^3} &= 0, & \int_l^u d\zeta &= -2iR \exp\left[-\frac{i\gamma}{2\pi}(m + \epsilon)\right] \end{aligned} \quad (87)$$

Where $l = (\pi/2) - \gamma(m + \epsilon)/(2\pi)$, $u = (3\pi/2) - \gamma(m + \epsilon)/(2\pi)$. It is clear from Eq 84 that a pole of order one at $\zeta = \gamma_2$ corresponds to a singularity of order one half in the z -plane. From the iteration procedure we see that $\varphi'(\zeta)$ does not have any poles in the ζ -plane. However, as long as $\epsilon \neq 0$ (the propagation branch is finite) $\psi'(\zeta)$ involves a pole of order two in view of Eqs 48 and 53. But the singular term due to $\psi'(\zeta)$ in the integrals, Eq 77, is annihilated by the jump term (the last term of Eq 77). Carrying out the integration with the help of Eqs 83 to 87 and 48 for the zero order and the first order iterations, we find the only contribution to

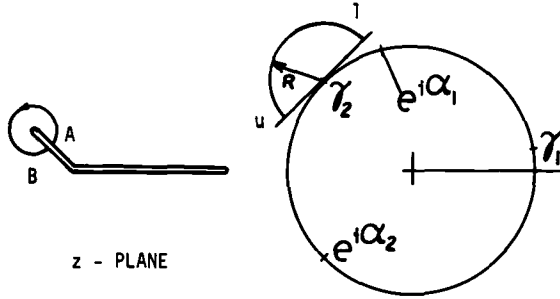


FIG. 6—Path of integration.

the integrals in Eq 77, in the limit as $R \rightarrow 0$ and then $\epsilon \rightarrow 0$, is due to simultaneous expansions of φ' and ψ' at $\zeta = \gamma_2$. The details are too lengthy to be included here; the results read

$$J_1 + iJ_2 = \frac{2\pi}{E} \left\{ \frac{\varphi'(\gamma_2)}{\omega''(\gamma_2)} + \overline{\left(\frac{2\varphi'(\gamma_2)\psi'(\gamma_2)}{\omega''(\gamma_2)} \right)} \right\} \quad (88)$$

Substituting into Eq 88 the asymptotic expansion for $\omega''(\gamma_2)$ given in the Appendix, $\varphi'(\gamma_2)$ and $\psi'(\gamma_2)$ given by Eqs 69 and 71 with $\Gamma = \bar{\Gamma}$, $2\Gamma + \bar{\Gamma}' = \sigma_y^\infty - i\tau_{xy}^\infty$, $2\Gamma + \Gamma' = \sigma_y^\infty + i\tau_{xy}^\infty$, we obtain

$$J_1 = -\frac{\pi A}{2E} \left(\frac{1 - \gamma/\pi}{1 + \gamma/\pi} \right)^{\gamma/\pi} \left(\frac{4}{3 + \cos^2 \gamma} \right)^2 \{ (5 \cos \gamma - \cos^3 \gamma) \sigma_y^{\infty 2} + 6 \sin^3 \gamma \sigma_y^\infty \tau_{xy}^\infty + (7 \cos^3 \gamma - 3 \cos \gamma) \tau_{xy}^{\infty 2} \} \quad (89)$$

$$J_2 = \frac{\pi A}{2E} \left(\frac{1 - \gamma/\pi}{1 + \gamma/\pi} \right)^{\gamma/\pi} \left(\frac{4}{3 + \cos^2 \gamma} \right)^2 \{ \sin \gamma (1 - \cos^2 \gamma) \sigma_y^{\infty 2} + (2 \cos \gamma + 6 \cos^3 \gamma) \sigma_y^\infty \tau_{xy}^\infty + \sin \gamma (9 + 7 \cos^2 \gamma) \tau_{xy}^{\infty 2} \} \quad (90)$$

In virtue of Eq 82, the final result is

$$\mathcal{G}(\gamma) = \frac{\pi A}{2E} \left(\frac{1 - \gamma/\pi}{1 + \gamma/\pi} \right)^{\gamma/\pi} \left(\frac{4}{3 + \cos^2 \gamma} \right)^2 \{ (1 + 3 \cos^2 \gamma) \sigma_y^{\infty 2} + 8 \sin \gamma \cos \gamma \sigma_y^\infty \tau_{xy}^\infty + (9 - 5 \cos^2 \gamma) \tau_{xy}^{\infty 2} \} \quad (91)$$

This equation gives the energy release rate for any angle γ in the limit as the propagation branch goes to zero and the main branch is a straight crack of length $4A$. We may extend Eq 91 into the following parametric form with $K_{\text{I}} = \sigma_y^\infty \sqrt{\pi 2A}$ and $K_{\text{II}} = \tau_{xy}^\infty \sqrt{\pi 2A}$

$$\mathcal{G}(\gamma) = \frac{1}{4E} \left(\frac{1 - \gamma/\pi}{1 + \gamma/\pi} \right)^{\gamma/\pi} \left(\frac{4}{3 + \cos^2 \gamma} \right)^2 \{ (1 + 3 \cos^2 \gamma) K_{\text{I}}^2 + 8 \sin \gamma \cos \gamma K_{\text{I}} K_{\text{II}} + (9 - 5 \cos^2 \gamma) K_{\text{II}}^2 \} \quad (3)$$

The advantage of Eq 3 is that now it can be applied to any crack, provided that the values of K_I , K_{II} are known at the crack tip.

Stress Intensity Factors

The stress intensity factors for the tip of the propagation branch in the limit as the branch goes to zero can be computed from the formula given by Andersson [11]

$$K = K_I - iK_{II} = \frac{2\sqrt{\pi} \varphi'(\gamma_2)}{[e^{i\delta}\omega''(\gamma_2)]^{1/2}} \quad (92)$$

where $\varphi'(\gamma_2)$ is given by Eq 69, $\omega''(\gamma_2)$ in the Appendix and $\delta = \pi - \gamma$ is the angle between the propagation branch and the main branch. The stress intensity factors thus obtained are different in meaning from those of the conventional definition, where the crack extension is assumed to be in the plane of the original crack. Let us use $K_I^{(2)}$, $K_{II}^{(2)}$ to denote the stress intensity factors obtained from the limiting process as the propagation branch goes to zero; we have from Eq 92

$$K_I^{(2)}(\gamma) = \sqrt{2\pi A} \left(\frac{4}{3 + \cos^2\gamma} \right) \left(\frac{1 - \gamma/\pi}{1 + \gamma/\pi} \right)^{\gamma/2\pi} \left(\sigma_y^\infty \cos \gamma + \frac{3}{2} \tau_{xy}^\infty \sin \gamma \right) \quad (93)$$

$$K_{II}^{(2)}(\gamma) = \sqrt{2\pi A} \left(\frac{4}{3 + \cos^2\gamma} \right) \left(\frac{1 - \gamma/\pi}{1 + \gamma/\pi} \right)^{\gamma/2\pi} \left(\tau_{xy}^\infty \cos \gamma - \frac{1}{2} \sigma_y^\infty \sin \gamma \right) \quad (94)$$

In the beginning of the paper, we pointed out that Eq 2 is not valid for the combined Mode I and Mode II loading condition unless it is interpreted properly. Now inserting the newly defined $K_I^{(2)}(\gamma)$ and $K_{II}^{(2)}(\gamma)$ into the Eq 2, we get

$$\begin{aligned} \mathcal{G}(\gamma) &= \frac{1}{E} [(K_I^{(2)}(\gamma))^2 + (K_{II}^{(2)}(\gamma))^2] \\ &= \frac{\pi A}{2E} \left(\frac{1 - \gamma/\pi}{1 + \gamma/\pi} \right)^{\gamma/\pi} \left(\frac{4}{3 + \cos^2\gamma} \right)^2 \{ (1 + 3 \cos^2 \gamma) \sigma_y^{\infty 2} \\ &\quad + 8 \sin \gamma \cos \gamma \sigma_y^\infty \tau_{xy}^\infty + (9 - 5 \cos^2 \gamma) \tau_{xy}^{\infty 2} \} \quad (95) \end{aligned}$$

The prior expression, which is exactly the same as Eq 91, indicates that the simple Irwin's formula, Eq 2, for computing the energy release rate can be extended to cracks under combined loads if the stress intensity factors involved in Eq 2 are interpreted as the "angular" stress intensity factors, $K_I^{(2)}$ and $K_{II}^{(2)}$. The relations between the "angular" and the "conventional" stress intensity factors can easily be obtained from Eqs 93 and 94.

$$K_I^{(2)}(\gamma) = \left(\frac{4}{3 + \cos^2\gamma} \right) \left(\frac{1 - \gamma/\pi}{1 + \gamma/\pi} \right)^{\gamma/2\pi} \left\{ K_I \cos \gamma + \frac{3}{2} K_{II} \sin \gamma \right\} \quad (96)$$

$$K_{II}^{(2)}(\gamma) = \left(\frac{4}{3 + \cos^2 \gamma} \right) \left(\frac{1 - \gamma/\pi}{1 + \gamma/\pi} \right)^{\gamma/2\pi} \left\{ K_{II} \cos \gamma - \frac{1}{2} K_I \sin \gamma \right\} \quad (97)$$

It should be noted from Eqs 95 to 97 that $\mathcal{G}(\gamma)$, $K_I^{(2)}$ and $K_{II}^{(2)}$ reduce to the classical values when γ is zero.

Now we reiterate the energy release rate criterion given in the introduction: "The crack subjected to combined loads will grow in the direction along which the strain energy release rate $\mathcal{G}(\gamma)$ is maximum and the crack will start to grow when this maximum energy release rate reaches a critical value."

Numerical and Experimental Results

Consider an infinite plate having a crack of length $4A$, and subjected to a load q at an angle α to the plane of the crack. The stress intensity factors are

$$K_I = \sqrt{2\pi A} q \sin^2 \alpha, \quad K_{II} = \sqrt{2\pi A} q \sin \alpha \cos \alpha \quad (98)$$

Upon substitution of Eq 98 into Eq 3, the energy release rate for this case is

$$\mathcal{G}(\gamma) = \frac{q^2 \pi A}{2E} \left(\frac{4}{3 + \cos^2 \gamma} \right)^2 \left(\frac{1 - \gamma/\pi}{1 + \gamma/\pi} \right)^{\gamma/\pi} \{ (1 + 3 \cos^2 \gamma) \sin^4 \alpha + 8 \sin \gamma \cos \gamma \sin^3 \alpha \cos \alpha + (9 - 5 \cos^2 \gamma) \sin^2 \alpha \cos^2 \alpha \} \quad (99)$$

The values of γ for which $\mathcal{G}(\gamma)$ in Eq 99 attains its maximum are plotted in Fig. 7 for various values of α . In the same figure we also present results

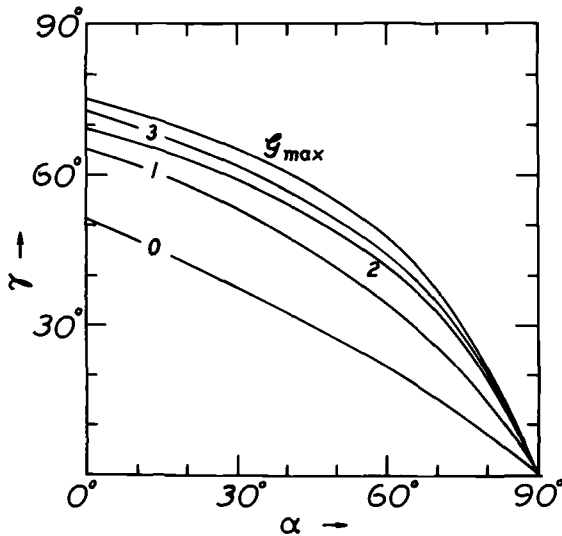


FIG. 7—The fracture angle γ for various values of α based on the maximum energy release rate.

obtained from the zero to third order iterations. The graph shows a fast convergence of the iteration procedure. If the Griffith-Irwin criterion, as formulated in the introduction, is valid then this graph should give us the direction of incipient propagation of the crack subjected to the mixed mode condition given by Eq 98. The theoretical results based on the maximum $\mathcal{G}(\gamma)$ and the maximum σ_θ are plotted in Fig. 8. It can be seen that the angle predicted by maximum $\mathcal{G}(\gamma)$ is in general close to that predicted by maximum stress criterion. In Fig. 9 we have plotted K_I/K_{Ic} versus K_{II}/K_{Ic} based on these two theories. The maximum stress theory predicts that K_{IIc} should be $0.89 K_{Ic}$, while the maximum energy release rate criterion gives $K_{IIc} = 0.63 K_{Ic}$. We believe that an experiment to accurately obtain K_{IIc}/K_{Ic} ratios is crucial. Unfortunately, most experiments with pure Mode II loading are difficult to perform. However, we shall describe a method of obtaining a Mode II condition in a simple way.

The elasticity solution for a curvilinear crack in an infinite plate under uniform tension is given by Muskhelishvili [14]. The stress intensity factors, in terms of parameters shown in Fig. 10, can be found. The results [19] are

$$\begin{aligned}
 K_I &= \frac{\sqrt{\pi} P}{2} \sqrt{\sin \eta} \cos (\eta/2) \{2 - \cos^2(\eta/2)\}^{-1} \\
 &\quad \times \{-3 \cos^4(\eta/2) + 10 \cos^2(\eta/2) - 5\} \\
 K_{II} &= -\frac{\sqrt{\pi} P}{2} \sqrt{\sin \eta} \sin (\eta/2) \{2 - \cos^2(\eta/2)\}^{-1} \\
 &\quad \times \{-3 \cos^4(\eta/2) + 8 \cos^2(\eta/2) - 1\}
 \end{aligned} \tag{100}$$

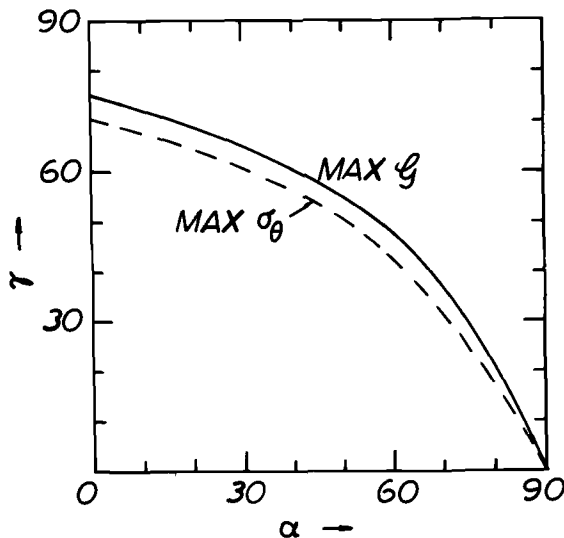


FIG. 8—The fracture angle γ predicted by maximum $\mathcal{G}(\gamma)$ and maximum σ_θ .

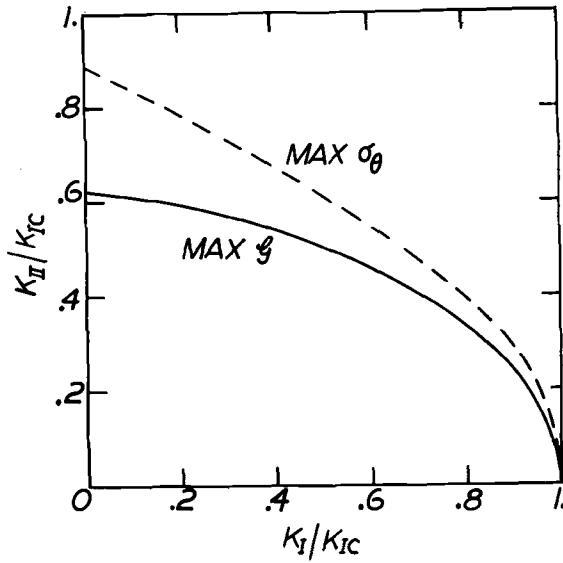


FIG. 9—The failure loci predicted by maximum $\mathcal{G}(\gamma)$ and maximum σ_θ .

Equation 100 shows that K_I vanishes for $\eta = 0, \pi$, and 79.6 deg. The first two values are trivial. The last one, namely, $\eta = 79.6$ deg, is interesting to us. At $\eta = 79.6$ deg, $K_I = 0$ but $K_{II} \neq 0$. Hence for a circular crack with $2\eta = 159.2$ deg, we obtain a pure shear mode if the pure tension is applied symmetrically to the bisector of the central angle 2η .

Such an experiment was performed in our laboratory. Tests were performed on four 6-in.-wide by 16-in.-long panels of 0.002-in.-thick steel foil.

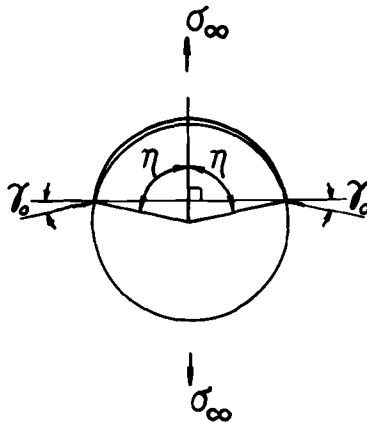


FIG. 10—Pure Mode II condition in a curvilinear crack under tension.

A 1.3-in.-diameter curvilinear crack was cut in the center of each panel, with a nominal value of 79.6 deg and oriented as shown in Fig. 10. Tensile load was applied and photos were taken of the crack paths after a small amount of crack growth and after complete separation, see Fig. 11. The measured angle between the initial 0.05 in. of crack growth and the $\alpha = 90$ deg line (shown in the photos of Fig. 11) varied between 3 and 6 deg. The average value of this angle was $\gamma_0 = 4.2$ deg. We believe this value to be a good measure of the direction of crack growth in pure Mode II shear, because of the following considerations; (a) the loading is symmetric, thus effects of buckling or twisting on crack growth are less likely; (b) the thin

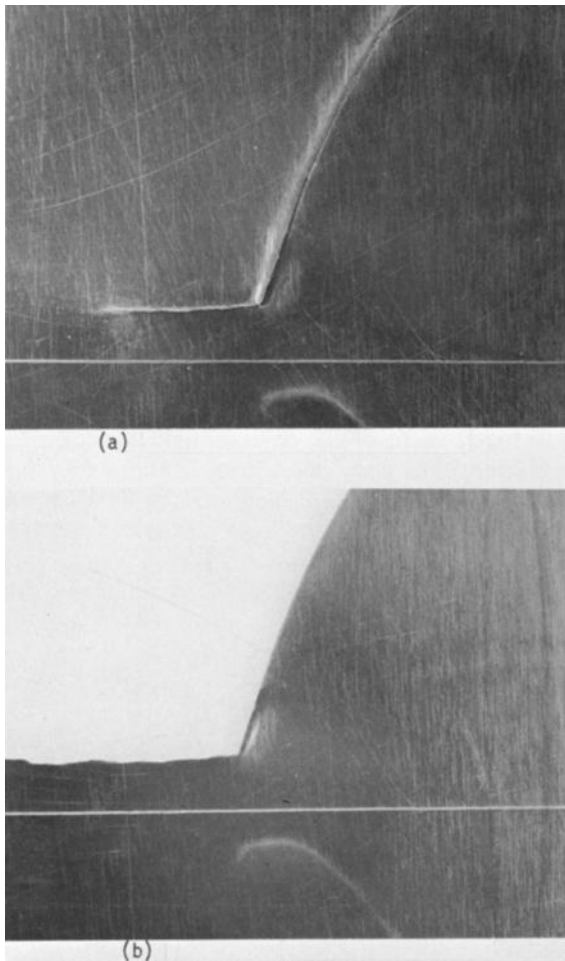


FIG. 11—Crack growth from a curvilinear notch on a steel foil; (a) after 0.12 in. crack growth and (b) after complete separation.

sheet essentially eliminates the possibility of thickness effects on the direction of crack growth; and (c) the crack is large enough to provide an adequate sized near field zone in which to observe the direction of crack growth.

According to the maximum energy release rate, the angle γ_0 , shown in Fig. 10, should be 4.4 deg. The same angle based on maximum stress theory should be 9.1 deg. The average value from these experiments, repeated from before, is $\gamma_0 = 4.2$ deg, in good agreement with the theoretical prediction $\gamma_0 = 4.4$ deg. Further tests concentrating on the measurement of critical K values and angles of crack growth in mixed mode loading are planned.

In Fig. 12 we have plotted a critical load ratio, that is, the critical load for a crack of fixed length at various angles α normalized with respect to the critical load normal to the crack ($\alpha = 90$ deg). These critical loads correspond to the maximum values of \mathcal{G} , at which fracture is assumed to occur. It is interesting to note that the weakest crack is not the crack normal to the load but the crack inclined at about 60 deg to the load. This is quite an unexpected result. Experimental verifications, though difficult, must

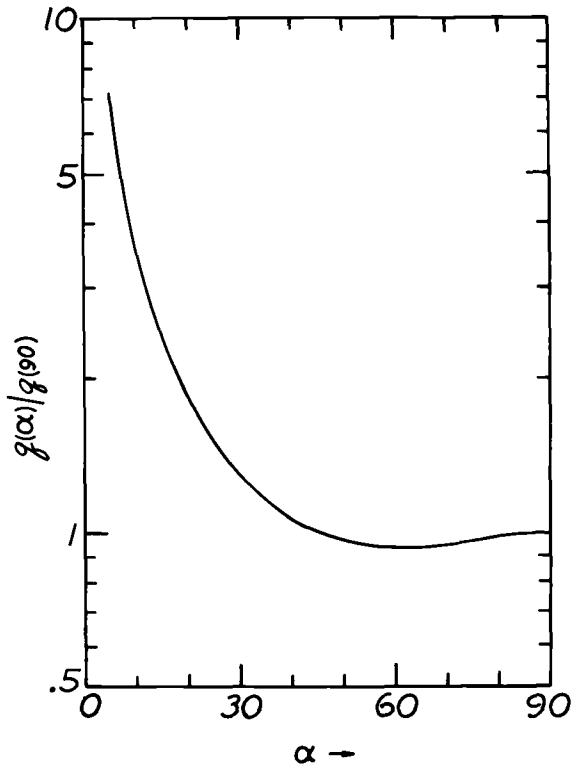


FIG. 12—The critical load ratio for various values of α .

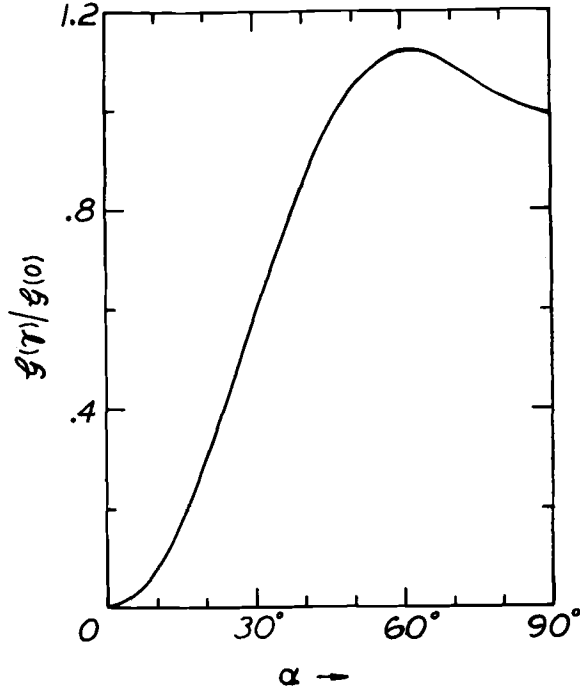


FIG. 13—The ratio of $G(\gamma)/G(0)$ versus α .

be carried out.⁷ In Fig. 13, the maximum $G(\gamma)$ normalized with respect to $G(0)$ (namely, the energy release rate for Mode I) is plotted versus the angle α . We see the similar trend; the maximum occurs at about $\alpha = 60$ deg.

In conclusion, we have presented an equation for energy release rate for cracks subjected to general in-plane loading. Once K_I and K_{II} are found, the path of crack extension and the energy release rate can easily be obtained. Some experimental results do indicate the utility of such an expression. However, more experiments should be performed to verify the Griffith-Irwin energy release rate fracture criterion for this mixed mode loading.

APPENDIX

A partial list of asymptotic values as $\alpha_2 - \alpha_1 = \epsilon \rightarrow 0$:

$$\gamma_2 = - \left\{ 1 - \frac{i\gamma\epsilon}{\pi} - \frac{\gamma^2\epsilon^2}{2\pi^2} + O(\epsilon^3) \right\}; \quad \gamma_j = e^{i\beta_j}, j = 1, 2$$

$$\gamma_2^2 = 1 - \frac{2i\gamma\epsilon}{\pi} - \frac{2\gamma^2\epsilon^2}{\pi^2} + O(\epsilon^3)$$

⁷ Recent experimental results in Ref 4 indicate such a trend.

$$\gamma_2^{-2} = 1 + \frac{2i\gamma\epsilon}{\pi} - \frac{2\gamma^2\epsilon^2}{\pi^2} + 0(\epsilon^3)$$

$$\gamma_2^{-4} = 1 + \frac{4i\gamma\epsilon}{\pi} - \frac{8\gamma^2\epsilon^2}{\pi^2} + 0(\epsilon^3)$$

$$\gamma_1 - \gamma_2 = 2 - \frac{i\gamma\epsilon}{\pi} - \frac{\gamma^2\epsilon^2}{2\pi^2} + 0(\epsilon^3)$$

$$(\gamma_1 - \gamma_2)^2 = 4 - \frac{4i\gamma\epsilon}{\pi} - \frac{3\gamma^2\epsilon^2}{\pi^2} + 0(\epsilon^3)$$

$$(\gamma_1 - \gamma_2)^{-1} = \frac{1}{2} \left\{ 1 + \frac{i\gamma\epsilon}{2\pi} + 0(\epsilon^3) \right\}$$

$$(\gamma_1 - \gamma_2)^{-2} = \frac{1}{4} \left\{ 1 + \frac{i\gamma\epsilon}{\pi} - \frac{\gamma^2\epsilon^2}{4\pi^2} + 0(\epsilon^3) \right\}$$

$$e^{i\alpha_1} = - \left\{ 1 - \frac{i\epsilon}{2} \left(1 + \frac{\gamma}{\pi} \right) - \frac{\epsilon^2}{8} \left(1 + \frac{\gamma}{\pi} \right)^2 + 0(\epsilon^3) \right\}$$

$$e^{i\alpha_2} = - \left\{ 1 + \frac{i\epsilon}{2} \left(1 - \frac{\gamma}{\pi} \right) - \frac{\epsilon^2}{8} \left(1 - \frac{\gamma}{\pi} \right)^2 + 0(\epsilon^3) \right\}$$

$$\gamma_1 = 1 + 0(\epsilon^3), \quad \gamma_1^2 = 1 + 0(\epsilon^3)$$

$$\gamma_1 - e^{i\alpha_1} = 2 - \frac{i\epsilon}{2} \left(1 + \frac{\gamma}{\pi} \right) - \frac{\epsilon^2}{8} \left(1 + \frac{\gamma}{\pi} \right)^2 + 0(\epsilon^3)$$

$$\gamma_1 - e^{i\alpha_2} = 2 + \frac{i\epsilon}{2} \left(1 - \frac{\gamma}{\pi} \right) - \frac{\epsilon^2}{8} \left(1 - \frac{\gamma}{\pi} \right)^2 + 0(\epsilon^3)$$

$$\gamma_2 - e^{i\alpha_1} = - \frac{i\epsilon}{2} \left(1 - \frac{\gamma}{\pi} \right) - \frac{\epsilon^2}{4} \left(\frac{1}{2} + \frac{\gamma}{\pi} - \frac{3\gamma^2}{2\pi^2} \right) + 0(\epsilon^3)$$

$$\gamma_2 - e^{i\alpha_2} = \frac{i\epsilon}{2} \left(1 + \frac{\gamma}{\pi} \right) - \frac{\epsilon^2}{4} \left(\frac{1}{2} - \frac{\gamma}{\pi} - \frac{3\gamma^2}{2\pi^2} \right) + 0(\epsilon^3)$$

$$\sin\left(\frac{\beta_2 - \alpha_1}{2}\right) = \frac{\epsilon}{4} \left(1 - \frac{\gamma}{\pi} \right) + 0(\epsilon^3); \quad \sin\left(\frac{\alpha_2 - \beta_2}{2}\right) = \frac{\epsilon}{4} \left(1 + \frac{\gamma}{\pi} \right) + 0(\epsilon^3)$$

From Eqs 48 to 50, we have as $\epsilon \rightarrow 0$

$$A_1 = 2 - \frac{\epsilon^2}{8} \left(1 - \frac{\gamma^2}{\pi^2} \right) + 0(\epsilon^3); \quad A_2 = \frac{\epsilon^2}{8} \left(1 - \frac{\gamma^2}{\pi^2} \right) + 0(\epsilon^3)$$

$$\omega(\gamma_2) = - \frac{A}{4} e^{-i\gamma} \epsilon^2 \left(\frac{1 + \gamma/\pi}{1 - \gamma/\pi} \right)^{\gamma/\pi} \left(1 - \frac{\gamma^2}{\pi^2} \right) + 0(\epsilon^3)$$

$$\omega''(\gamma_2) = -2Ae^{-i\gamma} \left(\frac{1 + \gamma/\pi}{1 - \gamma/\pi} \right)^{\gamma/\pi} + 0(\epsilon)$$

$$\frac{\gamma_2 - \gamma_1}{(\gamma_2 - e^{i\alpha_1})(\gamma_2 - e^{i\alpha_2})} = -8\epsilon^{-2} \left(1 - \frac{\gamma^2}{\pi^2} \right)^{-1}$$

$$|r_2| = (A\epsilon^2/4)(1 - \gamma/\pi)^{1-\gamma/\pi} (1 + \gamma/\pi)^{1+\gamma/\pi}$$

References

- [1] Irwin, G. R., *Journal of Applied Mechanics*, Vol. 24, 1957, pp. 361–364.
- [2] Bueckner, H. F., *Transactions*, American Society of Mechanical Engineers, Vol. 80, 1958, pp. 1225–1230.
- [3] Knowles, J. K. and Sternberg, E., “On a Class of Conservation Laws in Linearized and Finite Elastostatics,” Technical Report No. 24, California Institute of Technology and Archive of Rational Mechanics and Analysis, Vol. 44, No. 3, 1972, pp. 187–211.
- [4] Williams, J. G. and Ewing, P. D., *International Journal of Fracture Mechanics*, Vol. 8, No. 4, Dec. 1972, pp. 441–446.
- [5] Yoffe, E. H., *Philosophical Magazine*, Vol. 42, 1951, pp. 739–750.
- [6] Erdogan, F. and Sih, G. C., *Transactions*, American Society of Mechanical Engineers, *Journal of Basic Engineering*, Dec. 1963, pp. 519–527.
- [7] Stroh, A. H., “A Theory of the Fracture of Metals,” *Proceedings*, Royal Society, A-223, 1954.
- [8] Williams, M. L., *Journal of Applied Mechanics*, Vol. 24, March 1957, p. 114.
- [9] Sih, G. C. and Macdonald, B., “What the Designer Must Know About Fracture Mechanics,” IFSM-72-23, Lehigh University, Nov. 1972.
- [10] Darwin, C., “Some Conformal Transformations Involving Elliptic Functions,” *The Philosophical Magazine*, Series 7, Vol. 41, No. 312, Jan. 1950.
- [11] Andersson, H., *Journal of Mechanics and Physics of Solids*, Vol. 17, 1969, pp. 405–404.
- [12] Andersson, H., *Journal of Mechanics and Physics of Solids*, Vol. 18, 1970, p. 437.
- [13] Bowie, O. L., “Solution of Plane Crack Problems by Mapping Techniques,” *Methods of Analysis and Solutions to Crack Problems*, edited by G. S. Sih, Walters-Noordhoff Publishing, 1972.
- [14] Muskhelishvili, N., *Some Basic Problems of the Mathematical Theory of Elasticity*, Noordhoff, Groningen, 1963.
- [15] Gakhov, F. D., *Boundary Value Problems*, Addison-Wesley, 1963.
- [16] Rice, J. R., “A Path Independent Integral and the Approximate Analysis of Strain Concentration by Notches and Crack,” *Journal of Applied Mechanics*, Vol. 35, No. 2, June 1968.
- [17] Budiansky, B. and Rice, J. R., “Conservation Laws and Energy-Release Rates,” *Journal of Applied Mechanics*, Vol. 40, No. 1, March 1973.
- [18] Sanders, J. L., “On the Griffith-Irwin Fracture Theory,” *Journal of Applied Mechanics*, Vol. 27, No. 2, June 1960.
- [19] Hussain, M. A. and Pu, S. L., *Journal of Applied Mechanics*, Vol. 38, No. 3, Sept. 1971, pp. 627–628.

R. C. Shah¹

Fracture Under Combined Modes in 4340 Steel

REFERENCE: Shah, R. C., "Fracture Under Combined Modes in 4340 Steel," *Fracture Analysis, ASTM STP 560*, American Society for Testing and Materials, 1974, pp. 29-52.

ABSTRACT: An experimental investigation was conducted to study the interaction of combined modes of loading on crack instability in the presence of the opening and sliding modes of stress intensity factors (K_I and K_{II}), the opening and tearing modes of stress intensity factors (K_I and K_{III}), and all three modes of stress intensity factors (K_I , K_{II} , and K_{III}). Through-cracked and surface-cracked flat and round specimens, and round notched bar specimens fabricated from high strength 4340 steel were used for the investigation. The results are evaluated to determine fracture criteria under the combined modes of K_I and K_{II} , K_I and K_{III} and K_I , K_{II} , and K_{III} for the 4340 steel. These results are compared with the results of other investigators obtained for different materials. For the combined Mode I-II tests, it was found that the presence of K_{II} can have a significant effect on K_I at which fracture occurs and vice versa. For the combined Mode I-III tests, it was found that the application of K_{III} up to about 70 percent of K_{IIIc} has little effect on K_I at which fracture occurs. Similarly, the application of K_I up to about 70 percent of K_{Ic} has little effect on K_{III} at which failure occurs.

KEY WORDS: fracture properties, cracks, cracked specimens, combined mode loadings, mechanical properties, fracturing, fracture criterion, steels

The majority of past experimental and theoretical fracture and crack growth studies have dealt with the opening mode of deformation, Mode I, conditions. Many investigations have shown that under Mode I conditions, crack instability occurs when the stress intensity factor reaches some critical value. A limited number of theoretical and experimental investigations have been conducted to determine the effects of combined mode loadings on fracture starting from cracks [1-11].² For a cracked component under combined mode loading, two theories of fracture have been advanced; maximum stress criterion [1] and strain energy density factor theory [9,10]. In the maximum stress concept, it is assumed that the crack extension occurs in a plane perpendicular to the direction of the greatest

¹ Senior specialist engineer, Research and Engineering Division, Boeing Aerospace Company, Seattle, Wash. 98124.

² The italic numbers in brackets refer to the list of references appended to this paper.

tension for a combined Mode I-II problem. The angle of crack extension with respect to the initial crack plane, θ_0 , as shown in Fig. 1, is given as [1]

$$K_I \sin \theta_0 + K_{II}(3 \cos \theta_0 - 1) = 0 \quad (1)$$

For this combined mode loading, Erdogan and Sih [1] proposed the following fracture criterion, inferred from the strain energy release considerations.

$$a_{11}K_I^2 + 2a_{12}K_I K_{II} + a_{22}K_{II}^2 = \text{constant} \quad (2)$$

where the constants a_{11} , a_{12} , and a_{22} are functions of material properties. In the conventional theory of fracture, it is currently not possible to calculate the strain energy release rate when the crack extension is not coplanar with the initial crack. Sih [9,10] proposed a theory of fracture based on the field strength of local strain energy density to deal with the combined mode crack extension problems. In this theory, it is assumed that the critical strain energy density factor, S_c , is an intrinsic material

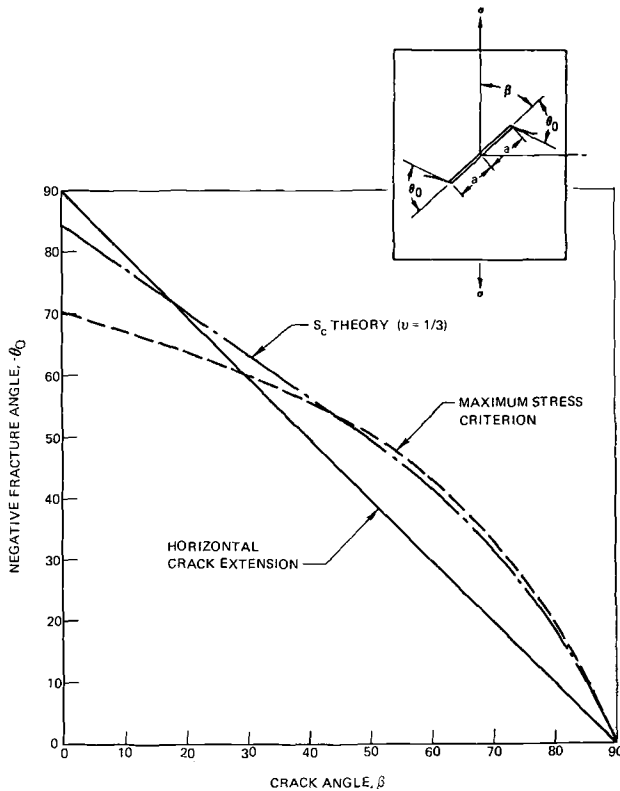


FIG. 1—Fracture angle versus crack angle in a cracked plate under uniform tension.

property independent of the loading conditions and crack configurations, and S_c governs the onset of crack propagation.

$$S_c = a_{11}K_I^2 + 2a_{12}K_I K_{II} + a_{22}K_{II}^2 + a_{33}K_{III}^2 \quad (3)$$

$a_{ij}(i, j = 1, 2, 3)$ are known functions of shear modulus μ , Poisson's ratio ν , and the polar angle θ measured with the crack plane. For the planar combined mode problem, the fracture angles θ_0 predicted by the prior two criteria with respect to inclined angle β is shown in Fig. 1. Figure 1 also shows the propagation of crack normal to the applied stress, that is, $\beta + \theta_0 = 90$ deg, labeled as horizontal crack extension. Figure 1 shows that the fracture angle is not a sensitive parameter to verify the prior theories of fracture under the combined mode.

Earlier experimental studies include the effects of Mode I-II interaction on plexiglass [1], balsa wood [2], fiberglass [2], and 2000 and 7000 series aluminum alloys [3-8] and Mode I-III interaction on 7000 series aluminum alloys [4,5] and K9 tool steel [5]. The present investigation was conducted to determine the effects of combined Modes I-II, I-III, and I-II-III on fractures initiating at cracks with specimens made from 4340 steel. 4340 steel was chosen since it has a homogeneous microstructure and can be heat treated to a high strength level where it is relatively brittle and has low fracture toughness.

Material and Procedures

A 4340 steel plate 1.0 by 20.0 by 72.0 in. normalized and tempered to 33 HRC maximum was purchased according to AMS 6359 specifications. Specimens were fabricated from this plate and starter slots with dimensions slightly less than the required crack dimensions were introduced using an electric discharge machine. The specimens then were subjected to heat treatment according to Boeing BAC 5617 specifications so that ultimate strength of the heat-treated 4340 steel is around 270 to 280 ksi at room temperature. Specifications are given in Table 1. The mechanical properties at room temperature and -200°F in the rolling (L) and the long transverse (T) directions are quite uniform and are given in Table 2.

Tests at -200°F were conducted by exposing test specimens to a gaseous nitrogen environment in a closed cryostat. The -200°F temperature was maintained in the cryostat by controlling the supply of gaseous nitrogen and liquid nitrogen in the cryostat. A thermocouple mounted on the speci-

TABLE 1—Specifications for heat-treatment of 4340 steel.

Austenitize	1550°F	30 to 90 min depending on specimen thickness
Oil quench	140°F max	
Double temper	400°F	3 to 4 h depending on specimen thickness

TABLE 2—Mechanical properties of 4340 steel.

Test Temperature, °F	Ultimate Tensile Strength, ksi	0.2% Yield Strength, ksi	Percent Elongation, 2.0-in. gage length
Room temperature	275	214	10
-200	294	225	3

men near the flaw was used to determine the specimen temperature. Loading was commenced 10 to 15 min after the specimen had reached a temperature of -200°F.

Inclined center-cracked specimens used for Mode I-II tests and inclined surface flawed specimens used for Mode I-II-III tests are shown in Fig. 2. Figure 3a shows through-cracked tube specimens used to determine critical stress intensity factor, K_{IIc} . Figure 3b shows a round notched bar specimen used for Mode I-III tests. Figure 3c shows a round specimen containing a surface flaw used for combined Mode I-II-III testing. All test specimens were precracked by growing fatigue cracks from starter slot under low stress tension fatigue. The maximum cyclic stress levels used were between 20 to 35 ksi.

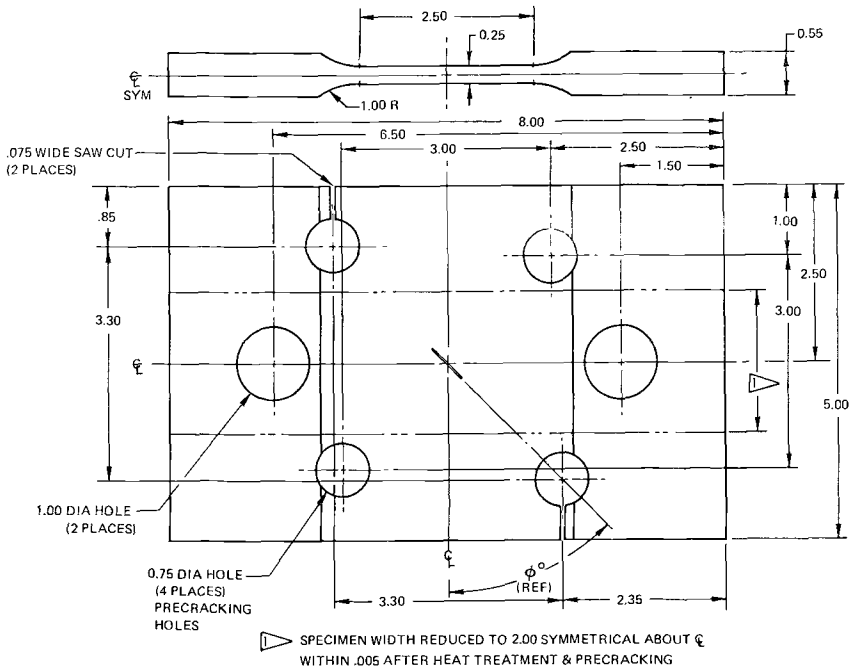


FIG. 2—Specimen for ϕ degree surface flaw or center crack for combined Mode I-II-III and I-II tests.

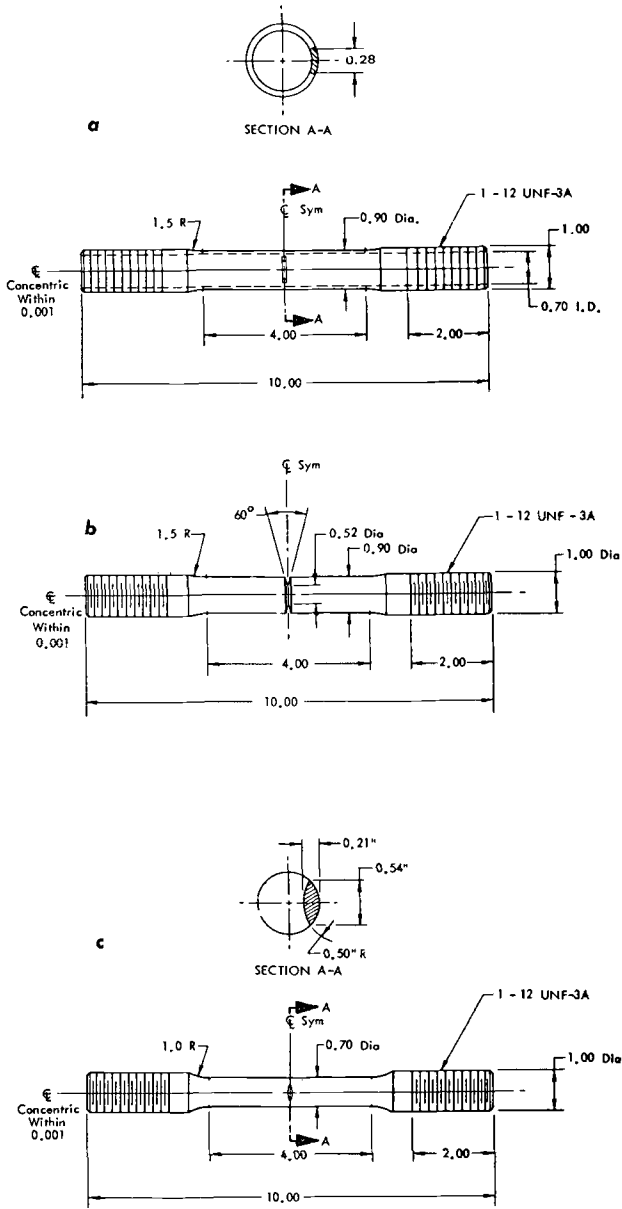


FIG. 3—(a) Tube with through-crack specimen; (b) round notched bar specimen; (c) surface flawed round specimen.

In order to extend the fatigue crack in the plane of the EDM slot in the specimen of Fig. 2, the specimen was precracked by loading through 0.75-in.-diameter holes whose centers were perpendicular to the EDM slot. In order to reduce the load required for precracking the EDM slot, two slotted holes, as shown in Fig. 2, were machined in the specimen along the axis of the EDM slot. After precracking the EDM slot to the required sized crack, the final specimen was cut such that the crack is oriented at the required angle with respect to the axis of loading.

The round notched bar specimens (Fig. 3*b*) were precracked under low stress tension high cycle fatigue. Since the fatigue cracks developing from notches tended to become eccentric, the fatigue cracks were kept small. Fatigue cracks as measured from the notch periphery were from 0.005 to 0.050 in. Most specimens had reasonably concentric cracks. Fatigue cracks, grown in other trial specimens of this material, under rotating bending fatigue were more eccentric than those grown under tension fatigue.

Test Machine and Instrumentation

Round notched bar specimens and round specimens with surface flaws were subjected to simultaneous tensile and torsional loading. They were loaded in a 150-kip capacity tension-compression machine which was modified to apply simultaneous tensile and torsional loading (Fig. 4 *top*). The specimen was loaded in tension by a vertical hydraulic cylinder and the torque was applied independently by a couple using two horizontal hydraulic cylinders (Fig. 4 *top*). At the lower end, the load cell was locked for any torsional motion. The hydraulic cylinders were actuated by servo valves responding to electrical signals to apply the programmed load. Directly in series with the specimen was the load cell providing a nulling feedback signal when the applied load reached the programmed value, thus forming a closed-loop control system. The load cell was made of a circular tube so that it could carry a relatively high axial load and be sensitive to torsional measurements. Axial load was measured and controlled by two independent, four-arm strain gage bridge circuits installed in the axial direction, and the torque was measured and controlled by two independent, four-arm strain gage bridge circuits installed at 45-deg angles with respect to the axial direction. The required ratio of the tension load with respect to the simultaneous torque was maintained by a drum programmer.

The axial and angular displacements across the flawed cross-section were measured by electrical displacement indicators. Load versus displacement curves were generated independently for axial and for angular displacement by X-Y plotters. For round specimens containing surface flaws, crack opening displacement measurements in the axial direction were taken using Srawley type clip gages [12]. Holding-tabs with knife edges were micro-spot welded with one spot weld close to the flaw edge along the centerline of the flaw, and the other end of the tab held down by a slip-joint.

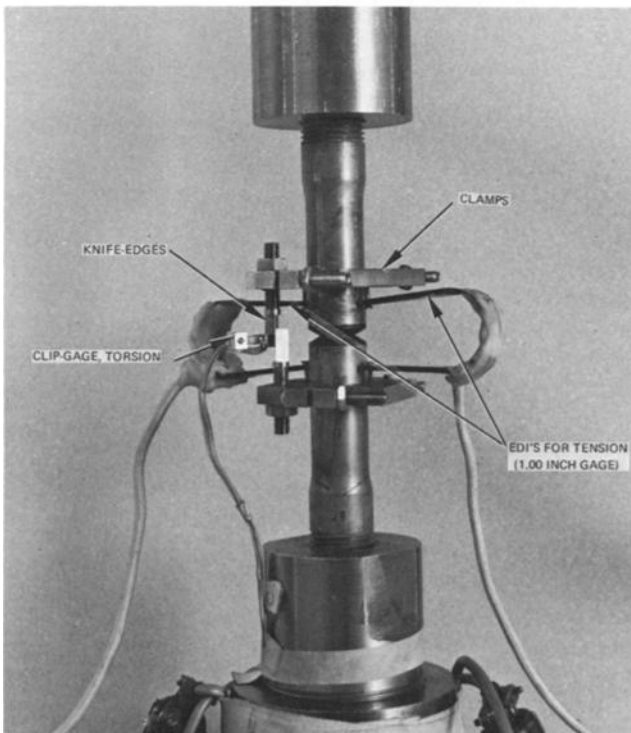
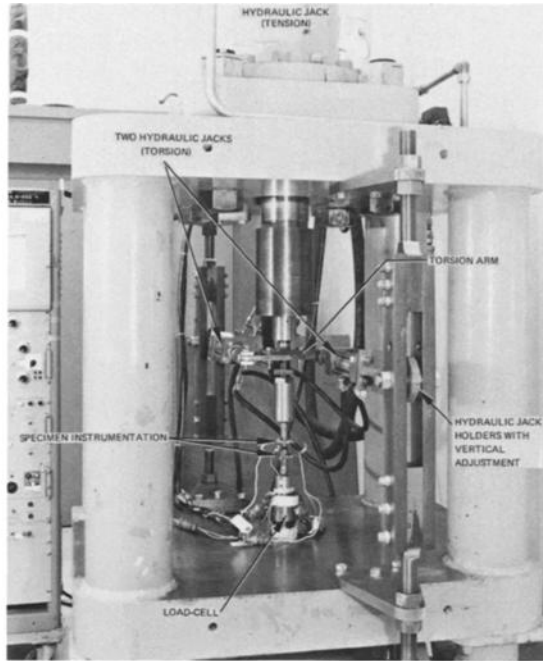


FIG. 4—Tension-torsion test machine and instrumentation.

For round notched bar specimens, axial displacement measurements were taken by using two electrical displacement indicators of the horseshoe type attached to clamps 1-in. apart on the specimen, as shown in Fig. 4 *bottom*. The average output of the two displacement indicators was used to generate the load-displacement curves. For angular displacement measurements, two clamps, 1-in. apart along the specimen were attached to the specimen as shown in Fig. 4 *bottom*. Knife edges were machined at the end of arms extended from the clamps to hold clip gages for angular displacement measurements. For convenience, the knife edges, where the clip gages were attached, were located 1-in. away from the vertical centerline of the specimen.

Test Results and Discussion

Fracture Toughness Tests

The plane-strain fracture toughness of 4340 steel at room temperature was determined in LS and LT directions of crack propagation by testing flat specimens containing a semi-elliptical surface crack or a central through-the-thickness crack, respectively. The fracture toughness at -200°F under gaseous nitrogen environment was determined in LS and TS directions of crack propagation by testing surface flawed specimens and in LT direction by testing specimens containing a central through-the-thickness crack. The plane-strain fracture toughness values for the LS and LT directions at room temperature were 72.6 and 73.8 $\text{ksi}\sqrt{\text{in.}}$, respectively. Raw data and detailed results of these tests and all the tests mentioned hereafter are presented in a NASA Contract Report [12]. The plane-strain fracture toughness values in LS, TS, and LT directions at -200°F were 40.1, 40.6, and 41.6 $\text{ksi}\sqrt{\text{in.}}$, respectively. All of these fracture toughness values mentioned were the average of two test results. The test results indicate that fracture toughness is essentially independent of the crack propagation directions in these planes. Hence in the tests mentioned hereafter of inclined through cracks and surface cracks in flat plates, the crack propagation directions were not kept in one particular direction.

Mode I-II Tests

Eight flat specimens containing central through-the-thickness cracks oriented at $\phi = 0, 25, 50,$ and 75 deg to the width direction (Fig. 2) were loaded to failure in pure tension to study the effects on fracture of opening mode K_I and the combined opening and sliding modes of crack extension K_I and K_{II} . Tests were conducted at -200°F in gaseous nitrogen. The ratio of crack length to specimen width for all specimens was approximately one half. The specimens were not instrumented with crack opening displacement gages. Fracture surfaces (crack propagation) were oriented perpendicular to the applied tension, as seen from photograph in Fig. 5.

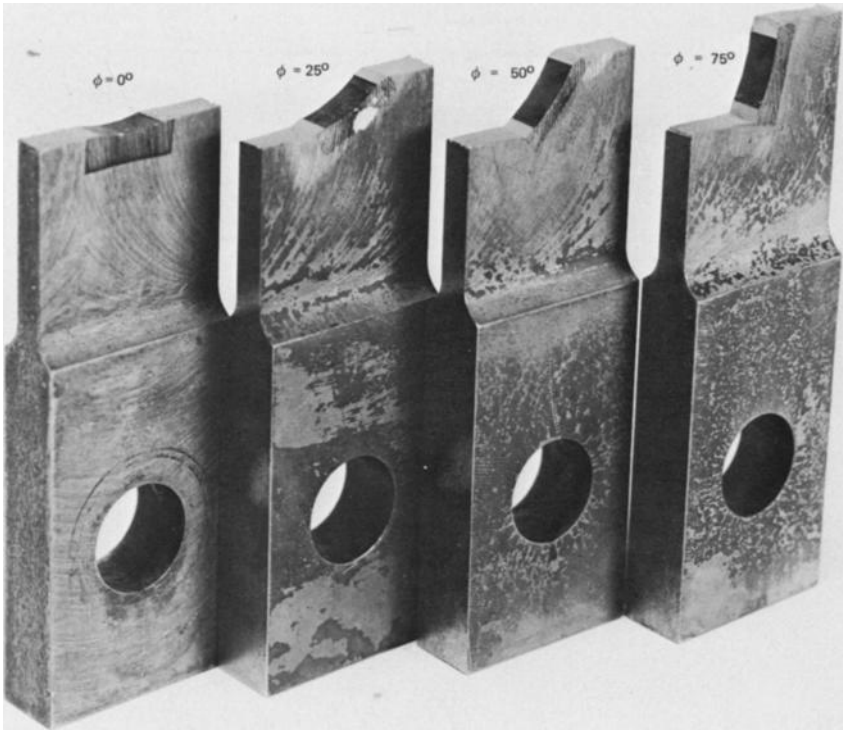


FIG. 5—Fracture surfaces of inclined center-cracked specimens of 4340 steel subjected to combined Modes I and II.

Examination of fracture surfaces did not reveal any apparent slow crack growth. (The same thickness specimens containing semi-elliptical surface cracks perpendicular to applied tension and instrumented with crack opening displacement gages did not show any slow crack growth at all prior to fracture at -200°F .) Stress intensity factors, K_I and K_{II} , for inclined cracks were calculated using the expressions given in Ref 4 for inclined through cracks obtained from the boundary collocation method. Data of the 4340 steel under the combined Mode I-II are shown by solid circles in Fig. 6. As explained in the subsequent paragraph, K_{IIc} of $45.2 \text{ ksi}\sqrt{\text{in}}$ was used in computing K_{II}/K_{IIc} in Fig. 6. Figure 6 also shows Mode I-II data obtained by: (1) Wilson for 0.45-in.-thick 7178-T651 aluminum alloy from inclined center-cracked specimens loaded in tension [4]; (2) Pook for 0.4 ~ 0.5-in.-thick DTD 5050 aluminum alloy (5.5% Zn, $\sigma_{ys} = 77 \text{ ksi}$, $\sigma_{ult} = 84 \text{ ksi}$) from inclined center-cracked specimens loaded in tension [5]; (3) Liu for 0.3-in.-thick 7075-T7651 and 2024-T3 aluminum alloys from cracked panels loaded in shear [7] and; (4) Boeing for 0.3-in.-thick 7075-T651 aluminum alloy from inclined edge cracked specimens loaded in tension [8].

SYMBOL		MATERIAL	THICKNESS (IN)	K_{Icr} (Ksi-In ^{1/2})	K_{IIcr} (Ksi-In ^{1/2})
●	SHAH	4340 Steel ($\sigma_{ys} = 225, \sigma_{ult} = 295$) @ -200°F	0.25	41.6	45.2
◇	LIU (7)	7075-T7651 ALUMINUM	0.3	81.2	81.2
■	BOEING (8)	7075-T651 ALUMINUM	0.3	63.7	63.7
◆	LIU (7)	2024-T3 ALUMINUM	0.312	90.5	67.5

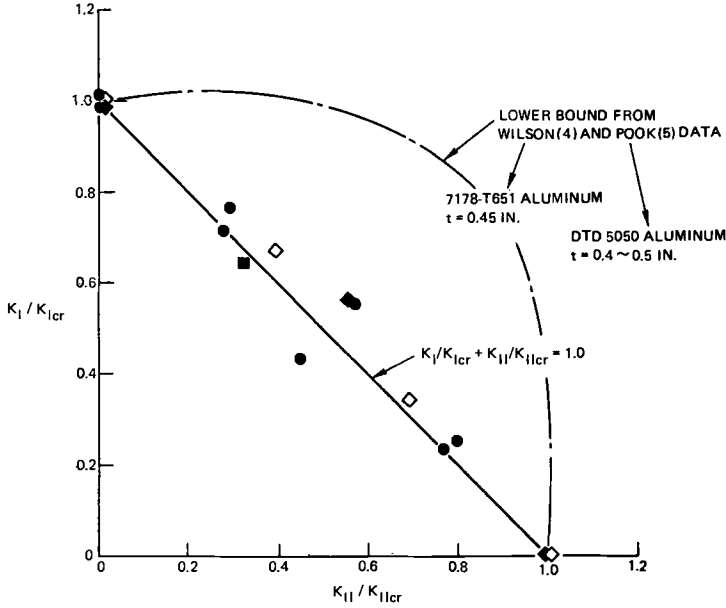


FIG. 6— K_I/K_{Icr} versus K_{II}/K_{IIcr} for a cracked plate under combined Mode I-II loading.

For all data presented in Fig. 6 and in Refs 4, 5, 7, and 8, K_I and K_{II} were calculated based on initial crack length and orientation and fracture load even though the tests conducted by Pook [5], Liu [7], and Boeing [8] did show that slow, stable, out-of-plane crack growth took place prior to fracture. A finite element solution [3] of the inclined through crack shows that as the crack turns out of its plane, K_I increases significantly and K_{II} decreases significantly. This indicates that the fracture data and criterion under combined mode loading should be evaluated using the crack configuration at the fracture load. The fracture criterion of combined mode $F(K_I, K_{II})$, obtained disregarding the crack growth and rotation, could be significantly in error.

The fracture criterion under combined Mode I-II for high strength 4340 steel at -200°F (Fig. 6) can be well described by $K_I + K_{II} \approx K_{Ic}$ or $K_I/K_{Ic} + K_{II}/K_{IIc} = 1$. This fracture criterion is significantly different

from that defined by either Eq 2 [1] or 3 [9,10]. Thus, presence of Mode II stress intensity factor has significant effect on Mode I stress intensity factor at which fracture occurs, that is, K_I at fracture is significantly less than K_{Ic} in the presence of K_{II} . Figure 6 suggests that the fracture criterion under combined Mode I-II crack surface deformations may be dependent on material, thickness, and test temperature combination.

Two cylindrical tubes of 4340 steel containing through-the-thickness cracks ($2a \approx 0.28$ in.) and subjected to pure torsion (Fig. 3a) were tested to obtain pure Mode II critical stress intensity factors, K_{IIc} . These tests were carried out at room temperature. The stress intensity factor for the cracked tube in torsion is calculated by using the expressions given in Ref 13. The specimens were instrumented with slip gages to continuously measure angular deflection across the crack plane against the applied torque. As seen from the plot of angular deflection against applied torque for Specimen B in Fig. 7, the abrupt crack extension (pop-in) occurred at the applied torque of 9200 in·lb. The sliding mode stress intensity factor K_{II} , based on the pop-in torque and initial crack length is $67.5 \text{ ksi} \sqrt{\text{in.}}$. Complete fracture of Specimen B occurred at the applied torque of 11 250 in·lb. The applied gross shear stress at failure is 116 ksi which is slightly below the shear yield stress of 124 ksi. Visual observation as well as Fig. 7 indicated that considerable crack growth had taken place prior to fracture. Fracture surfaces of the two tube specimens are shown in Fig. 8. Fracture

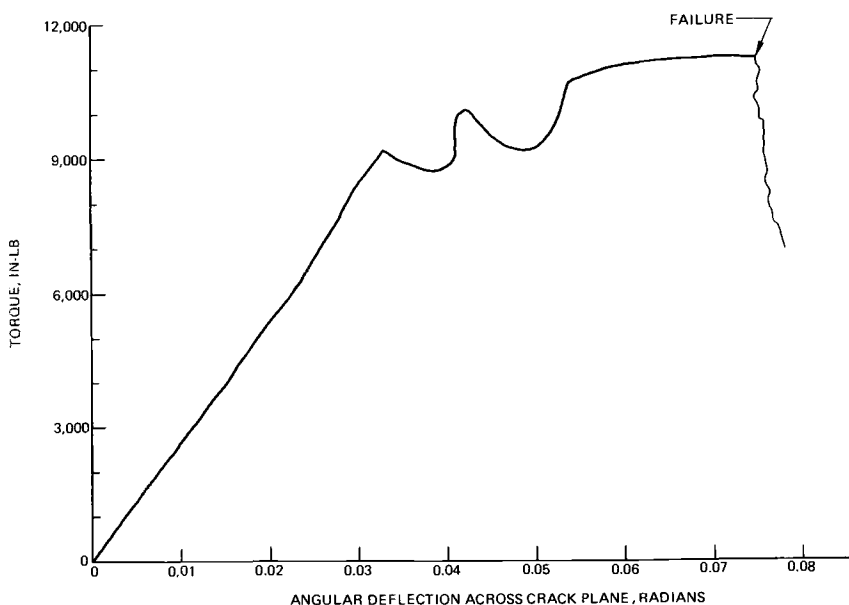


FIG. 7—Torque-angular deflection record from cracked round tube specimen of 4340 steel subjected to pure torsion and tested at room temperature.

for these specimens initiated at a Point A shown in Fig. 8, and the fracture angles (angle between the crack extension and the initial crack) were 70 and 75 deg for Specimens A and B, respectively. This compares very favorably with the fracture angles predicted by the maximum stress criterion. Critical stress intensity factors, K_{IIc} , based on initial crack lengths and fracture torque were 78.5 and 82.4 ksi $\sqrt{\text{in.}}$ for Specimens A and B, respectively. Thus, average K_{IIc} was 80.4 ksi $\sqrt{\text{in.}}$. Assuming the ratio of K_{IIc} at -200°F to K_{IIc} at room temperature is the same as K_{Ic} at -200°F

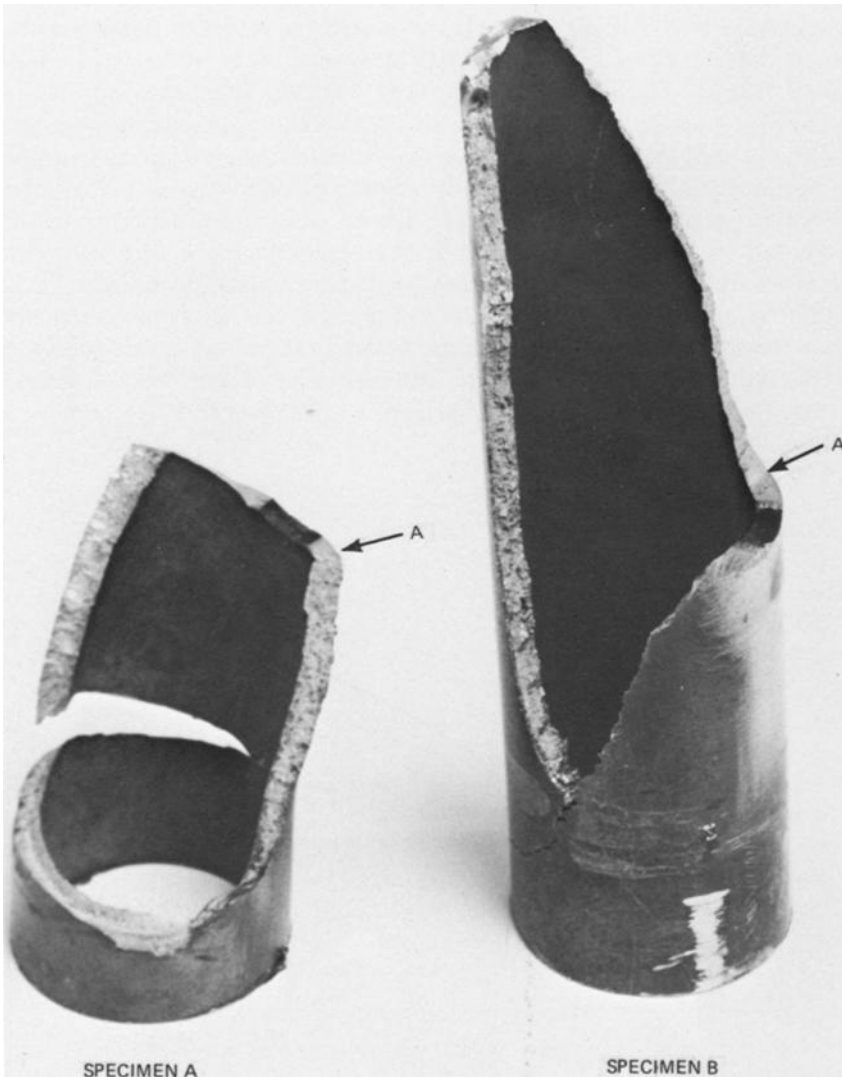


FIG. 8—Fracture surfaces of cracked tube specimens subjected to pure tension.

to K_{Ic} at room temperature, the calculated K_{IIc} for -200°F is $45.2 \text{ ksi } \sqrt{\text{in.}}$. A K_{IIc} of $45.2 \text{ ksi } \sqrt{\text{in.}}$ was used for 4340 steel at -200°F to calculate K_{II}/K_{IIc} ratios in Fig. 6. If K_{IIc} was based on the pop-in torque and the initial crack length, it would have been $37.4 \text{ ksi } \sqrt{\text{in.}}$

Some uncertainty exists in the determination of the exact value of critical plane strain sliding stress intensity factor, K_{IIc} as (1) the thickness of the tube does not meet the plane-strain criterion for the minimum thickness for tension-loaded-specimen and (2) the applied shear stress is high with respect to the shear yield stress. It is possible that the value of K_{IIc} is lower than $45.2 \text{ ksi } \sqrt{\text{in.}}$. This will change the shape of K_I/K_{Ic} versus K_{II}/K_{IIc} curve in Fig. 6 from a straight line to a slightly convex (elliptical shape) curve. However, as shown in Fig. 9, K_{IIc} cannot be much lower than $35.0 \text{ ksi } \sqrt{\text{in.}}$ since it required an applied K_{II} of $35.0 \text{ ksi } \sqrt{\text{in.}}$ in the presence of the applied K_I of $10.5 \text{ ksi } \sqrt{\text{in.}}$ to fracture the specimen.

In order to eliminate the effect of uncertain value of K_{IIc} on fracture criterion, the data of 4340 steel specimens of Fig. 6 are plotted as K_I versus K_{II} in Fig. 9. The plot shows that the fracture criterion $F(K_I, K_{II})$ for 4340 steel under combined Modes I-II is a straight line relationship between K_I and K_{II} , namely, $K_I + K_{II} \approx K_{Ic}$. As mentioned before, the fracture criterion for 4340 steel is significantly different from that defined by Eqs 2 or 3, or that inferred from the data of Wilson [4] and Pook [5].

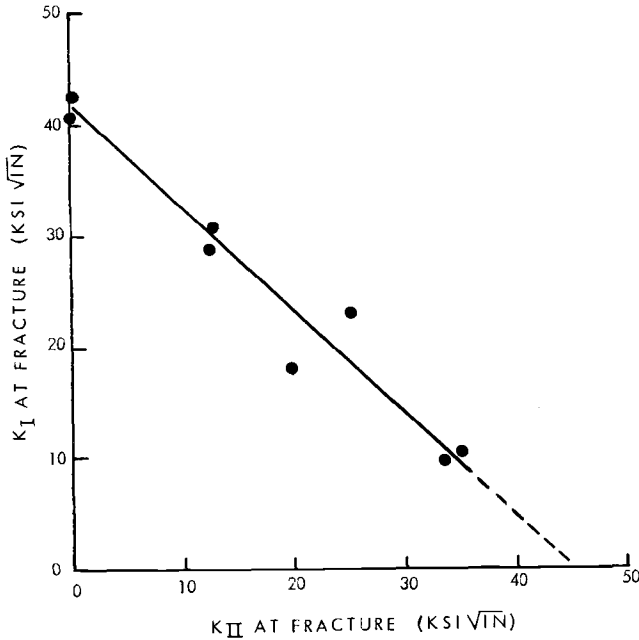


FIG. 9— K_I versus K_{II} at fracture for 4340 steel cracked plate under combined Mode I-II loading.

Mode I-III Tests

Ten cylindrical specimens containing circumferential cracks (round notched bars), as shown in Fig. 3*b*, were loaded to failure at room temperature in pure tension, in combined tension and torsion, and in pure torsion to investigate the effects on fracture of K_I , K_{II} and K_{III} , and K_{III} . Since K_I is dependent on the tensile load P only and K_{III} is dependent on the torque T only, the ratio of K_I/K_{III} was controlled by the proper ratio of P/T . Two specimens were tested for each of these approximate ratios of K_I/K_{III} : ∞ , 2, 1, 0.5, 0. The stress intensity factors K_I and K_{III} were calculated according to the following equations [4,14,15] based on the fracture load P_F and the fracture torque T_F

$$K_I = \left(1.72 \frac{D}{d} - 1.27 \right) \frac{P_F}{D^{1.5}} \quad (4)$$

$$K_{III} = 0.41 \frac{T_F}{r^{2.5}} \quad (5)$$

where D is the gross diameter of the bar and d and r are the diameter and the radius of the bar in the plane of the crack, respectively. The results of the combined mode fracture I and III are plotted in Fig. 10 as K_I versus K_{III} . The results in Fig. 10 indicate that the failure criterion can be reasonably described by a quadratic equation in K_I and K_{III} . The probable criterion under combined mode fracture is shown by the curve in Fig. 10. The results show that an applied tearing mode stress intensity factor (K_{III}) approximately equal to or less than 70 percent of K_{IIIc} has little effect on the opening mode stress intensity factor K_I , at which the specimen fails. Similar results for the combined Modes I-III interaction have been reported for 7075-T651 [4], DTD 5050 and HE 15W aluminum alloys [5], and K9 tool steel [5]. Similarly, applied K_I values approximately equal to or less than 70 percent of K_{Ic} have little effect on the tearing mode stress intensity factor K_{III} at which the specimen fails.

Figure 11 shows the tensile load versus tensile axial displacement and torque versus angular displacement for various K_I/K_{III} ratios. Tensile load versus displacement curves do not exhibit any nonlinearity almost up to fracture for any K_I/K_{III} ratio. However, torque versus angular displacement plots exhibit significant nonlinear behavior for K_I/K_{III} ratios smaller than 1.16, indicating plastic flow took place. The specimen (3 RNB-10) tested under pure tension fractured at net stress ($\sigma = 4P_F/\pi d^2$) in the cracked section of 68 percent of tensile yield stress while the specimen (3 RNB-5) tested under pure torque failed at the net maximum shear stress ($\tau = 16 T_F/\pi d^3$) of 169 percent of shear yield stress. This as well as torque-angular displacement records show that extensive plastic flow took place prior to fracture under pure torsion.

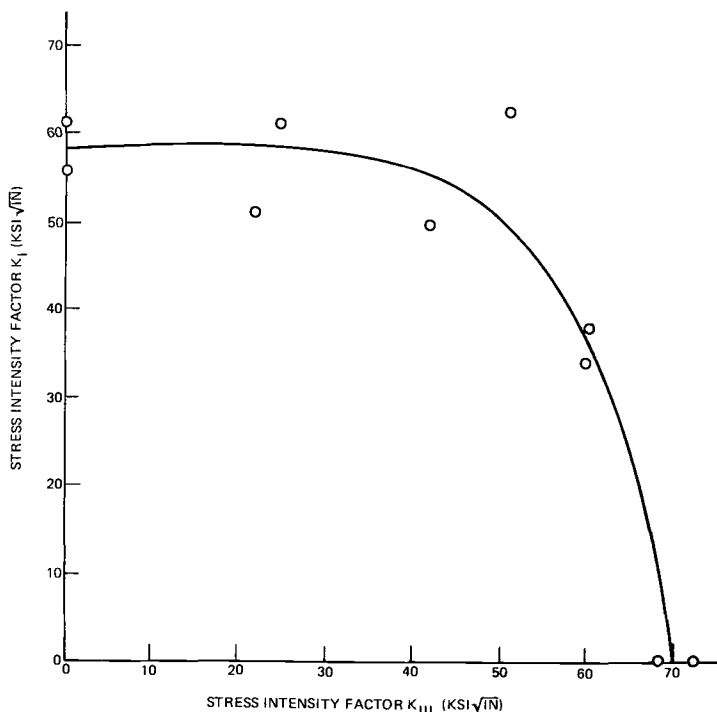
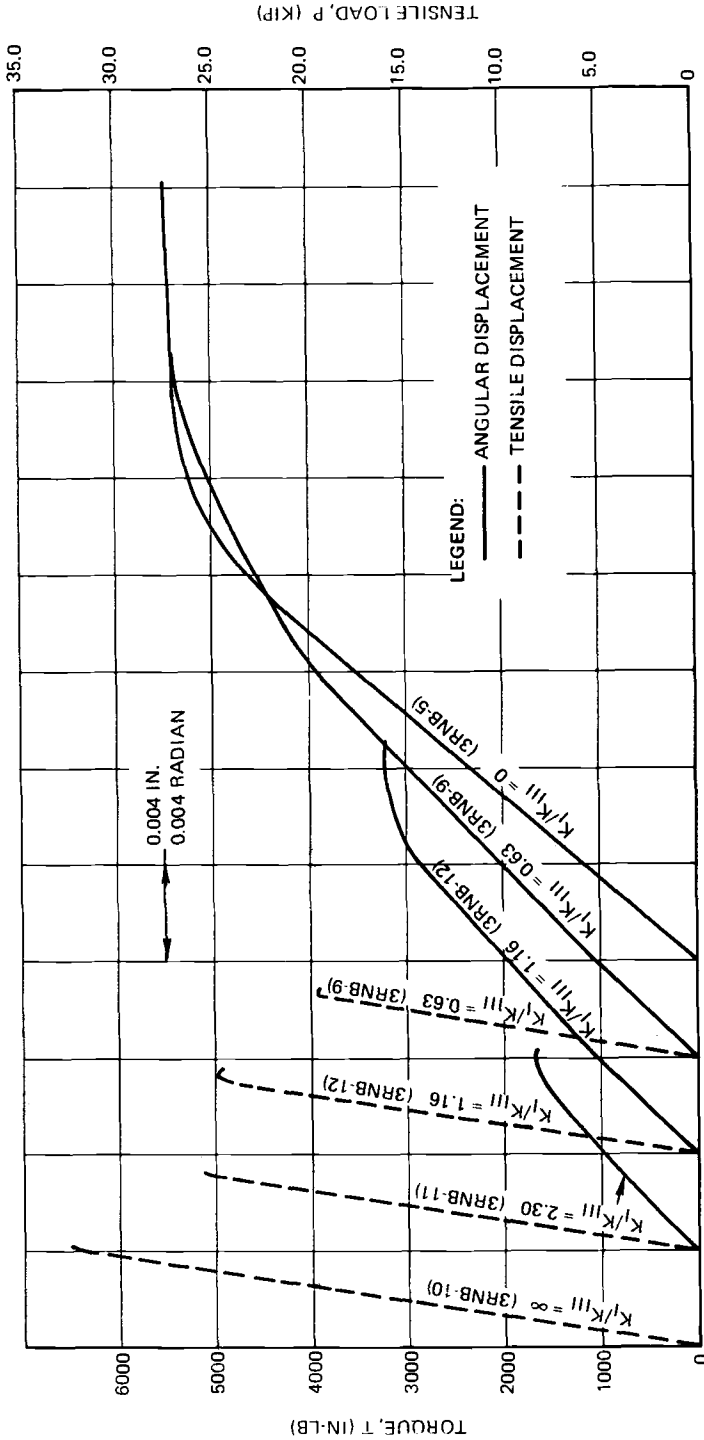


FIG. 10—Combined Mode I-III interaction curve for 4340 steel (round notched bar) at room temperature.

Figure 12 shows the fracture surfaces of the specimens subjected to various loading conditions of K_I/K_{III} . The specimen subjected to pure tension (3 RNB-10) had a flat fracture. Specimens with K_I/K_{III} ratios of 2.30 and 1.16 (3 RNB-11 and 3 RNB-12) did not have a flat fracture. However, the fracture surfaces had the same texture as that of the pure tension fracture. This, and the results in Fig. 10 indicate that Mode I (K_I) played the predominant role in the fracture of these specimens. The texture of the fracture surface of the specimen subjected to a K_I/K_{III} ratio of 0.63 (3 RNB-9) was similar to that of the fracture under pure torque indicating Mode III (K_{III}) played the dominant role in the fracture. The fracture surface of the specimen subjected to pure torsion was flat with shear rubbing marks.

Mode I-II-III Tests

Ten flat specimens containing semi-elliptical surface flaws initially oriented at $\phi = 0, 22.5, 45,$ and 60 deg to the width direction were loaded to failure in pure tension in a gaseous nitrogen environment at -200°F (Fig. 2) to study the effects of opening Mode K_I and the combined opening, sliding and tearing modes of crack extension $K_I, K_{II},$ and K_{III} on fracture.



DISPLACEMENT, IN OR RADIAN

FIG. 11—Load-displacement records for round notched bar specimens subjected to tension and torsion

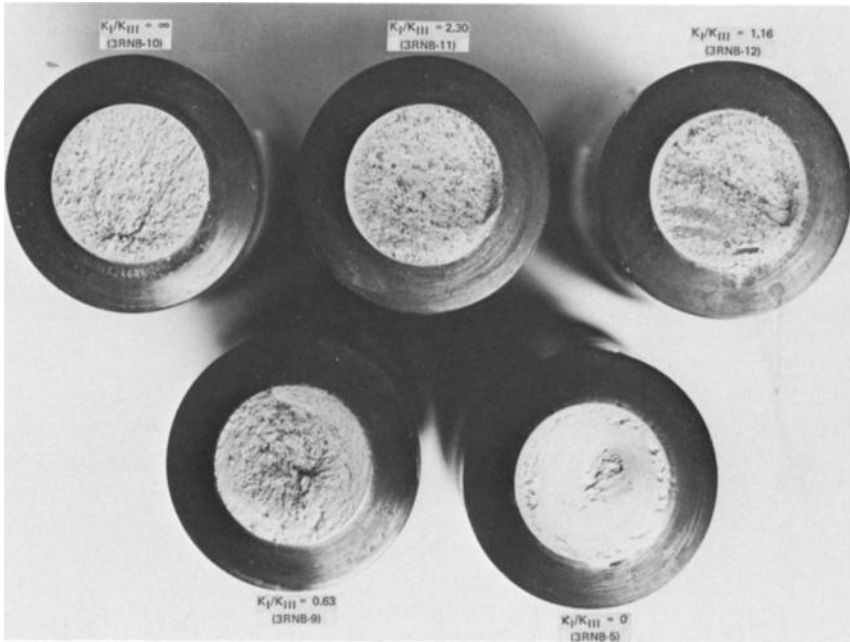


FIG. 12—Fracture surfaces of round notched bars of 4340 steel subjected to combined Modes I and III.

In these specimens, inclined flaw peripheries are subjected to continuously varying values of K_I , K_{II} , and K_{III} . K_{II} does not exist at the maximum crack depth and K_{III} is negligible near the free surface. Crack depths for these specimens were about 50 to 60 percent of the specimen thickness, and the aspect ratios ($a/2c$) of the cracks were about 0.25. The stress intensity factors were calculated at the maximum depth and the length, Points A and B, respectively, in Fig. 13. Since the stress intensity factor for a surface flaw subjected to uniform shear stress is not available, the stress intensity factors K_{II} and K_{III} for the specimens tested were calculated using a solution for an elliptical crack in a solid subjected to uniform shear stress [16]. The stress intensity factors K_I and K_{III} at the point of maximum depth were calculated by the following equations given in Refs 16 and 17.

$$K_I = M_K \sigma \cos^2 \phi \sqrt{\frac{\pi a}{Q}} \quad (6)$$

$$K_{III} = M_{III} \sigma \cos \phi \sin \phi \sqrt{\pi a} \quad (7)$$

where

$$M_{III} = \frac{(1 - \nu) k^2}{(k^2 - \nu) E(k) + k^2 K(k)} \quad (8)$$

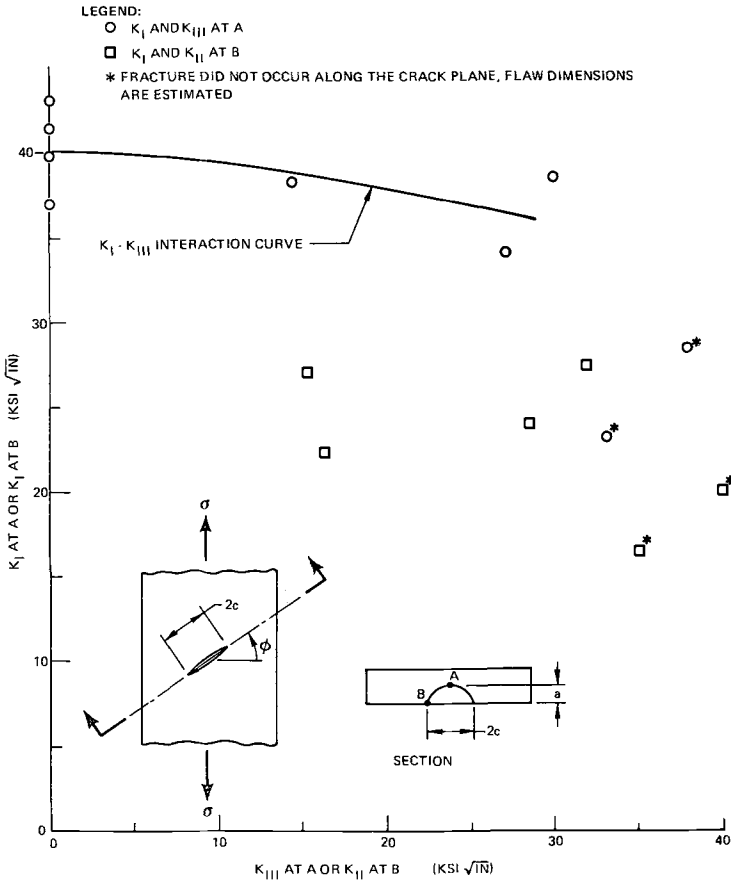


FIG. 13—Combined Modes I-III or I-II interaction for 4340 steel specimens containing slanted surface flaws and tested at -200°F .

The stress intensity factors at the surface (Point B) were calculated by the following equations.

$$K_I = 1.11 \sigma \cos^2 \phi \sqrt{\frac{\pi a}{Q}} \sqrt{a/c} \quad (9)$$

$$K_{II} = M_{II} \sigma \cos \phi \sin \phi \sqrt{\pi a} \quad (10)$$

where

$$M_{II} = - \frac{k^2 \sqrt{a/c}}{(k^2 - \nu) E(k) + k'^2 K(k)} \quad (11)$$

ν is the Poisson's ratio, $k'^2 = a^2/c^2$, $k^2 + k'^2 = 1$, and $K(k)$ and $E(k)$ are the complete elliptic integrals of the first and second kind, respectively. Figure 14 shows fracture surfaces for the specimens with $\phi = 0, 22.5, 45$, and

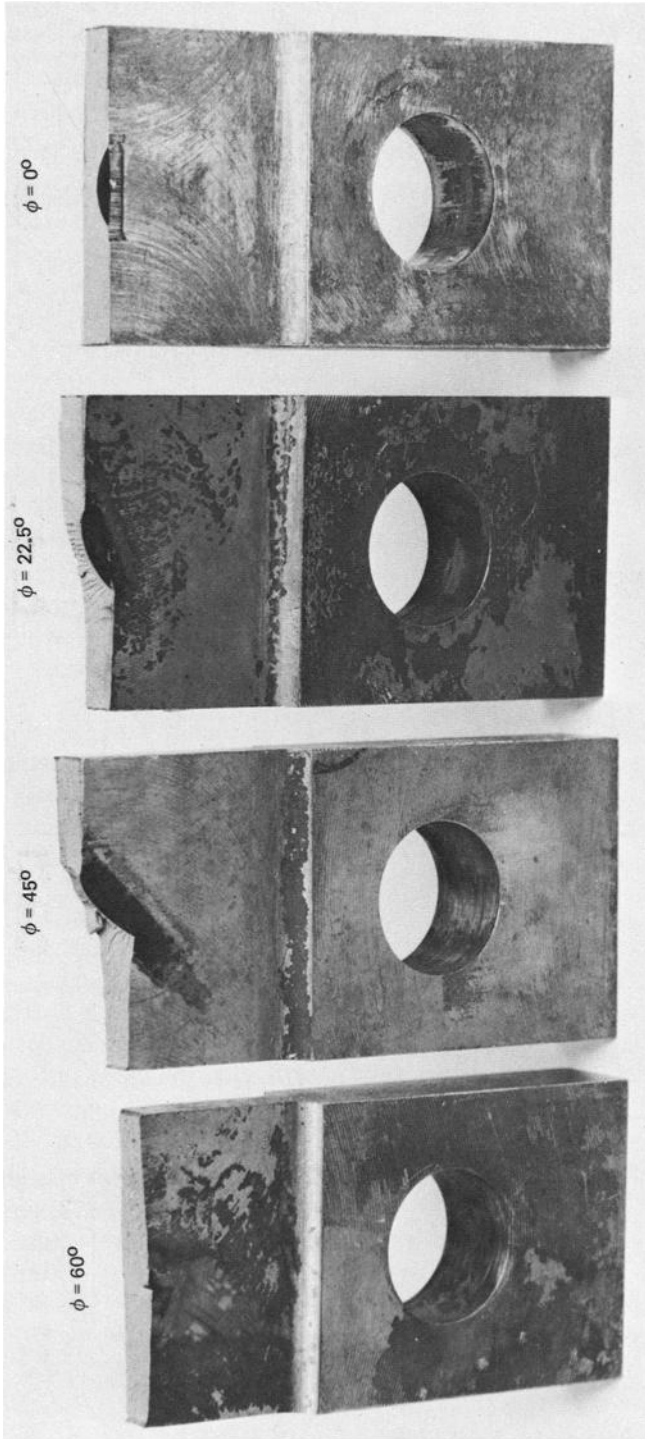


FIG. 14—Fracture surfaces of inclined surface flawed specimens subjected to combined Modes I, II, and III.

60 deg. The fracture surfaces were completely flat for Mode I specimens with surface cracks inclined at $\phi = 0$ deg. Fracture surfaces, for specimens with cracks inclined at $\phi = 22.5$ and 45 deg had a stepped (ladder type) appearance near and around the flaw periphery. Fracture surfaces were flat and perpendicular to the applied loading starting from the end of the crack at the free surface (Point B), as shown in Fig. 14. For specimens with cracks inclined at $\phi = 0, 22.5,$ and 45 deg, fracture appeared to initiate around the point of the maximum crack depth where K_{II} is nearly zero and K_I and K_{III} are the highest. For the specimens with cracks inclined at $\phi = 60$ deg, the fracture initiated near the point on the crack periphery at the free surface and transverse fracture, perpendicular to applied loading, occurred ignoring entirely the other portion of the flaw periphery. The combined mode data are evaluated in terms of K_I - K_{III} at the point of maximum crack depth, A, and K_I - K_{II} at the point near surface, B in Fig. 13. Figure 13 shows that applying K_{III} approximately up to 70 percent of K_{IIIc} has little effect on K_I at which fracture occurs.

Ten round specimens containing surface cracks (Fig. 3c) were loaded to failure at room temperature in pure tension, in combined tension and torsion, and in pure torsion. For the cracked specimen under only torsional loading, K_{II} does not exist at the maximum crack depth and K_{III} is negligible near the free surface. This is also shown by the results of three-dimensional frozen stress photoelastic experiments [12]. The flaw dimensions in all specimens were quite close except two specimens which had significantly large flaws. The range of flaw depths and lengths for the other eight specimens were 0.192 to 0.280 in. and 0.530 to 0.645 in., respectively. Results of these eight specimens are shown here. Since a good estimate for the stress intensity factor for this problem is not presently available, the results are shown in Fig. 15 in terms of the tensile stress at failure, σ_F , and the shear stress at failure, τ_F . The actual failure stresses σ_F' ($\sigma_F' = 4 P_F/\pi D^2$), and τ_F' ($\tau_F' = 16 T_F/\pi D^3$) for the specimens with flaw depth a ($0.192 \leq a \leq 0.280$) were converted to failure stresses σ_F and τ_F for the flaw depth of 0.240 in. by multiplying σ_F' and τ_F' by the factor $\sqrt{0.240/a}$. Failure stresses σ_F and τ_F are plotted in Fig. 15. Once again, the results show that the tensile stress at failure is almost unaffected by the presence of shear stress up to 100 ksi which is approximately 70 percent of shear stress at failure under pure shear. Figure 16 shows a photograph of the fracture surfaces for these surface cracked cylindrical specimens for various ratios of σ_F/τ_F . The specimen subjected to pure tension had a completely flat fracture. Most of the middle portion of the fracture surfaces of the specimens subjected to $\sigma_F/\tau_F = 1.12$ and 0.61 had textures similar to that of the pure tension specimens. Shear rubbing marks were observed on the periphery. The fractures appeared to be controlled by Mode I and to start at the maximum depth. The middle left portion of the fracture surface of the specimen subjected to $\sigma_F/\tau_F = 0.27$ had a texture similar to that of the pure tension specimen and the other portion of the fracture

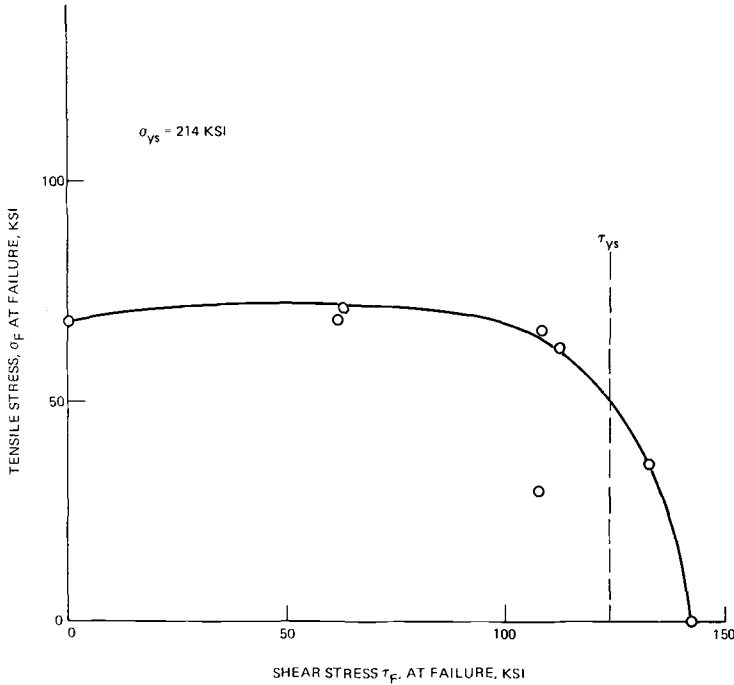


FIG. 15—Fracture tests of 4340 steel cylindrical specimens containing surface flaws ($a = 0.24$ in., $2c \approx 0.55$ in.) subjected to simultaneous tension and torsion.

resembled to that of the pure torsion specimen. The specimen subjected to pure torsion had a nearly flat fracture with shear rubbing marks over the fracture surface. From the examination of the fracture surfaces, it appears that fracture in all these specimens initiated near the maximum crack depth. Thus, it seems that for this specimen-loading configuration, the fracture originated under combined Mode I-III loading conditions. Since the constraint to crack tip deformation ratio is higher at the maximum crack depth than at the surface of the specimen, and since K_I and K_{III} are higher at the maximum crack depth [12], it is not surprising that the fracture did originate near the maximum crack depth.

A composite plot for the combined Mode I-III fracture is presented in Fig. 17 as K_I/K_{Ic} versus K_{III}/K_{IIIc} for round notched bar specimens, flat surface flawed specimens with inclined cracks and cylindrical surface flawed specimens. K_{IIIc} at -200°F was not determined experimentally. Hence, the following linear relation was assumed for estimating K_{IIIc} at -200°F .

$$\left. \frac{K_{IIIc}}{K_{Ic}} \right|_{-200^\circ\text{F}} = \left. \frac{K_{IIIc}}{K_{Ic}} \right|_{\text{room temperature}}$$

Since all the surface flawed cylindrical specimens had nearly the same flaw sizes, and the failure stresses σ_F and τ_F are adjusted for a single flaw



FIG. 16—Fracture surfaces of surface flawed round specimens of 4340 steel (left to right σ_F/τ_F are ∞ , 1.12, 0.61, 0.27, 0.0).

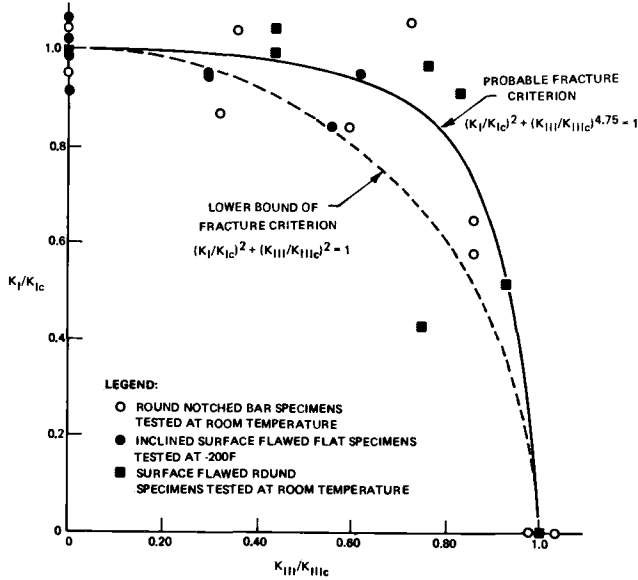


FIG. 17— K_I/K_{Ic} versus K_{III}/K_{IIIc} for round notched bar specimens, inclined surface flawed flat specimens, and surface flawed round specimens.

size, the ratios of K_I/K_{Ic} and K_{III}/K_{IIIc} can be calculated with little error by the following equations.

$$K_I/K_{Ic} = \frac{\sigma_F}{\sigma_F \text{ for the specimen subjected to pure tension}}$$

$$K_{III}/K_{IIIc} = \frac{\tau_F}{\tau_F \text{ for the specimen subjected to pure torsion}}$$

Figure 17 shows that the nondimensionalized data, obtained from the room temperature testing of round notched bar specimens and surface flawed cylindrical specimens, and from -200°F testing of inclined surface flawed flat specimens, are in a general agreement. The results in the plot bear out the same conclusions as drawn previously for the interaction of K_I and K_{III} on failure. Figure 17 shows the probable fracture criterion and the lower bound of the fracture criterion for the combined Mode I-III loadings. The probable fracture criterion is represented by the empirical equation $(K_I/K_{Ic})^2 + (K_{III}/K_{IIIc})^{4.75} = 1$. The lower bound of the fracture criterion is represented by the quadratic equation $(K_I/K_{Ic})^2 + (K_{III}/K_{IIIc})^2 = 1$.

Conclusions

The cracks subjected to the combined Mode I-II crack surface deformations propagate in a plane that is rotated with respect to the original crack plane and the direction of crack propagation can be well predicted. The

empirical relationship $K_I + K_{II} \approx K_{Ic}$ or $K_I/K_{Ic} + K_{II}/K_{IIc} = 1$ represents the fracture criterion adequately for 4340 steel specimens.

For the cracks subjected to combined Mode I-III and I-II-III crack surface deformations, it was found that the application of K_{III} up to about 70 percent of K_{IIIc} has little effect on K_I at which fracture occurs. Similarly, the application of K_I up to about 70 percent of K_{Ic} has little effect on K_{III} at which fracture occurs. The lower bound of the fracture criterion $F(K_I, K_{III})$ can be adequately described by a quadratic equation of K_I and K_{III} or K_I/K_{Ic} and K_{III}/K_{IIIc} .

Acknowledgments

The author wishes to acknowledge the support of NASA Lewis Research Center (Contract NAS3-14346) and G. T. Smith, Program Technical Manager. The author wishes to thank A. A. Ottlyk for conducting tests and L. R. Hall and A. S. Kobayashi for the advice and discussions.

References

- [1] Erdogan, F. and Sih, G. C., *Journal of Basic Engineering*, Transactions of the American Society of Mechanical Engineers, Series D, Vol. 85, 1963, pp. 519-527.
- [2] Wu, E. M., *Journal of Applied Mechanics*, Transactions of the American Society of Mechanical Engineers, Series E, Vol. 89, 1967, pp. 967-974.
- [3] Iida, S. and Kobayashi, A. S., *Journal of Basic Engineering*, Transactions of the American Society of Mechanical Engineers, Series D, Vol. 91, 1969, pp. 764-769.
- [4] Wilson, W. K., "On Combined Mode Fracture Mechanics," Research Report 69-1E7-FMECH-R1, Westinghouse Research Laboratories, June 1969.
- [5] Pook, L. P., *Journal of Engineering Fracture Mechanics*, Vol. 3, 1971, pp. 205-218.
- [6] Roberts, R. and Kibler, J. J., *Journal of Basic Engineering*, Transactions of the American Society of Mechanical Engineers, Series D, Vol. 93, 1971, pp. 671-680.
- [7] Liu, A. F., "Crack Growth and Failure of Aluminum Plate under In-Plane Shear," AIAA 73-253, 11th Aerospace Sciences Meeting, Washington, D. C., Jan. 1973.
- [8] Unpublished Data, Boeing Aerospace Co., Seattle, Wash.
- [9] Sih, G. C., "Introductory Chapter: A Special Theory of Crack Propagation," *Methods of Analysis and Solutions of Crack Problems*, G. C. Sih, Ed., Noordhoff International Publishing, 1972.
- [10] Sih, G. C. and Macdonald, B., "What the Designer Must Know About Fracture Mechanics," Applications of Fracture Mechanics to Engineering Problems, Lehigh University Report IFSM 72-23, No. 1972.
- [11] Palaniswamy, K. and Knauss, W. G., *International Journal of Fracture Mechanics*, Vol. 8, March 1972, pp. 114-117.
- [12] Shah, R. C., "Effects of Proof Loads and Combined Mode Loadings on Fracture and Flaw Growth Characteristics of Aerospace Alloys," NASA CR-134611, 1974.
- [13] Erdogan, F. and Ratwani, M., *International Journal of Fracture Mechanics*, Vol. 8, 1972, pp. 87-95.
- [14] Brown, W. F. and Srawley, J. E., *Plane Strain Crack Toughness Testing of High-Strength Metallic Materials*, ASTM STP 410, American Society for Testing and Materials, 1966.
- [15] Harris, D. O., *Journal of Basic Engineering*, Transactions of the American Society of Mechanical Engineers, Series D, Vol. 89, 1967, pp. 49-54.
- [16] Kassir, M. K. and Sih, G. C., *Journal of Applied Mechanics*, Transactions of the American Society of Mechanical Engineers, Series E, Vol. 89, 1966, pp. 601-611.
- [17] Shah, R. C. and Kobayashi, A. S. in *The Surface Crack: Physical Problems and Computational Solutions*, J. L. Swedlow, Ed., American Society of Mechanical Engineers, Nov. 1972, pp. 79-124.

A. S. Kobayashi,¹ B. Johnson,² and B. G. Wade³

Crack Approaching a Hole

REFERENCE: Kobayashi, A. S., Johnson, B., and Wade, B. G., "Crack Approaching a Hole," *Fracture Analysis, ASTM STP 560*, American Society for Testing and Materials, 1974, pp. 53-68.

ABSTRACT: Effects of region of stress concentration ahead of a running crack in Homalite-100 sheets with a centrally located hole were studied by dynamic photoelasticity. Mode I dynamic stress intensity factors and corresponding dynamic strain energy release rates and crack velocities as well as the corresponding Modes I and II static stress intensity factors, static strain energy release rates and strain energy density factors were determined. As the crack approached the hole, the static Mode II stress intensity factor rose to a peak value of approximately 10 to 25 percent of the Mode I stress intensity factor. The curved crack path appeared to have followed a path of maximum static strain energy release rate or of minimum static strain energy density factor. Our past experiences in dynamic crack propagation problems indicate that, other than local perturbations due to dynamic effects, either of the aforementioned static propagation laws should be the governing factor for the crack path in fracture dynamics.

KEY WORDS: crack propagation, fracture properties, mechanical properties, photoelasticity, stresses, strains

When a running crack in brittle material approaches a region of high stress concentration, one would expect the crack to curve into such region of high strain energy available for the fracturing process. The authors have, over a period of years, accumulated evidence that a region of high stress concentration is not necessarily a strong attraction to bend the path of a running crack from its intended straight path of propagation. Like many other experimental investigations, these results were obtained inadvertently while investigating the crack arrest capability of a hole ahead of a running crack [1].⁴ In the course of this and other investigations, cracks in six out of eighteen tests missed the arresting hole which was located straight ahead on the intended crack path. In two tests, the crack came as close as 0.09 in. from the hole boundary, passing through a region which was in a state of compression prior to the arrival of the crack tip. These near misses,

¹ Professor, Department of Mechanical Engineering, University of Washington, Seattle, Wash. 98195.

² Senior engineer, The Boeing Commercial Airplane Company, Seattle, Wash. 98124.

³ Consultant, J. Ray McDermott and Company, New Orleans, La. 70150.

⁴ The italic numbers in brackets refer to the list of references appended to this paper.

which apparently could not be explained solely by the presence of a region of high stress concentration, provided an opportunity to study some parameters which affect the path of a propagating crack. An effort was thus undertaken to evaluate these experimental results which otherwise would have been considered failures in experiments.

Since two-dimensional elastodynamic solutions of an accelerating or a decelerating crack as well as that of a constant velocity crack approaching a hole are not in sight, the authors resorted to their proven method of approach used in investigating other phenomena in dynamic fracture. Briefly, the procedure was to use appropriate static finite element analysis which was then interpreted together with the limited dynamic photoelasticity data of this intriguing problem where the crack missed its intended arresting hole. This approach was used with some success to analyze the complex problem of crack branching in a recent paper [2]. An account of our preliminary findings on parameters which govern the crack path is given in the following.

Experimental Procedure and Results

The modified Cranz-Schardin 16 spark-gap camera and associated dynamic polariscope used in this investigation were described in previous papers [3,4]. The test specimens considered in these series of tests consisted of $\frac{3}{8}$ -in. and $\frac{1}{8}$ -in. thick Homalite-100 plates with 10 by 10-in. test

TABLE 1—*Summary of experimental results.*

Test No.	Plate Thickness, in.	Hole Size and Location	ϵ Top ϵ Bottom	Remarks
1	0.382	0.500 in. dia, 7 in. from top of plate on centerline	0.00125 0.000625	Crack arrested at hole
2	0.395	0.150 in. dia, centrally located	0.001262 0.000841	Crack ran 0.09 in. by the hole
3	0.125	0.500 in. dia, 7 in. from top of plate and 0.5 in from centerline of plate	0.00130 0.00065	Crack ran 0.16 in. by the hole
4	0.383	0.250 in. dia, centrally located	0.0024 0.0006	Crack ran 0.01 in. by the hole, unstable crack initiated by impact
5	0.376	0.150 in. dia, centrally located	0.00109 0.00109	Crack ran 0.10 in. by the hole
6	0.393	0.150 in. dia, centrally located	0.00109 0.00109	Crack ran through the hole after being arrested (Ref 1)

section loaded in a fixed grip configuration. The prescribed boundary conditions included both uniform and linearly decreasing displacements along the fixed gripped edges of the specimen. Crack propagation was initiated by either loading the precracked single, edge-notched plate to its fracture load or impacting the crack by a wedge in a subcritically loaded plate [5]. The hole ahead of the running crack was either 0.50 or 0.15 in. in diameter. Testing conditions and some results from six tests are summarized in Table 1. Figure 1 shows a running crack being pulled into the arresting hole in the region where the state of stress was nearly compressive prior to the arrival of the crack tip. This test differed from similar test results reported in Ref 1 in that the crack almost missed the hole. Figures 2 and 3 show the running crack circumventing the hole with a gap as close as 0.16 in. in Fig. 2. The paths of running cracks shown in Fig. 3 started out

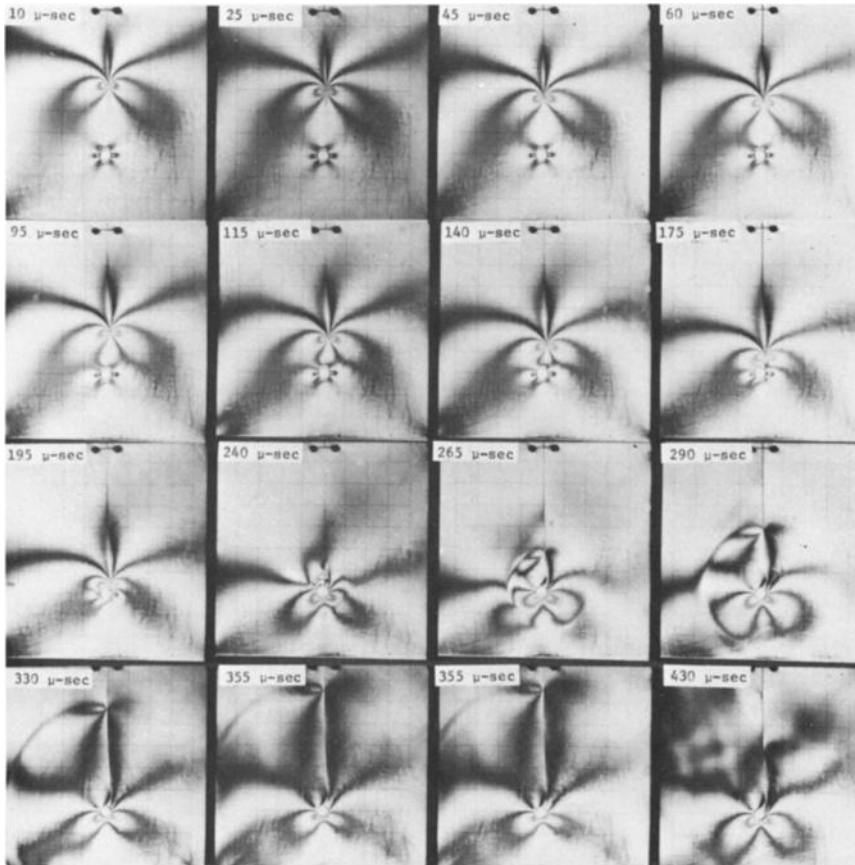


FIG. 1—Dynamic photoelastic patterns of a crack running into a 0.50-in.-diameter hole (Test 1).

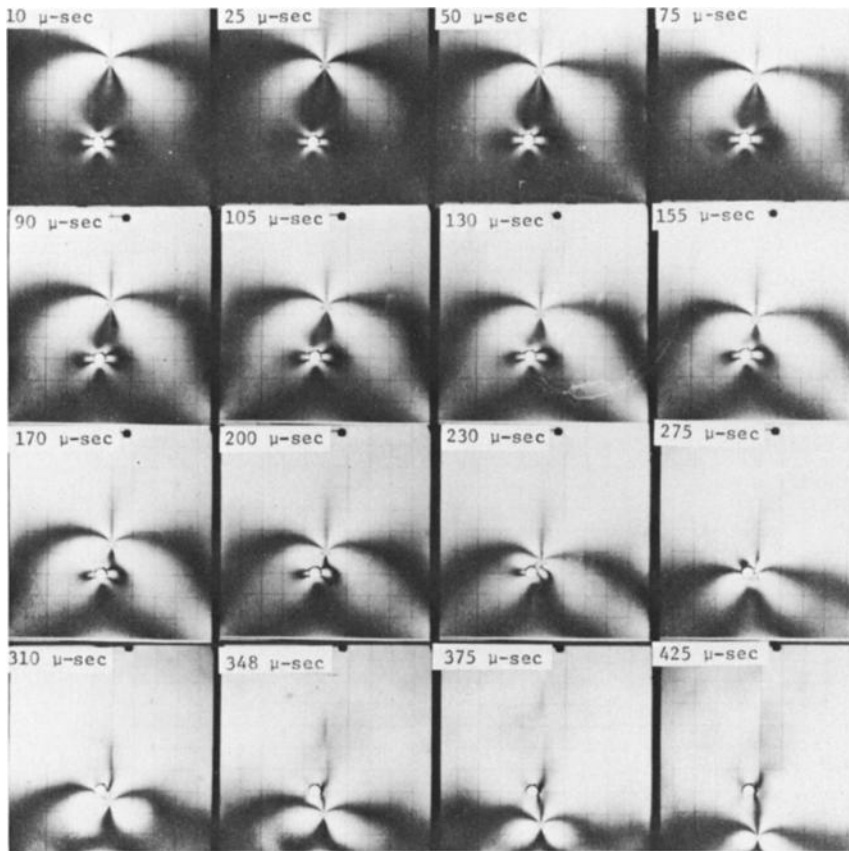


FIG. 2—Dynamic photoelastic patterns of a crack running past a 0.50-in.-diameter hole (Test 3).

inclined to the centerline of the plate due to misalignment of the starter crack. Such initial conditions apparently could not be offset by the localized region of static stress concentration at the hole despite the inner connected isochromatics shown in the intermediate frames of these figures. The crooked crack path in Fig. 3 shows evidences of intermittent arrests of the crack. The crack missed the hole in this test and continued through the plate despite such quasi-static running condition [5].

Most of the Homalite-100 sheets used in these experiments were calibrated by Bradley [3] who reported an average dynamic modulus of elasticity, Poisson's ratio, stress-optic coefficient, and static fracture toughness of 675 ksi, 0.345, 155 psi·in./fringe, and 579 psi $\sqrt{\text{in.}}$, respectively. Additional calibration data were obtained recently by Wade [6] on other batches of $\frac{3}{8}$ -in. thick sheets which yielded material and optical properties within 10 percent of those obtained by Bradley.

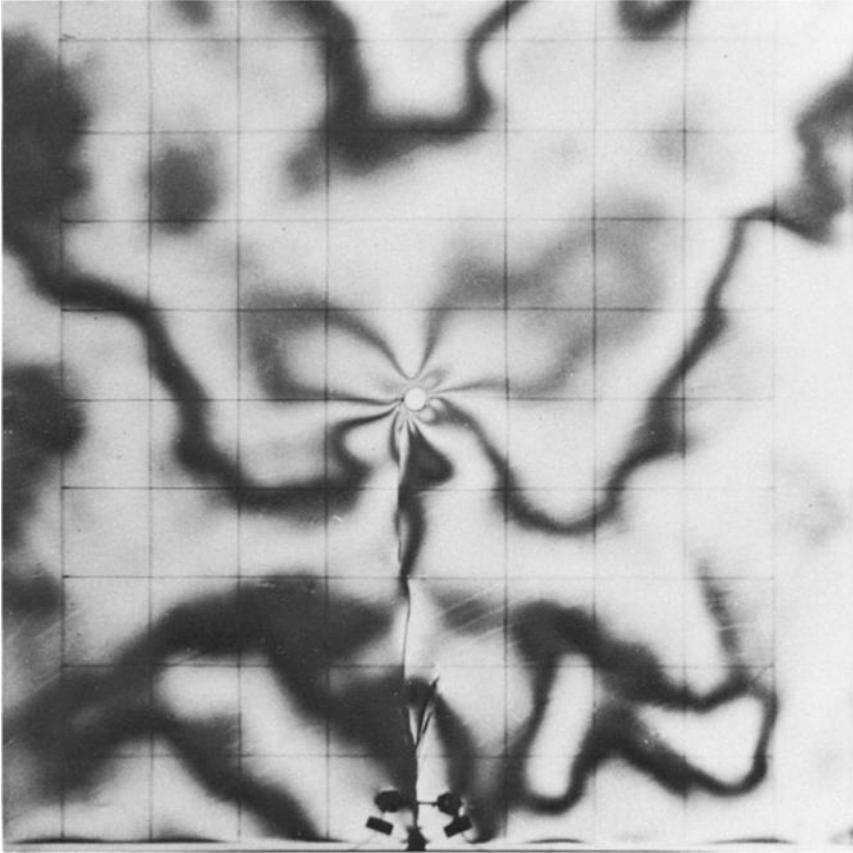


FIG. 3—Enlarged photograph of a running crack in a plate subjected to linearly increasing displacements at its two edges (Test 4). Crack was started by impacting the starter crack by a projectile with a velocity of 1300 inches per second. This frame was photographed 402 microseconds after the crack started to run.

Analytical Background

Initially, Mode I dynamic stress intensity factors, K_{ID} , were determined from dynamic isochromatics using Bradley's approximate procedure [4]. Curving of a running crack, however, cannot be explained by Mode I stress intensity factor alone. Unfortunately, Mode II dynamic stress intensity factor, K_{IID} , could not be determined separately due to insensitivity of the dynamic photoelastic procedure used. The fact that K_{IID} was small made it possible to estimate the dynamic strain energy release rate, \mathcal{G}_D , from K_{ID} alone following the procedure used in Ref 7. Briefly, this procedure uses Sih's near field solution [8,9] for a crack propagating at a constant velocity

in an infinite plate. The dynamic isochromatic lobe for a constant velocity crack can then be represented as

$$\tau_{\max}^2 = \left[\frac{K_I F_1(s_1, s_2)}{\sqrt{2\pi r}} \right]^2 \{ [(1 + s_2^2)(1 + s_1^2)f(s_1) - 4s_1s_2f(s_2)]^2 + 4s_1^2(1 + s_2^2)^2[g(s_1) - g(s_2)]^2 \} \quad (1)$$

where

K_I = the static Mode I stress intensity factor,

$$s_1 = \left[1 - \left(\frac{c}{c_1} \right)^2 \right]^{1/2};$$

$$s_2 = \left[1 - \left(\frac{c}{c_2} \right)^2 \right]^{1/2};$$

$$f^2(s_j) + g^2(s_j) = \frac{1}{\sqrt{\cos^2 \theta + s_j^2 \sin^2 \theta}}, \quad j = 1, 2;$$

$$f^2(s) - g^2(s_j) = \frac{1}{\cos \theta + s_j^2 \sin \theta \tan \theta}, \quad j = 1, 2;$$

c = the crack velocity;

$$c_1 = \sqrt{\frac{E(1 - \nu)}{(1 + \nu)(1 - 2\nu)}}, \text{ compressional wave velocity;}$$

$$c_2 = \sqrt{\frac{G}{\rho}}, \text{ shear wave velocity;}$$

E , G , and ν = the modulus of elasticity, shear modulus, and Poisson's ratio, respectively;

ρ = the mass density; and

$F_1(s_1, s_2)$ = the dynamic correction factor which varies with boundary and initial conditions.

Using Eq 1, the unknown function of $F_1(s_1, s_2)$ and hence the dynamic stress intensity factor, which varies slightly with angular orientation θ , can be determined from the dynamic isochromatics. A more logical criterion for fracture dynamics, however, would be from the viewpoint of strain energy release rate which is independent of such angular orientation. Sih has derived the dynamic strain energy release rate for a constant velocity crack as [7,8].

$$\frac{G_D}{G_S} = (1 + \nu)s_1(1 - s_2^2) [4s_1s_2 - (1 + s_2^2)^2] F_1^2(s_1, s_2) \quad (2)$$

where

- ν = the Poisson's ratio,
- \mathcal{G}_D = the dynamic strain energy release rate and is considered as the dynamic resistance to fracture, and
- \mathcal{G}_S = the elastic strain energy release rate determined from static analysis.

$$\mathcal{G}_D - \mathcal{G}_S + \frac{dT}{da} = 0 \quad (3)$$

where

$$\frac{dT}{da} = \text{the kinetic energy release rate.}^5$$

Recapitulating, the procedure for estimating a pseudodynamic strain energy release rate⁶ is to determine first, by Eq 1, the dynamic correction factor, $F_I(s_1, s_2)$, from the dynamic photoelastic pattern. The dynamic strain energy release rate is then calculated by using Eq 2. If necessary, the kinetic energy release rate can be computed by using Eq 3.

Static stress intensity factors and static strain energy release rate necessary in the previous procedure were determined by the method of finite element analysis. Unlike previous problems analyzed by the method of finite element analysis, problems considered in this investigation lacked symmetry and thus the entire plate had to be gridded for finite element analysis. Figure 4 shows a typical finite element layout involving 764 elements and 693 nodal points with crack tip element dimensions of 1.0×10^{-2} in. The static stress intensity factors were obtained from the strain energy release rate which can be determined directly by comparing values of total strain energy of two cracked plates with slightly different crack lengths. Since the curved crack in the vicinity of the hole was subjected to a combined Modes I and II deformation, the two Modes of I and II stress intensity factors, K_I and K_{II} , needed to be separated. An analytical relation between stress intensity factors and strain energy release rate is not available for a sharply bent crack but the well-known relation for a straight crack can be used for cracks with continuous curvature. The procedure used to separate K_I and K_{II} was to first calculate crack opening displacements within the acceptable 10 percent crack tip distance of a small segment which could be considered straight. From these crack opening displacements, the ratios of K_I and K_{II} were obtained and used to calculate more accurate stress intensity factors from the strain energy release rate.

The prior procedure of separating the two modes of stress intensity factors of a curved crack is cumbersome, particularly for a sharply curved

⁵ This term accounts for the difference between \mathcal{G}_D and \mathcal{G}_S [10].

⁶ The "pseudo" refers to a constant velocity crack which obviously is not the observed condition in our experiments.

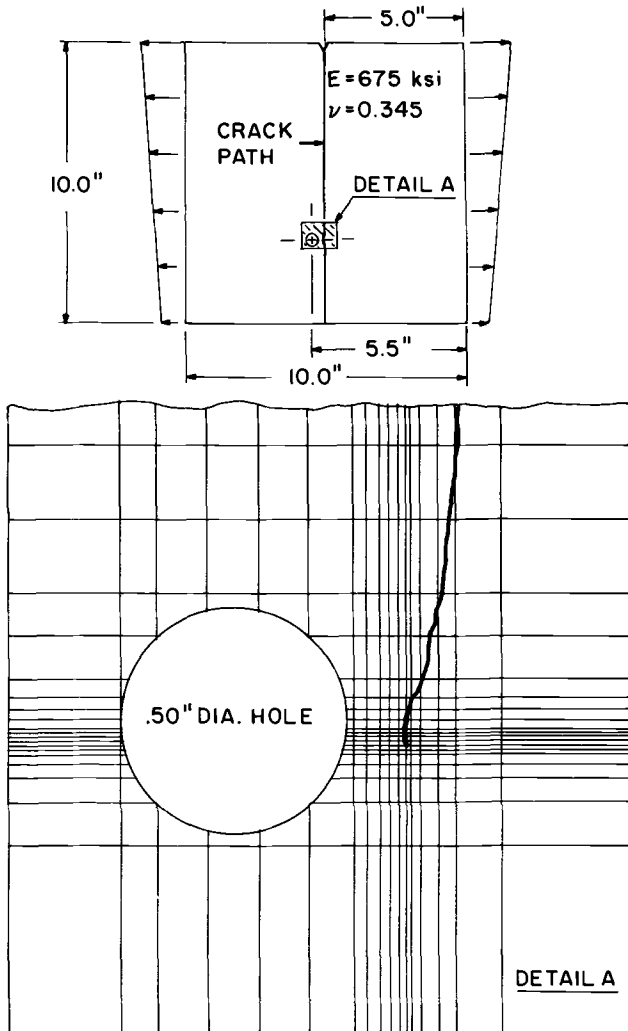


FIG. 4—Typical finite element mesh in the vicinity of hole (Specimen 3).

crack, but is not necessary if only the strain energy release rate due to crack extension around a sharp bend is sought for. Recent work by Palaniswamy and Knauss [11] suggests that static crack extension follows the maximum strain energy release criterion instead of the maximum K_I criterion by Erdogan and Sih [12]. This preliminary finding would also be applicable to dynamic crack extension.

The method of finite element analysis was thus used to estimate the directions of maximum static strain energy release rate and of minimum strain energy density factor in order to evaluate parameters which led to

the crack curving in or away from a hole. For the former, the strain energy before and after crack extension were calculated for the actual crack extension as well as two hypothetical directions of crack extension in order to assess the relative magnitude of the strain energy release rates with directions.

As for the strain energy density factor, S , Sih has shown that for the state of plane stress [13]

$$S = \frac{1}{\pi} [a_{11}K_I^2 + a_{12}K_I K_{II} + a_{22}K_{II}^2] \quad (4)$$

where

$$a_{11} = \frac{1}{16G} \left[\left(3 - 4 \frac{\nu}{1 + \nu} - \cos \theta \right) (1 + \cos \theta) \right],$$

$$a_{12} = \frac{1}{16G} (2 \sin \theta) \left[\cos \theta - \left(1 - 2 \frac{\nu}{1 + \nu} \right) \right], \text{ and}$$

$$a_{22} = \frac{1}{16G} \left[4 \left(1 - \frac{\nu}{1 + \nu} \right) (1 - \cos \theta) + (1 + \cos \theta) (3 \cos \theta - 1) \right].$$

Equation 4 involves the two current stress intensity factors before crack extension. With Sih's postulated criterion of fracture, which states that the crack propagates in the direction of minimum strain energy density factor, the direction of the crack path was then predicted and compared with actual measured values. Obviously, Sih's postulate is more convenient to use in comparison to the maximum strain energy criterion which requires a trial and error procedure to search for the direction of maximum strain energy release rate.

Results

Figure 5 shows a comparison between static and dynamic isochromatics in the vicinity of the hole for Specimen 1. Higher order dynamic and static isochromatic fringes are indicated on the left-hand side of the crack tip. By contrast, Frames 9 and 10 in Fig. 2 show an almost symmetric distribution of high stress regions on both sides of the crack tips accounting for the cracks running past the 0.50-in.-diameter hole. Regions of higher stress shown in Frames 11 and 12 of Fig. 2, on the other hand, were not influential enough to pull the crack into the 0.50-in.-diameter hole.

Figure 6 shows the static and dynamic strain energy release rates, G_S and G_D , and crack velocities, C , of Test 1. These results are similar to those reported previously [7] except for the fluctuation in stress intensity factors in the vicinity of the hole. The sudden drop in dynamic strain energy release rate prior to the crack tip passing the 0.150-in.-diameter hole as shown in Fig. 6 is probably due to the interaction with reflected stress

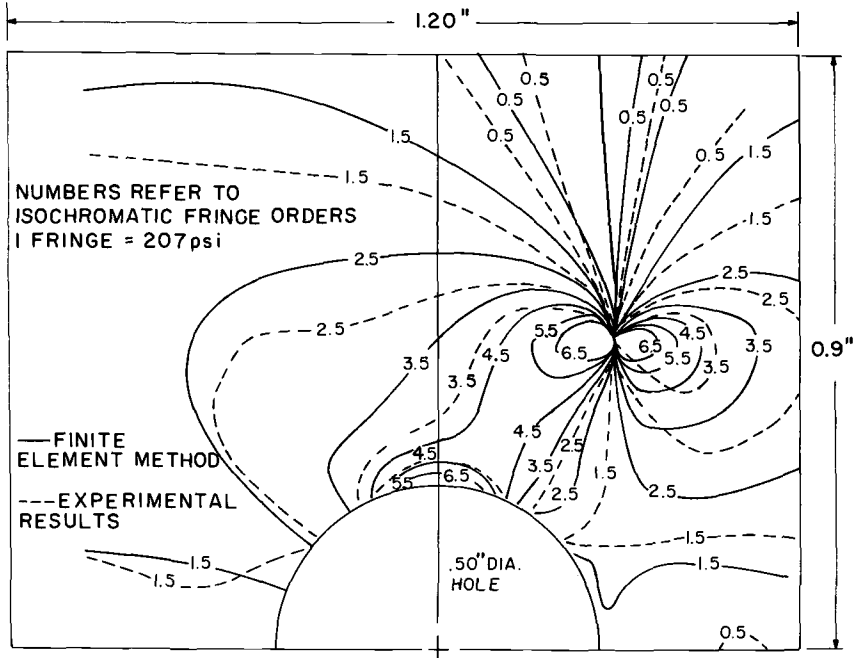


FIG. 5—Static and dynamic isochromatic as the crack top approaches the hole (Frame 9 in Fig. 1).

waves. The static strain energy release rate, and the crack velocity on the other hand, does not decrease until the crack tip is about to pass the edge of the hole.

Figures 7 and 8 show static strain energy release rate and strain energy density factors, G_S and S , and the static stress intensity factors, K_I and K_{II} , along the crack paths in the vicinity of the hole. Also shown are the predicted crack angles using Sih's postulate. Remarkable agreement between the measured and predicted crack paths is noted.

Discussion

Relations between the static strain energy release rate, the dynamic strain energy release rate and crack velocities obtained in this investigation are similar to those reported in Ref 6. The reflecting stress waves at the hole and at the plate boundaries caused time dependent fluctuations in dynamic strain energy release rates shown in Fig. 6. The large dynamic strain energy release rate, which remained larger in absolute value than the static strain energy release rate in Fig. 6, is due to the tension field in the wake of a circular stress wave emanating from the 0.150-in.-diameter hole. This circular pattern of stress wave was generated by the compression wave, which emanated from the moving crack tip and impacted on the

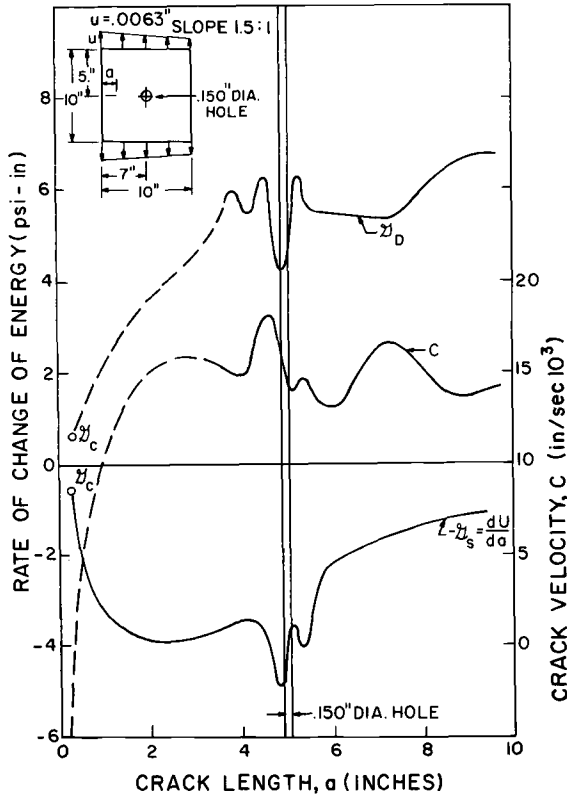


FIG. 6—Static and dynamic strain energy release rates and crack velocity (Specimen 2).

stress free hole boundary. The wave front of this circular stress wave can be identified in Frames 9 through 13 in Test 2.

Returning to Fig. 5, the dynamic isochromatic lobes left of the crack are larger in size and are tilted forward with respect to the corresponding lobes right of the crack. This difference in dynamic isochromatic lobes can be studied by matching the isochromatics of a straight crack for which an analytical solution exists. The close similarity in the dynamic and the matched isochromatics were discussed in Ref 7. The matched isochromatics can be represented in terms of the local stress field near the tip of a straight crack as

$$\begin{aligned}
 \tau_{\max}^2 = \frac{1}{8\pi r} \left\{ \left[K_{ID} \left(\sin^2 \theta + 2\delta \sqrt{\frac{2r}{a}} \sin \theta \sin \frac{3\theta}{2} + \frac{2r\delta^2}{a} \right) \right] \right. \\
 + K_{ID} K_{IID} \left[2 \sin 2\theta + \delta \sqrt{\frac{2r}{a}} \left(\sin \frac{3\theta}{2} + 3 \sin \frac{\theta}{2} \right) \right] \\
 \left. + K_{IID}^2 (1 + 3 \cos^2 \theta) \right\} \quad (5)
 \end{aligned}$$

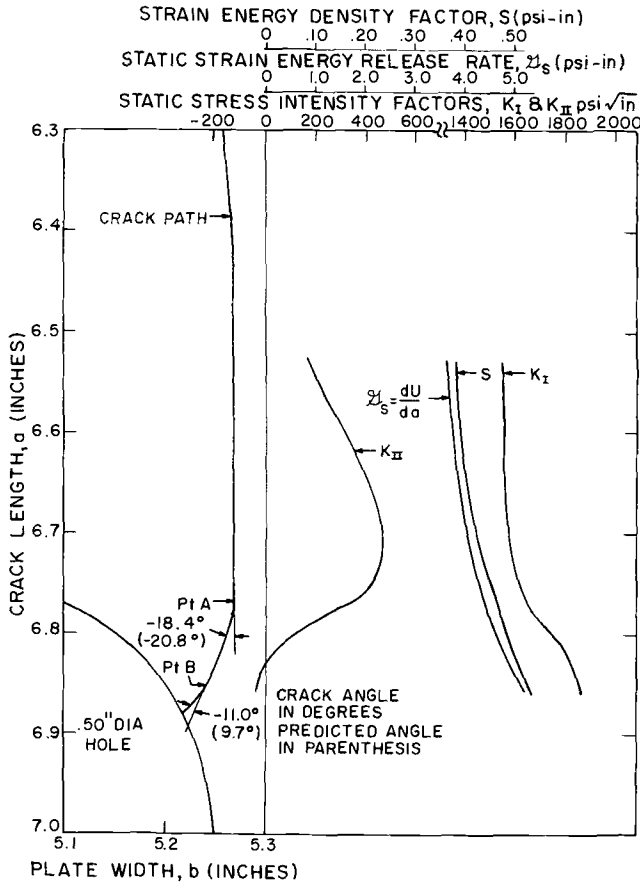


FIG. 7—Static strain energy release rate, stress intensity factor, and crack orientation in the vicinity of hole (Specimen 1).

where

- r and θ = the familiar local coordinates at the crack tip,
- a = the length of the straight crack in the edge-notched specimen, and
- $\delta = \sigma_{0x}/\sigma =$ the remote stress factor discussed in Ref 5.

Figure 9 shows shape changes in the local isochromatic lobes with varying K_{IID}/K_{ID} ratios and remote stress factors.

Using Fig. 9, the isochromatic pattern in Fig. 5 can be related to a local stress field with dynamic stress intensity factor ratio of $K_{IID}/K_{ID} = -0.1$ and $\delta \sim 1$ for an hypothetical straight crack. The relatively large value of K_{IID} indicates that the dynamic strain energy release rate determined by ignoring K_{IID} in Eqs 1 and 2 could be in error, particularly in the near

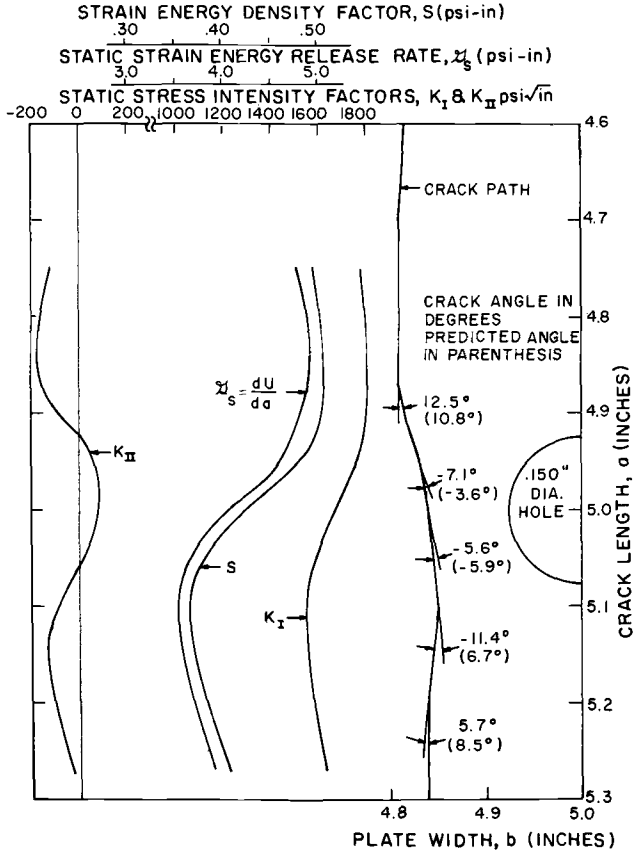


FIG. 8—Static strain energy release rate, stress intensity factor, and crack orientation in the vicinity of hole (Specimen 2).

vicinity of the hole. Unfortunately, the resolution limit of our present dynamic photoelasticity system is such that quantitative analysis of such a small region cannot be conducted; thus much must be inferred from the static finite element analyses. Inspection of Fig. 5 shows that as far as K_{IID}/K_{ID} ratios are concerned, these ratios can be inferred from the corresponding static K_{II}/K_I ratios derivable from the results shown in Figs. 7, 8, and 10.

Figure 7 shows a K_{II}/K_I ratio of approximately $\frac{1}{4}$ prior to the crack curving back towards the hole. Undoubtedly, this large component of K_{II} was instrumental in bending the crack path sharply at this point. In contrast, K_{II}/K_I ratios are less than 10 percent of the corresponding K_I in Fig. 8 where the crack bypassed the hole. The small static K_{II}/K_I ratios also imply local symmetry and thus this part of our finding is in agreement with earlier findings by Cotterell [14]. The high K_{II}/K_I ratio of $\frac{1}{4}$ in Fig. 7,

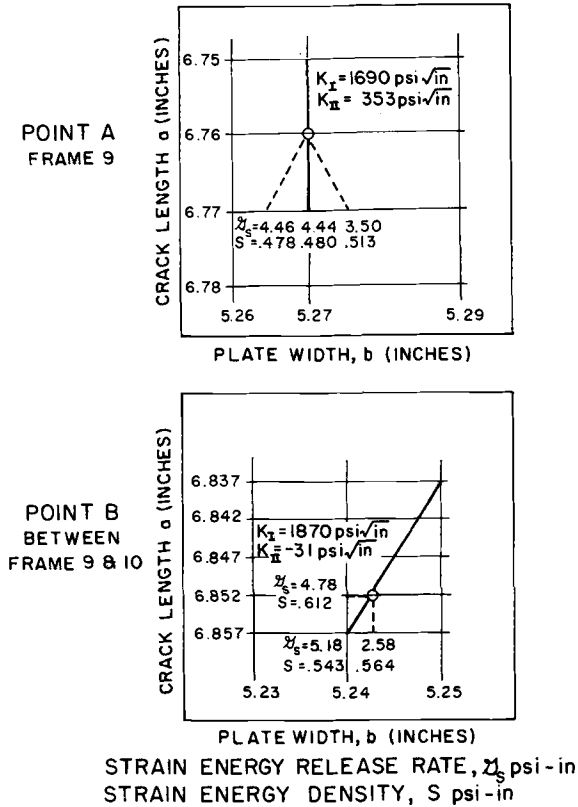


FIG. 9—Shape changes in isochromatics with K_{II}/K_I ratio.

on the other hand, showed that the crack curved to reduce such high K_{II}/K_I in order to run along the line of local symmetry.

Referring to Fig. 10, remarkable agreement between measured crack angles and angles predicted by Sih's postulate adds further evidence that the overall crack path of a propagating crack is probably predetermined by the static field prior to crack propagation. Rapid fluctuations in dynamic strain energy release rates can only sway the crack path temporarily from its predetermined path as evidenced in Fig. 3. If this instantaneous local disturbance occurs when the crack tip is very close to the hole boundary, conceivably such dynamic effect could be the difference between crack arrest at the hole or crack bypassing the hole. Local depressions of G_s and S in the vicinity of the hole as shown in Fig. 8 are in qualitative agreement with similar results obtained for a static crack bisecting the distance between two colinear holes [15].

The results in Fig. 10 show that the static strain energy release rate is slightly more sensitive to crack tip orientation than the corresponding

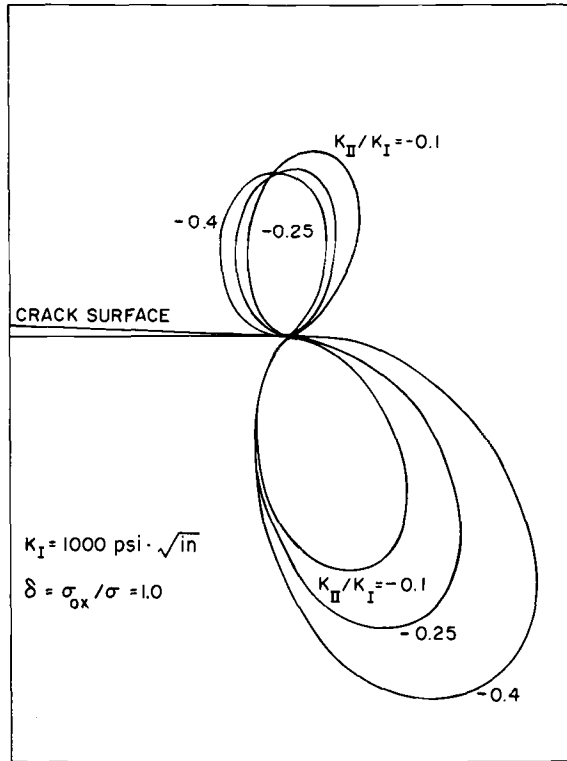


FIG. 10—Static strain energy release rate, stress intensity factor, and crack orientation (Specimen 1). See Fig. 7 for location of Points A and B.

static strain energy density factor. This small difference is more than compensated for by the closed form expression for predicting the direction of crack propagation by the S -theory. As mentioned earlier, the strain release rate criterion requires a trial and error procedure to establish the maximum direction.

Finally, the isolated results in Fig. 9 indicate that the $K_{II} = 0$ criterion for predicting crack path may not always be valid while the maximum \mathcal{G}_S criterion and the minimum S criterion apparently remained valid in this case.

Conclusions

Preliminary results show that the static stress field ahead of the propagating crack tip governs the crack path with the exception of local disturbances caused by transient stress waves. The static maximum strain energy release rate criterion and the static minimum strain energy density factor criterion can both be used to predict the crack path of a propagating crack. The seemingly mysterious phenomenon of a crack bypassing the

high stress concentration area of a hole can be readily explained on the basis of such static calculations.

Acknowledgment

This research project was sponsored by the Office of Naval Research Contract No. N00014-67-0103-0018 NR064 478. The writers wish to thank N. Basdagas and N. Perrone of ONR for their patience and encouragement during the course of this investigation.

References

- [1] Kobayashi, A. S., Wade, B. G., and Maiden, D. E., *Experimental Mechanics*, Vol. 12, Jan. 1972, pp. 32-37.
- [2] Kobayashi, A. S., Wade, B. G., Bradley, W. B., and Chiu, S. T., *International Journal of Engineering Fracture Mechanics*, Vol. 6, No. 1, March 1974, pp. 81-92.
- [3] Bradley, W. B. and Kobayashi, A. S., *Experimental Mechanics*, Vol. 10, No. 3, March 1970, pp. 106-113.
- [4] Bradley, W. B. and Kobayashi, A. S., *Engineering Fracture Mechanics*, Vol. 3, 1973, pp. 317-332.
- [5] Kobayashi, A. S. and Wade, B. G., "Crack Propagation and Arrest in Impacted Plates," *Proceedings*, International Conference on Dynamic Crack Propagation, Noordhoff International, 1973, pp. 663-678.
- [6] Wade, B. G., "A Photoelastic and Numerical Study on Fracture Dynamics of Stressed Panels," Ph.D. thesis, University of Washington, 1974.
- [7] Kobayashi, A. S., Wade, B. G., and Bradley, W. B. in *Deformation and Fracture of High Polymers*, H. H. Kausch, J. A. Hassell, and R. I. Jaffee, Eds., Plenum Press, New York, 1973, pp. 487-500.
- [8] Sih, G. C., *International Journal of Fracture Mechanics*, Vol. 5, 1968, pp. 51-68.
- [9] Sih, G. C. in *Inelastic Behavior of Solids*, M. R. Kanninen, W. F. Alder, A. R. Rosenfield, and R. I. Jaffee, Eds., McGraw-Hill, New York, 1970, pp. 607-639.
- [10] Hahn, G. T., Hoagland, R. G., Kanninen, M. F., and Rosenfield, A. R., "Fast Fracture and Arrest in 4340 Steel," *Proceedings*, International Conference on Dynamic Crack Propagation, Noordhoff International, 1973.
- [11] Paliniswamy, K. and Knauss, W. G., *International Journal of Fracture Mechanics*, Vol. 8, No. 1, March 1972, pp. 114-117.
- [12] Erdogan, F. and Sih, G. C., *Journal of Basic Engineering*, Vol. 85, Series E, Dec. 1963, pp. 518-527.
- [13] Sih, G. C. in *Mechanics of Fracture I, Methods of Analysis and Solutions to Crack Problems*, G. C. Sih, Ed., Walter-Noordhoff International, 1973, pp. XXI-XLV.
- [14] Cotterell, R., *International Journal of Fracture Mechanics*, Vol. 1, 1965, pp. 96-103.
- [15] Isida, M. in *Mechanics of Fracture I, Methods of Analysis and Solutions of Crack Problems*, G. C. Sih, Ed., Walter-Noordhoff International, 1973, pp. 56-130.

Influence of Three-Dimensional Effects on the Stress Intensity Factors of Compact Tension Specimens

REFERENCE: Schroedl, M. A. and Smith, C. W., "Influence of Three-Dimensional Effects on the Stress Intensity Factors of Compact Tension Specimens," *Fracture Analysis, ASTM STP 560*, American Society for Testing and Materials, pp. 69-80.

ABSTRACT: The stress freezing technique of photoelasticity was utilized to study the stress intensity variation between full thickness and center slices of compact tension specimens for various crack lengths. Specimen geometries covered an a/w range of 0.3 to 0.7 for values of w/B of 2 and 3.5.

Normalized stress intensity factor results for geometries within ASTM Test for Plane-Strain Fracture Toughness of Metallic Materials (E 399-72) specifications (that is, $w/B = 2.0$, $a/w = 0.50$) agreed with the ASTM solution to within experimental error. However, for a/w values outside the ASTM range (0.45 to 0.55), experimental results were measurably higher than the ASTM results for $w/B = 2.0$ and averaged 13 percent higher for all a/w studied at $w/B = 3.5$. The center slice SIF was found to be 5 to 10 percent higher than the through the thickness average on all tests.

KEY WORDS: fatigue (materials), photoelasticity, cracking (fracturing), stresses, fracture properties

Nomenclature

- σ_{ij} In-plane stress components
- K_I Mode I stress intensity factor (lbs/in.^{3/2})
- r, θ Polar coordinates (in., radians)
- a Crack length (in.) (see Fig. 2)
- w, B Specimen width (in.) (see Fig. 2), specimen thickness (in.)
- τ_{\max}, τ_m Maximum shearing stress in plane perpendicular to crack border (psi)
- K_{ap} Apparent stress intensity factor (lb/in.^{3/2})
- K_{TSCM} Approximate stress intensity factor (lb/in.^{3/2})

¹ Graduate research assistant and professor, respectively, Department of Engineering Science and Mechanics, Virginia Polytechnic Institute and State University, Blacksburg, Va. 24061.

- n* Fringe order
- f* Material fringe value (lb/in.)
- t* Thickness (in.)

A substantial effort, both from the point of view of analysis as well as fracture toughness testing, has been carried out in recent years towards the development of a universal compact plane-strain fracture toughness test specimen. The analyses have taken the form of boundary collocation [1-5]² and finite element solutions [4,5,6]. The correlation of the published results of fracture toughness testing programs is found in Refs 3 and 7 together with tentative test specifications and procedures. In a discussion in Ref 3, the importance of studying the three-dimensional effects photoelastically was noted. More specifically, the variation in the three-dimensional effect upon the stress intensity factor (SIF) with thickness and crack length was found to be virtually unknown. Although photoelastic stress analysis has been carried out on geometries similar to the current compact tension specimen [8], and the SIF has been estimated for the center slice [9], apparently no study has been directed towards measuring the three-dimensional effect upon the SIF directly for varying thickness and crack length. Moreover, except for the analysis of a highly idealized model [10], analytical studies have been essentially two dimensional. The present investigation was undertaken to study this effect photoelastically for a range of compact tension specimen crack lengths and thicknesses of interest to the American Society for Testing and Materials and agencies utilizing the compact tension test in order to determine the feasibility of extending the specimen geometrical ranges prescribed by ASTM Test for Plane-Strain Fractures Toughness of Metallic Materials (E 399-72).

Analytical Considerations

Photoelastic studies of crack tip stress fields have been carried out by a number of investigators [11-20]. One of the major difficulties in such studies has been the problem of extracting valid SIF values from the photoelastic data. This problem has received considerable attention recently by Marloff and his associates [9], Kobayashi and his associates [21-24], and more recently by the author and his associates [25-29]. The author and his associates have developed two methods for extracting the SIF which have been used in a wide variety of problems. One of these methods, called the Taylor Series Correction Method (TSCM) will be employed in the present study. The philosophy and use of the method are described in the sequel.

² The italic numbers in brackets refer to the list of references appended to this paper.

It is well known that the elastic stresses near a crack tip in a plane normal to the crack border take a familiar singular form which may be written as

$$\sigma_{ij} = \frac{K_I}{r^{1/2}} f_{ij}(\theta) \quad i,j = x,y \quad (1)$$

where K_I is the stress intensity factor and r, θ are measured from the crack tip as shown in Fig. 1. Since σ_{ij} involve singular terms, then the maximum in plane shearing stress

$$\tau_{\max} = \frac{1}{2} [(\sigma_{yy} - \sigma_{xx})^2 + 4\tau_{xy}^2]^{1/2} \quad (2)$$

will also involve singular stresses. The authors have shown [25] that the blunted zone created by stress freezing photoelasticity near a crack tip creates a nonlinear zone very near the crack tip, but this zone is very local and light reflections from the crack tip ordinarily preclude measurements this close to the crack tip. On the other hand, there is no way to determine precisely how far away from the crack tip one can be before nonsingular terms in the stress description begin to contribute appreciably to the photoelastically measured τ_{\max} . Since fringe loops around a crack tip tend to spread furthest along a line approximately in a direction normal to the crack surfaces and passing through the crack tip, data are always taken along this line, reducing τ_{\max} to the form

$$\tau_{\max} = \tau_{\max}(r) \quad (3)$$

In order to account for boundaries other than crack surfaces themselves, TSCM expresses τ_{\max} in the form

$$\tau_{\max} = \frac{A}{r^{1/2}} + \sum_{N=0}^M B_N r^N \quad (4)$$

A computer program has been written to receive input data in the form of τ_{\max} , r from the photoelastic data and to compute A , B_N from the data using a least squares procedure beginning with only the first term (namely,

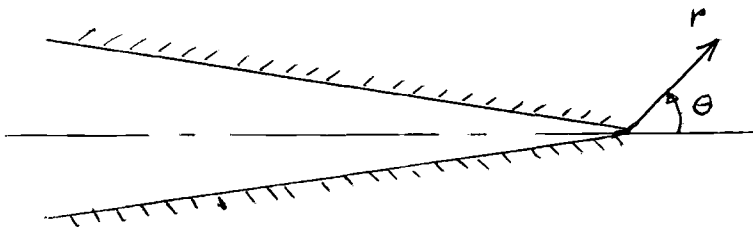


FIG. 1—Local coordinates.

A) then A , B_0 , then A , B_0 , B_1 , etc. recomputing A each time until the M th term contributes an amount to τ_{\max} less than the estimated experimental error. In this region, Eq 4 is truncated and $A = K_I/(8\pi)^{1/2}$ is determined. There is no specific truncation criterion and some judgement on the part of the investigator is required here. The convergence of the program is verified in Ref 27.

For two-dimensional problems, the method corresponds to the application of the Williams Stress Function along $\theta = \pi/2$. Details of the program are found in Ref 27.

The Experiments

A set of photoelastic experiments was designed to study the influence of crack length upon the stress intensity factor for two thicknesses and the three-dimensional effects thereof. The basic geometry of the test specimens is given in Fig. 2 and the dimensions are found in Table 1. The use of the 30 deg notch to simulate the crack tip stress field was suggested by the results of investigations in Ref 30 and was verified by comparing pilot test results with Wilson's boundary collocation solution. Pilot tests revealed that, due to the very low threshold value of K_{IC} for the model material above critical temperature, live loads were restricted to very small values and a counterweight was necessary in order to maintain Mode I loading on the crack tip. The force system consisting of the dead weight of the lower half of the specimen, the counterweight, and the added pin reaction served to intensify K_I . Moreover, the use of full-size pins above critical temperature produced erratic results due to variations in the contact surface and frictional effects as the soft material deformed around the pins. In order to alleviate the several difficulties just described, the authors used pins which were approximately one-half the hole size for the stress freezing tests and

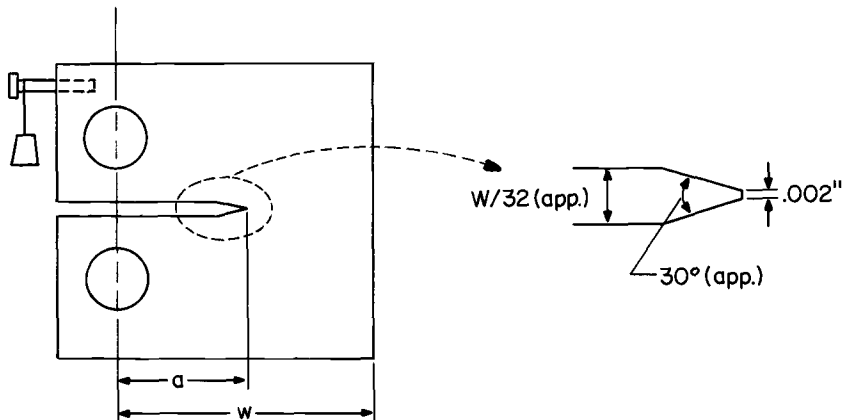


FIG. 2—Specimen configurations.

TABLE 1—Dimensions of the test specimens.

Test	Geometry					Room Temperature Values		Stress Freezing Values
	a (in.)	w (in.)	B (in.)	a/w	w/B	$K_{\text{exp}}^a B\sqrt{w}$	$K_{\text{theo}}^b B\sqrt{w}$	
						P^e	P	$K_{\text{cs}}^c / K_{\text{TT}}^d$
A-1	0.525	3.50	1.750	0.30	2.00	6.0	5.9	1.08
A-2	0.875	1.75	0.875	0.50	2.00	9.7 ^f	9.6	1.10
A-3	1.05	1.75	0.875	0.60	2.00	15.1 ^f	13.5	1.10
A-4	1.23	1.75	0.875	0.70	2.00	22.3 ^f	21.4	1.10 ^g
B-1	1.40	3.50	1.00	0.40	3.50	8.4	7.3	1.05 ^g
B-2	1.58	3.50	1.00	0.45	3.50	9.2 ^g	8.3	1.06
B-3	1.75	3.50	1.00	0.50	3.50	10.5	9.6	1.07
B-4	1.93	3.50	1.00	0.55	3.50	12.3 ^g	11.3	1.08 ^g
B-5	2.10	3.50	1.00	0.60	3.50	15.6	13.5	1.09
B-6	2.45	3.50	1.00	0.70	3.50	24.5	21.4	1.10

^a K_{exp} = experimental SIF averaged through thickness at room temperature.

^b K_{theo} = theoretical SIF ASTM E 399-72.

^c K_{cs} = experimental SIF center slice—stress frozen.

^d K_{TT} = experimental SIF through thickness.

^e P = applied load.

^f Average of two tests.

^g Estimated or extrapolated from tests on similar or identical geometry.

were able to obtain consistent results. Furthermore, the value of K_I was established from through the thickness room temperature fringe patterns for each test (using full-size pins and much larger loads than those at stress freezing temperatures) and the thickness effect was obtained by stress freezing in a subsequent test on the same specimen. This approach implies that the auxiliary loading system consisting of the weight of the lower half of the specimen, the counterweight, and additional pin forces have no influence upon the variation in K_I through the specimen thickness. Pilot tests using only the auxiliary load system with the A-3 geometry support this assumption.

Model Manufacture—All models were made from PLM-4B or Hysol 4290 stress freezing photoelastic materials by milling off 50 mils from all surfaces and maintaining ASTM tolerances throughout. All cracks were made with circular saws.

Test Procedure—After inspection in the polariscope to ensure stress-free specimens, the specimens were loaded at room temperature through full-size pins in a dead weight system and through the thickness fringe photographs were obtained. Specimens were then counterweighted, hung in the oven, and heated slowly to critical temperature (275 or 300°F). After a thermal soak of about 10 h, the live load was applied as a dead weight through the lower pin and cooling at a rate of about 2°F/h was carried out under full load. Upon cooling, the specimen was placed in a

tank of oil of the same index of refraction as the model material, and full scale and local fringe photographs were made. A full-scale fringe photo through the thickness is shown in Fig. 3. Next, a center slice about 0.10-in. thick was removed perpendicular to the crack border, and the fringe photography was repeated utilizing a partial mirror fringe multiplication system. All local fringe shots were made through a telescopic lens producing working prints of about $\times 15$ to $\times 20$. A typical slice photo is shown in Fig. 4.

Results

A typical set of raw fringe data from the stress freezing tests are shown in Fig. 5 together with the curves fitted by TSCM. Data scatter is small and the curves fitted by TSCM fit the data well. In order to obtain a more sensitive assessment of data scatter and to illustrate how TSCM is used to obtain the SIF by extrapolation, the data of Fig. 5 are replotted in Fig. 6.

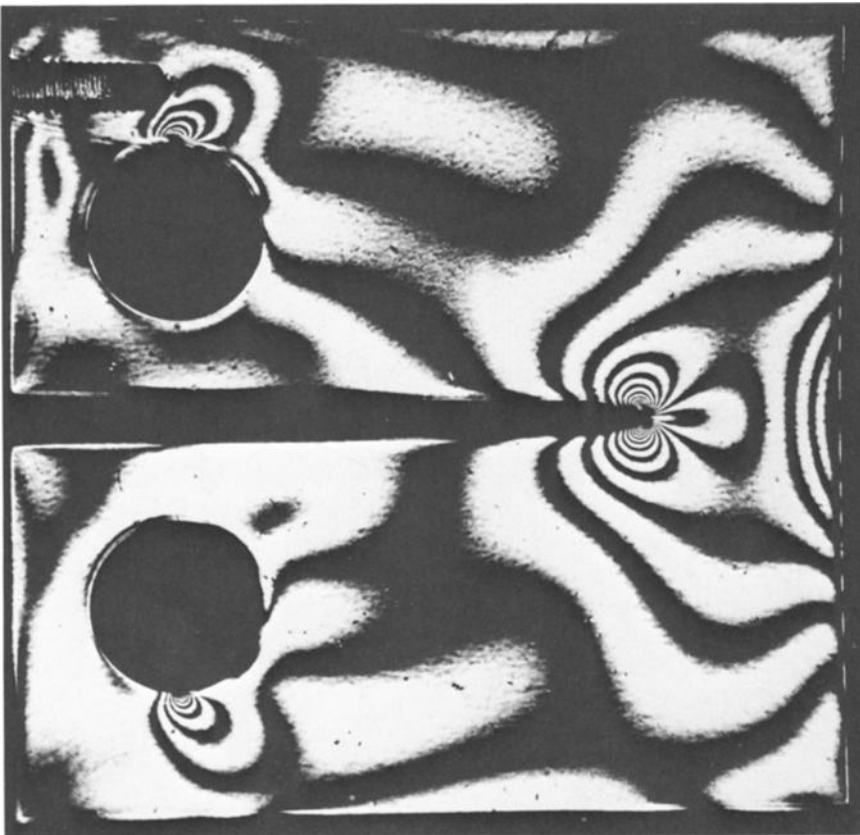


FIG. 3—Fringe pattern of full specimen.

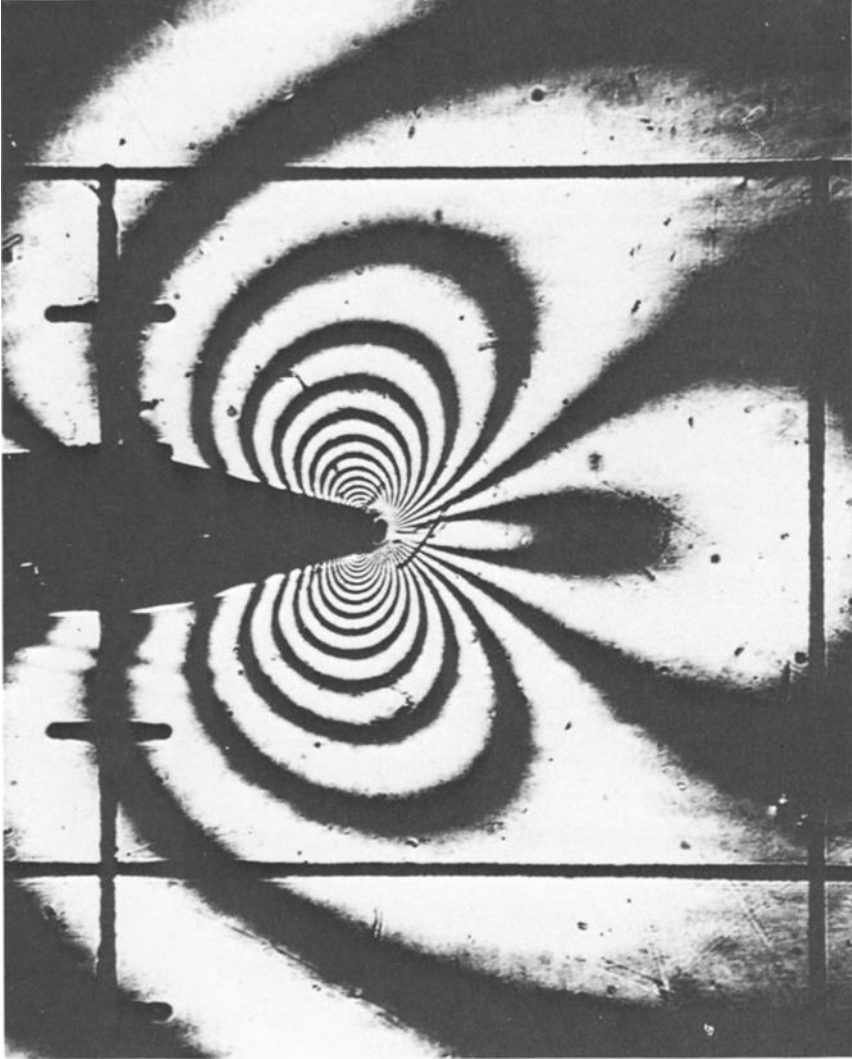


FIG. 4—Local multiplied fringe pattern.

Here the ordinate is the apparent SIF normalized with respect to the through the thickness value at the stress freezing temperature. In this case, the center slice SIF exceeded the through the thickness value by about 7 percent. As can be seen from Table 1, for the Type A specimens with $w/B = 2.0$, this figure was 10 percent for all crack lengths between $a/w = 0.5$ and 0.7 . However, for the Type B specimens with $w/B = 3.5$, the excess of the center slice SIF over the through the thickness value varied from 5 percent for $a/w = 0.5$ to 10 percent for $a/w = 0.7$. Since experimental

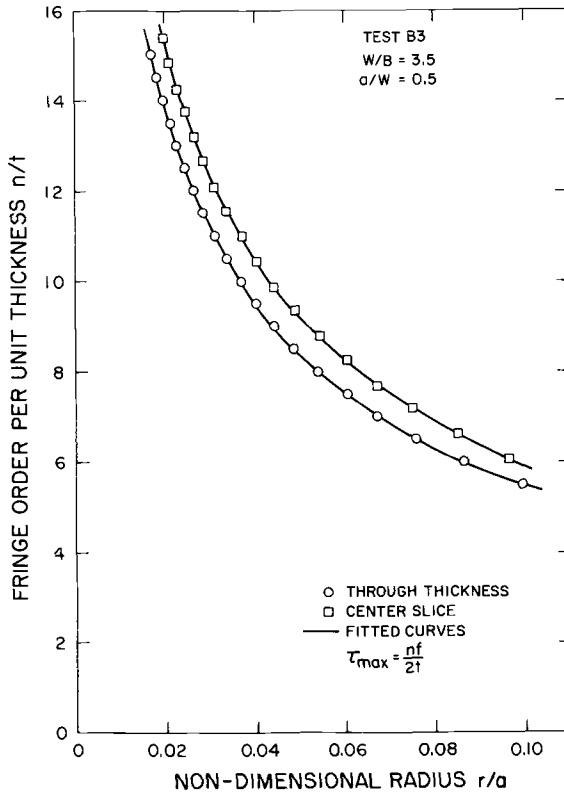


FIG. 5—Typical set of raw data with curve fitted by TSCM.

error, on occasion, can accrue to as much as 5 percent, the authors do not feel that the crack length effect as noted here is particularly significant.

A comparison of the room temperature test results with the ASTM E 399-72 equation is found in Fig. 7. Because of the high sensitivity of the Type A tests to the load alignment, two test specimens were tested independently at each value of a/w in order to ensure more reliable SIF values and each point on the $w/B = 2.0$ curve represents the average of two tests. For $w/B = 3.5$, pilot studies showed that one test was sufficient.

Results of the study may be summarized as follows:

(1) For $w/B = 2.0$ and $a/w = 0.50$, experimentally determined normalized SIF values were only 2 percent higher than the ASTM E 399-72 values. In view of a possible 5 percent experimental error, this difference is judged to be negligible.

(2) Normalized SIF values over the a/w range of 0.3 to 0.7 for $w/B = 2.0$ averaged 5 percent higher than the ASTM E 399-72 result and, for $w/B = 3.5$, averaged 13 percent higher than the ASTM E 399-72 result.

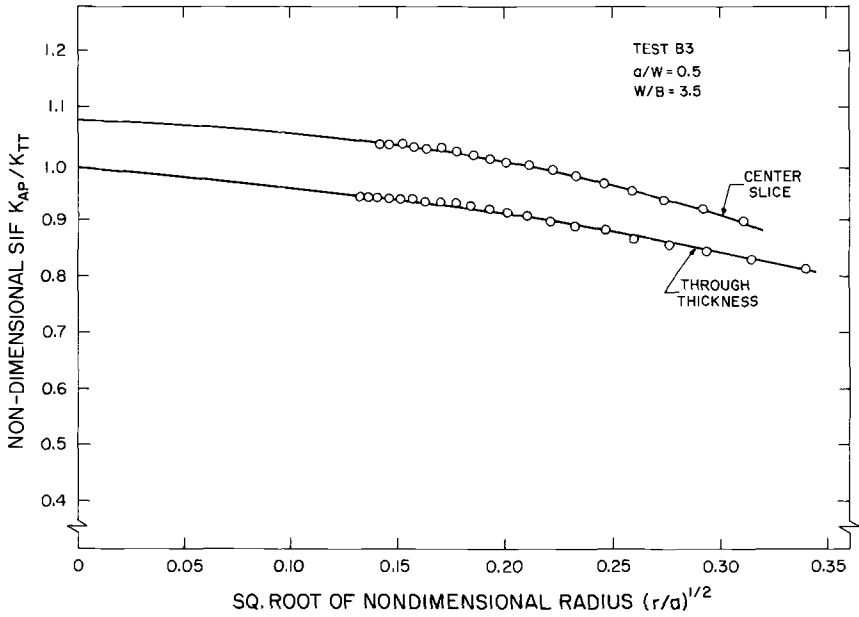


FIG. 6—Extrapolation from data by TSCM to obtain K_{TSCM} .

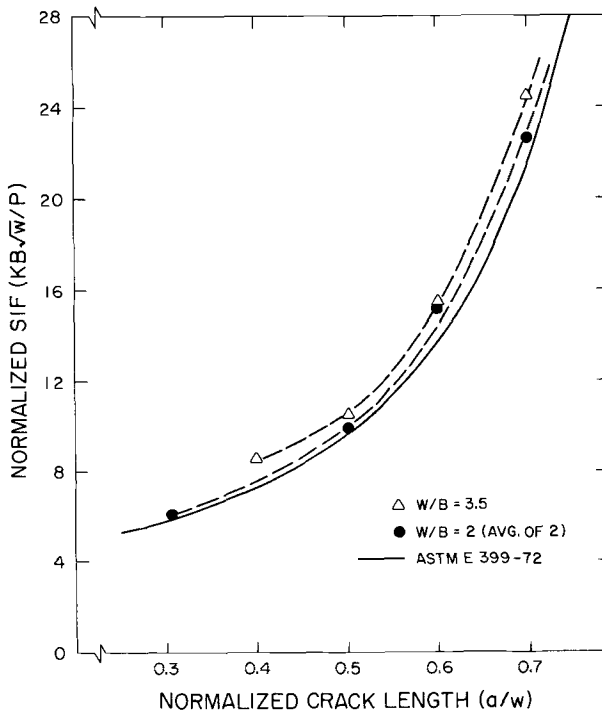


FIG. 7—Comparison of results with ASTM theory.

(3) Center slice normalized SIF values were 5 to 10 percent higher than through the thickness average values for both $w/B = 2.0$ and $w/B = 3.5$ (see Table 1).

Discussion

The existing ASTM E 399-72 solution is supported by a very accurate boundary collocation solution of an idealized compact tension specimen geometry which has been verified by compliance measurements by Wilson and his associates [5], by K calibration studies by Srawley and Brown and their associates (unpublished), and by a recent finite element solution by Wilson and his associates [31] where he used linear strain elements in conjunction with a J -integral SIF determination. Quite recently, using a different approach, Newman [32] has used a boundary collocation solution to study effects of the pin holes for various a/w which generally agrees with the other two-dimensional results.

The results cited in this study indicate that the ASTM E 399-72 result is quite accurate for $w/B = 2.0$ and $a/w = 0.50$. However, when the crack lengths are varied outside the ASTM allowable range of $a/w = 0.45$ to 0.55 , higher values of normalized SIF result for $w/B = 2.0$ and still higher results for $w/B = 3.5$. This suggests that if ASTM specimen geometry restrictions are to be relaxed, then additional analyses including three-dimensional effects may be necessary to account for results observed here.

The prior discussion is based solely upon linear elastic fracture mechanics since plasticity effects were not present in either the analytical or experimental models discussed here. In fracture toughness tests, however, plasticity is present and may exert a significant influence upon the tests results if the models are not thick enough. Moreover, there is the question of the variation of constraint through the thickness in the thinner models and, in fact, whether or not plane-strain predominates. Due to these complicating factors, the authors do not recommend prediction of fracture toughness results from their tests

Summary

A set of photoelastic experiments were conducted in order to study the influence of crack length and thickness upon the SIF for compact tension specimens within a crack length range a/w of 0.3 to 0.7 and for two thicknesses $w/B = 2.0$ and $w/B = 3.5$.

The experiments confirmed the validity of the ASTM E 399-72 solution within its limits (that is, $w/B = 2$, $a/w = 0.45$ to 0.55) but showed measurable increases in the normalized SIF for larger values of a/w and w/B . A variation in the SIF through the specimen thickness was also identified.

The authors estimate their results to be accurate to within about 5 percent for linear elastic fracture mechanics comparison. Moreover, the

differences in the SIF values for the two values of w/B was only about 8 percent. Even though the latter difference was established from average values of some dozen or more tests in each series, the authors recommend that further tests be conducted, particularly at values of w/B of 1.0 and 6.0 in order to determine if the trends observed here extend into those ranges as well as to further substantiate the present results.

Acknowledgments

The authors wish to acknowledge the contributions of A. E. Harms and J. J. McGowan for their laboratory and programming assistance to the project. Collocation solutions for checks were graciously supplied by W. K. Wilson. The interest and support of N. G. Tupper, Al Gunderson, and D. Frederick are also appreciated. This project was sponsored by the U. S. Air Force Systems Command, Wright Field, Ohio, under Contract No. 33615-72-C2111.

References

- [1] Wilson, W. K., "Analytical Determination of Stress Intensity Factors for the Manjoine Brittle Fracture Test Specimen," Report No. WERL-0029-3, Westinghouse Research Laboratories, Aug. 1965.
- [2] Wilson, W. K., "Optimization of WOL Brittle Fracture Test Specimen," Report No. 66-1B4-13TLFR-R1, Westinghouse Research Laboratories, Jan. 1966.
- [3] Brown, W. F., Jr. and Srawley, J. E. in *Plane Strain Crack Toughness Testing of High Strength Metallic Materials*, ASTM STP 410, American Society for Testing and Materials, March 1969, p. 14.
- [4] Wilson, W. K., *Journal of Engineering Fracture Mechanics*, Vol. 2, No. 2, Nov. 1970, pp. 169-171.
- [5] Wilson, W. K., Tuba, I. S., and Chan, S. K., "On the Finite Element Method in Linear Fracture Mechanics," *Journal of Engineering Fracture Mechanics*, Vol. 2, No. 1, July 1970, pp. 1-18.
- [6] Wilson, W. K. in *Stress Analysis and Growth of Cracks*, ASTM STP 513, American Society for Testing and Materials, Oct. 1972, pp. 90-105.
- [7] Brown, W. F., Jr. (Ed.), *Review of Developments in Plane Strain Fracture Toughness Testing*, ASTM STP 463, American Society for Testing and Materials, Sept. 1970.
- [8] Leven, M. M., "Stress Distribution in the M-4 Biaxial Fracture Specimen," Research Report 65-107-STRSS R-1, Westinghouse Research Laboratories, 19 March 1965.
- [9] Marloff, R. H., Leven, M. M., Johnson, R. L., and Ringler, T. N., *Experimental Mechanics*, Vol. 11, No. 12, Dec. 1971, pp. 529-539.
- [10] Cruse, T. A. and Van Buren, W., "Three Dimensional Elastic Stress Analysis of a Fracture Specimen with an Edge Crack," *International Journal of Fracture Mechanics*, Vol. 7, No. 1, March 1971.
- [11] Post, D., "Photoelastic Stress Analysis for an Edge Crack in a Tensile Field," *Proceedings, Society for Experimental Stress Analysis*, Vol. 12, No. 1, 1954, pp. 99-116.
- [12] Wells, A. A. and Post, D., *Proceedings, Society for Experimental Stress Analysis*, Vol. 16, No. 1, 1958, pp. 69-92.
- [13] Fessler, H. and Mansell, D. O., *Journal of Mechanical Engineering Science*, Vol. 4, No. 3, 1962, pp. 213-225.
- [14] Kerley, B., "Photoelastic Investigation of Crack Tip Stress Distributions," GT-5 Test Report Document No. 685D 597, The General Electric Co., 15 March 1965.
- [15] Dixon, J. R. and Strannigan, J. S., "A Photoelastic Investigation of the Stress Distribution in Uniaxially Loaded Thick Plates Containing Slits," NEL Report No. 288, National Engineering Laboratory, Glasgow, Scotland, May 1967.

- [16] Liebowitz, H. Vanderveldt, H., and Sanford, R. J., *Experimental Mechanics*, Vol. 7, No. 12, Dec 1967, pp. 513-517.
- [17] Smith, D. G. and Smith, C. W., *International Journal of Fracture Mechanics*, Vol. 6, No. 3, Sept. 1970, pp. 305-318.
- [18] Smith, D. G. and Smith, C. W., *Experimental Mechanics*, Vol. 11, No. 9, Sept. 1971, pp. 394-401.
- [19] Smith, D. G. and Smith, C. W., *Journal of Engineering Fracture Mechanics*, Vol. 4, No. 2, June 1972, pp. 357-366.
- [20] Marris, G. R. and Smith, C. W. in *Stress Analysis and Growth of Cracks*, ASTM STP 513, American Society for Testing and Materials, Oct. 1972, pp. 22-36.
- [21] Bradley, W. B. and Kobayashi, A. S., *Journal of Experimental Mechanics*, Vol. 10, No. 3, March 1970, pp. 106-113.
- [22] Bradley, W. B. and Kobayashi, A. S., *Journal of Engineering Fracture Mechanics*, Vol. 3, No. 3, Oct. 1971, pp. 317-332.
- [23] Kobayashi, A. S., Wade, B. G., Bradley, W. B., and Chiu, S. T., *Journal of Engineering Fracture Mechanics*, Vol. 6, No. 1, March 1974, pp. 81-92.
- [24] Kobayashi, A. S. and Wade, B. G., "Crack Propagation and Arrest in Impacted Plates," TR-14, Dept. of Mechanical Engineering, College of Engineering, University of Washington, July 1972.
- [25] Schroedl, M. A., McGowan, J. J., and Smith, G. W., *Journal of Engineering Fracture Mechanics*, Vol. 4, No. 4, Dec. 1972, pp. 801-809.
- [26] Schroedl, M. A. and Smith, C. W. in *Progress in Flaw Growth and Fracture Toughness Testing*, ASTM STP 536, American Society for Testing and Materials, 1973, pp. 45-63.
- [27] Schroedl, M. A., McGowan, J. J., and Smith, C. W., "Determination of Stress Intensity Factors from Photoelastic Data with Application to Surface Flaw Problems," VPI-E-73-1 Report, Virginia Polytechnic Institute and State University, 1973, *Journal of Experimental Mechanics*, (in press).
- [28] Harms, A. E. and Smith, C. W., "Stress Intensity Factors in Long Deep Surface Flaws in Plates Under Extensional Fields," VPI-E-73-2, Virginia Polytechnic Institute and State University, Feb 1973, *Proceedings*, 10th Anniversary Meeting of the Society for Engineering Science, (in press).
- [29] Smith, C. W., "Use of Three Dimensional Photoelasticity in Fracture Mechanics," invited paper, Fracture Mechanics Applications Session, Third International Congress on Experimental Mechanics, Los Angeles, Calif., May 13-18, 1973; also published in *Experimental Mechanics*, Vol. 13, No. 12, Dec. 1973, pp. 539-544.
- [30] Gross, B. and Mendelson, A., *International Journal of Fracture Mechanics*, Vol. 8, No. 3, Sept. 1972, pp. 267-276.
- [31] Wilson, W. K., Chan, S. K., and Gabrielse, S. E., "Elastic Displacements for Compact Tension Specimens," Westinghouse Research Laboratories, Scientific Paper No. 71-1E7-FMPWR-P5, 13 Sept. 1971.
- [32] Newman, J. C., in this volume.

J. H. Underwood,¹ R. D. Scanlon,¹ and D. P. Kendall¹

K Calibration for C-Shaped Specimens of Various Geometries

REFERENCE: Underwood, J. H., Scanlon, R. D., and Kendall, D. P., “**K Calibration for C-Shaped Specimens of Various Geometries,**” *Fracture Analysis, ASTM STP 560*, American Society for Testing and Materials, 1974, pp. 81–91.

ABSTRACT: Prior collocation results are combined with new collocation data and analyzed using two parameter data approximation methods and fracture mechanics methods. A general *K* calibration is obtained for C-shaped specimens which have outer to inner radius ratios, $W = r_2/r_1$, between 1.4 and 2.5.

The *K* calibration for C-shaped specimens is found to depend on the load eccentricity to specimen thickness ratio, x/t , as well as the usual crack depth to specimen thickness ratio, a/t . The *K* results are presented as tabular and plotted values from a cubic spline surface used to approximate the collocation data and as a polynomial approximation of the collocation data over a more limited range of x/t .

KEY WORDS: fracture properties, cylinders, crack propagation, strains, thickness, mechanical properties

Nomenclature

- a* Crack depth
- B* Specimen thickness
- h* Loading hole diameter
- K* Opening mode stress intensity factor
- P* Applied load
- r*₁ Inner radius
- r*₂ Outer radius
- t* Wall thickness, $r_2 - r_1$
- W* Wall ratio, r_2/r_1
- x* Eccentricity of load
- λ Arbitrary smoothing parameter

Kendall and Hussain [*I*]² have described the development of a new C-shaped fracture toughness specimen particularly well suited to measuring the plane-strain fracture toughness of samples from thick-walled cylinders.

¹ All, Benet Weapons Laboratory, Watervliet, N. Y. 12189.

² The italic numbers in brackets refer to the list of references appended to this paper.

They presented C-shaped K calibrations obtained from several independent methods: a compliance test, an approximate superposition of available solutions, fatigue crack propagation tests, and a finite element method.

Subsequent to the development work in Ref 1, a boundary value collocation method has been applied to the problem [2]. The collocation method has been modified from the classical method, for instance, Gross, Srawley, and Brown [3], to facilitate the numerical computations for C-shaped geometries where the boundary conditions are satisfied in the least-squares sense. Collocation results have been obtained for five different C-shaped geometries [2,4] as part of various fracture analysis programs.

Our purpose here is to use these available collocation results as the basis for a general K calibration for a wide range of C-shaped specimen geometries. By using a two parameter data approximation and interpretation method and standard fracture mechanics analysis, we can obtain a K calibration which is more useful than the original series of collocation results.

Collocation Results

The C-shaped specimen geometry is shown in Fig. 1, a sketch corresponding to the largest wall ratio, $W = r_2/r_1$, investigated. The dimensions of the specimens modeled by collocation are listed in Table 1. The collocation

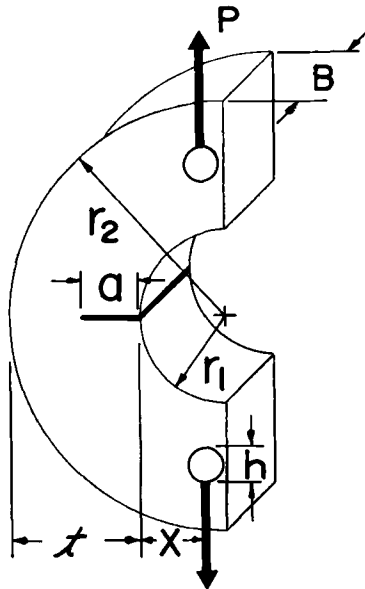


FIG. 1—C-shaped specimen geometry.

TABLE 1—C-shaped geometries modeled by collocation.

Specimen	Reference	Dimensions, in.				Wall Ratio, W	Relative Eccentricity of Load, x/t
		r_1	r_2	x	t		
T-2	[4]	2.05	5.11	1.050	3.060	2.49	0.343
T-3	[4]	2.53	5.26	1.530	2.730	2.08	0.560
K-1	[2]	4.00	8.00	2.850	4.000	2.00	0.712
T-1	[4]	2.50	4.28	1.750	1.780	1.71	0.983
U-1	...	3.00	4.50	2.400	1.500	1.50	1.600
S-1	[2]	2.38	3.30	1.875	0.926	1.39	2.025

tion results and the crack length values for which they apply are listed in Table 2. In addition to the five collocation results from previous work, we obtained results from an additional geometry, Specimen U-1, using the same collocation procedure described in Ref [2].

The collocation results are plotted as a/t versus $KB\sqrt{t}/P$ in Fig. 2 and are represented by one-dimensional cubic spline functions as described in Ref 5. The crack depth, a , is normalized by t , the specimen dimension in the direction of crack extension. This is the usual and appropriate procedure for finite geometries. The inclusion of \sqrt{t} in the K parameter is also the appropriate way to include the square root size factor characteristic of all K analyses. In addition, the \sqrt{t} factor makes the K parameter dimensionless.

When the collocation results are normalized and plotted as in Fig. 2, the K parameter (at a given value of a/t) increases as x/t increases or as W

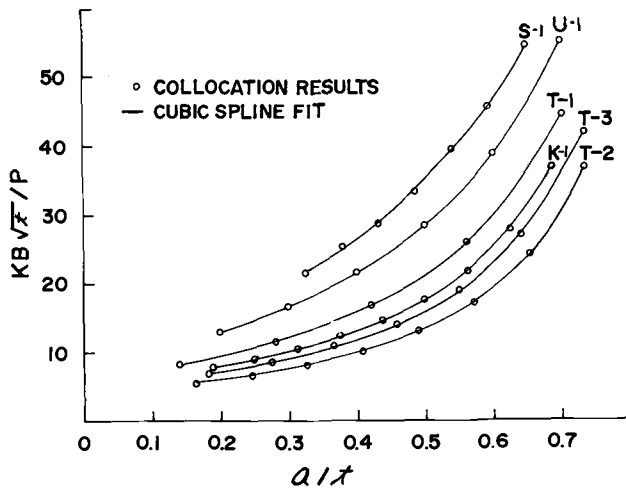


FIG. 2—Collocation K data for C-shaped specimens.

TABLE 2—C-shaped specimen collocation results.

T-2		T-3		K-1		T-1		U-1		S-1	
a_1 , in.	KB/P_1 , $1/\sqrt{\text{in.}}$										
0.50	3.15	0.50	4.21	0.75	3.90	0.25	6.20	0.30	10.6	0.30	22.4
0.75	3.85	0.75	5.21	1.00	4.53	0.50	8.69	0.45	13.5	0.35	26.3
1.00	4.70	1.00	6.59	1.25	5.27	0.75	12.6	0.60	17.6	0.40	29.8
1.25	5.85	1.25	8.51	1.50	6.18	1.00	19.6	0.75	23.1	0.45	34.6
1.50	7.48	1.50	11.5	1.75	7.34	1.25	33.4	0.90	31.5	0.50	40.9
1.75	9.90	1.75	16.4	2.00	8.87	1.05	44.7	0.55	47.5
2.00	13.8	2.00	25.3	2.25	10.9	0.60	56.5
2.25	21.0	2.50	13.9
...	2.75	18.4

decreases. Thus, it appears that either x/t , a measure of the load eccentricity, or W , the wall ratio, is a third parameter which must be considered in describing the general K analysis of C-shaped specimens.

In the descriptions of the data analysis and results which follow, it becomes clear that x/t is the third parameter required for the C specimen K calibration. This dependence on x/t is also apparent upon consideration of Kendall and Hussain's [1] approximation of the C specimen K calibration obtained by superposing known tension and bending solutions:

$$KB\sqrt{t}/P = \sqrt{a/t} [Y_T + 6Y_B(x/t + 1/2)] \tag{1}$$

The quantities Y_T and Y_B are from single edge notch tension and bending solutions, respectively [6], and are functions of a/t only. Thus, the K parameter in this approximate solution is a function of a/t and x/t only.

Data Analysis Procedures

Since only a limited number of collocation results were available (and these at arbitrary points), an approximating surface supported by these points was constructed so that additional values might be calculated as desired for graphs and tables.

Let

$$u = a/t$$

$$v = x/t$$

$$\Phi(u,v) = KB\sqrt{t}/P$$

$$Z_i = \Phi(u_i,v_i) + e_i; i = 1, \dots, N$$

where the Z_i are the available computed points, Φ is the true function (considered to be reasonably smooth in the region of interest), and the e_i represent a lumping together of all the discretizations, truncations, and round-offs of the original computations. It would be idle to assume that the e_i were random numbers with a Gaussian distribution, thus we merely hypothesized that $|e/\Phi| < 0.01$ and that the departures were more or less randomly plus and minus.

As one approach, Φ was approximated by a doubly cubic spline, ϕ , over a rectangular region divided into subrectangles by the lines

$$\begin{aligned} u_a = 0.15, & \quad u_b = 0.45, & \quad u_c = 0.75, \\ v_a = 0.3, & \quad v_b = 0.9, & \quad v_c = 2.2. \end{aligned}$$

The spline surface was constructed by minimizing the norm

$$\int_A \{f_1(\lambda) \phi_{uu}^2 + f_2(\lambda) \phi_{uv}^2 + f_3(\lambda) \phi_{vv}^2\} dA + \frac{1}{N} \sum_{i=1}^N w_i^2 \{\phi(u_i,v_i) - Z_i\}^2$$

over the spline parameter space where

$$w_i = \frac{Z_1}{Z_i}$$

since relative rather than absolute departures are of interest and

$$f_1(\lambda) = \frac{(\Delta u)^3}{\lambda \Delta v}$$

$$f_2(\lambda) = \frac{\Delta u \Delta v}{\lambda}$$

$$f_3(\lambda) = \frac{(\Delta v)^3}{\lambda \Delta u}$$

$$\Delta u = u_c - u_a$$

$$\Delta v = v_c - v_a$$

$$\lambda > 0$$

By numerical experimentation, $\lambda = 10^6$ was found to reasonably balance the requirement for smoothness against the desire to respect the integrity of the data as indicated by a patternless distribution of the relative departures of the data points above and below the fitted surface. Further information on this method of approximation can be found in Refs 5 and 7.

Alternatively, Φ was approximated by

$$\psi(u, v) = v \sum_{i=0}^4 b_i u^i + \sum_{i=0}^4 d_i u^i$$

since it appeared that in a restricted region $\Phi(k, v)$ could be reasonably approximated by a straight line. In this case, nothing is said about the smoothness of ψ but

$$\sum_{i=1}^N w_i^2 \{ \psi(u_i, v_i) - Z_i \}^2$$

is minimized with $w_i = Z_1/Z_i$ as before. The coefficients were evaluated in the usual way by constructing and solving the matrix of normal equations.

K Calibration Results

The data in Figs. 3 and 4 and in Table 3 are from the spline surface which was constructed as described before to represent the original collocation data. The surface was found to deviate from the original data points by a maximum of 2.5 percent. The missing data from Figs. 3 and 4 and Table 3 are for values of a/t and x/t which we believe are significantly outside the range of the original collocation data, so that the $KB\sqrt{t}/P$ values from the surface should not be used.

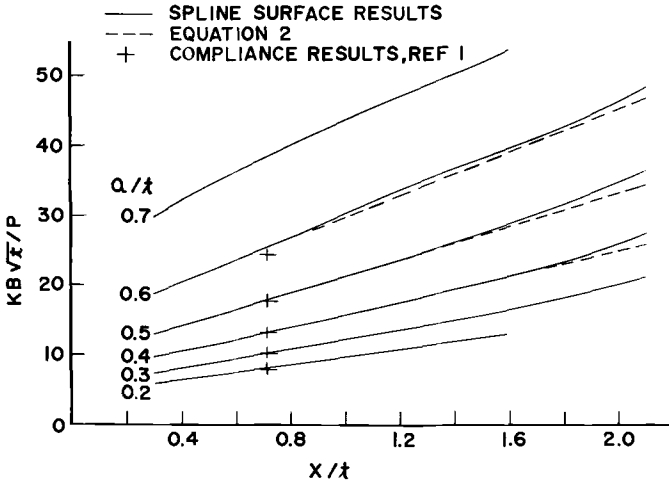


FIG. 3—Comparison of K results for C-shaped specimens.

In Fig. 3 each of the solid curves on the plot describes the intersection of a plane of constant a/t with the approximating spline surface. It is clear that, for constant a/t , the K parameter is nearly a linear function of x/t . This led to an attempt to represent the collocation data in the much simpler form:

$$KB\sqrt{t}/P = [b_0 + b_1(a/t) + b_2(a/t)^2 + b_3(a/t)^3 + b_4(a/t)^4] x/t + [d_0 + d_1(a/t) + d_2(a/t)^2 + d_3(a/t)^3 + d_4(a/t)^4] \quad (2)$$

for $0.3 < x/t < 1.6$, $0.2 < a/t < 0.6$

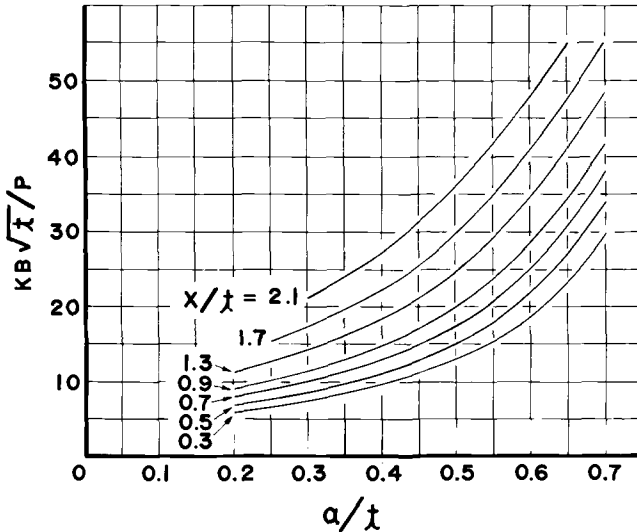


FIG. 4—K Calibration for C-shaped specimens of various geometries.

TABLE 3— $KB\sqrt{t}/P$ values from collocation data surface.

a/t	x/t	$KB\sqrt{t}/P$																	
		0.3	0.5	0.7	0.9	1.1	1.3	1.5	1.7	1.9	2.1								
0.20	5.80	6.87	8.01	9.16	10.26	11.34	14.09	15.47	17.44	19.21	21.19	24.07	27.43	31.45	36.30	41.93	48.26	55.19	63.00
0.25	6.54	7.75	9.00	10.27	11.52	12.78	15.83	17.44	19.67	21.73	24.73	28.41	32.96	38.35	44.52	51.39	59.00	67.00	
0.30	7.41	8.75	10.13	11.52	12.91	14.33	17.84	19.67	22.38	24.73	28.41	32.96	38.35	44.52	51.39	59.00	67.00	75.00	
0.35	8.44	9.92	11.46	13.02	14.57	16.16	20.31	22.38	25.78	28.41	32.96	38.35	44.52	51.39	59.00	67.00	75.00	83.00	
0.40	9.68	11.34	13.11	14.90	16.66	18.43	23.45	25.78	30.04	32.96	38.35	44.52	51.39	59.00	67.00	75.00	83.00	91.00	
0.45	11.15	13.06	15.15	17.26	19.30	21.33	27.43	30.04	35.17	38.35	44.52	51.39	59.00	67.00	75.00	83.00	91.00	99.00	
0.50	12.94	15.20	17.69	20.22	22.64	25.00	32.27	35.17	41.13	44.52	51.39	59.00	67.00	75.00	83.00	91.00	99.00	107.00	
0.55	15.34	18.04	21.00	23.98	26.80	29.52	37.99	41.13	47.89	51.39	59.00	67.00	75.00	83.00	91.00	99.00	107.00	115.00	
0.60	18.70	21.92	25.33	28.72	31.90	34.95	44.58	47.89	55.39	59.00	67.00	75.00	83.00	91.00	99.00	107.00	115.00	123.00	
0.65	23.38	27.17	30.96	34.63	38.06	41.34	52.05	55.39	63.00	67.00	75.00	83.00	91.00	99.00	107.00	115.00	123.00	131.00	
0.70	29.74	34.13	38.17	41.91	45.40	48.75	60.00	63.00	71.00	75.00	83.00	91.00	99.00	107.00	115.00	123.00	131.00	139.00	

The first bracketed term specifies the slopes of a set of straight lines; the second bracketed term specifies the intercept values, namely, the positions of the lines.

We found that Eq 2 with the following constants is a good approximation of the collocation data:

$$b_0 = 1.411, \quad b_1 = 33.68, \quad b_2 = -104.9, \quad b_3 = 221.8, \quad b_4 = -125.4$$

$$d_0 = 6.447, \quad d_1 = -48.17, \quad d_2 = 277.8, \quad d_3 = -575.0, \quad d_4 = 469.3$$

Equation 2 with these constants deviates from the original collocation data points by a maximum of 1.7 percent for the range of x/t and a/t indicated, that is, for $0.3 < x/t < 1.6$ and $0.2 < a/t < 0.6$. We have compared straight lines from Eq 2 with the spline surface results in Fig. 3 to indicate that for high x/t the surface results deviate more noticeably from linearity. This deviation led us to limit Eq 2 to $x/t < 1.6$.

Also shown in Fig. 3 are Kendall and Hussain's compliance K calibration results for a C shape specimen calculated from their Eq 7 as follows.

$$KB/P = \sqrt{18.54a + 1.206a^5} \quad (3)$$

The compliance specimen dimensions required for the dimensionless parameters used here are $t = 4.04$ in., $x = 2.85$ in. We take this opportunity to point out that Eq 7 in Ref 1 is in error due to the omission of the square root sign. The form of the equation which appears here is correct as verified with the authors of Ref 1. The deviation of the compliance results from the collocation data surface is not disconcerting since end-point compliance data often result in inaccurate K values due to less accurate end-point differentiation.

Table 3 lists $KB\sqrt{t}/P$ values from the collocation data surface. Considering again the near linear plots in Fig. 3, it is a simple matter to obtain $KB\sqrt{t}/P$ values for any given x/t by linear interpolation.

Figure 4 is a plot from the collocation data surface in the more common form of a K parameter versus a crack length parameter. A comparison of Fig. 4 with Table 2 is a good summary of this work. Starting with collocation K data from six C-shaped specimen geometries we arrived at a general K calibration which applies over a significant range of relative crack depth and relative load eccentricity.

Discussion

We can estimate how close these results are to the "true" K calibration for C specimens by considering (1) the estimated accuracy of the original collocation results, (2) the strengths and weaknesses of a two parameter approximation, and (3) the comparison with the compliance results of Ref 1. We believe that both Eq 2 and the surface results in Fig. 3 and 4

and Table 3 represent the "true" K calibration for C-shaped specimens within 4 percent over the whole range of a/t and x/t indicated. Furthermore, since the deviation of our results from the original collocation data becomes significantly smaller at lower values of a/t and x/t , we believe that the equation and surface results represent the true K calibration within 2 percent for a/t up to 0.6 and x/t up to 1.0.

Another indication of the accuracy of our results would be measurement of critical K values using C-shaped specimens from material with a known K_{Ic} value. As of this writing tests of this sort are underway [8].

The following considerations relate to the K results and to some extent limit their use.

(a) The collocation procedure [2] simulates the applied load by replacing the loading hole arrangement with a shear stress applied over the vertical end surfaces of the specimen, where the location of the end surfaces is the same distance, x , from the inner radius as the loading hole (see Fig. 1). This simulation becomes less accurate for large values of wall ratio. For wall ratios at least up to 2.5, we believe it to be a good simulation.

(b) The eccentricity of the applied load, x , relative to the inner radius, r_1 , may affect K , even though x/t is clearly the critical parameter. The x/r_1 values for the six collocation geometries vary between 0.5 and 0.8. Since there was no apparent effect of x/r_1 on K for these geometries, we believe that the K calibration can be used for any x/r_1 in this range. This means that the inner and outer radii of C specimens can vary significantly and not affect the K calibration as long as x and t do not vary.

(c) The relative loading hole size, h/t , used in C specimens could also have a small effect on K . The only guidance we can offer is that in fracture testing of C specimens [8] with h/t values up to 0.5, we have seen no evidence of an effect on K .

Acknowledgment

The authors acknowledge the help of S. L. Pu in the computation and analysis of the collocation results.

References

- [1] Kendall, D. P. and Hussain, M. A., *Experimental Mechanics*, Vol. 12, April 1972, pp. 184-189.
- [2] Hussain, M. A., Lorensen, W. E., Kendall, D. P., and Pu, S. L., "A Modified Collocation Method For C-Shaped Specimens," Benet Weapons Laboratory Technical Report, R-WV-T-X-6-73, Watervliet, N. Y., Feb. 1973.
- [3] Gross, B., Srawley, J. E., and Brown, W. F., "Stress-Intensity Factors For A Single-Edge-Notch Tension Specimen By Boundary Collocation Of A Stress Function," NASA Technical Note D-2395, Aug. 1964.
- [4] Hussain, M. A. and Pu, S. L., Benet Weapons Laboratory, Watervliet, N. Y., unreported results.
- [5] Ahlberg, J. H., Nilson, E. N., and Walsh, J. L., *The Theory of Splines and Their Applications*, Academic Press, New York, 1967.

- [6] Brown, W. F., Jr. and Srawley, J. E. in *Plane Strain Crack Toughness Testing of High Strength Metallic Materials*, ASTM STP 410, American Society for Testing and Materials, 1966.
- [7] Scanlon, R. D., "An Interpolating Cubic Spline Fortran Subroutine," Benet R&E Laboratories Technical Report WVT-7010, Watervliet, N. Y., Jan. 1970.
- [8] Kendall, D. P., Underwood, J. H., and Winters, D. C., "Fracture Toughness and Crack Growth Measurements with "C" Shape Specimens," Benet Weapons Laboratory Technical Report, R-WV-T-6-39-73, Watervliet, N. Y., Oct. 1973.

G. P. Sendeckyj¹

A Class of Interface Crack Problems

REFERENCE: Sendeckyj, G. P., "A Class of Interface Crack Problems," *Fracture Analysis, ASTM STP 560*, American Society for Testing and Materials, 1974, pp. 92-104.

ABSTRACT: The problem of an arc crack lying within the interface between a rigid curvilinear inclusion and an unbounded matrix is considered under the assumption of plane deformation, and a general solution method is presented. The particular examples of a single arc crack debonding one end of a rigid elliptic, a square with rounded corners, and a circular inclusion under uniaxial and equal biaxial loading at infinity are considered in detail. It is shown that there is an oscillating square root stress singularity at the crack tips unless the crack tips happen to lie at a geometrical discontinuity of the inclusion boundary. In that case, the singularity is different. In particular, the singularity is three-quarter power for a crack tip at an inclusion cusp.

KEY WORDS: fracture properties, crack propagation, inclusions, cracking (fracturing), deformation, mechanical properties

The strength of heterogeneous materials, such as fiber reinforced composites and polycrystalline metals, depends strongly on the failure modes operative under given loading conditions. A commonly observed failure mode is the debonding under an applied load of an inclusion (modeling a fiber in a composite, a grain in a polycrystal, or a precipitate particle in a precipitate hardening alloy) by an interface crack.

Historically, the earliest investigation of a crack lying within the interface between a finite inclusion and the surrounding matrix can be attributed to Mintsberg [1],² who solved the problem of a circular cavity, reinforced rigidly over an arc, in an infinite plate. The problem can be reinterpreted as the debonding of a rigid circular inclusion by an interface crack. Mintsberg's approach was adopted by Cherepanov [2] in his investigation of the interface crack between an elastic inclusion and the matrix around it. This problem was later investigated independently by England [3].

An unsuccessful attempt to analyze the interface crack problem for a rigid elliptic inclusion was made by Wilson [4]. This particular problem

¹ Aerospace engineer, Advanced Composites Branch, Structures Division, Air Force Flight Dynamics Laboratory, Wright-Patterson Air Force Base, Ohio 45433.

² The italic numbers in brackets refer to the list of references appended to this paper.

was recently solved by Sendeckyj [5]. As a limiting case applicable to fiber reinforced composites, Sendeckyj discussed the debonding of a rigid line inclusion. This case was also recently considered by Brussat [6], who used a different approach.

The present work is a continuation of Ref 5. Herein, the conformal mapping method used for the case of the rigid elliptic inclusion is extended to the case of a general rigid inclusion being debonded by an interface crack.

Basic Equations

Let z and ζ be two complex variables related by the transformation

$$z = \omega(\zeta) = c \left[\zeta + \sum_{n=1}^{\infty} \lambda_n \zeta^{-n} \right], c \text{ real} \tag{1}$$

Equation 1 maps the unit circle $|\zeta| = 1$, or $\rho = 1$ where $\zeta = \rho e^{i\theta}$, in the ζ -plane into a closed curvilinear contour Σ in the z -plane. Points exterior to the circle $|\zeta| = 1$ are mapped uniquely into points exterior to Σ if and only if the coefficients λ_n are restricted appropriately. It will be assumed in what follows that the transformation (Eq 1) is properly restricted.

Variables ρ and θ can be thought of as forming a curvilinear coordinate system for the z -plane, with $\rho = 1$ corresponding to the curvilinear contour Σ . In terms of ρ and θ , the displacements and stresses in the z -plane can be written as

$$\begin{aligned} 2\mu(u + iv) &= \kappa\phi(\zeta) - \omega(\zeta) \overline{\Phi(\zeta)} - \overline{\psi(\zeta)} \\ \sigma_{\rho\rho} + \sigma_{\theta\theta} &= 2[\Phi(\zeta) + \overline{\Phi(\zeta)}] \\ \sigma_{\rho\rho} - i\sigma_{\rho\theta} &= \Phi(\zeta) + \overline{\Phi(\zeta)} - e^{2i\theta} [\overline{\omega(\zeta)}\Phi'(\zeta) + \overline{\psi'(\zeta)}] \end{aligned} \tag{2}$$

where

$$\Phi(\zeta) = \phi'(\zeta)/\omega'(\zeta), \tag{3}$$

$$\kappa = \begin{cases} 3 - 4\nu & \text{for plane strain, and} \\ (3 - \nu)/(1 + \nu) & \text{for generalized plane stress:} \end{cases} \tag{4}$$

μ and ν are the shear modulus and Poisson's ratio, respectively [7]. A prime on a function denotes differentiation with respect to its argument. A bar over a function symbol and its argument denotes the complex conjugate, while a bar over a function symbol only is used to denote the conjugate of the function with z being treated as though it were a real quantity. Thus

$$\overline{\overline{F(z)}} = -i + \bar{z}, \quad \overline{F(z)} = -i + z \tag{5}$$

when $F(z) = i + z$.

General Interface Crack Problem

Consider an elastic matrix containing a partially bonded *rigid* curvilinear inclusion. Let the bond imperfection consist of an arc crack, placed as shown in Fig. 1a. When mapped into the ζ -plane, the region outside the curvilinear inclusion is transformed into the region $|\zeta| \geq 1$, shown in Fig. 1b. In the ζ -plane, the crack tips are located at the points $\zeta_1 = e^{i\beta}$, $\zeta_2 = e^{-i\alpha}$. The corresponding points in the z -plane are given by $z_1 = \omega(e^{i\beta})$, $z_2 = \omega(e^{-i\alpha})$. The boundary conditions to be satisfied at the inclusion-matrix interface are

$$u + iv = 0 \quad \text{for } \beta < \theta < 2\pi - \alpha \quad (6)$$

$$\sigma_{\rho\rho} - i\sigma_{\rho\theta} = 0 \quad \text{for } -\alpha < \theta < \beta \quad (7)$$

on $\rho = 1$. The formulation of the problem is completed by specifying conditions on the other boundaries of the matrix region. It should be noted that the boundary condition (Eq 6) holds to within rigid body displacements and rotation. This condition must be supplemented by requiring that the net force and moment acting on the inclusion is zero.

As for many problems in elasticity, the solution of the interface crack problem is normally sought by attempting to satisfy all the boundary conditions simultaneously. In the present work, a somewhat different approach is adopted. First, a sequence of complex potentials satisfying only boundary conditions of Eqs 6 and 7 is obtained. Guidance in constructing the desired sequence of potentials is provided by the known limiting cases. Then, particular combinations of members of this sequence are selected to satisfy the remaining boundary conditions.

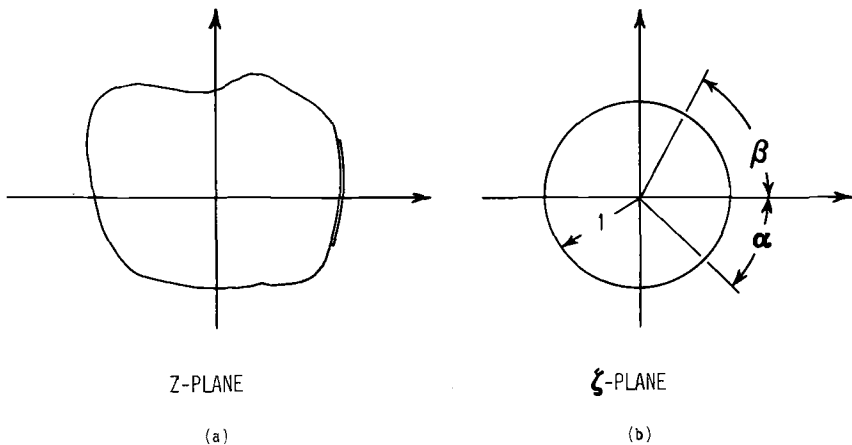


FIG. 1—Interface crack at rigid inclusion in z -plane and ζ -plane.

In the problem being considered here, the desired sequence of complex potentials is given by

$$\phi(\zeta) = f_n(\zeta) + (1/\kappa) \bar{h}_n(1/\zeta) \quad (8)$$

$$\psi(\zeta) = h_n(\zeta) + \kappa \bar{f}_n(1/\zeta) - \frac{\Omega(\zeta)}{\omega'(\zeta)} \left[\frac{1}{\kappa} \frac{d}{d\zeta} \bar{h}_n(1/\zeta) + f_n'(\zeta) \right] \quad (9)$$

where

$$\Omega(\zeta) = \bar{\omega}(1/\zeta), \quad (10)$$

$$f_n(\zeta) = A_n \zeta^n (\zeta - e^{i\beta})^{1/2+i\gamma} (\zeta - e^{-i\alpha})^{1/2-i\gamma}, \text{ and} \quad (11)$$

$$h_n(\zeta) = B_n \zeta^n (\zeta - e^{i\beta})^{1/2-i\gamma} (\zeta - e^{-i\alpha})^{1/2+i\gamma}; \quad (12)$$

where

$$\gamma = (1/2\pi) \ln \kappa$$

and $A_n, B_n (n = 0, 1, 2, \dots)$ are complex constants which have to be determined from the conditions imposed on the other boundaries. It should be noted that:

(1) For arbitrary $f(\zeta)$ and $h(\zeta)$, complex potentials, Eqs 8 and 9, are the potentials for the case of a rigid inclusion in an unbounded matrix in the absence of the interface crack [8]. The influence of the crack enters through the proper choice of $f(\zeta)$ and $h(\zeta)$, namely, that given by Eqs 11 and 12. Thus, the present general results reduce to the correct limit for a crack of zero length.

(2) Complex potentials, Eqs 8 and 9, with $f_n(\zeta)$ and $h_n(\zeta)$ defined by Eqs 11 and 12 satisfy the boundary condition of zero traction acting over the crack length ($-\alpha < \theta < \beta, \rho = 1$). Under given loading conditions, it is possible that the displacement field will be such that the crack surface will move into the region occupied by the rigid inclusion. This is physically inadmissible with the exception of the small region around the crack tips, where due to the crack idealization the solution exhibits an oscillating phenomenon. Thus, the displacements given by any solution obtained by using the present method must be checked. If contact occurs between the crack surface and the rigid inclusion, the results must be supplemented by functions having a different structure. Finally, it should be noted that this displacement check is not performed in the examples discussed later. Hence, the reader must show a certain amount of caution when using the results.

(3) If the crack surface is loaded, potentials, Eqs 8 and 9, must include simple polynomial terms. This will be illustrated in the following.

Examples

Consider an interface crack between a rigid hypotrochoidal inclusion and an unbounded matrix. The mapping function transforming the exterior

of the unit circle in the ζ -plane into the exterior of a hypotrochoid is given by

$$z = \omega(\zeta) = \zeta + \lambda\zeta^{-n}, \quad -1/n \leq \lambda \leq 1/n \quad (14)$$

Herein, the scaling constant c in Eq 1 has been set equal to unity. Equation 14 gives an elliptic boundary in the z -plane for $n = 1$. For $n = 3$, Eq 14 maps the exterior of the unit circle in the ζ -plane into the exterior of a curvilinear square with rounded corners in the z -plane. The diagonals (sides) of the square are parallel to the coordinate axes for $\lambda > 0$ (< 0). The inclusion has cusps for $|\lambda| = 1/3$. Segments of the boundary of the curvilinear square with rounded corners are shown in Fig. 2 for discrete positive values of λ . In the first quadrant, $\lambda = 1/3$; $\lambda = 2/9$ in the second quadrant; $\lambda = 1/9$ in the third quadrant; and $\lambda = 0$ in the fourth quadrant.

For the sake of simplicity, assume that the interface crack is symmetrical with respect to the x -axis; that is, $\alpha = \beta$. Let the boundary conditions at infinity be given by

$$\sigma_{xx} = p, \quad \sigma_{yy} = q, \quad \sigma_{xy} = 0 \quad (15)$$

which is equivalent to requiring that

$$\phi(\zeta) = (p + q)\zeta/4 + o(\zeta), \quad \psi(\zeta) = (q - p)\zeta/2 + o(\zeta) \quad (16)$$

The boundary conditions at the interface are given by Eqs 6 and 7.

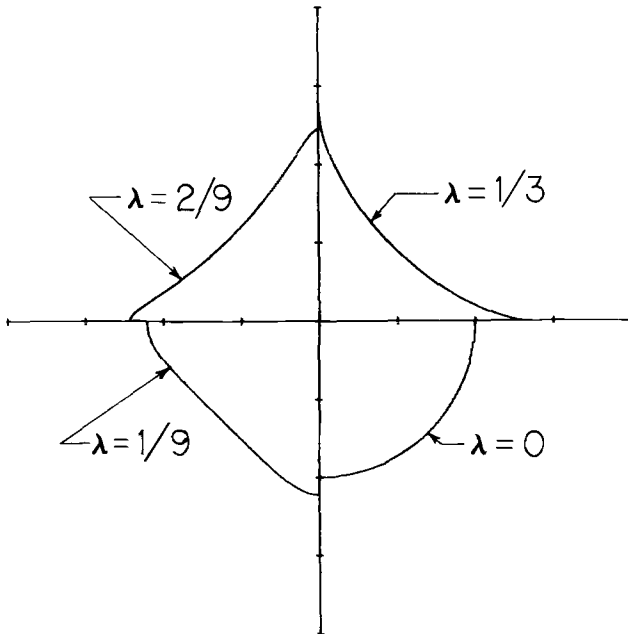


FIG. 2—Boundary of curvilinear square with rounded corners for discrete values of the shape parameter λ .

Rigid Elliptic Inclusion [5]

As the first example of the application of the complex potentials, consider the case of a rigid elliptic inclusion ($n = 1$ in Eq 14) for which

$$\Omega(\zeta)/\omega'(\zeta) = \zeta(1 + \lambda\zeta^2)/(\zeta^2 - \lambda) = \lambda\zeta + (1 + \lambda^2)\zeta/(\zeta^2 - \lambda), \text{ as } |\zeta| \rightarrow \infty. \tag{17}$$

Since $\phi(\zeta)$ and $\psi(\zeta)$ must behave like ζ as ζ tends to infinity by the boundary conditions of Eq 16, the obvious choice of the complex potentials is given by Eqs 8 and 9 with $f_n(\zeta)$ and $h_n(\zeta)$ given by Eqs 11 and 12 with

$$A_n = B_n = 0 \ (n = 1, 2, \dots), \quad A_0 \text{ and } B_0 \text{ real} \tag{17}$$

Expanding the resulting potentials about the point at infinity gives

$$\phi(\zeta) = A_0\zeta + o(\zeta), \quad \psi(\zeta) = (B_0 - \lambda A_0)\zeta + o(\zeta) \tag{18}$$

Upon comparing Eqs 16 and 18, it follows that

$$A_0 = (p + q)/4, \quad B_0 = [(2 + \lambda)q - (2 - \lambda)p]/4 \tag{19}$$

which completes the solution of the problem.

Rigid Square Inclusion with Rounded Corners

As the second example, consider the case of a rigid square inclusion with rounded corners ($n = 3$ in Eq 14) for which

$$\Omega(\zeta)/\omega'(\zeta) = \lambda\zeta^3 + (1 + 3\lambda^2)\zeta^3/(\zeta^4 - 3\lambda) \tag{20}$$

Since $\Omega(\zeta)/\omega'(\zeta) \sim \zeta^3$ for large ζ , it follows that the choice of the complex potentials is not as simple as in the case of the rigid elliptic inclusion. Upon a little contemplation, it becomes obvious that the solution will be given by Eqs 8 and 9 with

$$f(\zeta) = f_0(\zeta) \tag{21}$$

$$h(\zeta) = h_2(\zeta) + h_1(\zeta) + h_0(\zeta) \tag{22}$$

where $f_0(\zeta)$ and $h_i(\zeta)$ are given by Eqs 11 and 12. Expanding the resulting complex potentials about the point at infinity gives

$$\phi(\zeta) = A_0\zeta + o(\zeta) \tag{23a}$$

$$\begin{aligned} \psi(\zeta) = & (B_2 - \lambda A_0)\zeta^3 + [(B_1 - B_2 \cos \beta) + 2A_0 \lambda \gamma \sin \beta]\zeta^2 \\ & + \{[B_0 - B_1 \cos \beta - B_2(1 - \cos^2 \beta)/2] - B_1 \lambda e^{2\beta\gamma/\kappa} \\ & + B_0(\cos \beta - 2\gamma \sin \beta)e^{2\beta\gamma/\kappa} \\ & + A_0(0.5 + 0.5 \cos^2 \beta + 2\gamma \sin \beta \cos \beta)\}\zeta + o(\zeta), \text{ as } |\zeta| \rightarrow \infty. \end{aligned} \tag{23b}$$

Upon comparing Eqs 16 and 23, it follows that

$$\begin{aligned}
 A_0 &= (p + q)/4, \quad B_2 = \lambda(p + q)/4 \\
 B_1 &= \lambda(\cos \beta - 2\gamma \sin \beta) (p + q)/4 \\
 B_0 &= [2(q - p) + (p + q)\lambda^2 e^{2\beta\gamma} (\cos \beta - 2\gamma \sin \beta)/\kappa] \\
 &\quad \times [1 + \lambda e^{2\beta\gamma} (\cos \beta - 2\gamma \sin \beta)/\kappa]^{-1}/4
 \end{aligned} \tag{24}$$

which completes the solution of the problem.

Rigid Circular Inclusion

As the final group of examples, consider the case of a rigid circular inclusion ($\lambda = 0$ in Eq 14). In this case

$$\Omega(\zeta)/\omega'(\zeta) = \zeta^{-1} = z^{-1} \tag{25}$$

and the desired solution follows from the results for the rigid elliptic or square inclusion as a limiting case. In particular, the solution reduces to the simple form

$$\begin{aligned}
 \phi(z) &= \frac{P}{2} (z - e^{i\beta})^{1/2+i\gamma} (z - e^{-i\beta})^{1/2-i\gamma} \\
 \psi(z) &= -\frac{1}{z} \phi'(z) - \frac{P\kappa}{2} e^{-2\beta\gamma} z^{-1} (z - e^{i\beta})^{1/2-i\gamma} (z - e^{-i\beta})^{1/2+i\gamma}
 \end{aligned} \tag{26}$$

for the case of equal biaxial extension at infinity, which agrees with the solution due to England [3]. Herein, P is the magnitude of the applied biaxial stress.

To get the solution for a pressurized crack with no stress at infinity, one must subtract the solution for an unbounded matrix, loaded by an equal biaxial stress, containing a rigid inclusion. Doing this gives

$$\phi(z) = \frac{P}{2} \{(z - e^{i\beta})^{1/2+i\gamma} (z - e^{-i\beta})^{1/2-i\gamma} - z\} \tag{27a}$$

$$\begin{aligned}
 \psi(z) &= -\frac{1}{z} \phi'(z) - \frac{P\kappa}{2z} \\
 &\quad - \frac{P\kappa}{2} e^{-2\beta\gamma} z^{-1} (z - e^{i\beta})^{1/2-i\gamma} (z - e^{-i\beta})^{1/2+i\gamma}
 \end{aligned} \tag{27b}$$

where now P is the pressure acting on the crack.

Nature of Crack Tip Singularity

A number of examples were solved in the previous section. In all of these, $\phi(\zeta)$ has a common structure. In fact after some elementary manipu-

lations, $\phi(\zeta)$ can be written as

$$\phi(\zeta) = [A_0 - e^{2\beta\gamma}(B_2\zeta^{-2} + B_1\zeta^{-1} + B_0)/(\kappa\zeta)] \times (\zeta - e^{i\beta})^{1/2+i\gamma}(\zeta - e^{-i\beta})^{1/2-i\gamma} \quad (28)$$

where $B_2 = B_1 = 0$ and A_0, B_0 are given by Eq 19 for the case of the rigid elliptic inclusion; A_0, B_i ($i = 0, 1, 2$) are given by Eq 24 for the case of the rigid square inclusion with rounded corners; and

$$A_0 = (p + q)/4, \quad B_0 = (q - p)/2 \quad (29)$$

for the rigid circular inclusion.

In order to establish the nature of the crack tip stress singularity, $\phi(\zeta)$ must be expressed in terms of z instead of ζ . In general, this is difficult to do. Fortunately, it is sufficient to establish the leading terms of the expansion of $\phi(\zeta) = \phi(z)$ about the crack tip. With this in mind, let $\eta = z - \omega(e^{i\beta})$. Expanding η in a series about the crack tip gives

$$\eta = \omega'(e^{i\beta})[\zeta - e^{i\beta}] + 0.5\omega''(e^{i\beta})[\zeta - e^{i\beta}]^2 + \dots \quad (30)$$

which is term-by-term invertable [9]. If $\omega'(e^{i\beta}) \neq 0$, Eq 30 can be locally inverted to give

$$\zeta = e^{i\beta} + \eta/\omega'(e^{i\beta}) \quad (31)$$

Upon using this result, Eq 28 can be written as

$$\phi(\eta) = [A_0 - e^{2\beta\gamma}(B_2e^{-3i\beta} + B_1e^{-2i\beta} + B_0e^{-i\beta})/\kappa] \times (2i \sin \beta)^{1/2-i\gamma}[\eta/\omega'(e^{i\beta})]^{1/2+i\gamma} + o(\eta) \quad (32)$$

from which it follows that there is an oscillating square root stress singularity at the crack tips. In arriving at this result, it was assumed that $\omega'(e^{i\beta}) \neq 0$. This condition holds in all cases with one exception, namely, the crack tip is at a geometrical discontinuity of the inclusion.

If $\omega'(e^{i\beta}) = 0$, Eq 30 can be locally inverted to give

$$\zeta = e^{i\beta} + [2\eta/\omega''(e^{i\beta})]^{1/2} \quad (33)$$

Upon using this result, Eq 28 can be written as

$$\phi(\eta) = [A_0 - e^{2\beta\gamma}(B_2e^{-3i\beta} + B_1e^{-2i\beta} + B_0e^{-i\beta})/\kappa] \times (2i \sin \beta)^{1/2-i\gamma}[2\eta/\omega''(e^{i\beta})]^{1/4+i\gamma/2} + \dots \quad (34)$$

from which it follows that there is an oscillating three-quarter power stress singularity at the crack tip whenever $\omega'(e^{i\beta}) = 0$ and $\sin \beta \neq 0$. This occurs for

(a) a rigid line inclusion with one side debonded ($n = 1, \lambda = -1, \beta = \pi/2$); and

(b) a rigid square inclusion with cusps ($|\lambda| = 1/3, n = 3$) when one side of the cusp is debonded ($\lambda = 1/3, \beta = \pi/2, 3\pi/2$ and $\lambda = -1/3, \beta = (1 + 2m)\pi/4$ where $m = 0, 1, 2, 3$).

Crack Tip Stress Intensity Factors

The crack tip stress intensity factors k_1 and k_2 , defined as the coefficients of the (oscillating) square root stress singularity present at the crack tips, play an important role in discussions of fracture behavior. They are normally computed by evaluating the stresses in a local coordinate system with origin at the crack tip. Since computation of the stresses is tedious in the present case, k_1 and k_2 will be calculated directly from the complex potentials. Equation 32 is the expression for $\phi(\eta)$ in the z -plane in a local coordinate system with origin at the crack tip. As can be seen from Fig. 3, the complex variable η is not the natural one for studying the local behavior in the vicinity of the crack tip. It is most convenient to rotate the local coordinates to ξ so that the crack lies along the ξ_1 -axis. Upon doing this, one gets

$$\begin{aligned} \phi(\xi) = & [A_0 - e^{2\beta\gamma}(B_2e^{-3i\beta} + B_1e^{-2i\beta} + B_0e^{-i\beta})/\kappa] \\ & \times [2\kappa(\sin \beta)/|\omega'(e^{i\beta})|]^{1/2}e^{-\beta\gamma} \\ & \times e^{i[\beta/2 - \gamma \ln|\omega'(e^{i\beta})| - \gamma \ln(2 \sin \beta)]} \xi^{1/2+i\gamma} \end{aligned} \tag{35}$$

Since $\phi(\xi)$ is sufficient for defining the crack tip stress intensity factors, $\psi(\xi)$ need not be computed.

Now let us define the crack tip stress intensity factors k_1 and k_2 as the coefficient of $\xi^{1/2+i\gamma}$ in Eq 35; that is, let

$$\phi(\xi) = (1/2)^{1/2} (k_1 + ik_2)\xi^{1/2+i\gamma} \tag{36}$$

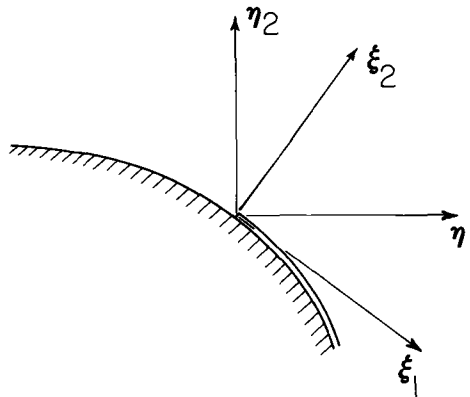


FIG. 3—Local coordinate axes at crack tip.

Comparing Eqs 35 and 36 gives

$$k_1 = 2[\kappa |\omega'(e^{i\beta})|^{-1} \sin \beta]^{1/2} \{A_0 e^{-\beta\gamma} \cos \alpha - (e^{\beta\gamma}/\kappa)[B_2 \cos(3\beta - \alpha) + B_1 \cos(2\beta - \alpha) + B_0 \cos(\beta - \alpha)]\} \quad (37a)$$

$$k_2 = 2[\kappa |\omega'(e^{i\beta})|^{-1} \sin \beta]^{1/2} \{A_0 e^{-\beta\gamma} \sin \alpha - (e^{\beta\gamma}/\kappa)[B_2 \sin(3\beta - \alpha) + B_1 \sin(2\beta - \alpha) + B_0 \sin(\beta - \alpha)]\} \quad (37b)$$

where

$$\alpha = \beta/2 - \gamma \ln |\omega'(e^{i\beta})| - \gamma \ln(2 \sin \beta) \quad (38)$$

It should be noted that the present definition of k_1 and k_2 differs at most by a multiplicative constant from those adopted by other authors [10,11]. Moreover, it should be realized that the apparent nondimensionality of Eq 37 for the crack tip stress intensity factors is a direct consequence of the particular choice of mapping function, Eq 14, that was used in the derivations.

Since the behavior of the crack tip stress intensity factors for the case of a rigid elliptic inclusion was discussed in detail in Ref 5, only the results for the rigid curvilinear square inclusion with rounded corners will be discussed in the following.

Rigid Curvilinear Square Inclusion—Incompressible Matrix

If the matrix is incompressible and in a state of plane strain, $\kappa = 1$ and the expressions for k_1 and k_2 simplify considerably. In this case, $\gamma = 0$ and

$$k_1 = 2[(1 + 9\lambda^2 - 6\lambda \cos 4\beta)^{-1/2} \sin \beta]^{1/2} [A_0 \cos \beta/2 - \lambda A_0 \cos(5\beta/2) - \lambda A_0 \cos \beta \cos(3\beta/2) - B_0 \cos \beta/2] \quad (39)$$

$$k_2 = 2[(1 + 9\lambda^2 - 6\lambda \cos 4\beta)^{-1/2} \sin \beta]^{1/2} [A_0 \sin \beta/2 + \lambda A_0 \sin(5\beta/2) + \lambda A_0 \cos \beta \sin(3\beta/2) + B_0 \sin \beta/2] \quad (40)$$

where

$$B_0 = [(q - p)/2 + A_0 \lambda^2 \cos \beta] [1 + \lambda \cos \beta]^{-1} \quad (41)$$

and A_0 is given by Eq 24.

The variation of the crack tip stress intensity factors as a function of the crack half angle β for discrete values of the shape parameter λ is shown in Figs. 4 and 5 for the case of equal biaxial tension of unit magnitude at infinity ($p = q = 1$). As can be seen from these figures, the behavior of k_i is rather complex with the main features being:

1. For positive λ (square inclusion with diagonals on the coordinate axes), the crack tip stress intensity factors increase at $\beta = \pi/2$ as λ increases. Since $\beta = \pi/2$ corresponds to the curvilinear corners of the inclusion, this implies that an interface crack (constrained to propagate along the interface) once set in motion would propagate to the corners of the inclusion.

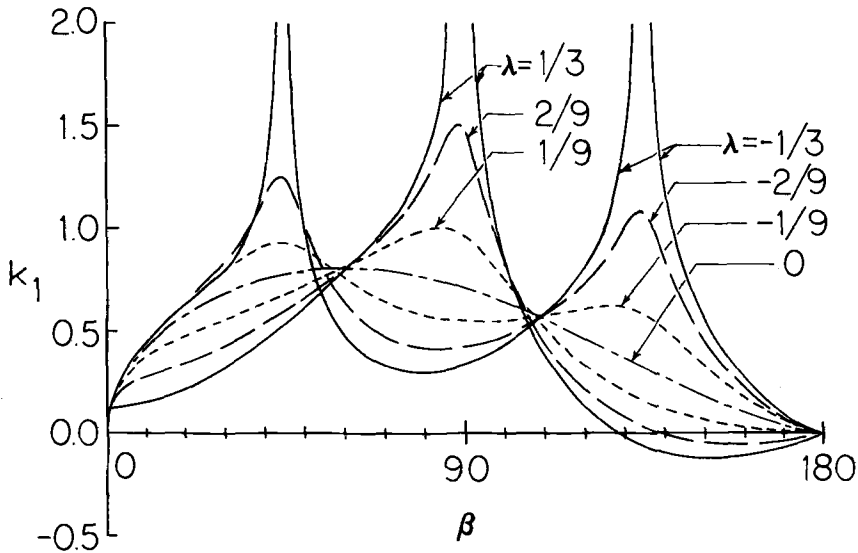


FIG. 4—Variation of k_1 as a function of crack half angle β for discrete values of the shape parameter λ and equal biaxial tension at infinity of unit magnitude.

After turning the corners, the crack would tend to arrest. Moreover, the crack would propagate in a mixed mode.

2. For $\lambda = 1/3$ (square inclusion with cusps on the coordinate axes), the k_i become unbounded at $\beta = \pi/2$. This is a direct consequence of the change in the nature of the singularity as a crack debonds one side of a rigid cusp. Moreover, k_1 remains finite when β goes to zero (absence of the crack). This is due to the presence of a square root singularity at a perfectly bonded rigid cusp. Finally, k_2 remains finite as β approaches π (crack completely debonding the rigid inclusion) implying that the final stage of debonding is in Mode 2.

3. For negative λ (square inclusion with sides parallel to the coordinate axes), the crack tip stress intensity factors increase at $\beta = \pi/4$ and $\beta = 3\pi/4$ as $|\lambda|$ increases, becoming unbounded for $\lambda = -1/3$. Since $\beta = \pi/4$ and $\beta = 3\pi/4$ correspond to the corners of the curvilinear inclusion, this implies that an interface crack once set in motion would propagate until the corners of the inclusion are debonded. After turning the corners, the crack would tend to arrest. Moreover, crack propagation would be in mixed mode.

4. For $\lambda = -1/3$ (square inclusion with cusps and sides parallel to the coordinate axes), the k_i become unbounded at $\beta = \pi/4$ and $\beta = 3\pi/4$. This is a direct consequence of the change in the nature of the singularity as the crack debonds one side of a rigid cusp. The situation is somewhat more complicated for the more general case of loading $p \neq q$.

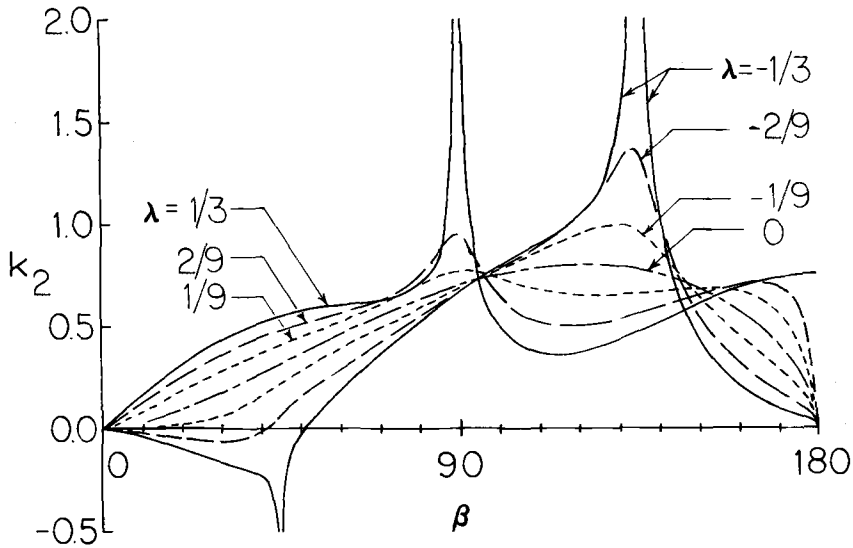


FIG. 5—Variation of k_2 as a function of crack half angle β for discrete values of the shape parameter λ and equal biaxial tension of unit magnitude applied at infinity.

Rigid Curvilinear Square Inclusion—Compressible Matrix

Analysis of the crack tip stress intensity factors for the case of a compressible matrix ($\kappa \neq 1$) is much more complicated. Since the trends are similar to those for an incompressible matrix and Eq 37 are rather easy to evaluate for various combinations of β , λ , and κ , no graphical results will be given here.

Conclusion

The method used to discuss the interface crack problem for the cases of circular, elliptic, and square with rounded corners rigid inclusions may be used to solve other examples, some of which are of considerable interest. Some of these will be discussed in subsequent works.

The use of the present analysis method is not restricted to an unbounded matrix. If the matrix is finite, Eqs 8 and 9 with $f(\zeta)$ and $h(\zeta)$ defined by Eqs 11 and 12 may be used to generate a sequence of stress functions satisfying the boundary conditions at the matrix-inclusion interface. The conditions at the other boundaries may then be satisfied by a point matching, boundary collocation, or some other method for satisfying boundary conditions approximately. Thus, the results just presented may be used in principle to get solutions for finite solids containing partially bonded rigid inclusions.

References

- [1] Mintsberg, B. L., *Prikladnaya Matematika i Mekhanika*, Vol. 12, 1948, pp. 415–422.
- [2] Cherepanov, G. P., *Izv. Akad. Nauk SSSR, Mekh. Mash.*, No. 1, 1962, pp. 131–137.
- [3] England, A. H., *Journal of Applied Mechanics*, Vol. 33, 1966, pp. 637–640.
- [4] Wilson, H. B., Jr., "Mathematical Studies of Composite Materials," Rohm and Haas Co. Report No. S-42, Dec. 1963, pp. 38–48.
- [5] Sendeckyj, G. P. in *Composite Materials: Testing and Design (Third Conference)*, ASTM STP 546, American Society for Testing and Materials, 1974.
- [6] Brussat, T. R., "Line-Inclusion Models of Failure Mechanisms in Fiber Composites," University of California at Los Angeles, Ph.D. dissertation, 1973.
- [7] Muskhelishvili, N. I., *Some Basic Problems of the Mathematical Theory of Elasticity*, 4th ed., P. Noordhoff, Amsterdam, 1963.
- [8] Sendeckyj, G. P., *International Journal of Solids and Structures*, Vol. 6, 1970, pp. 1535–1543.
- [9] Bliss, G. A., *Algebraic Functions*, Dover, New York, 1966.
- [10] Erdogan, F., *Journal of Applied Mechanics*, Vol. 30, 1963, pp. 232–236.
- [11] Rice, J. R. and Sih, G. S., *Journal of Applied Mechanics*, Vol. 32, 1965, pp. 418–422.

Stress Analysis of the Compact Specimen Including the Effects of Pin Loading

REFERENCE: Newman, J. C., Jr., "Stress Analysis of the Compact Specimen Including the Effects of Pin Loading," *Fracture Analysis, ASTM STP 560*, American Society for Testing and Materials, 1974, pp. 105–121.

ABSTRACT: An improved method of boundary collocation was applied to the two-dimensional stress analysis of the compact specimen. The effects of the pin-loaded holes on stress-intensity factors and crack-opening displacements were investigated for various crack-length-to-specimen-width ratios, hole locations, and internal loadings.

The stress-intensity factors for the "standard" compact specimen under plane-stress or plane-strain conditions were found to be within 1 percent of the stress-intensity factors reported in the ASTM Test for Plane-Strain Fracture Toughness of Metallic Materials (E 399-72) over a range of crack-length-to-specimen-width ratios of 0.4 to 0.7. However, for crack-length-to-specimen-width ratios less than 0.4, the pin-loaded holes (which were not previously accounted for) had a significant effect on stress intensity and crack-opening displacements.

KEY WORDS: strains, mechanical properties, stress analysis, crack initiation, pin-loaded holes, fatigue (materials)

Nomenclature

$A_n, B_n, C_n,$	
$\tilde{C}_n, D_n, \tilde{D}_n$	Coefficients in the series stress functions
a	Distance from center line of applied load to crack tip
c	Crack length measured from the edge of the plate
d	Distance from the plane of the crack to the center of the circular hole
E	Young's modulus
F_x, F_y	Resultant force per unit thickness acting in the x and y directions, respectively
f, g	Resultant forces or displacements
H	One-half height of the compact specimen
$i = \sqrt{-1}$	
j, n	Indices
K	Stress-intensity factor

¹ Research engineer, NASA Langley Research Center, Hampton, Va. 23665.

N	Number of coefficients in the stress functions
N_T	Total number of coefficients used in collocation analysis
P	Concentrated force per unit thickness acting in the y direction
p	Uniformly distributed line load per unit length acting in the y direction
R	Radius of the circular holes
s	One-half length of the distributed load segment
u, v	Displacements in the x and y direction, respectively
W	Width of the compact specimen measured from center line of applied load
W_0	Total width of the compact specimen
z	Complex variable, $z = x + iy$
z_h, \bar{z}_h	Locations of the centers of the circular holes, $z_h \approx x_h + iy_h$
z_0, \bar{z}_0	Location of centers of distributed line loads, $z_0 = x_0 + iy_0$
α	Angle measured between the x axis and the outward normal to a boundary
ζ	Coordinate along the contour of a boundary
θ_0	Angle over which a radial stress acts on the hole boundary
κ	Material constant, $\kappa = 3 - 4\nu$ for plane strain and $\kappa = (3 - \nu)/(1 + \nu)$ for generalized plane stress
μ	Lamé's constant (shear modulus)
ν	Poisson's ratio
ξ	Coordinate measured from edge of plate along the crack line
σ_n	Normal stress at a boundary
τ_{nt}	Shear stress at a boundary
Φ, ψ	Complex stress functions
	Bars denote complex conjugates
	Primes denote differentiation with respect to z .

The currently used stress-intensity solution for the standard ASTM compact specimen, according to ASTM Test for Plane-Strain Fracture Toughness of Metallic Materials (E 399-72), was obtained by boundary collocation analysis of a configuration and loading quite different from those of the standard specimen [1-3].² The configuration did not include the pin-loaded holes and was subjected to only externally applied loads. Finite-element models [4] have included the pin-loaded holes but have had difficulty in accounting for the crack-tip singularity.

In order to represent the configuration, loading, and the crack-tip behavior more accurately, an improved method of boundary collocation [5,6] was herein applied to the two-dimensional stress analysis of the compact specimen (see Fig. 1). The improved method requires that the resultant forces on the boundaries be specified (in a least-squares sense) in

² The italic numbers in brackets refer to the list of references appended to this paper.

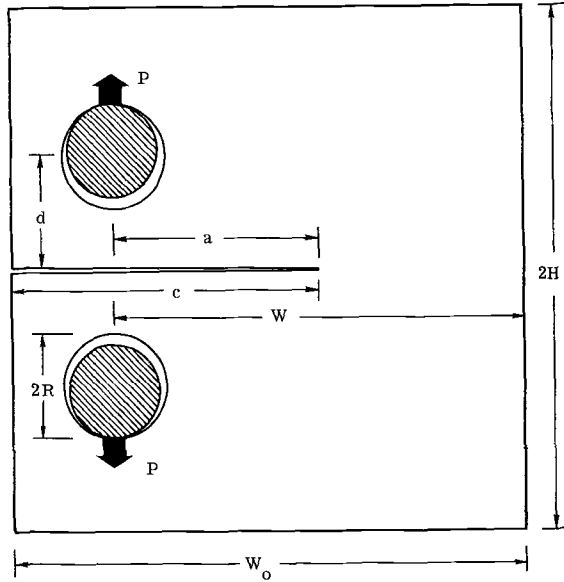


FIG. 1—Compact specimen subjected to pin loading.

contrast to previous collocation methods in which the boundary stresses were specified. The improved method was shown in Ref 6 to converge to a solution more rapidly than previously used collocation methods. The solution, presented in terms of stress intensity, was based on the complex variable method of Muskhelishvili [7]. The complex-series stress functions for the compact specimen were constructed so that the boundary conditions on the crack surfaces were satisfied exactly, while the conditions on the external boundary and the circular-hole boundaries were satisfied approximately.

Stress-intensity factors and crack-opening displacements were calculated for the compact specimen configuration (a rectangular plate with an edge crack) with and without circular holes. These configurations were subjected to either internally or externally applied loads.

Analysis of the Compact Specimen

An improved collocation method [6] was used to analyze the compact specimen (see Fig. 1) and other similar configurations. The configurations investigated were grouped into two categories: an edge crack in a rectangular plate, and an edge crack in a rectangular plate containing circular holes. Each configuration was subjected to various boundary conditions and internal loading.

For the compact specimen configuration, consider a semi-infinite crack located along the x axis in an infinite plate subjected to a uniformly dis-

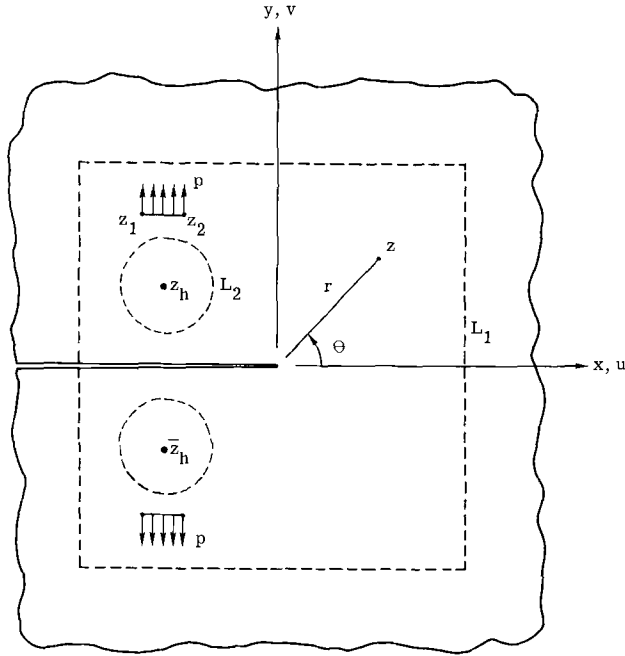


FIG. 2—Semi-infinite crack in an infinite plate subjected to a uniformly distributed internal line load.

tributed line load, p , as shown in Fig. 2. The dashed lines L_1 and L_2 define the boundaries of the compact specimen. The boundaries L_1 and L_2 may have any simple shape and may be subjected to any boundary conditions which are symmetric about the x axis. The stress functions for this configuration are taken in the forms

$$\begin{aligned}\Phi(z) &= \Phi_0(z) + \Phi_1(z) + \Phi_2(z) \\ \psi(z) &= \psi_0(z) + \psi_1(z) + \psi_2(z)\end{aligned}\quad (1)$$

The subscripts denote functions which are needed to satisfy conditions for the uniformly distributed line load (Φ_0, ψ_0) and to approximately satisfy conditions on boundaries L_1 and L_2 , respectively.

The stress functions for a semi-infinite crack in an infinite plate subjected to a uniformly distributed line load, symmetric about the x axis, were derived from equations given in Ref 8. They are

$$\begin{aligned}\Phi_0'(z) &= I_0(z, z_2) - I_0(z, z_1) \\ \psi_0'(z) &= J_0(z, z_2) - J_0(z, z_1)\end{aligned}\quad (2)$$

where $z_1 = z_0 - s$ and $z_2 = z_0 + s$. The functions I_0 and J_0 are given by

$$\left. \begin{aligned} I_0(z, z_j) \\ J_0(z, z_j) \end{aligned} \right\} = \frac{ip}{4\pi} \left[2\sqrt{\frac{z_j}{z}} - 2\sqrt{\frac{\bar{z}_j}{z}} + \ln\left(\frac{\sqrt{z} + \sqrt{z_j}}{\sqrt{z} - \sqrt{z_j}}\right) - \ln\left(\frac{\sqrt{z} + \sqrt{\bar{z}_j}}{\sqrt{z} - \sqrt{\bar{z}_j}}\right) \right] \\ - \frac{py_j}{2\pi(\kappa + 1)} \left[\frac{1}{z - z_j} \sqrt{\frac{z_j}{z}} + \frac{1}{z - \bar{z}_j} \sqrt{\frac{\bar{z}_j}{z}} \right] \\ \pm \frac{ip}{4\pi} \left(\frac{\kappa - 1}{\kappa + 1} \right) \ln\left(\frac{z - \bar{z}_j}{z - z_j}\right) \\ \pm \frac{py_j}{2\pi(\kappa + 1)} \left[\frac{1}{z - z_j} + \frac{1}{z - \bar{z}_j} \right]$$

where $j = 1, 2$. The primes and bars denote differentiation and complex conjugates, respectively. The functions I_0 and J_0 are identical except for the last two terms which differ by signs. In the limit as s approaches zero while $2ps$ approaches P , these stress functions reduce to those for a pair of concentrated forces in an infinite plate containing a semi-infinite crack.

The stress functions used to approximately satisfy boundary conditions on the external boundary L_1 are

$$\left. \begin{aligned} \Phi_1(z) \\ \psi_1(z) \end{aligned} \right\} = \sqrt{z} \sum_{n=1}^N A_n z^{n-1} \pm \sum_{n=1}^N B_n z^n \tag{3}$$

where the coefficients A_n and B_n are real. These stress functions will, of course, produce stresses on the internal boundary L_2 .

The stress functions used to approximately satisfy boundary conditions on boundary L_2 are

$$\left. \begin{aligned} \Phi_2(z) \\ \psi_2(z) \end{aligned} \right\} = \sqrt{z} \sum_{n=1}^N C_n i \left[\frac{1}{(z - z_h)^n} - \frac{1}{(z - \bar{z}_h)^n} \right] \\ + \sqrt{z} \sum_{n=1}^N D_n \left[\frac{1}{(z - z_h)^n} + \frac{1}{(z - \bar{z}_h)^n} \right] \\ \pm \sum_{n=1}^N \tilde{C}_n i \left[\frac{1}{(z - z_h)^n} - \frac{1}{(z - \bar{z}_h)^n} \right] \\ \pm \sum_{n=1}^N \tilde{D}_n \left[\frac{1}{(z - z_h)^n} + \frac{1}{(z - \bar{z}_h)^n} \right] \tag{4}$$

where C_n , \bar{C}_n , D_n , and \bar{D}_n are real. In these stress functions, the poles z_h and \bar{z}_h were located at the centers of the two holes (see Fig. 2). The stress functions in Eqs 2, 3, and 4 automatically satisfy the conditions of stress-free crack surfaces and the single-valuedness of displacement condition for multiply connected regions. The conditions on boundaries L_1 and L_2 were approximately satisfied by the series solution using the method described in Ref 6.

The resultant forces and displacements on the boundaries are expressed in terms of the complex stress functions as

$$\beta\Phi(z) + \psi(\bar{z}) + (z - \bar{z})\overline{\Phi'(z)} = f(x,y) + ig(x,y) \quad (5)$$

For resultant forces ($\beta = 1$) acting over the arc $\zeta - \zeta_0$ on the boundary

$$F_y - iF_x = -[f(x,y) + ig(x,y)] \Big|_{\zeta_0}^{\zeta} \quad (6)$$

For displacements ($\beta = -\kappa$) at a point ζ on the boundary

$$2\mu(u + iv) = -[f(x,y) + ig(x,y)]_{z=\zeta} \quad (7)$$

The complex equation for the stress components on the boundary is

$$\sigma_n - ir_{nt} = \Phi'(z) + \overline{\Phi'(z)} - [(\bar{z} - z)\Phi''(z) - \Phi'(z) + \overline{\psi'(z)}]e^{2i\alpha} \quad (8)$$

The crack-tip stress-intensity factor, as defined in Ref 8, is given by

$$K = 2\sqrt{2\pi} \lim_{z \rightarrow 0} \sqrt{z} \Phi'(z) \quad (9)$$

The stress-intensity factor calculated from Eq 9 using Eqs 1 to 4 is

$$K = K_0 + \sqrt{2\pi} \left[A_1 + 2 \sum_{n=1}^N (-1)^n C_n r_h^{-n} \sin(n\theta_h) + 2 \sum_{n=1}^N (-1)^n D_n r_h^{-n} \cos(n\theta_h) \right] \quad (10)$$

where $r_h^2 = x_h^2 + y_h^2$, $\theta_h = \tan^{-1}(y_h/x_h)$, and K_0 is the stress-intensity factor for the uniformly distributed line load. The stress-intensity factor K_0 is given by

$$K_0 = I(z_2) - I(z_1) \quad (11)$$

where

$$I(z_j) = \frac{4p\sqrt{r_j}}{\sqrt{2\pi}} \left[\frac{1}{\kappa + 1} \sin \theta_j \cos \left(\frac{\theta_j}{2} \right) - \sin \left(\frac{\theta_j}{2} \right) \right]$$

Results and Discussion

Edge Crack in a Rectangular Plate

In the following section the stress-intensity factors for two cases of an edge crack in a rectangular plate are presented. The edge-cracked plate was

subjected to either a uniformly distributed internal line load or surface tractions on the external boundary.

Uniformly Distributed Internal Line Load—For the edge-cracked plate subjected to a uniformly distributed internal line load, p_1 (see Fig. 3), the stress functions are given by Eqs 2 and 3. The coefficients in Eq 3 were evaluated by approximately satisfying the conditions of zero tractions on the external boundary, as described in Ref 6.

Because boundary collocation is a numerical method, convergence of the solution must be investigated. Example problems with $a/w = 0.2$ and 0.8 were solved using several values of N . The configuration with $a/w = 0.8$ was selected because the close proximity of the crack tip to the external boundary was expected to pose convergence difficulties. In Fig. 4, the stress-intensity factors are plotted as functions of $N_T (= 2N)$, the total number of coefficients. For ease of comparison, the stress-intensity factors are normalized with respect to their values for $N_T = 80$. As the number of terms in the series increases, the differences between the specified boundary conditions and those obtained from the series solution become smaller and the stress-intensity ratio converges to unity. The convergence, although considerably faster for the smaller value of a/w , was quite sufficient at $N_T = 70$, even for $a/w = 0.8$, the largest ratio considered. Thus, for all other a/w ratios investigated for this configuration, 70 coefficients were used.

The stress-intensity factors for the case of internal loading, and crack-opening displacements for both internal and external loading are functions of Poisson's ratio and the plane-stress or plane-strain assumptions. The effects on stress intensity of both Poisson's ratio and plane-stress or plane-

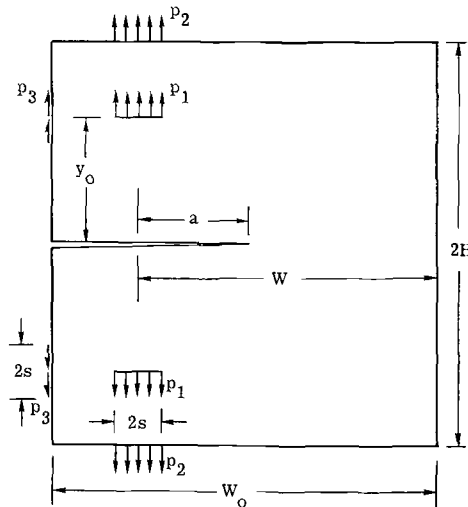


FIG. 3—Edge-cracked plate subjected to internal and external loading.

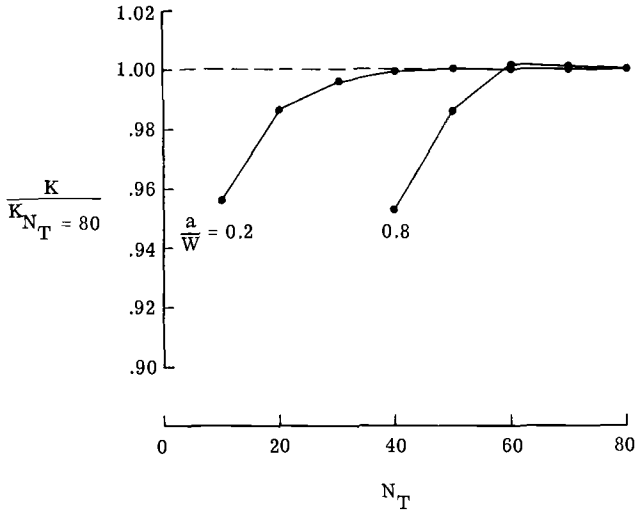


FIG. 4—Convergence curve for edge-cracked plate.

strain assumptions can be unified by considering variations in κ only. A number of edge-cracked plates were analyzed for several values of κ and several internal loading locations. The results indicated that variations in κ (hence, plane-stress or plane-strain assumptions) had an extremely small effect on stress intensity. For example, for an a/w ratio of 0.2 and y_0/H ratios between 0 and 1, the stress-intensity factor varied by less than 0.5 percent for κ between 1 and 3. The effects of κ on stress intensity were even smaller for larger values of a/w .

The stress-intensity factors for the edge-cracked plate ($H/w = 0.6$) subjected to a uniformly distributed internal line load are given in Table 1 for various a/w and y_0/H ratios. The results are presented in terms of the coefficient form $K\sqrt{W}/P$, where $P = 2p_1s$ is the force per unit thickness. For a given value of a/w , the stress intensity increased as the point of load

TABLE 1—Dimensionless coefficient $K\sqrt{W}/P$ for an edge-cracked plate with $H/W = 0.6$ and $2s/W = 0.125$ as a function of y_0/H and a/W .

Type of Loading	$\frac{y_0}{H}$	a/W							
		0.2	0.3	0.4	0.5	0.6	0.7	0.8	
Normal ($W_0 = 1.25 W$)	0	4.97	5.92	7.36	9.65	13.64	21.58	41.18	
	0.33	4.85	5.88	7.35	9.63	13.62	21.56	41.15	
	0.67	4.64	5.80	7.32	9.63	13.62	21.56	41.15	
	1.0	4.62	5.78	7.32	9.63	13.62	21.56	41.15	
Shear ($W_0 = W$)	0.67	4.52	5.79	7.35	9.66	13.65	21.60	41.18	

application approached the crack surfaces. This increase was as much as 7.5 percent for an a/w ratio of 0.2.

External Boundary Traction—For edge-cracked plates subjected to tractions, p_2 or p_3 , as shown in Fig. 3, stress functions are given by Eq 3. Again, the coefficients were determined by approximately satisfying the stress-free and uniform stress conditions on the appropriate segments of the boundary. Two loadings were considered separately: (1) a uniform normal stress, p_2 , and (2) a uniform shear stress, p_3 , applied to the external boundary. The loading in the latter case was similar to the loading used in Refs 1, 2, 3, and 9 for the standard compact specimen analysis. The stress-intensity factors obtained by the present method for the uniform shear stress applied to the boundary ($W_0 = W$) were within 1.5 percent of the previously obtained values for similar loading. The tabulated stress-intensity factors for the cases of uniform normal stress ($P = 2p_2s$) and uniform shear stress ($P = 2p_3s$) are given in Table 1.

Edge Crack in a Rectangular Plate Containing Circular Holes

In this section the stress-intensity factors for an edge-cracked plate containing circular holes are presented. The configuration was subjected to either a uniformly distributed internal line load, as shown in Fig. 5, or a uniform radial stress applied to the edge of holes, as shown in Fig. 6. The uniformly distributed line load was used to show the influence of the holes on stress intensity and crack-opening displacements. This loading was identical to the internal loading applied in the edge-cracked plate

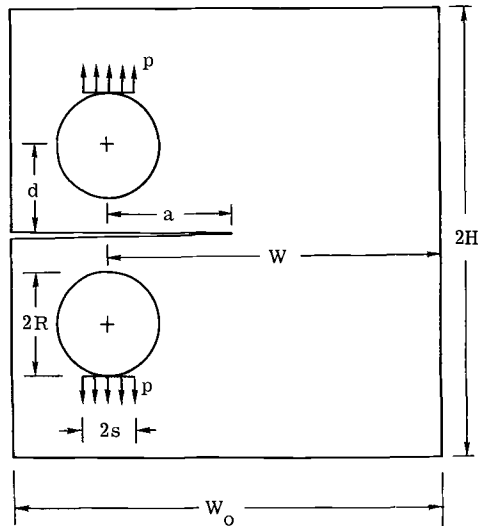


FIG. 5—Compact specimen subjected to the uniformly distributed internal line load.

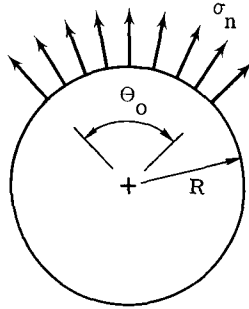


FIG. 6—Simulated pin loading for compact specimen.

without holes. The uniform radial stress applied on the edge of the holes was used to simulate the pin loading which was applied in the actual compact specimen. In the actual specimen, the bearing stresses caused by the pin loading are concentrated over a small arc (θ_0 probably less than 45 deg) on the boundary of the holes due to the undersized pin requirements (see ASTM E 399-72).

Uniformly Distributed Internal Line Load—For an edge-cracked plate containing circular holes and subjected to the uniformly distributed line load (see Fig. 5), the stress functions are given by Eqs 2, 3, and 4. The distributed line load was applied tangent to the edge of the holes with $s = 0.5 R$. The coefficients in Eqs 3 and 4 were determined by approximately satisfying the stress-free conditions on the internal and external boundaries. Again, numerical convergence was investigated because of the creation of internal boundaries. Example problems with $a/w = 0.2$ and 0.8 were solved for several values of N_T and the results are shown in Fig. 7. The results are

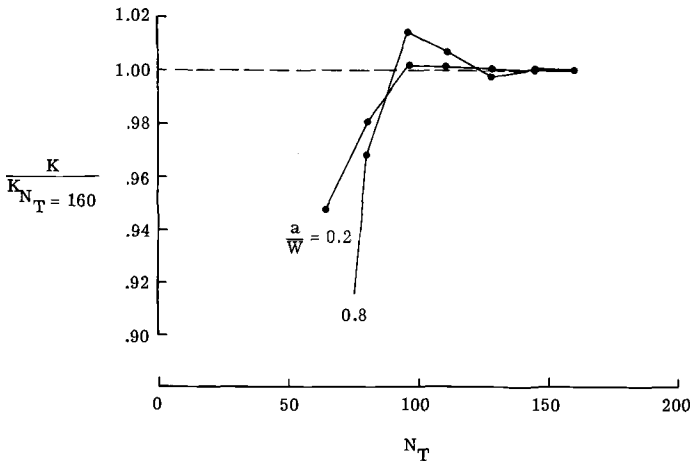


FIG. 7—Convergence curve for the compact specimen.

presented as a ratio of the stress-intensity factor for a given value of N_T to that for $N_T = 160$ as a function of the total number of coefficients. The convergence was again faster for smaller values of a/w . For this configuration, 144 coefficients were used in subsequent analyses. The number of coefficients was equally divided among the internal and external boundaries.

The stress-intensity factors for the case of internal loading are a function of Poisson's ratio and the plane-stress or plane-strain assumptions, as previously mentioned. However, because the previous results indicated that κ had an extremely small effect on stress intensity, the following analysis was performed using a value of $\kappa = 1.8$.

The stress-intensity factors for the edge-cracked plate with circular holes ($H/W = 0.6$ and $2R/W = 0.25$), and subjected to a uniformly distributed internal line load which was tangent to the edges of the holes, are given in Table 2 for several values of d/H (hole location). These results are shown in Fig. 8 as a ratio of stress-intensity factors for the configuration with and without the circular holes. For a/w ratios greater than 0.4, the effects of the circular holes were less than 1.5 percent. However, for a/w ratios less than 0.4, the holes had a significant effect on stress intensity. In the standard compact specimen ($d/H = 0.458$) and for an a/W ratio of 0.2, the holes reduced the stress-intensity factor approximately 8 percent. When the holes were placed closer together (smaller d/H) a further reduction in stress intensity occurred. However, for $d/H = 0$ (the crack-line loaded specimen) and small values of a/W , the stress concentration due to the hole caused an increase in stress intensity over that for other values of d/H .

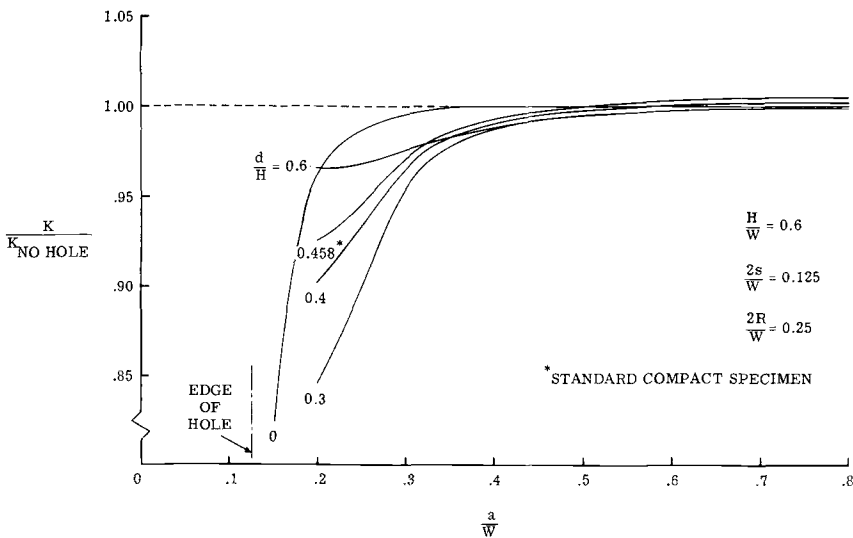


FIG. 8—Influence of the pin-loaded holes on stress intensity.

TABLE 2—Dimensionless coefficient $K \sqrt{W}/P$ for the compact specimen with $H/W = 0.6$, $2R/W = 0.25$, and $2s/W = 0.125$ as a function of d/H and a/W .

$\frac{d}{H}$	a/W						
	0.2	0.3	0.4	0.5	0.6	0.7	0.8
0	4.75	5.87	7.34	9.62	13.61	21.54	41.05
0.3	4.01	5.61	7.28	9.62	13.61	21.53	41.03
0.4	4.20	5.62	7.27	9.63	13.63	21.57	41.09
0.458 ^a	4.29	5.63	7.27	9.63	13.64	21.57	41.13
0.6	4.47	5.68	7.26	9.61	13.61	21.54	41.05
^b	4.46	5.76	7.33	9.64	13.64	21.56	41.07
^c	...	5.85	7.32	9.60	13.54	21.43	...

^a Standard compact specimen.

^b Reference 9.

^c Reference 1 and ASTM E 399-72.

Of course, as the crack length approaches zero, so does the stress-intensity factor.

The stress-intensity factors for the standard compact specimen for various a/W ratios are also compared in Table 2 with results from ASTM E 399-72 and Refs 1 and 9, which neglected the pin-loaded holes. For a/W ratios greater than 0.4, the present stress-intensity factors were within 1 percent of the previously obtained values. However, the present stress-intensity factors were approximately 4 percent lower than the values given in Ref 1 for $a/W = 0.3$ and in Ref 9 for $a/W = 0.2$.

The effects of the circular holes on crack-opening displacements are shown in Fig. 9, where the nondimensional crack-surface displacement, $E\nu/P$, is plotted as a function of location on the crack surface. These results were for the standard compact specimen with and without circular holes for $a/W = 0.5$. The state of deformation was assumed to be plane strain with $\kappa = 1.8$ (or $\nu = 0.3$). The stress-intensity factors for the specimens with and without the holes agreed to within 0.1 percent. However, the crack-opening displacements calculated at the load line (hole center line) and the outer edge of the plate ($W_0 = 1.25 W$) for the specimen with holes were 2.5 and 8.5 percent larger, respectively, than for the specimen without holes subjected to the same loading. The crack-opening displacements at the load line and the outer edge of plate for the specimen with holes are given in Table 3 for three values of κ (plane-strain condition) and several values of a/W . Also given in Table 3 are the crack-opening displacements at the load line from Ref 10 for an edge-cracked plate without holes under plane-stress (or plane-strain) condition with $\kappa = 3$.

The displacements under plane-stress conditions can be obtained from the plane-strain displacements for a given value of κ by multiplying the plane-strain displacements by $16/[(1 + \kappa)(7 - \kappa)]$. It should be noted

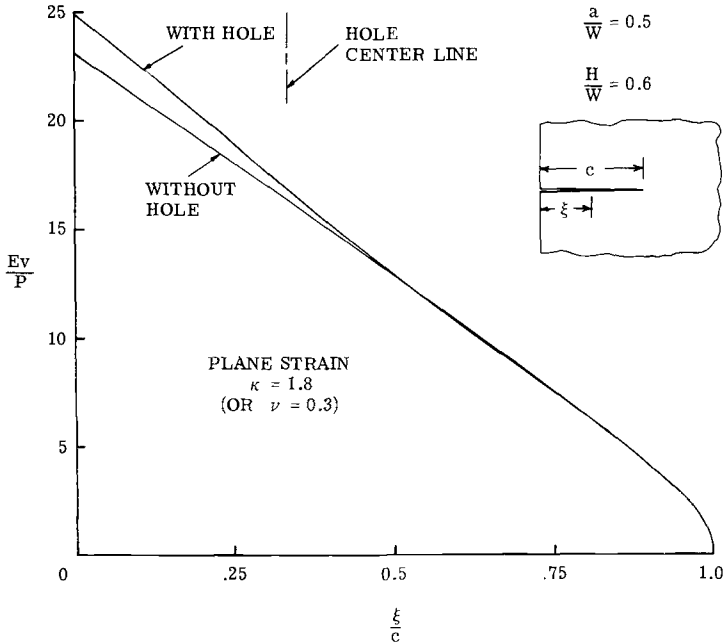


FIG. 9—Crack-opening displacements for the compact specimen with and without the pin-loaded holes.

that the admissible range of κ for plane stress is $5/3 \leq \kappa \leq 3$, whereas for plane strain the range is $1 \leq \kappa \leq 3$.

In Table 4, the crack-opening displacements, Ev/P , at the outer edge of the standard compact specimen from the present analysis are compared with experimental results (NASA-Lewis unpublished data, Bubsey and Jones) for specimens with loose- and tight-fit pins. The experimental displacements for the case with loose-fit pins are in good agreement with

TABLE 3—Dimensionless crack-opening displacement, Ev/P , for standard compact specimen as a function of κ and a/W for plane-strain conditions.

Point of Calculation (x)	κ	a/W						
		0.2	0.3	0.4	0.5	0.6	0.7	0.8
Load line (x = -a)	1	3.19	5.31	8.53	13.83	23.72	47.05	115.7
	1.8	3.90	6.49	10.39	16.82	28.81	57.12	140.4
	3	4.33	7.16	11.45	18.52	31.69	62.80	154.4
	3 ^a	...	7.13	11.48	18.51	31.66	61.02	...
Edge of plate (x = -c)	1	6.36	9.06	13.30	20.26	33.12	62.61	150.1
	1.8	7.99	11.27	16.40	24.86	40.45	76.23	182.4
	3	9.00	12.61	18.25	27.54	44.67	83.99	200.9

^a Reference 10.

TABLE 4—Comparison of theoretical and experimental crack-opening displacements, $E\nu/P$, at the outer edge of the standard compact specimen ($x = -c$).

Reference	a/W						
	0.2	0.3	0.4	0.5	0.6	0.7	0.8
Present results with holes (Plane strain $\nu = 0.3$)	7.99	11.27	16.40	24.86	40.45	76.23	182.4
Present results with holes (Plane stress $\nu = 0.3$)	8.84	12.45	18.09	27.38	44.51	82.74	198.7
Bubsey and Jones, loose-fit pins ^a (measured)	8.6	12.1	17.7	26.9	44.4	80.5	190
Bubsey and Jones, tight-fit pins ^a (measured)	6.3	10.1	16.0	25.1	41.8	78.6	189
Present results with no holes (Plane stress $\nu = 0.3$)	6.27	10.10	15.87	25.21	42.34	80.53	196.5
Present results with no holes (Plane strain $\nu = 0.3$)	5.71	9.19	14.44	22.94	38.53	73.28	178.8

^a NASA-Lewis unpublished data.

the present results for specimens with holes under plane-stress conditions ($\nu = 0.3$). In the case with tight-fit pins (push fit), the radius of the holes was approximately one half of the size specified for the standard specimen. These results are also compared in Table 4 with the present results for a specimen without holes, but subjected to the uniformly distributed internal line load (see Fig. 3, $y_0/H = 0.67$ and $s/R = 0.5$). Again, the agreement between the experimental and theoretical displacements is considered good. For all a/W ratios considered, the measured displacements were bounded by the calculated displacements for plane stress and plane strain.

Uniform Radial Stress—For an edge-cracked plate containing circular holes and subjected to the uniform radial stress on the edge of the holes, as shown in Fig. 6, the stress functions are, again, given by Eqs 2, 3, and 4. However, for loading in the hole the locations of z_1 and z_2 in Eq 2 must lie inside the hole boundary. They were placed at $z_1 = z_0 - s$ and $z_2 = z_0 + s$, where $z_0 = -a + id$ and $s = 0.5R$. The total resultant force acting on the boundary of each hole was P . The particular stress distribution, σ_n , on the hole boundary was specified and was approximately satisfied by the series solution.

The stress-intensity factors for the standard compact specimen, for various a/W ratios, are shown in Fig. 10 as a function of θ_0 , the angle over which the uniform radial stress acts on the hole boundary. The results are shown as the ratio of the stress-intensity factor for a particular value of θ_0 to that for $\theta_0 = 20$ deg. For values of θ_0 much less than 20 deg, the radial stress distribution approaches a concentrated force and the series solution becomes inefficient. However, the stress-intensity factors for smaller values of θ_0 are not expected to differ significantly from those for $\theta_0 = 20$ deg.

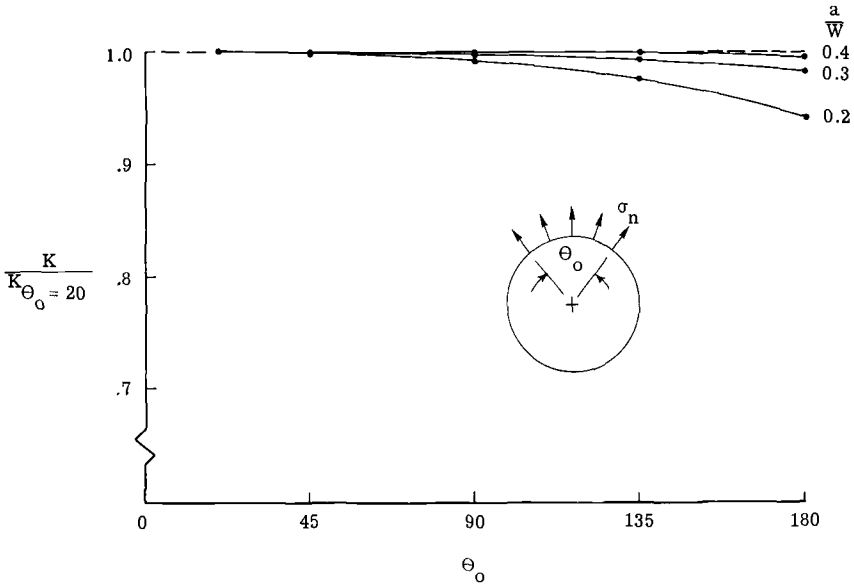


FIG. 10—Influence on stress intensity of the radial stress distribution at the hole boundary.

Stress-intensity factors for values of θ_0 less than approximately 90 deg were within 1 percent of the values given in Table 2 for the standard compact specimen. Therefore, it appears that the undersized pins in the standard compact specimen (ASTM E 399-72) do not significantly affect the stress-intensity factors for $a/W \leq 0.2$. However, assuming that the solution for $\theta_0 = 180$ deg roughly approximates the solution for tightly fitting pins, it appears that tightly fitting pins can reduce the stress intensity for $a/W < 0.3$.

Comparison with Other Stress-Intensity Solutions

The results presented in this paper indicated that the pin-loaded holes had a significant effect on stress-intensity factors for a/W ratios less than 0.4. Therefore, when the compact specimen is used at crack-length-to-specimen-width ratios less than 0.4 the effects of the holes should be included. Figure 11 shows a comparison between the nondimensional stress-intensity factors from the equation given in ASTM E 399-72 and Ref 1 (dashed line), Ref 9 (open symbols), and the present results (solid symbols). The equation in ASTM E 399-72 was restricted (in Ref 1) to $0.3 \leq a/W \leq 0.7$. The results from Refs 1 and 9 and ASTM E 399-72 did not include the effects of the pin-loaded holes. An improved equation for stress intensity which accounts for the influence of the pin-loaded holes and applies over a wider range of a/W .

$$K = \frac{P}{\sqrt{W}} F\left(\frac{a}{W}\right) \tag{12}$$

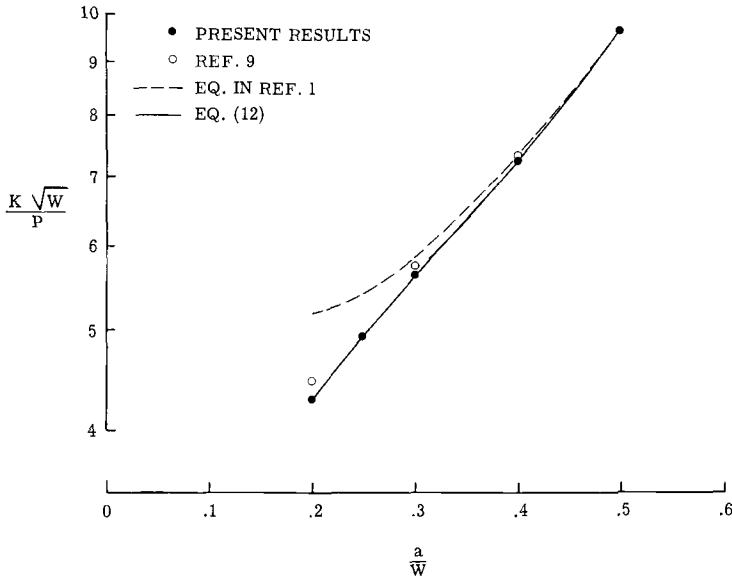


FIG. 11—Comparison of stress-intensity factors for compact specimen.

where

$$F\left(\frac{a}{W}\right) = 4.55 - 40.32\left(\frac{a}{W}\right) + 414.7\left(\frac{a}{W}\right)^2 - 1698\left(\frac{a}{W}\right)^3 \\ + 3781\left(\frac{a}{W}\right)^4 - 4287\left(\frac{a}{W}\right)^5 + 2017\left(\frac{a}{W}\right)^6$$

for $0.2 \leq a/W \leq 0.8$.

Equation 12, which is a least-squares fit to the present results, agrees to within 0.5 percent with the results given in Table 2 for the standard compact specimen.

Concluding Remarks

An improved method of boundary collocation was employed in the two-dimensional stress analysis of the compact specimen. The effects of the pin-loaded holes on stress-intensity factors and crack-opening displacements were investigated for various crack-length-to-specimen-width ratios, hole locations, and internal loadings.

The pin-loaded holes were found to reduce stress-intensity factors for a/W ratios less than 0.4. They also increased crack-opening displacements at the load line and at the outer edge of the plate, for all a/W ratios considered, over those obtained from the configuration without holes. The effects of Poisson's ratio and the plane-stress or plane-strain assumptions

on stress intensity were found to be less than 0.5 percent for all a/W ratios considered. An improved equation for stress intensity was presented which accounts for the pin-loaded holes and applies over a wider range of a/W .

References

- [1] Wessel, E. T., "State of the Art of the WOL Specimen for K_{Ic} Fracture Toughness Testing," *Engineering Fracture Mechanics Journal*, Vol. 1, No. 1, June 1968.
- [2] Brown, W. F., Jr. and Srawley, J. E. in *Plane Strain Crack Toughness Testing of High Strength Metallic Materials*, ASTM STP 410, American Society for Testing and Materials, March 1969, p. 14.
- [3] Wilson, W. K., "Stress Intensity Factors for Deep Cracks in Bending and Compact Tension Specimens," *Engineering Fracture Mechanics Journal*, Vol. 2, No. 2, Nov. 1970.
- [4] Chan, S. K., Tuba, I. S., and Wilson, W. K., "On the Finite Element Method in Linear Fracture Mechanics," *Engineering Fracture Mechanics Journal*, Vol. 2, No. 1, July 1970.
- [5] Newman, J. C., Jr., "Stress Analysis of Simply and Multiply Connected Regions Containing Cracks by the Method of Boundary Collocation," M.S. thesis, Virginia Polytechnic Institute, Blacksburg, Va., May 1969.
- [6] Newman, J. C., Jr., "An Improved Method of Collocation for the Stress Analysis of Cracked Plates With Various Shaped Boundaries," NASA TN D-6376, Aug. 1971.
- [7] Muskhelishvili, N. I., (J. R. M. Radok, transl.), *Some Basic Problems of the Mathematical Theory of Elasticity*, Third Ed., P. Noordhoff, Ltd. (Groningen), 1953.
- [8] Erdogan, Fazil in *Proceedings*, Fourth U.S. National Congress of Applied Mechanics, Vol. 1, American Society of Mechanical Engineers, 1962, pp. 547-553.
- [9] Srawley, J. E. and Gross, B., "Stress Intensity Factors for Bend and Compact Specimens," *Engineering Fracture Mechanics Journal*, Vol. 4, No. 3, Sept. 1972.
- [10] Gross, B., Roberts, E., Jr., and Srawley, J. E., "Elastic Displacements for Various Edge-Cracked Plate Specimens," *International Journal of Fracture Mechanics*, Vol. 4, No. 3, Sept. 1968.

T. W. Orange¹

Some Effects of Experimental Error in Fracture Testing

REFERENCE: Orange, T. W., "Some Effects of Experimental Error in Fracture Testing," *Fracture Analysis, ASTM STP 560*, American Society for Testing and Materials, 1974, pp. 122-133.

ABSTRACT: The purpose of this paper is to show the effects of experimental imprecision on the stress intensity factors calculated for various practical specimen types. A general form equation for the stress intensity factor is presented, and a general error equation is derived. The expected error in the stress intensity factor is given in terms of the precision levels of the basic experimental measurements and derivatives of the stress intensity calibration factor. Nine common fracture specimen types are considered, and the sensitivity of the various types to experimental error is illustrated. Some implications for fracture toughness testing and crack growth rate testing are discussed, and methods of analysis are proposed to compensate for the effects of experimental error.

KEY WORDS: fracture properties, errors, error analysis, experimentation, mechanical properties, crack initiation

Scientific experiments, even when carefully controlled, will always contain experimental errors. Prior knowledge of the effects of these errors will allow the proper design of an experiment before it is run. The purpose of this paper is to show the effects of precision errors on the stress intensity factors computed for nine common specimen types.

In most experiments the quantity of interest cannot be measured directly. Rather, other quantities must be measured (often simultaneously) and then combined through some mathematical process. If the process involves only simple functions of the measurements, it is not difficult to compute the expected error in the quantity of interest from the precision levels of the individual measurements. But if the process involves more complicated functions, then the computation is not as simple and the effect of imprecision in any one measurement may be hard to visualize.

In this paper a general form equation for the stress intensity factor is presented and a general error equation is derived. The expected error in the stress intensity factor is given in terms of the expected errors (precision levels) of the measurable constituents and a derivative of the stress intensity

¹ Aerospace technologist, Structures Section, Materials and Structures Division, NASA—Lewis Research Center, Cleveland, Ohio 44135.

calibration factor. Calibration factor expressions for nine common fracture specimen types are collected, tabulated, and differentiated. The sensitivity of the different specimen types to experimental error is illustrated. Some implications for fracture toughness testing and crack growth rate testing are discussed.

Analysis

An expression for the stress intensity factor can be written in a general form as

$$K = Y\sigma\sqrt{a + r} \tag{1}$$

where

- K = stress intensity factor,
- Y = calibration factor,
- σ = nominal applied stress,
- a = characteristic crack dimension, and
- r = plastic zone correction factor.

If Irwin's $[l]^2$ form is taken for the plastic zone correction factor, then

$$r = (K/\sigma_{ys})^2/n\pi \tag{2}$$

where n is 2 for plane stress or $4\sqrt{2}$ for plane strain, and σ_{ys} is the material yield strength.

The expected error in the computed value of the stress intensity factor is

$$E_K = \left| \frac{\partial K}{\partial \sigma} \right| E_\sigma + \left| \frac{\partial K}{\partial \sigma_{ys}} \right| E_{ys} + \left| \frac{\partial K}{\partial a} \right| E_a \tag{3}$$

where E_σ and E_a are the expected errors (precision levels) in the measured values of nominal stress and crack length, and E_{ys} is the expected variation of the material yield strength. After substituting Eq 2 into Eq 1, performing the required differentiations, and rearranging terms, Eq 3 becomes

$$\frac{E_K}{K} = \left(1 + \frac{r}{a}\right) \frac{E_\sigma}{\sigma} + \left(\frac{r}{a}\right) \frac{E_{ys}}{\sigma_{ys}} + \left[\frac{1}{2} + \left(1 + \frac{r}{a}\right) \frac{a}{Y} \frac{\partial Y}{\partial a}\right] \frac{E_a}{a} \tag{4}$$

But a fundamental tenet of applied linear elastic fracture mechanics is that $r \ll a$. Thus, the presence of a small plastic zone will have little effect on the precision of a K -calculation (although it may affect the accuracy) and we can write Eq 4 as

$$E_K/K = E_\sigma/\sigma + \alpha E_a/a \tag{5}$$

where

$$\alpha = \left[\frac{1}{2} + \frac{a}{Y} \frac{\partial Y}{\partial a} \right]$$

and α may be considered a crack length sensitivity factor.

² The italic numbers in brackets refer to the list of references appended to this paper.

It remains to differentiate the calibration factor appropriate to the specimen geometry in question. Calibration factors [2-7] for the nine specimen geometries considered (Fig. 1) are compiled in Table 1. They and their claimed ranges of applicability are expressed in terms of λ , the relative crack length (see Fig. 1). Where necessary, the original expressions were rewritten in the form prescribed by Eq 1. Calculated values of the crack length sensitivity factor α are plotted in Fig. 2 for six specimen configurations. On this scale, curves for the SENB4 and SENB8 specimens would be almost indistinguishable from that for the SENB specimen.

For the PTC specimen two crack dimensions must be considered, the depth (a) and the half-length (c) of the semiellipse. Thus, the terms

$$\left| \frac{\partial K}{\partial c} \right| E_c \quad \text{and} \quad \left(1 + \frac{r}{a} \right) \frac{c}{Y} \frac{\partial Y}{\partial c} \left| \frac{E_c}{c} \right|$$

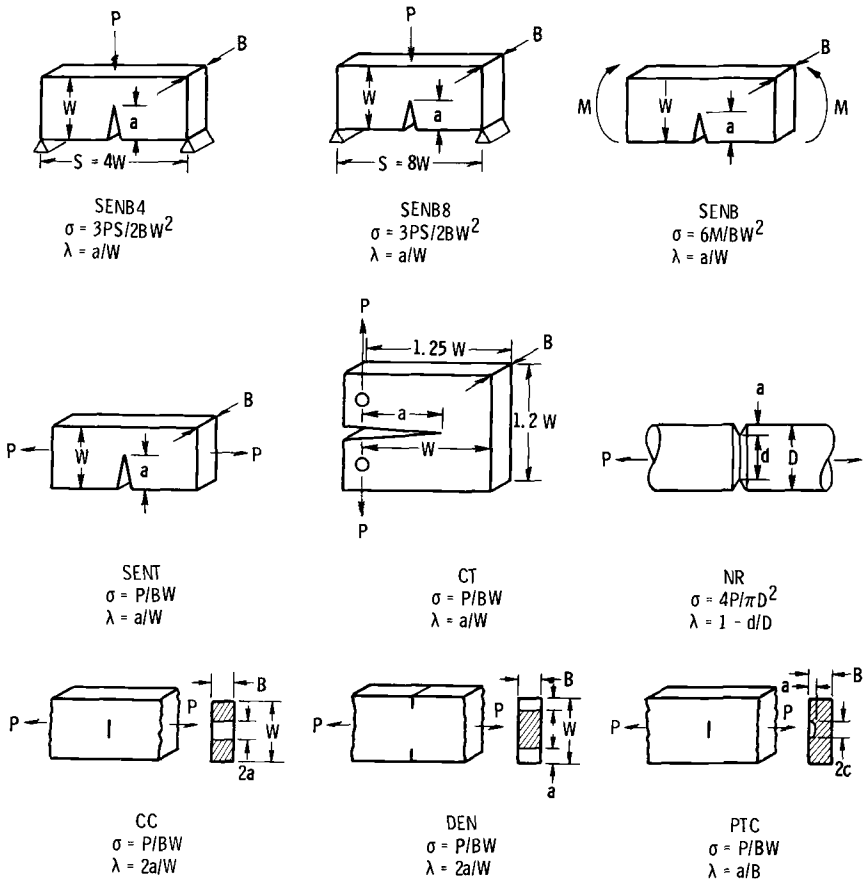


FIG. 1—Specimens and nomenclature.

TABLE 1—Calibration factors.

Specimen	Y	Range	Ref
SENB4	$1.93 - 3.07\lambda + 14.53\lambda^2 - 25.11\lambda^3 + 25.80\lambda^4$	$0 \leq \lambda \leq 0.6$	[2]
SENB8	$1.96 - 2.75\lambda + 13.66\lambda^2 - 23.98\lambda^3 + 25.22\lambda^4$	$0 \leq \lambda \leq 0.6$	[2]
SENB	$\left\{ \begin{array}{l} 1.99 - 2.47\lambda + 12.97\lambda^2 - 23.17\lambda^3 + 24.80\lambda^4 \\ \frac{2}{3}\lambda^{-1/2}(1 - \lambda)^{-3/2} \end{array} \right.$	$0 \leq \lambda \leq 0.6$	[2]
	$\left\{ \begin{array}{l} 1.99 - 0.41\lambda + 18.70\lambda^2 - 38.48\lambda^3 + 53.85\lambda^4 \\ \frac{1}{2}\lambda^{-1/2}(1 - \lambda)^{-3/2}(1 + 3\lambda) \end{array} \right.$	$0.5 \leq \lambda \leq 1.0$	[3]
SENT	$\left\{ \begin{array}{l} 1.99 - 0.41\lambda + 18.70\lambda^2 - 38.48\lambda^3 + 53.85\lambda^4 \\ \frac{1}{2}\lambda^{-1/2}(1 - \lambda)^{-3/2}(1 + 3\lambda) \end{array} \right.$	$0 \leq \lambda \leq 0.6$	[2]
CT	$\left\{ \begin{array}{l} 29.6 - 185.5\lambda + 655.7\lambda^2 - 1017.0\lambda^3 + 638.9\lambda^4 \\ \frac{1}{2}\lambda^{-1/2}(1 - \lambda)^{-3/2}(5 + 3\lambda) \end{array} \right.$	$0.3 \leq \lambda < 1.0$	[4]
	$\left\{ \begin{array}{l} 29.6 - 185.5\lambda + 655.7\lambda^2 - 1017.0\lambda^3 + 638.9\lambda^4 \\ \frac{1}{2}\lambda^{-1/2}(1 - \lambda)^{-3/2}(5 + 3\lambda) \end{array} \right.$	$0.3 \leq \lambda \leq 0.7$	[2]
CC	$(1 - 0.025\lambda^2 + 0.06\lambda^4) \left(\pi \operatorname{secat} \frac{\pi\lambda}{2} \right)^{1/2}$	$0.8 < \lambda < 1.0$	[3]
	$(1 - 0.025\lambda^2 + 0.06\lambda^4) \left(\pi \operatorname{secat} \frac{\pi\lambda}{2} \right)^{1/2}$	$0 \leq \lambda < 1.0$	[5]
DEN	$\sqrt{\pi} (1.122 - 0.561\lambda - 0.015\lambda^2 + 0.091\lambda^3) (1 - \lambda)^{-1/2}$	$0 \leq \lambda \leq 1.0$	[6]
NR	$\sqrt{\pi} (1.122 - 1.542\lambda + 1.836\lambda^2 - 1.280\lambda^3 + 0.366\lambda^4) (1 - \lambda)^{-3/2}$	$0 \leq \lambda < 1.0$	[6]
PTC ^a	$\sqrt{\pi} \Phi^{-1} \left[1 + \sum_0^b f_n \lambda^n \cdot \sum_0^c g_n \left(\frac{a}{2c} \right)^n \right]$	$0 \leq \lambda \leq 0.96$	[7]

n	0	1	2	3	4	5	6	7	8
f _n	+0.091	+0.1014	-1.606	+15.81	-76.2	+197.9	-276.9	+195.9	-54.13
g _n	+1.433	-5.305	+6.81	+26.42	-109.4	+106.77

^a

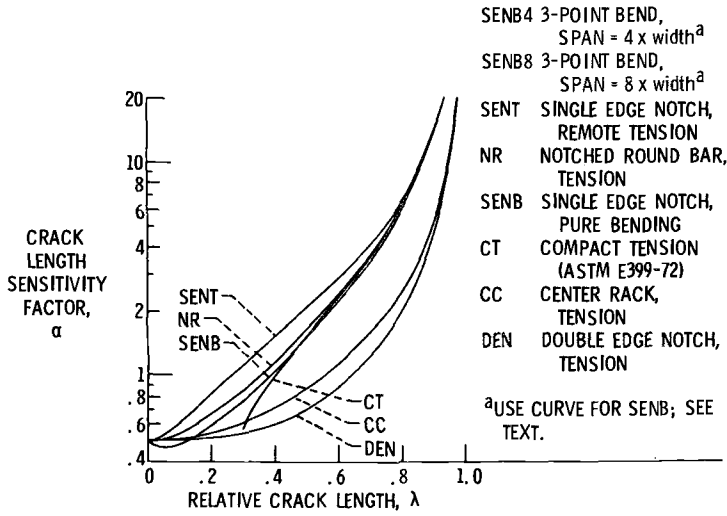


FIG. 2.—Crack length sensitivity factor.

must be added to the right sides of Eq 3 and Eq 4, respectively. It is reasonable to assume that the error in crack half-length measurement (E_c) will be the same as the error in crack depth measurement (E_a). Then for the PTC specimen the term α in Eq 5 can be replaced by

$$\beta = \left| \frac{1}{2} + \frac{a}{Y} \frac{\partial Y}{\partial a} \right| + \frac{a}{c} \left| \frac{c}{Y} \frac{\partial Y}{\partial c} \right|$$

To simplify differentiation, the approximation [8]

$$\Phi^2 \approx 1 + 4.59(a/2c)^{1.65}$$

was used here. Calculated values of the crack dimension sensitivity factor β for the PTC specimen are presented in Fig. 3.

In cyclic crack propagation testing, a parameter of interest is the stress intensity factor range,

$$\Delta K = K_{\max} - K_{\min} \approx (\sigma_{\max} - \sigma_{\min}) Y \sqrt{a} \tag{6}$$

If we assume that the maximum and minimum cyclic stresses will both have the same absolute error E_σ , then corresponding to Eq 5 we have

$$\frac{E_{\Delta K}}{\Delta K} = \frac{2}{1 - R} \frac{E_\sigma}{\sigma_{\max}} + \alpha \frac{E_a}{a} \tag{7}$$

where

$$R = \sigma_{\min}/\sigma_{\max}$$

Note that the first term on the right side of Eq 7 becomes large as R approaches unity. In other words, in a test where the alternating load is

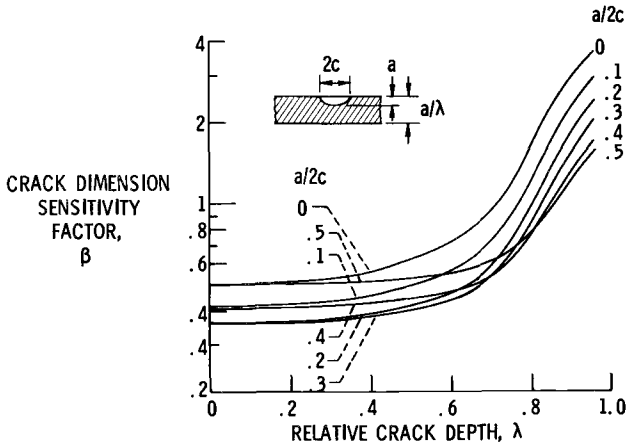


FIG. 3—Crack dimension sensitivity factor for PTC specimen.

small compared with the mean load, ΔK is extremely sensitive to errors in load control and measurement.

Discussion

General Comments

After examining Fig. 2 we can make the following general conclusions regarding the sensitivity of various specimen types to errors in crack length measurement. Sensitivity generally increases with increasing relative crack length. The single-tip-crack specimens (SENT, SENB, SENB4, SENB8, CT) are more sensitive than the double-tip-crack specimens (DEN, CC). Specifically, the SENT specimen is the most sensitive specimen of all. The remaining single-tip-crack specimens and the NR specimen are less sensitive, and all have very nearly the same sensitivity for $\lambda > 0.4$. The DEN specimen is less sensitive than the CC specimen and is the least sensitive of the types so far considered.

The reader should be cautioned that some values of α may not be very accurate at the lowest applicable values of λ . The calibration factor expressions were originally obtained by fitting polynomials to sets of boundary collocation data points. Differentiation of a fitted polynomial often gives highly unsatisfactory slopes, especially near either end of the fitting range. This seems to be especially true for the CT specimen below about $\lambda = 0.4$. At the higher ends of the polynomials' ranges, a slight amount of fairing was used in Fig. 2 to blend the curves derived from polynomials into those derived from extrapolation equations [3,4].

Equation 5 and Fig. 2 can prove useful in any of the following applications. For given measurement precision levels (E_σ/σ and E_a/a), the expected error E_K/K can be determined for any specimen. This will be done

later for the specimens described in the ASTM Test for Plane-Strain Toughness of Metallic Materials (E 399-72). Or, for any given specimen the effect of changes in the measurement precision levels can be determined. This in turn could help determine, for example, whether available funds would be better spent on new load cells or on a new optical micrometer.

In the discussion so far it has been tacitly assumed that the expected error in the applied load is unrelated to specimen type and crack length. This is true if the load in question is an independently-defined occurrence such as the maximum load. But in some tests (for example, ASTM E 399-72) the load in question is the load corresponding to a given percent crack extension. That load is usually determined by the intersection of the load-COD (crack opening displacement) trace and a secant offset line. The secant offset corresponding to a fixed percent crack extension varies with specimen type and relative crack length. This is discussed in more detail in Ref 2. In general, the secant offset is larger for the single-tip-crack specimens than for the double-tip-crack specimens and increases with the relative crack length. In most practical applications, if the required secant offset becomes too small it may become difficult to achieve the desired load precision level with existing instrumentation.

The PTC Specimen

Discussion of the PTC specimen must be prefaced with a consideration of the calibration factor. At present there is no exact solution for the problem of a semielliptical surface crack in a finite plate. The expression used [7] is a polynomial approximation to curves presented by Kobayashi and Moss [9], which in turn are based on analogy to an earlier approximate solution [10]. Although lacking in rigor, the Kobayashi-Moss estimation is probably adequate for illustrative purposes. The polynomial approximation is a fairly good fit, it is mathematically tractable, and its derivatives appear reasonable for, say, $\lambda \leq 0.9$.

The sensitivity factor β for the PTC specimen is shown in Fig. 3. Sensitivity to dimensional measurement error appears to be relatively low and independent of λ for shallow surface cracks, but increases markedly above about $\lambda = 0.7$. Although the analysis is only approximate, the PTC specimen would appear to be inherently more precise than the specimens of Fig. 2. However, there are many difficulties involved in the application of the PTC specimen, some of which are discussed in Refs 2 and 11.

ASTM Test Method E 399-72

This test method is thorough in that it specifies precision levels for every possible measurement, but it does not give the expected error in fracture toughness associated with these precision levels. The error can be calculated using Eq 5, Fig. 1, and Fig. 2, with one precaution.

The test method allows some misalignment of load, crack, and supports for the bend specimen. If the load and the crack are not in line, an in-plane shear (Mode II) loading will be present. This shear load will alter both the crack-tip stress field and the crack mouth displacement. At present there seems to be no adequate analysis for the misaligned bend specimen. But unpublished crack mouth displacement measurements by M. H. Jones and R. T. Bubsey of NASA-Lewis imply that the effect of the allowable misalignment will be quite small. For lack of a proper analysis (but having some experimental justification), errors due to bend specimen misalignment will be neglected.

Based on the precision levels specified in the test method for specimens thicker than 1.0 in. (25 mm), Eq 5 becomes

$$E_K/K = 0.018 + 0.005\alpha \text{ for the bend specimen}$$

$$E_K/K = 0.012 + 0.005\alpha \text{ for the compact specimen}$$

and these are plotted in Fig. 4. For the dimensions B or W less than 1.0 in. (25 mm), the test method specifies an absolute rather than a percentage precision level. In this case the error in applied stress (E_σ/σ) will increase with decreasing width or thickness and the curves of Fig. 4 will translate upwards. For thick specimens, the maximum error in fracture toughness due only to imprecision of physical measurements will be about $2\frac{1}{2}$ percent for the bend specimen and about 2 percent for the compact specimen. Although there may be other reasons for selecting one specimen over the other, the compact specimen appears to be inherently more precise than the bend specimen, and this was found in Ref 12 to be the case. In two series of round robin tests involving about 400 bend and compact specimens of four materials, the reported standard deviations of K_{Ic} ranged from 4.2 to 5.85 percent for bend specimens and from 2.6 to 3.75 percent for

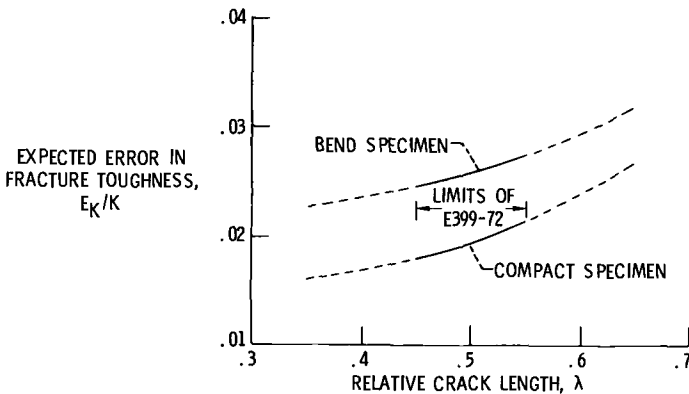


FIG. 4—Expected error in fracture toughness due to test imprecision (ASTM E 399-72: specimens thicker than 1 in., misalignment of bend specimen neglected).

compact specimens. The maximum error due to imprecision of physical measurements is not insignificant when compared with these measures of experimental data scatter.

The test method itself does not consider the question of replicate tests. In a smooth tensile test, for example, all replicate data will normally have the same precision, and a simple average is an appropriate characterization. But it is not reasonable to expect that replicate fatigue-cracked fracture specimens will all have exactly the same crack length. If the crack lengths vary, even over the narrow range permitted by the test method, the replicates will not all have the same precision. In this case we want to place the greatest emphasis on the test which is expected to be the most precise, and so a weighted average is called for. A weighted average should give a better estimate of the true population mean (namely, K_{Ic}) by accounting for the precision of the individual observations. It is customary [13] to weight each observation inversely proportional to the square of its expected error. If this is done for the fracture specimens, a specimen having $\lambda = 0.45$ will carry about 40 percent (compact specimen) or 26 percent (bend specimen) more weight than a specimen with $\lambda = 0.55$. Or, a compact specimen will have about 78 percent more weight than a bend specimen of the same relative crack length.

Cyclic Crack Propagation Testing

The treatment of experimental error is even more important in analysis of cyclic crack growth data than in fracture toughness testing, and may even be of critical importance. It is more important for two reasons. First, the errors in the basic measurements are generally larger, since load control and measurement and crack length measurement are more difficult in cyclic testing. Some of the factors affecting the precision levels of the basic experimental measurements are discussed by Wei [14]. Secondly, the reduction and analysis of the basic data is a three- or four-step process. Experimental errors enter into each step in a different way, and errors in any one step will be carried into subsequent steps.

When the crack length is obtained indirectly, as in the compliance and electric potential methods [2], the basic measurement represents some function (usually nonlinear) of the crack length. The expected error in the inferred crack length can be calculated in terms of the precision level of the basic measurement and a derivative of the functional relationship, and will probably be nonlinear. Now having the crack lengths a_i at cycle numbers N_i , we must obtain the growth rate da/dN , preferably by mathematical means. Several methods of numerical differentiation are evaluated by Frank and Fisher [15]. If we know the expected error in crack length and have a closed-form expression for the derivative, we can compute the expected error in growth rate, which again will probably be nonlinear. The stress intensity range, ΔK , is then computed (Eq 6) at each value of

crack length. The errors that may occur in this step have been discussed earlier in this paper, and they are overlooked by most investigators. If the cyclic loads are fixed, the error in ΔK will change as the crack grows; a short-crack high-load specimen and a long-crack low-load specimen may have the same ΔK but different error expectations; tests having the same ΔK but different load ratios will have different expected errors (see Eq 7). The presence and variability of these errors severely complicate the final step, wherein an attempt is made to correlate the crack growth rate with the stress intensity range using one or more analytical models. The most popular model is that of Paris [16],

$$\frac{da}{dN} = C(\Delta K)^n$$

where C and n are empirical constants. This exponential equation can be linearized by taking the logarithm of both sides. One is then tempted to fit a straight line using the method of least squares. However, to do so in this case would be to violate one of the basic assumptions of the method.

The classical method of least squares assumes that errors E_y in the dependent variable y are normally distributed and that the independent variable x is known without error (or at least that $E_x \ll E_y$). But here we have error in the independent variable ($\log \Delta K$) which is not always insignificant. The very complicated problem of linear regression with error in both variables is often cited in the literature [17,18], and there are solutions for special cases, but there appears to be no generalized solution applicable to the crack growth rate problem. In the absence of a rigorous method, a good engineering approximation might be to use a weighted least-squares fit with the weighting factor being the inverse square root of the sum of the squares of the expected errors in $\log (da/dN)$ and $\log (\Delta K)$. Such an approach would be relatively simple mathematically and would tend to place greatest emphasis on the points expected to be the most precise.

The errors involved in cyclic crack growth testing can be quite large even when the tests are carefully controlled. Frank and Fisher [15] used a test from the literature as an illustrative example. In this test, the crack half-length increased from 2 to 55 mm in a CC specimen 160-mm wide of 2024-T3 aluminum alloy 2-mm thick as the stress was cycled between 6.5 and 11.5 kg/mm². Assume that the errors in the cyclic stresses were 0.115 kg/mm² and the error in crack half-length measurement (E_a) was 0.25 mm (0.010 in.). Then at the beginning of the test the error in growth rate (secant method, [15]) is 50 percent and the error in ΔK (Eq 7) is about 11 percent; at the end of the test the error in growth rate has decreased to 10 percent and the error in ΔK to about 5 percent. In the opinion of this author, such errors are much too large to be ignored.

Summary and Conclusions

For the specimen types considered here, the sensitivity of the computed stress intensity factors to errors in crack length measurement increases with the relative crack length, and is greater for single-tip-crack specimens than for double-tip-crack specimens. Sensitivity is greatest for the remote-load single edge notch tension specimen and least for the double edge notch tension specimen. Based on an approximate stress intensity analysis, the part-through-crack specimen is relatively insensitive for crack depths less than about 70 percent of the plate thickness.

Based on the precision levels specified in ASTM E 399-72, the maximum expected error in K_{Ic} due to test imprecision is about 2 percent for the compact specimen and about $2\frac{1}{2}$ percent for the bend specimen (only for specimens thicker than 1 in.). It is suggested that replicate tests be weighted inversely proportional to the square of their expected error. If this is done, a specimen with a relative crack length of 0.45 will have 40 percent (compact specimen) or 26 percent (bend specimen) more weight than one with a relative crack length of 0.55; or, a compact specimen will have 78 percent more weight than a bend specimen with the same relative crack length.

The treatment of experimental error is even more important in analysis of cyclic crack growth data than in fracture toughness testing, and may even be of critical importance. Even in carefully controlled tests the errors can become quite large due to accumulation and compounding.

References

- [1] Irwin, G. R. in *Proceedings, Seventh Sagamore Ordnance Materials Research Conference*, Aug. 1960, Syracuse University Press, MET.E.661-611/F.
- [2] Brown, W. F., Jr. and Srawley, J. E. in *Plane Strain Crack Toughness Testing of High Strength Metallic Materials, ASTM STP 410*, American Society for Testing and Materials, 1966.
- [3] Wilson, W. K., *Engineering Fracture Mechanics*, Vol. 2, 1970, pp. 169-171.
- [4] Orange, T. W. in *Stress Analysis and Growth of Cracks, Proceedings, 1971 National Symposium on Fracture Mechanics, Part 1, ASTM STP 513*, American Society for Testing and Materials, 1972, pp. 71-78.
- [5] Tada, H., *Engineering Fracture Mechanics*, Vol. 3, 1971, pp. 345-347.
- [6] Benthem, J. P. and Koiter, W. T., "Asymptotic Approximations to Crack Problems," Report No. 461, Laboratory of Engineering Mechanics, Technological University, Delft, The Netherlands, 1972.
- [7] Collipriest, J. E. and Ehret, R. M., "Computer Modeling of Part-Through Crack Growth," Report SD 72-CE-0015, North American Rockwell, July 1971.
- [8] Rawe, R. A., Schwab, D. E., Wroth, R. S., and Taketani, H., "Fracture Toughness of Aft (LOX) Dome Meridian Welds for the Saturn S-IVB," Report No. DAC-62138, McDonnell-Douglas Corp., Aug. 1968.
- [9] Kobayashi, A. S. and Moss, L. W. in *Fracture: Proceedings of the Second International Conference on Fracture*, Chapman & Hall Ltd., 1959, pp. 31-45.
- [10] Hall, L. R. and Kobayashi, A. S., "On the Approximation of Maximum Stress Intensity Factor for Two Embedded Coplanar Cracks," Structural Development Research Memorandum No. 9, The Boeing Co., May 1964.
- [11] Swedlow, J. L., Ed., *The Surface Crack: Physical Problems and Computational Solutions*, American Society of Mechanical Engineers, 1972.

- [12] McCabe, D. E., *Journal of Materials*, Vol. 7, No. 4, Dec. 1972, pp. 449-454.
- [13] Wilson, E. B., Jr., *An Introduction to Scientific Research*, McGraw-Hill Book Co., 1952.
- [14] Wei, R. P., *Engineering Fracture Mechanics*, Vol. 1, 1970, pp. 633-652.
- [15] Frank, K. and Fisher, J., "Analysis of Error in Determining Fatigue Crack Growth Rates," Fritz Engineering Laboratory Report No. 358.10, Lehigh University, March 1971.
- [16] Paris, P. C. and Erdogan, F., *Journal of Basic Engineering*, Vol. 85, No. 4, 1963, pp. 528-534.
- [17] Kendall, M. G. and Stuart, A., *The Advanced Theory of Statistics*, Vol. 2: Inference and Relationship, Chapter 29, Hafner Publishing Co., 1967.
- [18] Acton, F., *Analysis of Straight-Line Data*, Wiley, New York, 1959.

A Combined Analytical-Experimental Fracture Study*

REFERENCE: Riccardella, P. C. and Swedlow, J. L., "A Combined Analytical-Experimental Fracture Study," *Fracture Analysis, ASTM STP 560*, American Society for Testing and Materials, 1974, pp. 134-154.

ABSTRACT: Using A533, Grade B, Class 1 low-alloy steel (HSST plate 04), a number of standard tests were performed in the laboratory, all at 50°F. Material characterization was established in terms of tension tests on specimens taken from the longitudinal and transverse directions, and the stress-strain curves were virtually identical. Fracture toughness data were obtained from 36 compact tension specimens of the standard ASTM configuration, ranging in thickness from 0.4 to 4 in. J-integral and equivalent energy approaches were used to interpret fracture toughness from the test data. In spite of the wide range of specimen size, and even though no specimen met ASTM validity requirements, the toughness data were highly consistent.

The tension data were used as the basis for a series of elastic-plastic finite element analyses of a center-cracked plate, under conditions of plane stress and plane strain. In addition to the usual stress and deformation field results, the analyses provided information which include load-deflection curves for a specific gage length, values of the J-integral, and total energy in the specimen. Three center-cracked plate specimens were fabricated from the same block of material as that used in the characterization tests, and were tested in the laboratory (at 50°F) under conditions simulated by the analyses.

Using the fracture toughness data from the compact tension tests in conjunction with the analytical values of J and total energy, preliminary fracture predictions were made for the center-cracked plates. Predictions based on the J-integral and equivalent energy approaches were consistent, but actual specimen performance was considerably tougher. Apparent reasons for the difference between predicted and actual behavior include incompleteness of the analytical model, inability to observe onset of slow crack growth, and less than fully plane strain constraint in the test specimens.

KEY WORDS: mechanical properties, elastic-plastic analysis, fracture tests, fracture properties, steels, strains, stresses

A significant portion of the fracture studies currently in progress is motivated by the increasingly urgent problem of how one deals with the

* Work sponsored by Heavy Section Steel Technology (HSST) Program under UCCND Subcontract No. 3196.

¹ Senior engineer, General Atomic Company, San Diego, Calif. 92138.

² Professor, Department of Mechanical Engineering, Carnegie Mellon University, Pittsburgh, Pa. 15213.

event of fracture in the presence of considerable plastic flow (on the macro scale). To this end, many studies focus primarily on experimental characterization of specific configurations viewed as typifying practical circumstances, or on analytical description of particular situations. The results thus generated are interesting and useful in that they provide performance data, or sometimes, insights which lead to more generalized study.

It is somewhat unusual, however, for experiment and analysis to be pursued simultaneously. Exclusivity of method is symptomatic of the gulf between the capabilities of the two approaches. That is, the kinds of things one may do in the laboratory and on paper (or on the computer) are at present quite distinct; and the kinds of information obtainable are, sometimes frustratingly, incompatible. It is nonetheless valuable to attempt combined effort if for no other reason than to articulate the problems involved. In this paper, we report such a study and seek to indicate areas of success and failure.

More information is in hand than is appropriate to report, and some findings are listed without full resolution. Yet such results contribute to the emerging theme that analysis can replicate physical behavior to a fair degree, so long as inquiry is limited to overall performance parameters. Moreover, while the design of experiments to be coordinated with analysis is more exacting than might be expected, there is real potential for narrowing the gulf between the two approaches.

Laboratory Experiments

To characterize the material properties of the steel used in the experimental portion of this study (A533 Grade B Class 1 low-alloy steel—HSST Plate 04), a number of standard laboratory tests were performed, including uniaxial tension tests and compact tension fracture toughness tests. The test temperature was chosen at $+50^{\circ}\text{F}$ in order to obtain fractures in the transition range between linear elastic (frangible) behavior and limit load (fully ductile) behavior. All testing was carried out at this temperature. Three center-cracked plate specimens were then tested for comparison with analysis.

A total of five standard 0.505-in. diameter tension specimens were machined from the HSST plate as shown in Fig. 1. Specimens were taken in both the longitudinal (RW) and transverse (WR) directions with respect to rolling of the material in order to determine the degree of anisotropy. The specimens were also taken at various depths through the thickness of the plate (after removing 2 in. of surface material from the top and bottom of the plate) to determine thickness variations of the tensile properties. The resulting true stress versus true strain data are shown in Fig. 2. Note that the tensile properties are essentially homogeneous and isotropic, and that all of the specimens exhibited a yield point instability at about 70 000

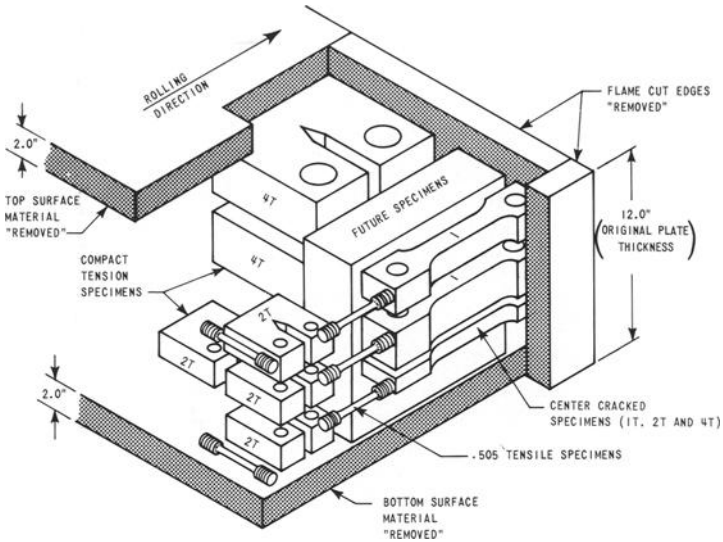


FIG. 1—Specimen sawing sketch for experimental fracture study.

psi and a subsequent post yield plateau on which no strain hardening occurs up to a strain level of approximately 1.5 percent.

The standard fracture toughness tests consisted of 36 compact tension specimens which were machined as shown in Figs. 1 and 3. The specimens were taken at various depths through the thickness after removal of

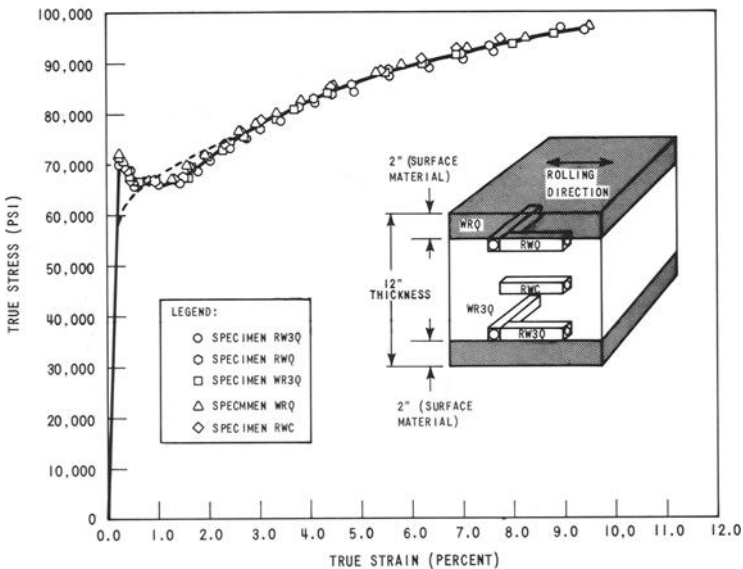


FIG. 2—Stress versus strain data from uniaxial tension tests.

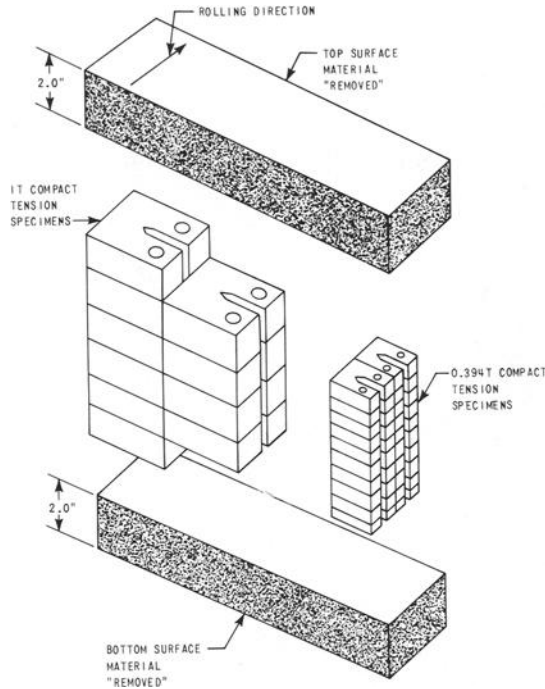


FIG. 3—Additional fracture toughness specimens for experimental fracture study.

surface material; however all of the specimens were machined in the longitudinal (RW) direction since this was the direction of interest for fracture toughness. Specimen sizes ranged from relatively large (4-in.-thick compact tension specimens) to quite small (0.394-in.-thick compact tension specimens). As noted below, however, none of the specimen sizes was large enough to satisfy the size requirements of the American Society for Testing and Materials (ASTM) Test for Plane-Strain Fracture Toughness of Metallic Materials (E 399-72). For this reason, fracture toughness data were interpreted from the experiments using the two proposed elastic-plastic fracture theories (the J-integral and equivalent energy approaches) [1,2].³

Lower bound fracture toughness data can be obtained from nonlinear load-displacement traces such as that shown in Fig. 4 using Witt's equivalent energy theory [2]. Basically, two quantities are required from the load-displacement curve, the area under the curve to maximum load (A_1) and the area under the curve to any point (P_Q) on the linear portion of the curve (A_2). The lower bound fracture toughness is then given by

$$K_{Ic} = \frac{P_Q \sqrt{A_1/A_2} f(a/W)}{B \sqrt{W}} \tag{1}$$

³ The italic numbers in brackets refer to the list of references appended to this paper.

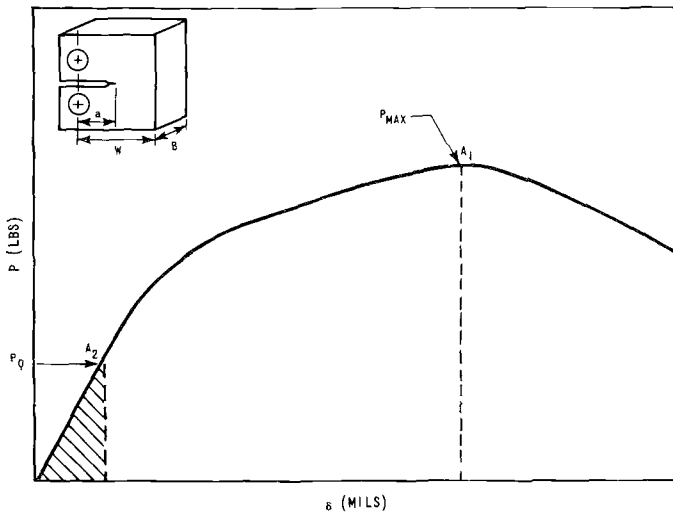


FIG. 4—Typical nonlinear load-displacement curve for a compact tension specimen illustrating data required for elastic-plastic fracture toughness interpretations.

where the geometric quantities a , W , and B refer to specimen crack depth, width, and thickness as shown in Fig. 4, and where $f(a/W)$ is a geometric shape factor which is commonly available in the literature (ASTM E 399-72 and Ref 3). Values of K_{Ic} were determined in this manner and the data from the 36 compact tension specimens are shown as a plot of fracture toughness versus specimen size in Fig. 5. The average toughness value for the 36 specimens was $117\,000\text{ psi}\sqrt{\text{in.}}$ with a standard deviation (σ) of $13\,200\text{ psi}\sqrt{\text{in.}}$. This average value is shown as a solid horizontal line in Fig. 5 and a $\pm 3\sigma$ scatter band is shown by dashed lines. The size requirement for a valid test according to ASTM E 399-72 is shown along with an approximate scatter band from ASTM valid tests which were performed on a similar heat of material (HSST plate 02) at the same temperature [4]. The proposed size requirements for valid J-integral testing are also shown on this figure, and all of the present tests satisfied these limits. In spite of the wide range of specimen size, and even though none of the present specimens met ASTM validity requirements, the toughness data reproduce the valid data quite well. These data illustrate that an order of magnitude reduction in specimen size (and thus cost) can be achieved through use of elastic-plastic interpretations. It should also be noted that the standard deviation drops to $10\,200\text{ psi}\sqrt{\text{in.}}$ if the one point outside the dotted lines in Fig. 5 is not taken into consideration.

A second method for evaluating fracture toughness data from nonlinear load-displacement curves can be formulated from the J-integral approach of Rice, Begley, and Landes [1,5]. Rice has shown [6] that for relatively deep cracked bend bar and compact tension geometries, the J-integral at

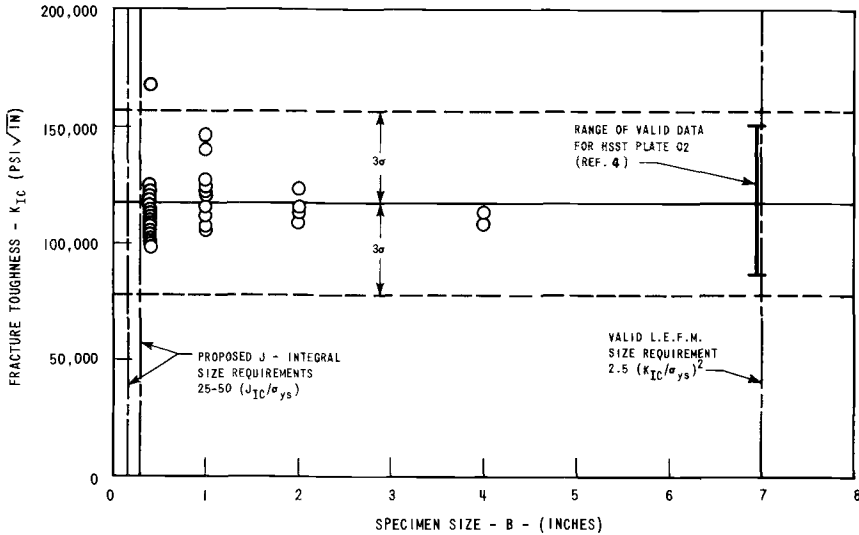


FIG. 5—Fracture toughness data from experimental fracture study (equivalent energy interpretation).

any point on the load-displacement curve is proportional to the area under the curve to that point (A)

$$J_I = \frac{2A}{B(W - a)} \tag{2}$$

where the geometric quantities B , W , and a are defined as in Fig. 4. Thus, the area under the curve to the point of initiation of crack growth should be proportional to the critical value of J_I , denoted J_{Ic} . For the present study it has been assumed that the point of initiation of crack growth corresponds to the maximum load point on the load displacement curve, and thus

$$J_{Ic} = \frac{2A_1}{B(W - a)} \tag{3}$$

It should be pointed out that there is no theoretical basis for this assumption, and that although there is considerable experimental evidence that crack growth does not occur prior to maximum load for this particular steel and specimen type [7], it will be seen later that the assumption should not be generalized to other materials and specimen types. Finally, fracture toughness can be computed from J_{Ic} values determined according to Eq 3 using the standard conversion

$$K_{Ic} = \sqrt{EJ_{Ic}/(1 - \nu^2)} \tag{4}$$

where E and ν are Young's modulus and Poisson's ratio, respectively.

Substituting load-displacement data from the 36 compact tension specimens into Eqs 3 and 4 yields the fracture toughness data shown in Fig. 6. Fracture toughness values from each specimen are again shown as a function of specimen size. The average toughness value in this case was $119\,000 \text{ psi}\sqrt{\text{in.}}$ with a standard deviation of $13\,900 \text{ psi}\sqrt{\text{in.}}$. The standard deviation drops to $10\,700 \text{ psi}\sqrt{\text{in.}}$ if the one point outside the present 3σ band is not considered. The average toughness, $\pm 3\sigma$ band, ASTM and J-integral size requirements, and valid data from HSST plate 02 [4] are illustrated as before, and the data are virtually identical to that of Fig. 5. Thus, the two elastic-plastic fracture theories are very similar from the standpoint of measuring fracture toughness from small compact tension specimens, and both reproduce valid toughness data obtained on much larger specimens quite well.

One difference between the two approaches which was encountered involves the point at which displacement is measured. When using the J-integral approach, the area used in Eq 3 must represent the total work input to the specimen. Thus, care must be taken to measure the displacement of the load point. On the other hand with the equivalent energy approach, the areas used in Eq 1 need only be proportional to work input, and thus almost any displacement measurement can be used. Furthermore, the equivalent energy approach is not sensitive to calibration of the displacement gage. (In fact, no calibration at all is required.) These features of the equivalent energy approach may become quite convenient if the test method is adopted as a standard material qualification test.

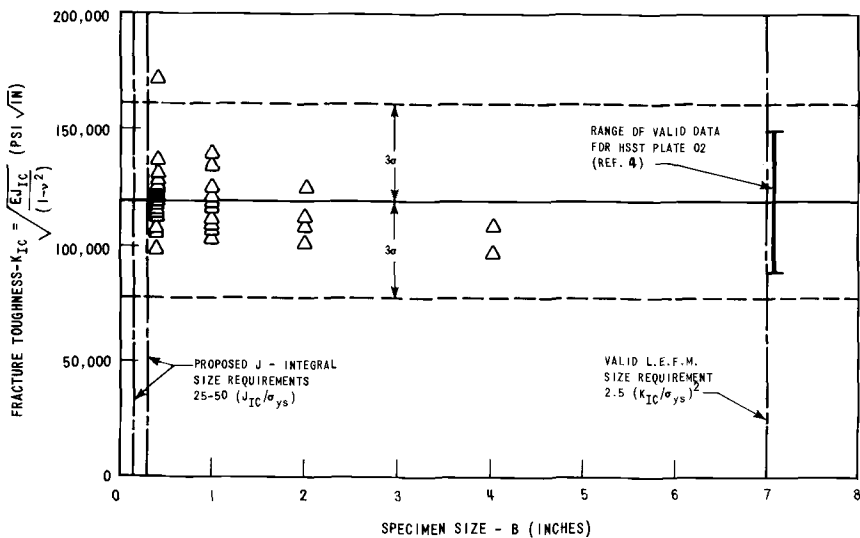


FIG. 6—Fracture toughness data from experimental fracture study (J-integral interpretation).

The final set of laboratory experiments was the center-cracked specimen tests which were run for purposes of comparison with analysis. Three center-cracked specimens were fabricated with the in-plane dimensions given in Fig. 7, and with thicknesses of 1.0, 2.0, and 4.0 in. (see Fig. 1). The center slot was produced using an electric arc discharge machining (EDM) process, and then fatigue sharpened as shown in Fig. 7. The specimens were loaded monotonically to fracture, at +50°F, and values of load versus displacement were recorded continuously during the test. Two displacement gages were used and were located at the specimen centerline on the front and back face, with a gage length of 3.5 in. which was preselected on the basis of preliminary analysis. An acoustic emission monitoring scheme was used on the final (4.OT) specimen when it became apparent from the first two tests (1.OT and 2.OT) that considerable amounts of subcritical crack growth were occurring prior to ultimate fracture of the specimens. The results of these tests are discussed in the analytical-experimental comparison section.

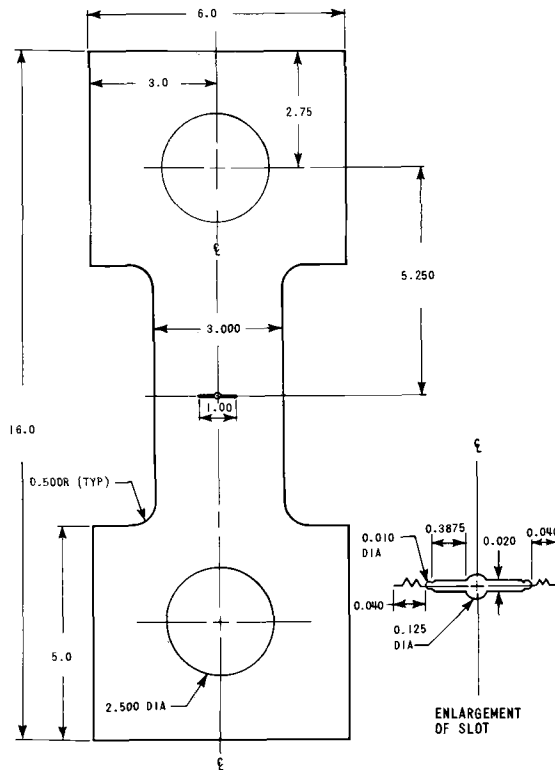


FIG. 7—Center-cracked specimen for comparison with analysis.

Analyses

A series of finite element analyses was performed as an integral part of this work. All such studies used linear-displacement triangular elements, and all were performed in core on a CDC-7600 computer.

Complexities of the pin-loaded, center-cracked specimen precluded detailed analysis of the full configuration, so a subsized model was developed. To establish the appropriate dimensions, an elastic analysis of the full geometry was performed using a relatively crude element array (334 degrees of freedom) as shown in Fig. 8. Along several lines parallel to the crack, axial displacements were determined, the overall deformation pattern being as shown in Fig. 9 for one quadrant of the specimen. It is evident that a region of uniform displacement occurs at a vertical distance of 1.75 in. from the crack, or an effective gage length of 3.5 in. Therefore, the full specimen was modeled by one 3.0-in. wide by 3.5-in. high, and con-

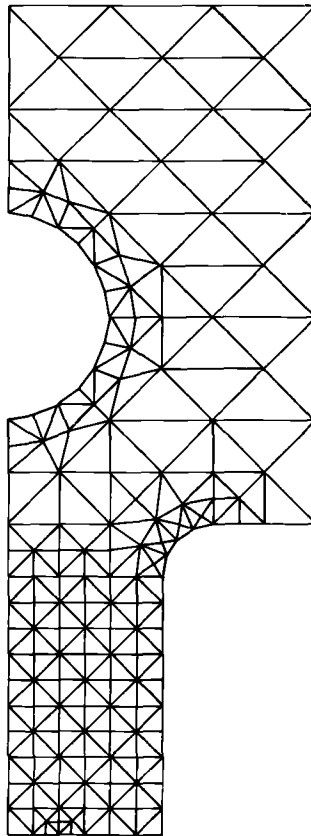


FIG. 8—Elastic model of center-cracked specimen used to determine gage length.

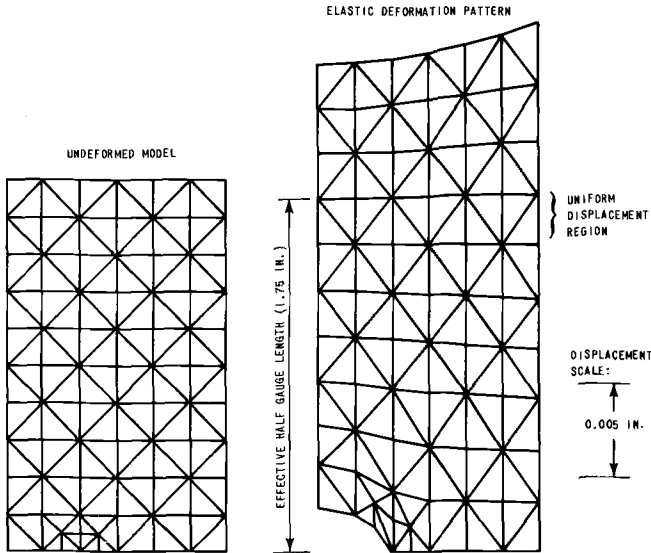


FIG. 9—Deflection results of elastic analysis of center-cracked specimen.

taining a 1.0-in. center crack; the model is loaded by uniform longitudinal displacements imposed along its upper and lower edges. A more refined element array was devised (474 degrees of freedom in the quadrant), as shown in Figs. 10 and 11, the smallest elements at the crack tip having a characteristic length of approximately 0.0005 in.

Two elasto-plastic analyses were performed using the refined map, one in plane strain, the other in plane stress. The computational procedures follow those described in Ref 8 and, except for the matter of adapting the measured stress-strain curve of Fig. 2 for use in the analyses, the approach was straightforward. As is clear from Fig. 2, the measured curves all exhibited a yield point instability which the analysis is incapable of representing [8]. The physical curves were therefore replaced by the one shape shown by the dashed curve in Fig. 2, which was the result of a simple smoothing operation. A total of 140 displacement increments was imposed in each of the elasto-plastic analyses, ranging from a gage length deflection of 0.00016 in. in plane strain and 0.00014 in. in plane stress to values of 0.00663 and 0.00588 in., respectively. In both cases, increments were sized as 5 percent of the currently accumulated excitation. Machine time requirements for each problem were 5.4 min per problem, or 2.32 s per increment.

Among the various results provided by the analysis, several are germane to the present investigation, including the load-deflection response of the specimen, as modeled; energy in the specimen, elastic and plastic; and values of the J-integral evaluated along several paths surrounding the crack tip.

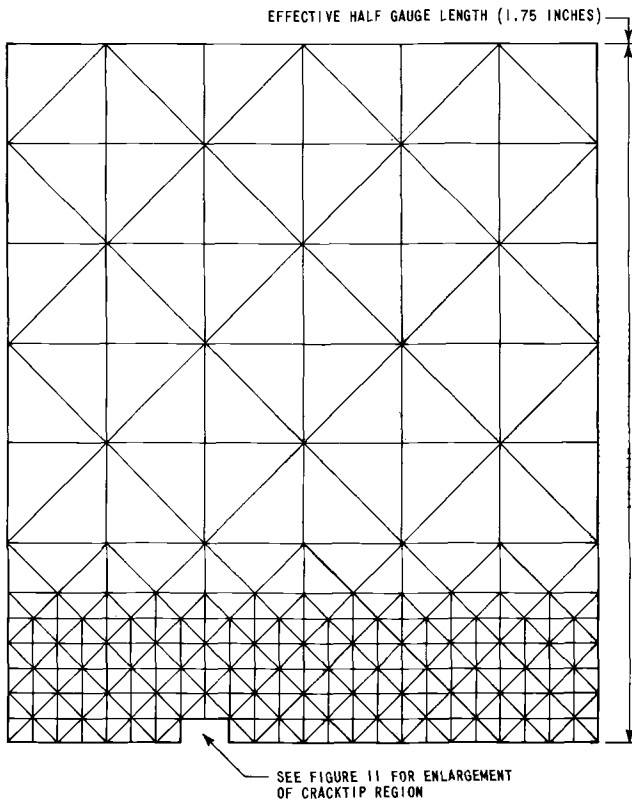


FIG. 10—Elastic-plastic model of center-cracked specimen.

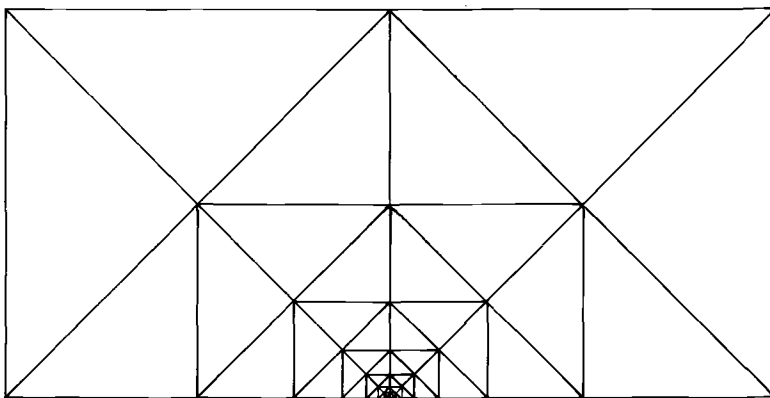


FIG. 11—Elastic-plastic model of center-cracked specimen (enlargement of cracktip region).

The computed load-deflection curves of the specimen appear in Fig. 12, along with experimental results for the three center-cracked specimens tested. It is obvious that, at a given value of the imposed deflection, the computed loads are too large, especially for the case of plane strain which is more constrained and therefore stiffer than any physical specimen of finite thickness can be. The plane stress curve is also high in that, over parts of the load range, two of the experimental curves fall below the computed curve. To an extent, the reason for this excess in load is the method of analysis itself; finite element results tend to overestimate structural stiffness as compared to continuum response. More significant, however, is the fact that the analyses did not include slow crack growth whereas there is evidence to believe that such extension occurred in testing. Further comment on this point appears in the following.

Energy in the specimen model is shown in Fig. 13 as a function of applied, or gage-point displacement. Both total energy and the elastic component are shown, and it is clear that the latter changes relatively little once a significant amount of yield has occurred. Beyond this point, the elastic energy increases by less than a factor of two while the plastic energy grows by more than an order of magnitude.

The procedure for computing the J-integral over a specified path follows that described by Hayes [9]. Actually, 13 paths were traversed at each load step, but the innermost three were erratic even in the elastic range owing largely to the minuteness of the elements immediately adjacent to the crack tip. Results along these paths were discarded. The growth of an averaged value of J (taken over the outer 10 paths) with applied displacement is shown in Fig. 14. Initially parabolic, J varies almost linearly with displacement at high levels of excitation but is never completely so. This

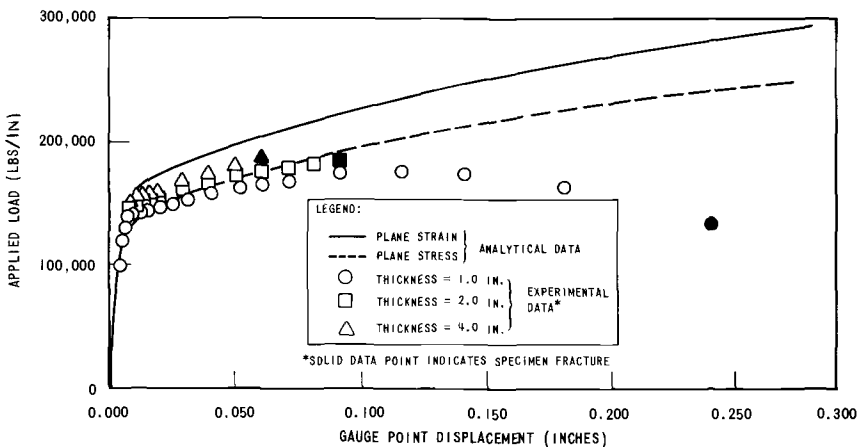


FIG. 12—Analytical and experimental compliance data for center-cracked specimen.

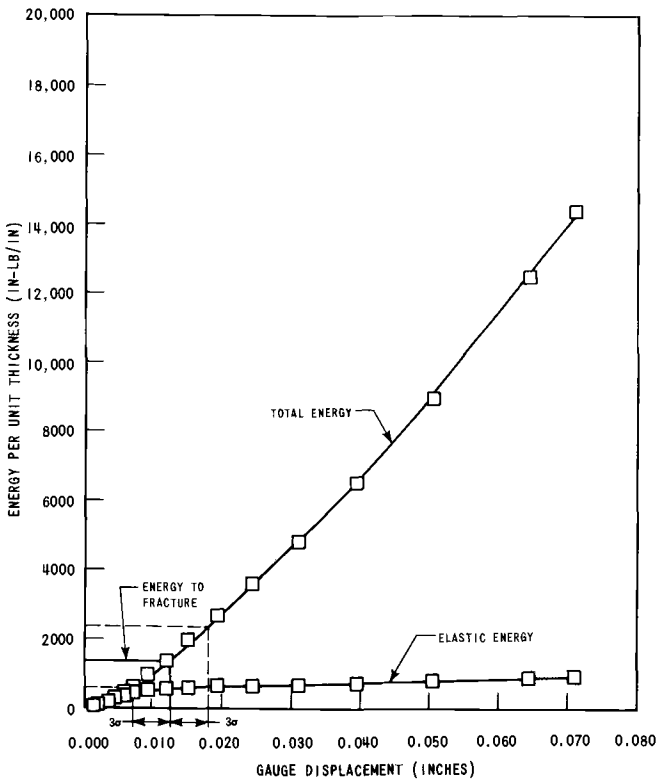


FIG. 13—Computed energy in center-cracked specimen.

feature is consistent with the analysis in that considerable work-hardening is present and no limit load can be realized due to geometric effects.

Variation of J over the various paths of integration is shown in Fig. 15. In this figure J itself is not plotted, but $K_{J-INT} = \sqrt{[JE/(1 - \nu^2)]}$ normalized on an elastic value of K calculated in the standard way [3]

$$K = Y \cdot \frac{Pa^{1/2}}{BW} \quad (5)$$

where a , B , and W are the specimen half-crack length, thickness, and width (Fig. 7), respectively, Y is a geometric correction factor, and P is the applied load on the specimen. It is seen that the path independence of the J computation deteriorates as excitation increases, owing largely to the magnitude of stress in near-tip elements. This evident departure from path independence is thought to result from having performed an incremental analysis for which the requirements of path independence are violated. Further from the tip, however, consistent results are obtained with some variation in the discrete values. The average of such values may be taken to represent the magnitude of J .

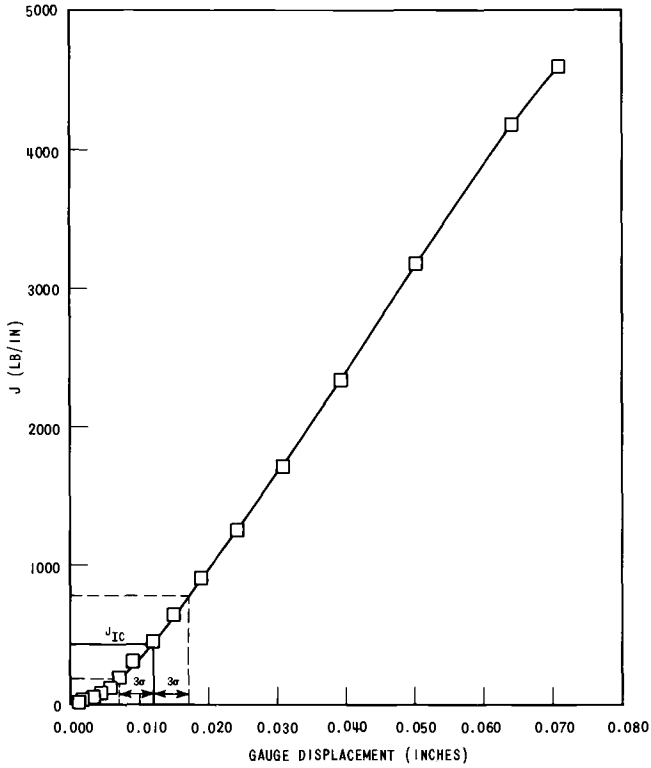


FIG. 14—Computed values of the J-integral in center-cracked specimen.

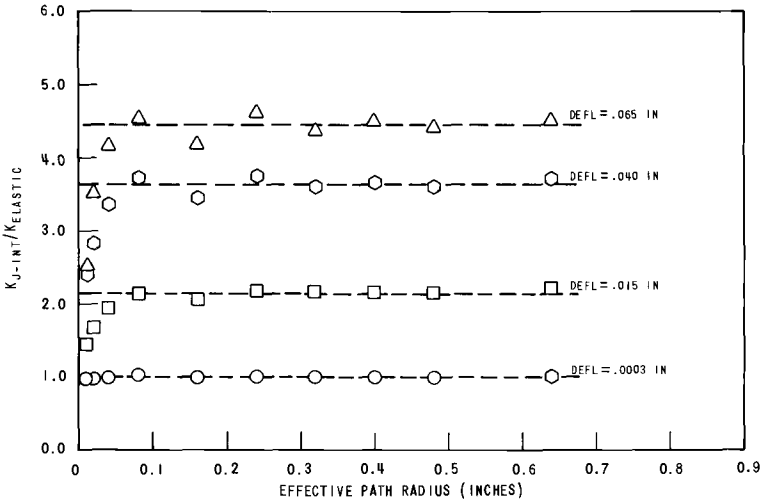


FIG. 15—Path dependence of analytical J-integral data.

The normalization procedure used for the path independence study leads to another interesting observation concerning J which is illustrated in Figs. 16 and 17. Figure 16 shows values of K_{J-INT} from the elasto-plastic J -integral computation plotted as a function of applied load. Calculating K elastically on the basis of applied load using Eq 5 leads to the elastic line shown in this figure. Figure 17 shows the same values of K_{J-INT} only plotted against gage displacement rather than load. In this figure, the elastic line was computed using a pseudo-elastic load for each gage displacement rather than the applied load in Eq 5. Referring to Fig. 12, an approximate yield point of 150 000 lb and 0.007-in. gage displacement can be identified on the analytical (plane strain) curve. This yield point has been transcribed onto Figs. 16 and 17 as a reference point. Note that for the load based comparison (Fig. 16), the elastic line deviates severely from the J -integral based curve as soon as the yield point is exceeded. On the other hand, the displacement based comparison (Fig. 17) shows reason-

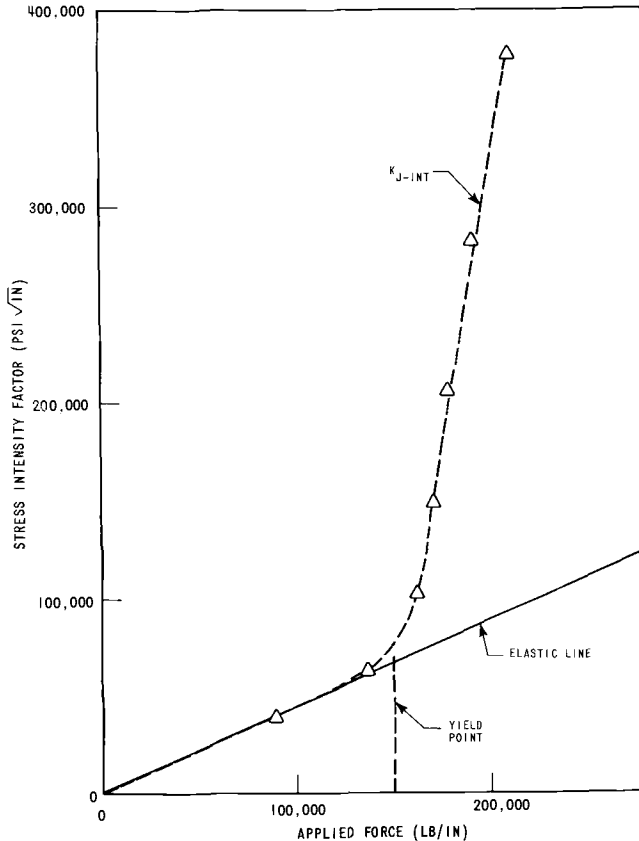


FIG. 16—Comparison of elasto-plastic J -integral computation with load based elastic calculation.

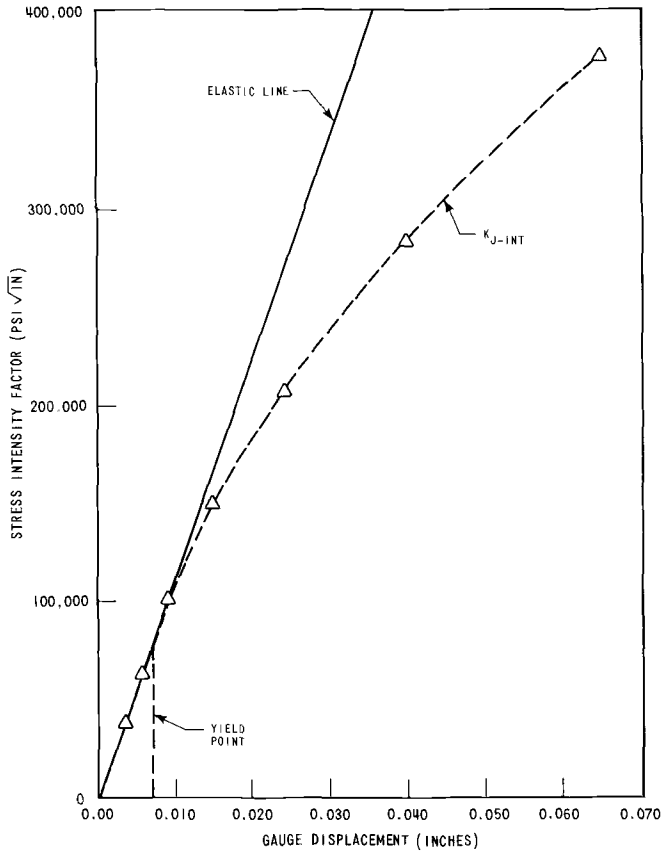


FIG. 17—Comparison of elasto-plastic J-integral computation with displacement based elastic calculation.

able agreement to displacements up to three times the yield point and the deviation thereafter is not as severe. Furthermore, the nature of the deviation in these comparisons is such that load based elastic calculations give unconservative J-integral estimates while displacement based elastic calculations are conservative. This observation strongly suggests that one should use displacement based methods when attempting to extend linear elastic fracture mechanics techniques into the elasto-plastic range. It also implies that displacement based elastic methods will work quite well for many practical elasto-plastic problems.

No attempt was made to examine other data produced during the analysis, beyond ascertaining that the computer program had executed properly. The reason, of course, is that without extensive instrumentation, none of the detailed data normally computed admit to direct comparison with experiment.

Analytical-Experimental Comparison

Obviously, an attempt was made to design the center-cracked specimens and the companion analysis in a manner that admits to a reasonable comparison and, as evidenced by Fig. 12, some success has been achieved. On the other hand, the physical and computational models do not replicate one another completely, in terms both of formal modelling and of performance. It is useful, therefore, to examine the differences briefly.

For the most part, the material was modelled accurately in that the stress-strain curve was largely a representation of data actually obtained in tests. As just noted, the yield point instability cannot be handled; however, since this feature does not appear on the center-cracked specimen load-deflection curves, it is not viewed to be a serious matter for the present analysis. The material is assumed to harden isotropically according to a Mises criterion [8]. Since the stress-strain curves in two directions are indistinguishable, and since the Mises criterion is usually held to be reasonable, this aspect of material representation is probably of reasonable acceptance. Other instances of comparison between analysis and experiment [10] have indicated such an approach to be appropriate.

Geometric representation is somewhat more problematic. While the method used to determine the gage section of the specimen is satisfactory for elastic response, or elastic plus limited plastic behavior, the same may not be true for the load range used in analysis. In fact, it was observed that with uniform displacements imposed along the upper edge of the specimen model, the load distribution changed as yield progressed into advanced stages. To assess this matter, an additional run was performed in which excitation was specified in terms of load, so that displacement might be tracked. While in the region of load application there were differences between the two problems, the types of data we reported here are virtually the same for the two cases. In particular, load, J values, and energy when plotted against average deflection were not affected to a significant degree. Thus, it is concluded that use of the elastically developed gage section of the original specimen geometry is acceptable practice.

Geometric representation also involved a fixed crack length, whereas it is evident in Fig. 18 that subcritical crack growth prior to fracture did in fact occur in all three specimens. It should be evident that crack growth at any one excitation level will lead to reduced stiffness (increased compliance) for additional loading. Thus at a given gage displacement, the experimental load will be less than the computed level to the extent that the crack has grown. Qualitative evidence exists that the crack did in fact grow throughout the loading: acoustic emission traces such as the one shown in Fig. 19, although uncalibrated, strongly suggest this point.

With this information in hand, Fig. 12 can be examined in closer detail. Looking, for example, at the curves for the 2.OT specimen and the plane stress analysis, we observe very closely the same elastic behavior, and

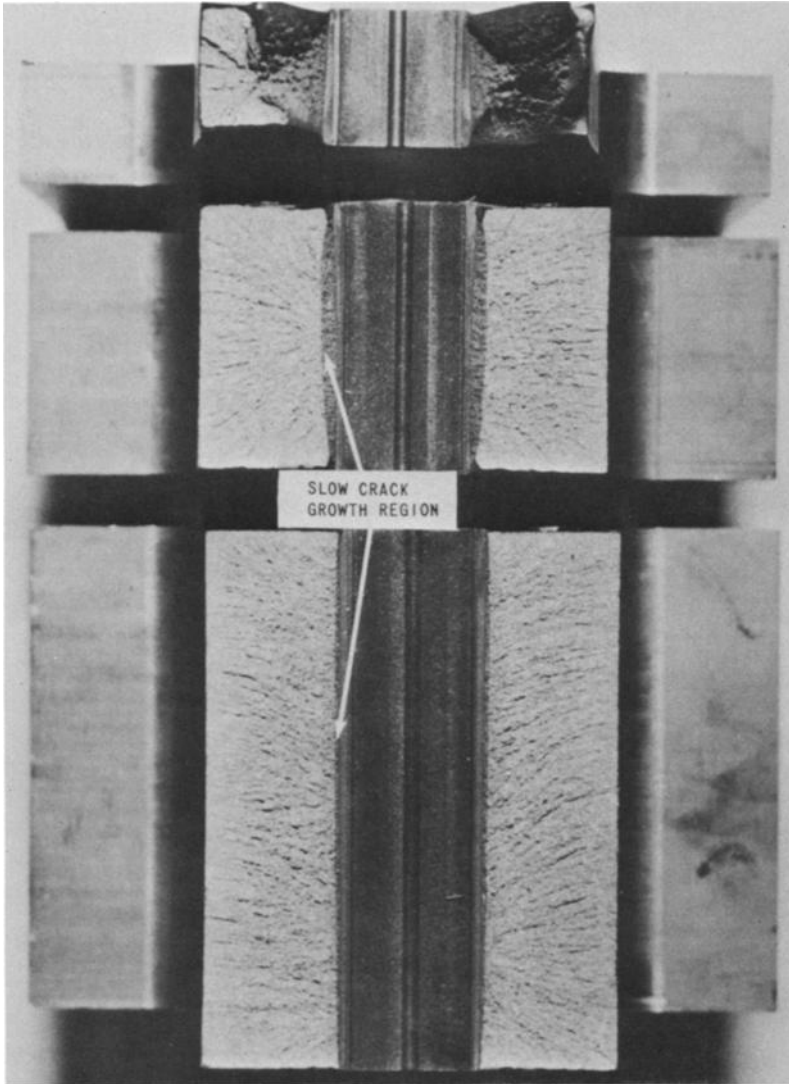


FIG. 18—*Fracture surfaces from center-cracked specimens.*

nearly parallel response beyond the knee of the two curves, out to a gage deflection of about 0.040 in. At that point the experimental curve flattens while the analytical curve continues with slope virtually unchanged. Analogous commentary obtains for the plane stress curve compared to any of the test records, or for the plane strain curve similarly compared. As far as can be discerned, therefore, this divergence is due to subcritical crack growth in the specimens which was not included in the model.

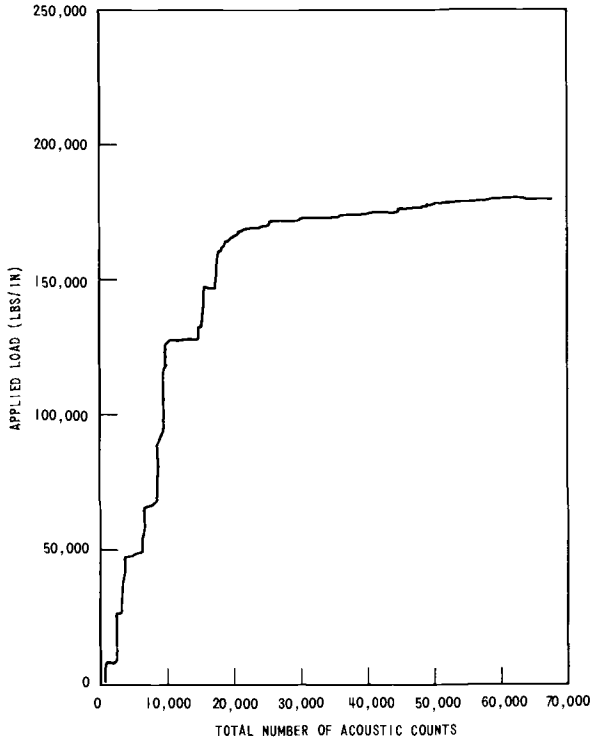


FIG. 19—Acoustic emission trace for 4-in.-thick center-cracked specimen.

As a result of slow crack growth, the traces in Figs. 13 and 14 are greater than what is experienced by the specimen, too. Crack growth has the effect of lowering the energy in the specimen at a given gage displacement, thus the analysis tends to over-predict this quantity. The same is true of J_I although the reasoning is necessarily more complex. For an increase in crack length, J_I tends to become larger. Since a process is involved, the load drops with crack growth (relative to its value for fixed crack length), and the J computation is such that its value for the specimen experiencing crack growth would be less than is computed from analysis.

For the prior reasons, fracture predictions based on equivalent energy J -integral approaches which utilize the analytical data of Figs. 13 and 14 are conservatively low. For instance, the $\pm 3\sigma$ fracture toughness band from Fig. 5, when translated into terms of energy to fracture [2] leads to fracture predictions on the order of 0.007 to 0.018 in. as shown in Fig. 13. Likewise, the $\pm 3\sigma$ fracture toughness band from Fig. 6, when converted into a J_{Ic} band leads to fracture displacements of 0.007 to 0.017 in. as shown in Fig. 14. While the two fracture predictions are self-consistent, the experimental fracture points from Fig. 12 are much higher (0.060 in. for the 4T specimen). However, the fracture predictions may be viewed as a

prediction of the point of initiation of subcritical crack growth for all three specimens. Unfortunately, the occurrence of slow crack growth was not foreseen, and no measures were taken to quantitatively assess the point of initiation. Acoustic emissions were monitored during the 4-in.-thick specimen test (Fig. 19), and showed significant increase in activity in the 160 000 lb/in. load range, which corresponds to approximately 0.015-in. displacement. However, the acoustic technique used has not been calibrated with respect to crack growth, and quantitative estimates of slow crack growth based on this data are highly speculative to say the least.

Recommendations

In order to further pursue the analytical-experimental efforts described herein, one is faced with certain choices. One might continue with the present approach, arguing that it is straightforward, economical, and conservative when viewed in the context of service configurations. That is, the type of analysis is well within the capability of many practitioners and, to the extent that an elastic-plastic analysis may be performed for a given geometric and load configuration, conservative results will obtain.

Alternatively, one might choose to model the growth process. While the computation is certainly feasible, the difficulty is that there is no basis for postulating the point and extent of growth and, without such information, the attempt to create a more meaningful model is not clearly founded. Furthermore, the theoretical basis of the J -integral as a fracture criteria does not admit specimen unloading due to crack growth.

A third option is to limit study to specimen configurations for which experience indicates that little or no slow crack growth occurs. The difficulty is not resolved, but it is bypassed. In so doing, one is able to demonstrate more conclusively the fidelity of analysis, thereby providing a test bed for alternate fracture criteria.

Regardless of which option is chosen, there is an obvious need for a reliable experimental method for detecting the presence of subcritical crack growth. Some success has been achieved recently by testing specimens to prespecified load levels, heat tinting, and sectioning [11], however this method is characteristically inefficient since it requires multiple specimen testing per datum point. The acoustic emission approach used on the 4T center-cracked specimen test is promising, and work should be pursued to calibrate this method with respect to crack growth.

Even should additional effort, using the third alternative, be successful in the sense of providing more accurate records of load, energy, and J for specified or gage displacement, the slow crack growth problem remains. Because the event has been bypassed for purposes of study does not mean that such growth will not occur in a service situation. Indeed, if cracks in some specimens grow but others do not, a point of interest is the condition(s) distinguishing the two cases.

Conclusions

On the basis of the data reported herein, several conclusions can be drawn which are germane to the general problem of fracture characterization in the elasto-plastic range.

1. The J-Integral and equivalent energy approaches to elasto-plastic fracture represent considerable advances in the important engineering task of characterizing plane strain fracture toughness of materials using small inexpensive fracture specimens.

2. Meaningful application of these theories to elasto-plastic service situations requires, in the general case, a full elasto-plastic analysis. Such analyses can be conducted with a reasonable degree of success using present analytical tools.

3. In many service situations, a simple elastic J-Integral approach will suffice well into the plastic range provided that a displacement based rather than load based excitation parameter is used.

4. Slow or subcritical crack growth prior to fracture causes serious uncertainties in characterization of elasto-plastic fracture behavior, and a great deal of further effort is required in this area, both analytically and experimentally, before the phenomenon is fully understood. At present, however, these difficulties can be circumvented by choosing specimens for fracture toughness characterization which do not exhibit slow crack growth, and by assuming in fracture evaluations that the initiation of slow crack growth in a structure corresponds to overall fracture.

References

- [1] Begley, J. A. and Landes, J. D. in *Fracture Toughness, Part II, ASTM STP 514*, American Society for Testing and Materials, 1972, pp. 1-20.
- [2] Witt, F. J., "A Procedure for Determining Bounding Values on Fracture Toughness at any Temperature," HSSST Program 5th Annual Information Meeting, Paper No. 13, March 1971.
- [3] Brown, W. F. and Srawley, J. E., *Plane Strain Crack Toughness Testing of High Strength Metallic Materials, ASTM STP 410*, American Society for Testing and Materials, 1966.
- [4] Mager, T. R., "Fracture Toughness Characterization Study of A-533 Class 1 Steel," HSSST Technical Report No. 10, Westinghouse Nuclear Energy Systems Report WCAP-7578, Oct. 1970.
- [5] Landes, J. D. and Begley, J. A. in *Fracture Toughness, Part II, ASTM STP 514*, American Society for Testing and Materials, 1972, pp. 24-39.
- [6] Private communication, J. R. Rice, Brown University.
- [7] Mager, T. R., "Experimental Verification of Lower Bound K_{Ic} Values Using the Equivalent Energy Concept," HSSST Program 6th Annual Information Meeting, Paper No. 23, April 1972.
- [8] Swedlow, J. L., *Computers and Structures*, Vol. 3, 1973, to be published.
- [9] Hayes, D. J., "Some Applications of Elastic-Plastic Analysis to Fracture Mechanics, Ph.D. thesis, Imperial College of Science and Technology, University of London, 1970.
- [10] Swedlow, J. L., *International Journal of Fracture Mechanics*, Vol. 5, 1969, pp. 25-31.
- [11] Private communication, J. A. Begley and J. D. Landes, Westinghouse Electric Corporation.

J. A. Begley,¹ J. D. Landes,¹ and W. K. Wilson¹

An Estimation Model for the Application of the J-Integral

REFERENCE: Begley, J. A., Landes, J. D., and Wilson, W. K., "An Estimation Model for the Application of the J-Integral," *Fracture Analysis, ASTM STP 560*, American Society for Testing and Materials, 1974, pp. 155-169.

ABSTRACT: A technique is developed for estimating the J-integral for the case of a crack imbedded in a uniform strain field. Use of this technique provides a possible simple engineering method for applying the J-integral fracture criterion to small cracks imbedded in a plastic zone. Reliability of structural components could be evaluated without the need for sophisticated elastic-plastic stress analysis.

The application of this model to the case of a small crack emanating from a stress concentration illustrates how an attempt to extend linear elastic fracture concepts may lead to erroneous results.

KEY WORDS: stress analysis, fracture properties, crack initiation, mechanical properties, strains

The engineering application of the J_{Ic} fracture criterion requires calculation of the J-integral for the crack sizes, component geometries, and loadings of interest. In the general case, this requires versatile elastic-plastic computer programs. For simple geometries a procedure has been developed for estimating J based on linear elastic fracture mechanics and rigid plastic limit load theory [1].² This technique is a first step in developing the engineering usefulness of the J_{Ic} approach to fracture. However, one of the limitations of the prior estimation method is that gross section, as opposed to net section, yielding cannot be handled easily. For this reason it is instructive to study an extreme case where gross section yielding dominates, that is, a situation where a crack has a negligible effect on the macroscopic flow field.

The specific problem to be discussed is that of an infinite sheet uniformly stressed at infinity containing a finite crack. The solution to this problem is very useful in the engineering use of linear elastic fracture mechanics

¹Senior engineers, Mechanics Department, Westinghouse Research Laboratories, Pittsburgh, Pa. 15235.

²The italic numbers in brackets refer to the list of references appended to this paper.

and an estimated solution in the plastic range should be of utility in elastic-plastic and fully plastic fracture mechanics.

The estimated solution for the fully plastic case is used to approximate solutions to the problem of a crack emanating from a stress riser where the crack is surrounded by a plastic zone. A limiting case solution is obtained by a simple analysis technique. A more accurate solution is also obtained from an elastic-plastic finite element solution to the stress riser problem. These solutions are used to evaluate linear elastic fracture mechanics (LEFM) methods which attempt an extrapolated solution to this problem.

The Infinite Plate Problem

Linear Elastic Case

One of the classic problems of linear elastic fracture mechanics is a crack in an infinite sheet shown in Fig. 1. The uniform stress at infinity is σ , and the total crack length is $2a$. The expression for the stress intensity [2] K is

$$K = \sigma\sqrt{\pi a} \quad (1)$$

This solution permits estimation of stress intensities for a range of additional problems. For example, with a finite width sheet, one would suspect Eq 1 to be negligibly in error if the sheet width was an order of magnitude greater than the crack length. In fact numerical results [3] show Eq 1 to underestimate K by only 10 percent when the sheet width is only three times the total crack length.

If we cut Fig. 1 in half through the middle of the crack, we have a semi-infinite sheet with an edge crack. Equation 1 seems a reasonable estimate of the stress intensity for this case also. Accurate results for the edge cracked problem show Eq 1 to underestimate K by 12 percent [2]. Some care must now be taken in estimating K for a finite plate with an edge crack. As the crack becomes comparable to the plate width, bending stresses become large. However, if the width is greater than ten times the crack length, Eq 1 with the 12 percent free edge correction should still be a reasonable guess. Boundary collocation computer results [3] show this to be true. The estimated K is low by less than 10 percent.

With the semi-finite sheet edge crack solution

$$K = 1.12\sigma\sqrt{\pi a} \quad (2)$$

one can tackle a significant engineering problem of a crack emanating from a stress raiser. Consider, for example, a large sheet with a central hole with a crack as illustrated in Fig. 2. In the uncracked state the stress adjacent to the hole is three times the stress at infinity. This stress diminishes with distance from the hole. If the crack is small compared to the hole

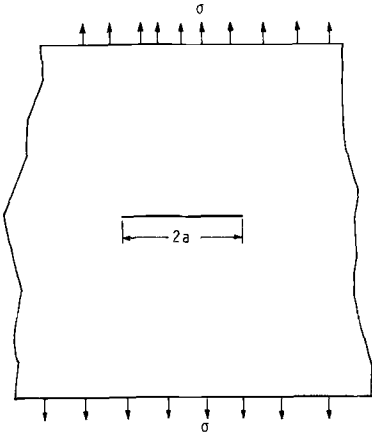


FIG. 1—Central crack in an infinite plate.

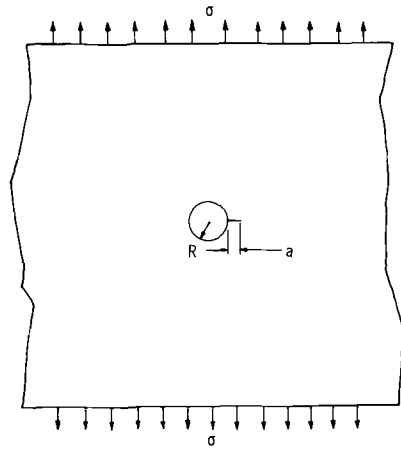


FIG. 2—Crack emanating from a stress raiser.

radius it may be considered as an edge crack imbedded in a uniform stress field of 3σ . The estimated K is then

$$K = 3.36 \sigma \sqrt{\pi a} \quad (3)$$

The general solution to this problem by Bowie [2,4] shows Eq 3 to be a reasonable approach for crack length to hole radius ratios, a/R , up to 0.10. At this point Eq 3 overestimates the actual stress intensity by 20 percent. For smaller a/R ratios the agreement becomes better.

The foregoing is intended to illustrate that in the linear elastic case a solution to a simple problem can be used to estimate stress intensities for a range of other problems including problems of general engineering interest. The next section presents an estimate of the J -integral for a finite crack in an infinite sheet subjected to general yielding. Hopefully, this procedure will yield useful estimates of J for problems of engineering interest where the extent of plasticity rules out linear elastic fracture mechanics.

Fully Plastic Case

Consider the cracked geometry shown in Fig. 1. Let us now assume the stress increases beyond the yield point. Plastic deformation spreads throughout the whole body. Since the crack is finite, its effect on the general flow field is negligible. One can speak of the problem as a crack imbedded in a uniform strain field.

The only characteristic parameters of the problem are the crack size and value of the strain, ϵ , at infinity. The stress may be related to the strain by an appropriate flow rule. The value of J must be expressed in terms of the crack size and strain value, the only characteristic parameters of the problem.

In the linear elastic realm of behavior J can be computed from the following

$$J = G = \frac{K^2}{E} = \frac{\sigma^2 \pi a}{E} \quad (4)$$

and $\sigma = \epsilon E$ where E is Young's modulus. Thus,

$$J = \epsilon^2 E \pi a \quad (5)$$

This expression is valid up to the onset of significant plastic deformation.

To estimate the functional dependence of J on ϵ in the plastic range, it is instructive to consider a problem solved by Rice [5]. Figure 3 shows an infinite plate of height, h . It is clamped at the edges and contains a semi-infinite crack. The solution for J is

$$J = W_{\infty} h \quad (6)$$

where W_{∞} is the strain energy density at infinity

$$W = \int_0^{\epsilon} \sigma d\epsilon \quad (7)$$

If one assumes a power hardening flow rule

$$\sigma = C_0 \epsilon^n \quad (8)$$

W becomes

$$W = \frac{C_0}{n+1} \epsilon^{n+1} \quad (9)$$

Thus,

$$J = \frac{C_0}{n+1} \epsilon^{n+1} h \quad (10)$$

Since, for most metals, n is in the range 0.05 to 0.2, J for this case is nearly a linear function of strain in the plastic range. In the linear elastic range J would be proportional to the strain squared. The assumption is now made that J for the fully plastic center cracked panel is a linear function of strain. This seems reasonable from the previous example and the fact that rigid plastic analyses of finite net section yielding problems give J as a linear function of displacement [1].

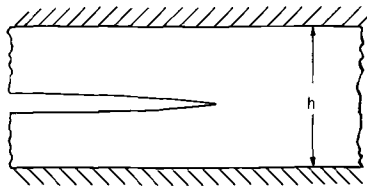


FIG. 3—Crack infinite strip with clamped edges.

With this assumption we can construct a plot of J versus uniform strain level. In the linear range

$$J = \epsilon^2 E \pi a \tag{11}$$

Beyond the yield strain, ϵ_y , J is a linear function of strain. Since J should be a continuous, well-behaved function of strain, the slope of J versus strain in the plastic range should be nearly equal to the elastic results at a strain equal to the yield strain. Thus, for a strain greater than the yield strain

$$J = \epsilon_y^2 E \pi a + (\epsilon - \epsilon_y) 2\epsilon_y E \pi a \tag{12}$$

This reduces to

$$J = E \pi a \epsilon_y (2\epsilon - \epsilon_y) \tag{13}$$

Naturally, for a strain level less than ϵ_y , J is given by Eq 11.

Equations 11 and 13 can be combined to give a graph of J versus strain. As shown in Fig. 4, the curve is a parabola in the linear elastic range. At the yield strain, a straight line is drawn tangent to the elastic curve.

As in the linear elastic case, the approximate fully plastic solution (Eq 13) to the infinite center cracked panel problem should be applicable to other problems. The requirement is made that the problem can be reasonably reduced to that of a crack in a uniform strain field.

Crack in a Plastic Zone

A Limiting Case Solution

Consider the case of a crack emanating from a stress riser such that the crack is small compared with the radius, R , of the stress riser and the

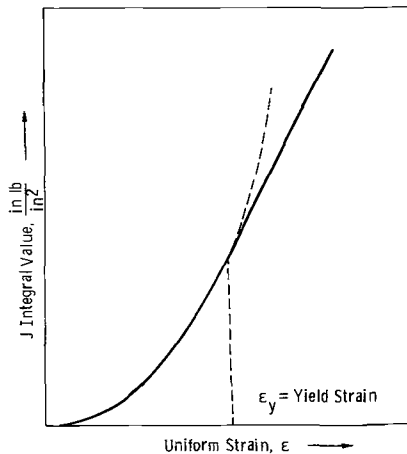


FIG. 4—Generalized plot of J versus strain for infinite center cracked panel.

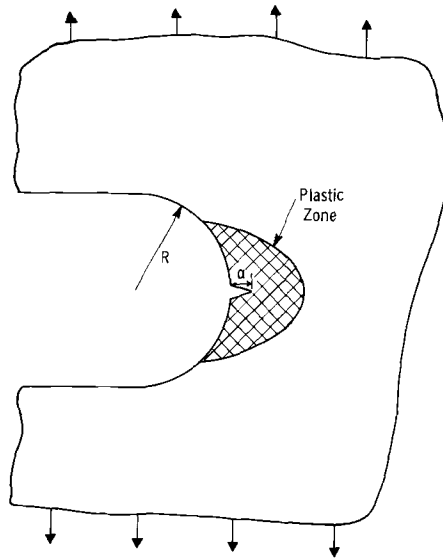


FIG. 5—Schematic of stress concentrator with plastic zone surrounding the crack.

stresses are high enough to cause the crack to be surrounded by a plastic zone, Fig. 5. Since this example is beyond the range of LEFM, it is appropriate to apply the J -integral. An accurate calculation of J for this problem would require a numerical solution to an elastic-plastic analysis. Applying the approximate fully plastic method to this problem leads to a limiting case solution.

To apply the method, a uniform strain field is required. Since the strain field may have a high gradient ahead of the stress riser this will be difficult to approximate. However, if a uniform strain field equal to the surface strain is assumed, the approximated value of J should always be an overestimate. In the limit as ratio of crack length to radius approaches zero, the approximate solution for J should approach one computed from an accurate stress-strain analysis.

To compute a value for surface strain, an elastic-plastic analysis is again needed. However, surface strain can also be estimated using the Neuber relation [6]

$$K_T^2 = K_\sigma K_\epsilon \quad (14)$$

All that is required to estimate surface strain is the elastic stress concentration factor for the particular stress riser, K_T , and a stress-strain curve for the material, Fig. 6. From these an estimate of the plastic stress concentration factor, K_σ , and plastic strain concentration factor, K_ϵ , can be obtained and surface strain can be calculated. Using the Neuber relation should

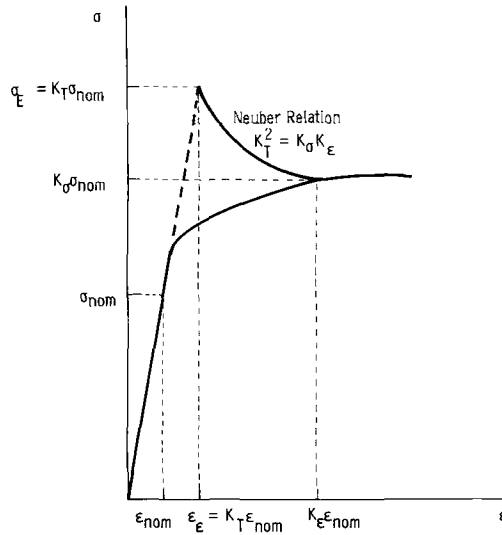


FIG. 6—Schematic of Neuber relation used to calculate surface strain.

introduce an additional conservatism because it tends to overestimate the plastic strain concentration, K_ϵ , for the case of plane strain.

Applying an additional constant of 1.12 to the elastic stress intensity factor for edge cracks, the expression for J from Eq 13 becomes

$$J = (1.12)^2 E \pi a \epsilon_y (2\epsilon - \epsilon_y) \tag{15}$$

where ϵ is the surface strain given by

$$\epsilon = K_\epsilon \epsilon_{nom} \tag{16}$$

Comparison with LEFM Extrapolations

This limiting case example can be compared with some techniques used to extrapolate LEFM to obtain estimates for the same problem of a crack in a plastic zone ahead of a stress riser. Two techniques from LEFM will be discussed.

One technique used to estimate K for this case is to assume that the stress in the plastic zone ahead of the stress riser is at yield point, σ_y . This stress can be used in the stress intensity expression to calculate a K value such that

$$K = K_y = 1.12 \sigma_y \sqrt{\pi a} \tag{17}$$

This can be converted to an energy value G by

$$G_y = \frac{K_y^2}{E} \tag{18}$$

A second technique used is to assume that the stress field is approximately the pseudo-elastic surface stress, σ_E , given by the elastic stress concentration factor K_T , Fig. 6. The stress intensity factor becomes

$$\begin{aligned} K &= K_E = 1.12\sigma_E\sqrt{\pi a} \\ &= 1.12K_T\sigma_{nom}\sqrt{\pi a} \end{aligned} \tag{19}$$

Again, this can be converted to G for comparison with J ,

$$G_E = \frac{K_E^2}{E} \tag{20}$$

The question of whether these values will be conservative can be explored schematically from Fig. 7 by comparing the estimated G values with J . Notice that the first technique of using K_y or G_y will never be conservative when surface stress or strain is above the yield point. It must be concluded that this method for estimating K values can be dangerously unconservative.

The second technique of using K_E or G_E is not so obviously unconservative, however, Fig. 7 shows that it may be unconservative. In the case illustrated the actual surface strain is assumed to be about twice the pseudo-elastic strain $\epsilon_E = K_T\epsilon_{nom}$. For this case the estimated J value is higher than the value of G_E .

This can be explored further by assuming a simple stress-strain relationship as given by the power hardening law to compute J values by the approximate fully plastic method.

$$\frac{\sigma}{\sigma_y} = \left(\frac{\epsilon}{\epsilon_y} \right)^n \tag{21}$$

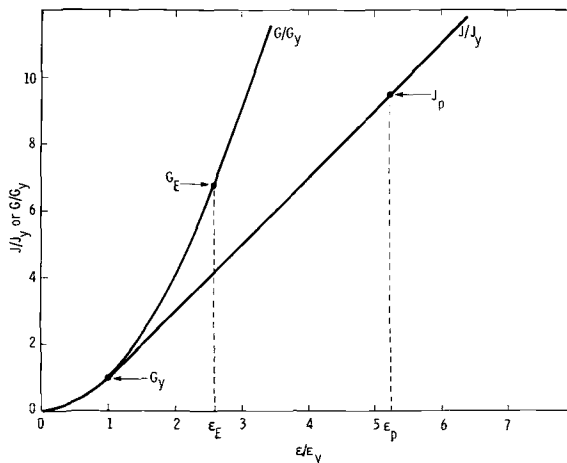


FIG. 7—Schematic of J and LEFM estimations.

where n is the strain hardening exponent. For this stress-strain law the Neuber relation gives

$$\frac{\sigma_E^2}{E} = \sigma \epsilon = \frac{\sigma_y}{\epsilon_y^n} \epsilon^{n+1} \quad (22)$$

Comparing the elastic value of G_E with the plastic estimate of J by taking a ratio gives

$$\begin{aligned} \frac{G_E}{J} &= \frac{K_E^2/E}{J} \\ &= \frac{(1.12)^2(\sigma_E^2/E)\pi a}{(1.12)^2 E \pi a \epsilon_y (2\epsilon - \epsilon_y)} \\ &= \frac{\left(\frac{\sigma_y}{\epsilon_y^n}\right) \epsilon^{n+1}}{E \epsilon_y (2\epsilon - \epsilon_y)} \\ &= \frac{(\epsilon/\epsilon_y)^{n+1}}{[2(\epsilon/\epsilon_y) - 1]} \end{aligned} \quad (23)$$

This result is plotted on Fig. 8 for various values of n . In all cases G_E/J starts from a value of 1 for elastic surface strain and becomes less than 1 as the surface strain becomes plastic. This would indicate that the LFM estimate used is unconservative. Notice that as the strain hardening exponent decreases this becomes more unconservative reaching a limit at $G_E/J \rightarrow 0.5$ for $n = 0$ and $\epsilon/\epsilon_y \rightarrow \infty$.

Since the assumptions used for estimating J in this example give an overestimate of J , the unconservatism is probably not so bad as it appears in Fig. 8. The Neuber relation tends to overestimate strain, hence J , for

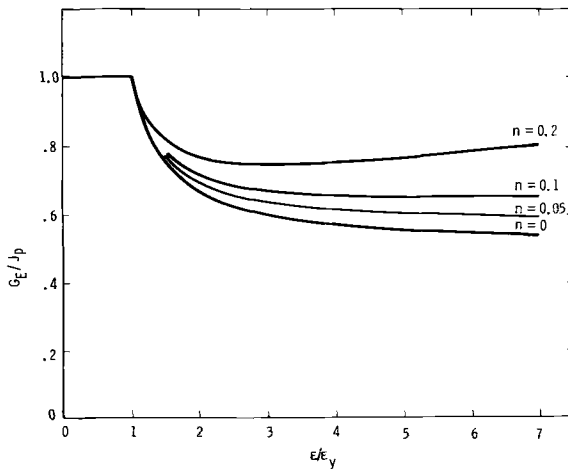


FIG. 8—Ratio of G_E/J versus surface strain.

the case of plane strain. For small ratios of crack length to radius of the stress riser the elastically calculated value of G_E and J calculated from surface strain may be close if the strain hardening exponent, n , is fairly high. For smaller values of n , calculated values of G_E may be significantly smaller than J values. For larger ratios of crack length to radius, calculation made with surface stress or strain may be too conservative since some average of the stress or strain gradient over the crack length may be more appropriate for the calculations. In this case the overconservatism may be great enough to actually penalize the application. In the following section results from a numerical elastic-plastic stress-strain analysis will be used to more accurately evaluate this example.

More Exact Elastic-Plastic Solution for Case of a Hole in a Plate

A very accurate and practical way of determining the strain distribution at a stress concentration as a function of applied load is by means of the finite element method [7]. By this numerical method, the strain history at a stress concentration can be found even in the nonlinear elastic-plastic regime. Existing finite element computer programs, applicable to an extremely wide variety of geometries and loading conditions, are generally available. By simply inputting the material properties, a finite element mesh to represent the structural geometry, and the loading conditions an elastic-plastic solution of acceptable accuracy can usually be obtained.

Once the maximum strain at the stress concentration is calculated as a function of load by means of a finite element computer program, then the critical size crack at any load level of concern can be calculated in the manner just described. To demonstrate this procedure a simple example is analyzed. A plate (Fig. 9) of finite width, $2W$, containing a centrally located circular hole of radius $R = W/7$ and subject to a uniaxial tensile load σ_0 is considered here. The stress-strain curve of the plate material

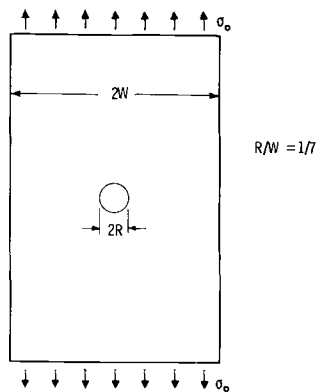


FIG. 9—Rectangular plate containing central circular hole and subject to a uniaxial tensile stress.

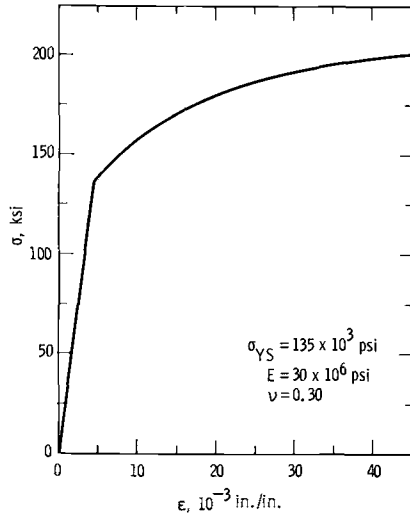


FIG. 10—Stress-strain curve for plate containing circular hole.

and some of the other material properties are shown in Fig. 10. While the material does not harden according to a power law relation, Eq 21, in the strain range of concern it has an effective hardening exponent of about $n = 0.15$.

The plane-strain elastic-plastic analysis of the plate was carried out using the finite element computer program developed by Visser, Gabrielse, and VanBuren [8]. The incremental plasticity program is based upon a linear strain triangular element. The finite element representation of one quarter of the plate is shown in Fig. 11. The quadrilateral elements each represent four triangular elements. The elastic-plastic numerical solution was obtained in incremental load steps up to a nominal stress to yield stress ratio of $\sigma_{nom}/\sigma_{YS} = 1.32$ where

$$\sigma_{nom} = \frac{\sigma_0}{[1 - (R/W)]} \tag{24}$$

The stress concentration factor

$$K_\sigma = \frac{\sigma_{max}}{\sigma_{nom}} \tag{25}$$

and the strain concentration factor

$$K_\epsilon = \frac{\epsilon_{max}}{\epsilon_{nom}} \tag{26}$$

where

$$\epsilon_{nom} = \frac{(1 - \nu^2)}{E} \sigma_n \tag{27}$$

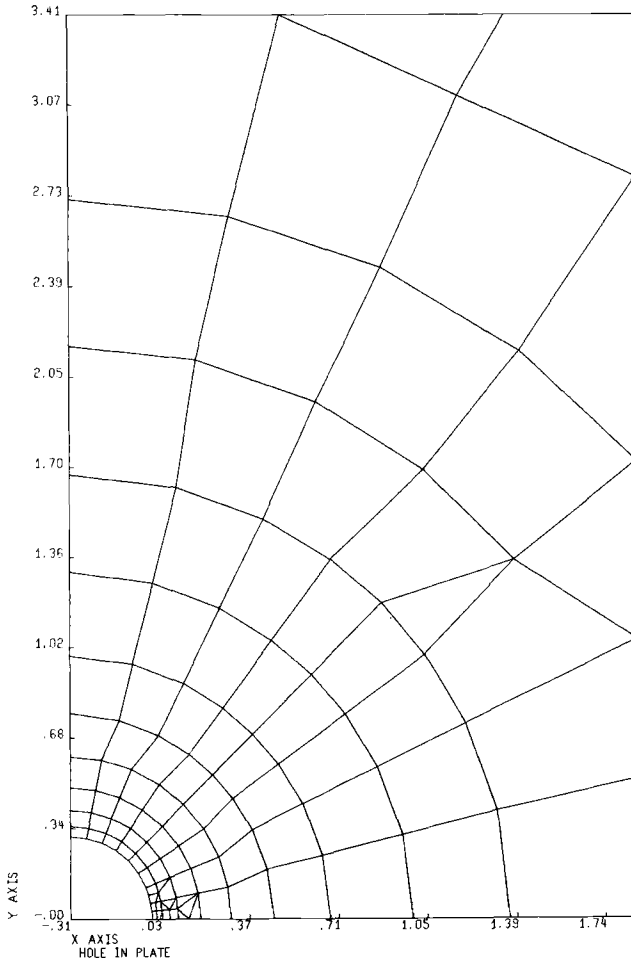


FIG. 11—*The finite element representation of one quarter of the plate.*

are shown in Fig. 12 as a function of applied load level. The elastic stress concentration factor, $K_t = 2.62$, calculated with this mesh differs from the value given by Peterson [9] for this case by 0.5 percent.

Also shown on Fig. 12 are the concentration factors which were calculated by means of Neuber's product rule (Eq 14) and the stress-strain curve of Fig. 10. Neuber's rule as used here is actually applicable to a plane stress condition. This is the reason for initial yield at a lower load level than that predicted by the finite element analysis and also one of the reasons for the higher strain than that calculated from the finite element method at equal load levels. Neuber's relation is also not capable of sensing gross section yielding and accounting for it. The Neuber strain concentration curve shows no sign of a rapid increase in magnitude as

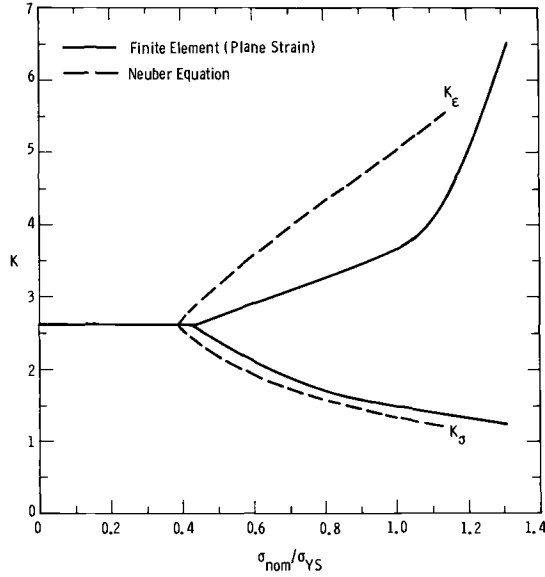


FIG. 12—Stress and strain concentration factors for plate containing circular hole ($R/W = 1/7$).

gross section yielding is reached, but the finite element curve does show the expected increase at a load level of approximately $\sigma_{nom}/\sigma_{YS} = 1.0$.

Once the elastic-plastic strain distributions have been determined then critical crack size can be estimated using the procedure described in the previous section. In the elastic-plastic regime the equation for critical crack size emanating from the hole at the point of maximum strain can be obtained from Eq 15.

$$a_{cr(p)} = \frac{(1 - \nu^2)J_{Ic}}{(1.12)^2 \pi E \epsilon_{YS}^2} \frac{1}{[2(\epsilon/\epsilon_{YS}) - 1]} \quad (28)$$

where ϵ is the maximum strain, which can be obtained from Fig. 12, and ϵ_{YS} is the yield strain under plane-strain conditions. An LEFM calculation of critical crack size can also be made

$$a_{cr(e)} = \frac{(1 - \nu^2)J_{Ic}}{(1.12)^2 \pi E \epsilon_{YS}^2} \left(\frac{\epsilon_{YS}}{\epsilon} \right)^2 \quad (29)$$

where the elastic relation between J and ϵ has been used and the strain ϵ is calculated elastically at the load of interest. In Fig. 13 the ratio of $a_{cr(p)}/a_{cr(e)}$ is shown as a function of load level, σ_n/σ_{YS} . As found in previous examples, the elastically calculated, critical crack size is larger than that calculated by means of elastic-plastic relations. For $\sigma_n/\sigma_{YS} < 1.0$, the difference is less than 6 percent with the elastic calculations being unconservative.

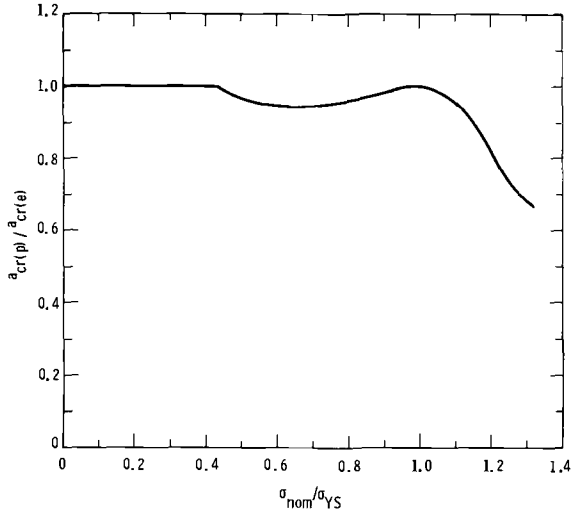


FIG. 13—Comparison of critical crack sizes calculated by linear elastic relations, $a_{cr(e)}$, with those calculated by means of an elastic-plastic analysis, $a_{cr(p)}$.

As σ_n/σ_{YS} increases beyond a value of 1.0 the elastic calculations become increasingly unconservative.

In the prior analysis, it was assumed that the critical crack size is small compared to the radius of the hole. Only the maximum strain was considered and the influence of the strain gradient was not considered. The effect of the strain gradient can be accounted for in an approximate manner by using some effective value of strain in Eq 28.

Conclusions

1. The simple method proposed for calculating the J-integral in a plastic field could be used to estimate J in components where a uniform strain field is approximated.
2. Attempts to extrapolate LEFM to account for plasticity effects may lead to unconservative estimates of fracture values.

References

- [1] Bucci, R. J., Paris, P. C., Landes, J. D., and Rice, J. R., in *Fracture Toughness, Part II, ASTM STP 514*, American Society for Testing and Materials, 1972, pp. 40-69.
- [2] Paris, P. C. and Sih, G. C. in *Fracture Toughness Testing and Its Applications, ASTM STP 381*, American Society for Testing and Materials, 1966, pp. 30-83.
- [3] Brown, W. F., Jr. and Srawley, J. E., *Plane Strain Crack Toughness Testing of High Strength Metallic Materials, ASTM STP 410*, American Society for Testing and Materials, 1966.
- [4] Bowie, O. L., "Analysis of an Infinite Plate Containing Radial Cracks Originating from the Boundary of an Internal Circular Hole," *Journal of Mathematics and Physics*, Vol. 35, 1956.

- [5] Rice, J. R., "A Path Independent Integral and the Approximate Analysis of Strain Concentration by Notches and Cracks," *Journal of Applied Mechanics, Transactions, American Society of Mechanical Engineers*, June 1968.
- [6] Neuber, H., "Theoretical Determination of Fatigue Strength at Stress Concentrations," Technical Report AFML-TR-68-20, Wright-Patterson Air Force Base, Ohio, 1968.
- [7] Zienkiewicz, O. C. and Cheung, Y. K., *The Finite Element Method in Structural and Continuum Mechanics*, McGraw-Hill, New York, 1967.
- [8] Visser, C., Gabrielse, S. E., and VanBuren, W., "A Two Dimensional Elastic-Plastic Analysis of Fracture Test Specimens," HSST Technical Report No. 4, Oak Ridge National Laboratory, 1970.
- [9] Peterson, R. E., *Stress Concentration Design Factors*, Wiley, New York, 1953.

Test Results from J-Integral Studies: An Attempt to Establish a J_{Ic} Testing Procedure

REFERENCE: Landes, J. D. and Begley, J. A., "Test Results from J-Integral Studies: An Attempt to Establish a J_{Ic} Testing Procedure," *Fracture Analysis, ASTM STP 560*, American Society for Testing and Materials, 1974, pp. 170-186.

ABSTRACT: Test results from J_{Ic} studies are analyzed by a resistance curve technique. J values from bend type specimens containing a deep precrack are plotted as a function of crack extension measured from the specimen fracture surface. Using these plots a technique is suggested for establishing a J_{Ic} measurement point.

Data from an A216 steel are presented for describing this method of J_{Ic} analysis. In addition, J_{Ic} versus temperature data are presented to compare J_{Ic} with previous K_{Ic} results. Finally, a step-by-step procedure for measuring J_{Ic} is outlined.

KEY WORDS: fractures (materials), mechanical properties, tests, elastic-plastic cracking (fracturing), fracture tests, fracture properties

The J-integral proposed by Rice [1]² as an analytical tool for elastic-plastic crack tip field analysis has been successfully used by Begley and Landes [2,3] as an elastic-plastic fracture criterion. The J-integral was first measured from experimental load versus load point displacement curves using a compliance technique where several specimens of varying crack lengths were needed [2,3]. Methods were later developed for measuring J from single specimen tests [4,5]. The method developed by Rice [5] for measuring J on deeply notched, bend type specimens offered the simplest single specimen technique for measuring J . For this technique a bend type specimen, bend bar, or compact tension specimen with a deep crack ($a/W \geq 0.6$) is loaded to the displacement of interest and J is determined as a function of displacement from the expression

$$J = \frac{2A}{Bb} \quad (1)$$

where A is the area under the load-displacement curve taken at the displacement of interest, B is the thickness, and b is the uncracked ligament.

¹ Senior engineers, Mechanics Department, Westinghouse Research Laboratories, Pittsburgh, Pa. 15235.

² The italic numbers in brackets refer to the list of references appended to this paper.

Critical values of J were labeled J_{Ic} and taken when crack extension was first encountered. This method for determining a critical J value was patterned after the K_{Ic} measurement technique where 2 percent crack growth was set as the measurement point (see Ref 6 and ASTM Test for Plane-Strain Fracture Toughness of Metallic Materials (E 399-72)). The measurement point for J_{Ic} has never been precisely defined. The question of whether this measurement point should be relative to specimen size as in the case of K_{Ic} , or be absolute depending on the capability of instrumentation was left to the discretion of the individual investigator. If a J_{Ic} test is to be used as a measurement of material fracture toughness, a standard procedure must be established. The most difficult problem in establishing a standard procedure appears to be the question of where to take the measurement point for J_{Ic} .

A possible aid in solving the problem of picking a measurement point may come from presenting the J data in the form of a resistance (R) curve. Linear elastic fracture data can be presented in this form where G , energy per unit area available for crack extension, or K is plotted against crack length or crack extension [7]. The K_{Ic} value is then simply one point on the R -curve. A similar R -curve plot for elastic-plastic data, plotting J versus crack extension, may be of help in determining a measurement point for J_{Ic} .

In this paper, test data from an A216 steel are presented. Extensive tests were conducted on this material in the hope of answering several questions about the J_{Ic} fracture criterion. The most important question is that of the measurement point for J_{Ic} . The data was collected and analyzed in a manner that a J resistance curve could be constructed. From this curve, a method for establishing a J_{Ic} measurement point is discussed. Using this method for measuring J_{Ic} , a tentative test procedure is presented.

Other questions which have been studied in this work are those of specimen size requirements for J_{Ic} testing and the equivalence of J_{Ic} and K_{Ic} values. To study the effect of specimen size on J_{Ic} values, specimens ranging from 1/2-in.-square bend bars to 4T-CT compact tension specimens were tested. To study the equivalence of J_{Ic} and K_{Ic} values, tests were conducted over a range of temperatures. These temperatures started well below FATT where fracture occurred completely by cleavage and increased through the fracture mode transition range until fracture occurred completely by dimpled rupture. Results from K_{Ic} tests in part of this temperature range were then compared with the J_{Ic} results.

Test Program

Material and Specimens

The material tested was an ASTM A216 WCC Grade cast steel, Heat 4394, which is a relatively low strength, high toughness material. Material

TABLE 1—Material properties for A216 WCC grade cast steel—heat 4394 [8].

<i>Chemistry</i>									
C	Mn	Si	P	S	Ni	Cr	Mo	Al	Cu
0.24	1.18	0.45	0.008	0.011	0.28	0.16	0.03	0.044	0.09
<i>Heat Treatment</i>									
Foundry Anneal				1600°F—8 h, furnace cool to 600°F					
Burn Stress				1125°F—8 h, furnace cool to 600°F					
Normalize				1750°F—8 h, decrease to 1650°F, water quench					
Temper				1200°F—8 h, air cool					
<i>Mechanical Properties (75°F unless noted)</i>									
Yield, ksi	Ultimate, ksi	Elongation, %	Reduction of Area, %	K_{Ic} (0°F), ksi $\sqrt{\text{in.}}$	FATT				
44	74	16	34	77	100°F				

chemistry, heat treatment, and mechanical properties are presented in Table 1 [8].

All of the specimens tested were of the bend type, 3-point bend bars, and compact tension specimens. A range of sizes were included. The 3-point bend bars included $\frac{1}{2}$ by $\frac{1}{2}$ in. and 1 by 2 in., the 1-in. dimension being the specimen thickness. Note that a 1 by 2-in. bend bar is the same dimension as a 1T compact tension specimen. The compact tension specimens included 1T, 2T, 3T, and 4T sizes. For the 1T-CT, a modification was made so that displacement could be measured on the specimen loadline. This is shown in Fig. 1. For the larger compact tension specimens, displacement was measured across the loading clevises.

All specimens were prepared with deep notches, $a/W \approx 0.6$, and were precracked prior to testing. Precracking loads were less than half the specimen limit load or K_{max} was less than $36 \text{ ksi } \sqrt{\text{in.}}$.

Experimental Procedure

Specimens were tested in a universal testing machine where loading displacement was controlled. Load versus load point displacement was measured and monitored on an X-Y recorder. For the compact tension specimens load versus load line displacement was monitored. Specimens of identical crack length were loaded to the desired displacement and then unloaded. An attempt was made to unload one specimen before crack extension began and unload several others after various amounts of crack extension. This is shown schematically in Fig. 2. (Displacement values for unloading were generally chosen by selecting a value of J for unloading before the test. Loading rates were kept sufficiently slow so that J could be instantaneously estimated from Eq 1 during the test.)

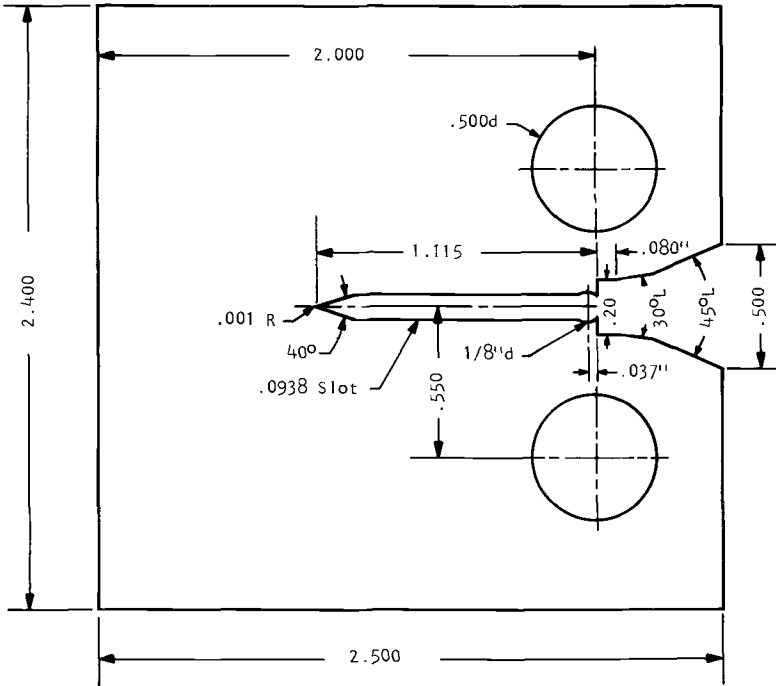


FIG. 1—IT compact J_{Ic} specimen for measuring load line displacement.

After unloading, crack extension was marked by heat tinting the crack. Heat tinting was done by heating the specimen to 600°F and holding it at temperature for 10 min. (Note: In cases where heat tinting is impractical, the crack could be marked by an alternate technique, for example, fatigue marking.) Specimens were subsequently broken open so that the fracture surface could be examined.

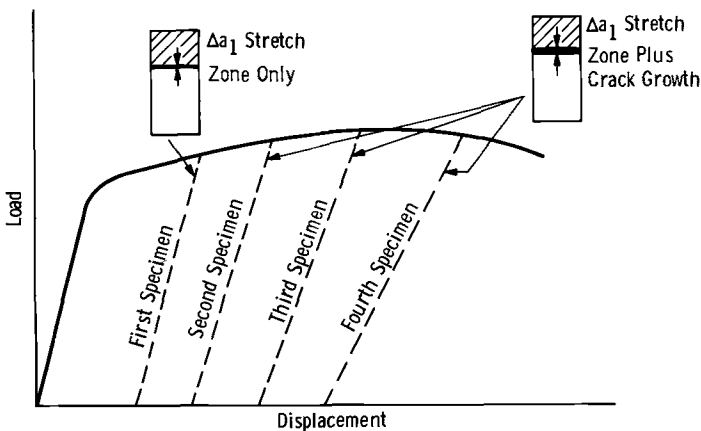


FIG. 2—Load-displacement schematic showing unloading points for various specimens.

Measurement of crack extension was made on the fracture surface. Crack extension was taken to be the maximum distance from the pre-fatigue mark to the end of the heat tint mark. Maximum extension generally occurred about mid-thickness. The heat tinting technique displayed the crack extension very clearly, Fig. 3a. Crack extension seemed to have a dual character which made the analysis somewhat difficult. The first part of the crack extension had the appearance of a stretch zone. This part of the extension was assumed to be associated with "crack opening stretch" (COS) and was primarily a crack front geometry change rather than actual material separation. The second part of the crack extension appeared to be actual material separation associated with an advancing crack front. The two types of crack extension could be distinguished by looking at a side profile of the crack, Fig. 3b. The stretch zone region appeared to be

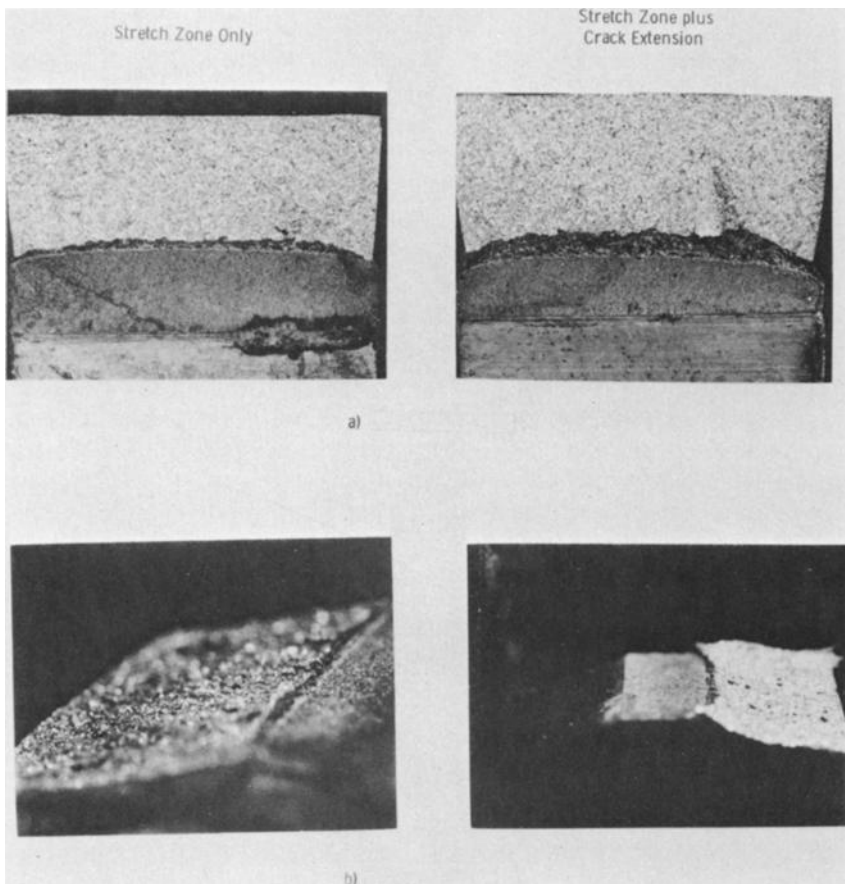


FIG. 3—Fracture appearance of A216 steel J_{1c} specimens. (a) Fracture surface, and (b) fracture profile.

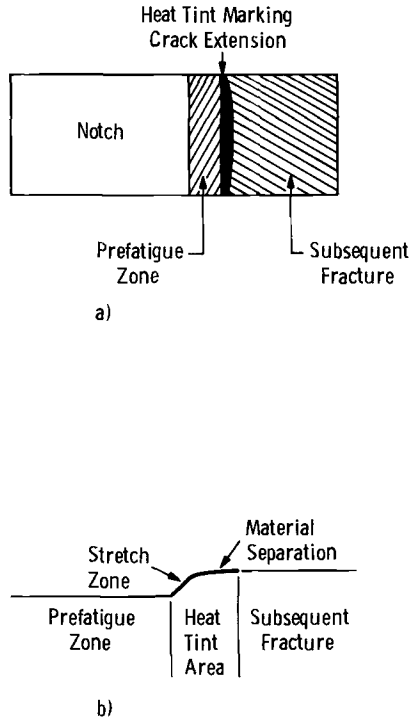


FIG. 4—Fracture appearance of J_{1c} specimen. (a) Fracture surface, and (b) fracture profile.

at an angle of approximately 45 deg whereas the actual material separation appeared to be nearly flat. This is shown schematically in Figs. 4a and b. The crack profile then appeared to have two flat regions which were on different planes, the prefatigue region being flat and on one plane while the crack growth region was flat and on a separate plane. The two planes were connected by an angled region, the stretch zone, Fig. 4b. The difficulty in analysis was caused by the fact that the transition between the stretch zone and the material separation region were not always clearly defined. This caused some problem in deciding where to take the measurement point. The crack extension was, therefore, taken to be the total of the two regions measured horizontally from the prefatigue line. The method of analysis used for dealing with this problem is discussed in the next section.

The test temperature was controlled to within $\pm 2^\circ\text{F}$.

Analysis Techniques

The data was analyzed by plotting the value of J as a function of crack extension. The J value calculated by Eq 1 does not give an exact J value for the case of an advancing crack. J should always be overestimated as a result of the area under the load displacement curve being overestimated.

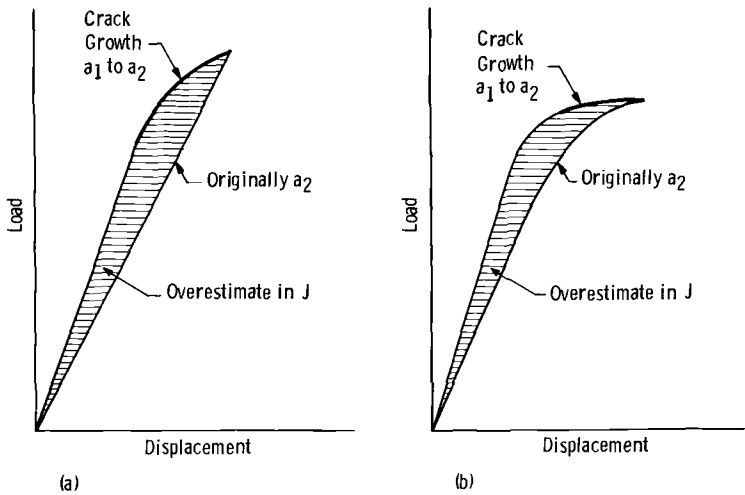


FIG. 5—Schematic showing error in measuring J caused by slow crack growth. (a) Non-linear curve due only to crack growth, and (b) non-linear curve due to both crack growth and plasticity.

This is shown schematically in Fig. 5. Consider the case where the non-linear part of the load displacement curve is caused only by crack extension (no plastic deformation), Fig. 5a. The non-linear curve has an original crack length of a_1 . On loading to the point shown, assume that the crack extends to length a_2 . The actual J value corresponding to the displacement shown at crack length a_2 should be a function of the area under the linear curve in Eq 1. The calculated value of J will correspond to the area under the non-linear curve. The area between these two curves is a measure of the overestimate in J . Figure 5b shows the same problem for the case where nonlinearity is caused by crack growth and plasticity. The curve on the left has the advancing crack and is originally steeper with more non-linearity at higher load. The curve at the right shows what the curve should be with no crack extension. Hence, the area under this curve corresponds to the actual J value, and the area between the curves corresponds to the overestimate in J . Notice that this overestimate should increase with increasing crack extension.

In addition, the problem of unloading associated with slow-stable crack extension causes problems with the calculation of an exact J . The analytical definition of the J -integral was for deformation theory of plasticity and did allow for unloading [1]. However, the problems associated with calculating J during slow-crack advance are not important to the technique present here for calculating J_{Ic} . As will be shown later, these inexact values of J are used only for extrapolation purposes.

The data can be plotted in the form of an R-curve by plotting J versus measured crack extension. An estimate of how this should look is shown

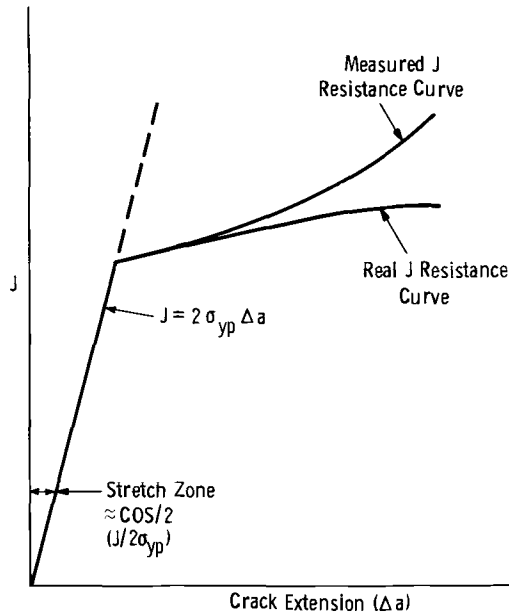


FIG. 6—Schematic of J resistance curve.

schematically in Fig. 6. Before any actual crack extension due to material separation occurs, there should be an apparent crack extension caused by the stretch zone formation. Assuming that the stretch zone is approximately half of the COS and that $\text{COS} \approx J/\sigma_{yp}$, where σ_{yp} is the yield stress, the curve should follow a straight line $J = (2\sigma_{yp})(\Delta a)$ where Δa is the crack extension. As crack extension occurs due to material separation, the actual R-curve should probably have a shallow slope with a slight concave downward appearance. However, since J is increasingly overestimated with increasing crack extension, the actual plotted curve may be less shallow with a slight concave upward appearance.

The plot of J versus crack extension is shown in Fig. 7 for the 2T, 3T, and 4T compact tension specimens. For the specimens tested at low J values, the points fall along the stretch zone line. At higher values of J , the points appear to fall along a curve that is concave upward; however the scatter in the data is large enough so that this cannot be exactly determined. Data plotted in a similar manner from the 1T compact tension specimens and the bend bars is shown in Fig. 8.

J_{Ic} Measurement Point

Plotting the data in the form of an R-curve gives more information than a single J_{Ic} value. In many cases this may be sufficient for material evaluation. However, there are other cases where a J_{Ic} value may be desired.

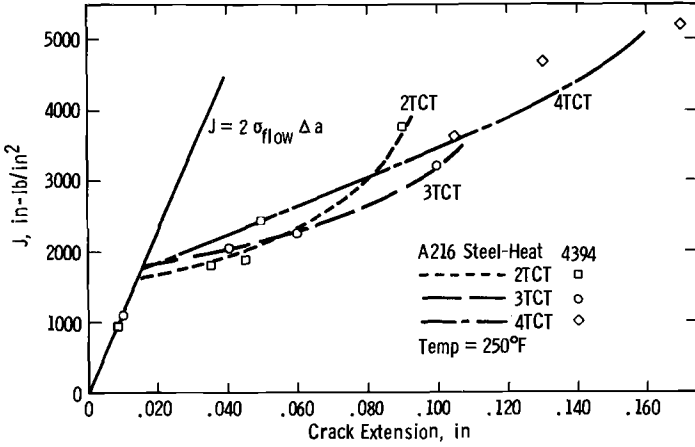


FIG. 7—J versus crack extension for larger specimens of A216 steel.

Such would be the case where a structural reliability analysis is being performed or where K_{Ic} is being estimated from a subsize specimen test. The following proposal for establishing a measurement point is given only as a suggestion and may be altered in the future.

To establish a J_{Ic} measurement point it is desirable to pick a point where crack extension has taken place by actual material separation rather than by crack front geometry change. Many points could be considered. One question is whether to take a relative amount of crack extension as in the K_{Ic} test or an absolute amount of crack extension. From Figs. 7 and 8 it

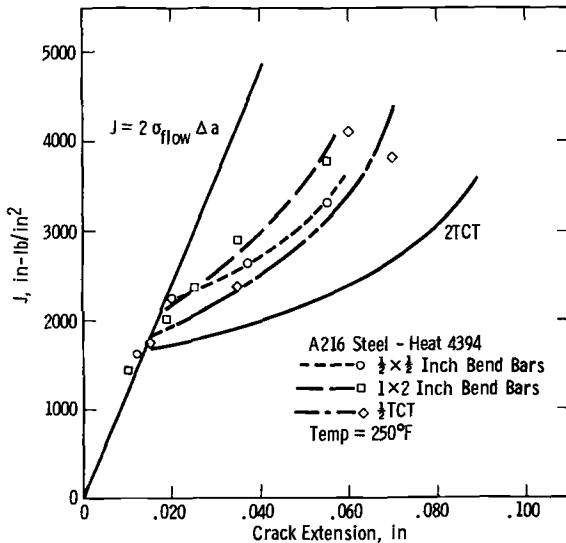


FIG. 8—J versus crack extension for smaller specimens of A216 steel.

can be seen that a measurement point taken relative to specimen size would give an artificial size effect on J_{Ic} values. It is therefore concluded that an absolute measure of crack extension is more desirable. Picking an absolute value of crack extension for all materials can cause problems. A value chosen conveniently for a low toughness material may be hard to distinguish from the stretch zone in a high toughness material. Therefore, a value of crack extension which is relative to material toughness but absolute in terms of specimen size would be most desirable. An obvious point would be where the curve from crack extension intersects the stretch zone line ($J = 2\sigma_{yp}\Delta a$). This point has several drawbacks. At this point no actual crack extension due to material separation has occurred. Also the stretch zone may not develop strictly as a function of $J/2\sigma_{yp}$. Estimates of COS have been written in the form

$$\text{COS} = C_1 G / \sigma_{yp} = C_1 J / \sigma_{yp} \quad (2)$$

where the constant C_1 has been estimated to range from $\pi/4$ to greater than two. However, recent work has shown experimentally that C_1 is very nearly one [9]. Despite these objections, this point appears to be the best choice for a J_{Ic} measurement point in the A216 results, Figs. 7 and 8. For this case the stretch zone line was taken to be $J = 2\sigma_{flow}\Delta a$ where σ_{flow} was a stress taken half way between yield stress and ultimate stress. This help accounts for cases where there is a high strain hardening exponent. The J_{Ic} measurement point was taken where a best fit line to the crack extension points intersected the line $J = 2\sigma_{flow}\Delta a$. Using this technique J_{Ic} values were calculated for each specimen size and are given in Table 2.

TABLE 2— J_{Ic} at 250°F for different specimen sizes, A216 steel.

Specimen	J_{Ic} (in.·lb/in. ²)
1/2 by 1/2 in. bend bars	2150
1 by 2 in. bend bars	2000
1T CT	1800
2T CT	1600
3T CT	1750
4T CT	1650

Discussion

The values of J_{Ic} measured from six different specimen sizes show a fair degree of consistency, Table 2. The measurement point described may be subject to future reevaluation and certainly cannot be accurately set by the study of one material. However, for the A216 steel this measurement point appears to be the best possible choice. Crack extension due to material separation is about to occur or has already taken place to some small degree at this point. A measurement point taken earlier would

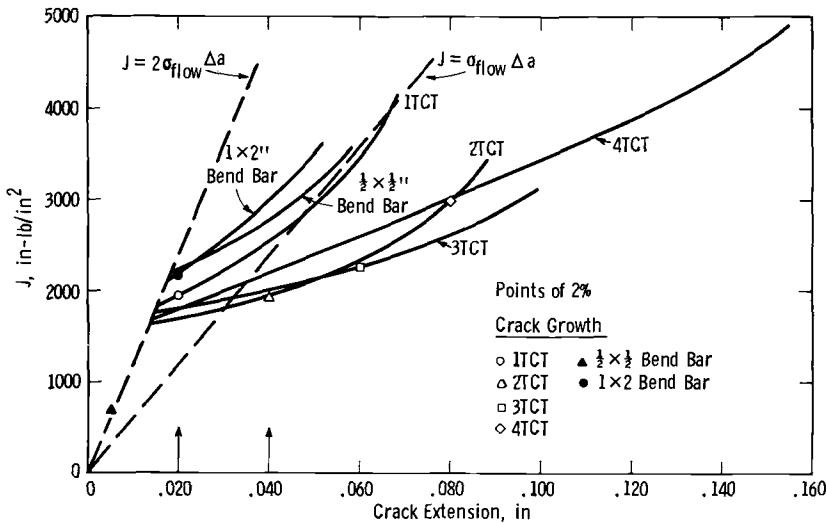


FIG. 9— J versus crack extension showing various methods for taking a measurement point.

measure J_{Ic} for a crack front geometry change only. A measurement point taken later would introduce specimen size effects artificially.

The result of choosing a different measurement point is shown in Fig. 9. The fitted lines from all the data are shown here and various measurement points are considered. Results from these are shown in Table 3. The measurement point used in K_{Ic} testing is 2 percent crack growth. These points are marked in Fig. 9. It is obvious that this method would introduce a large specimen size effect. This criterion may be responsible for some of the size effect encountered in K_{Ic} testing. Another method considered was to take twice the stretch zone value for crack extension. This is given by the intersection of the line $J = \sigma_{flow} \Delta a$ and the fitted curves. Taking this amount of crack extension again introduces a specimen size effect. Another possibility would be to an absolute measure of crack extension. Two values are considered, 0.020 in. and 0.040 in. The 0.02-in. criterion gives a fairly consistent J_{Ic} value whereas the 0.040-in. criterion give a size effect scatter.

TABLE 3— J values obtained from various measurement points A216 steel at 250°F J (in.·lb/in.²).

Specimen	2% Crack Growth	$J = \sigma_{flow} \Delta a$ Intersection	0.020 in. Growth	0.040 in. Growth
1/2 by 1/2 in. bend bar	700	3500	2250	2750
1 by 2 in. bend bar	2150	...	2150	3000
1T CT	1950	2800	1950	2550
2T CT	1900	1800	1700	1950
3T CT	2250	2000	1850	2150
4T CT	3000	2100	1800	2200

Establishing an absolute measurement point such as this for all materials would indeed be difficult at this time.

The method used there for measuring J_{Ic} may have some drawbacks. To construct a resistance type curve for calculating a single J_{Ic} value takes more specimens and more test steps than a K_{Ic} test. It may appear easier to instrument the specimen in some way so that crack initiation can be determined and J_{Ic} measured from a single specimen. Several methods of instrumentation were attempted with this hope. They included ultrasonics, acoustic emission, an electrical potential system, and multiple displacement gages on the specimen. In all cases it was concluded that whenever large-scale plasticity occurs in the specimen the effects of material deformation are often indistinguishable from first crack advance. Thus, the success of using a single instrumented specimen to determine J_{Ic} could depend on the skill of the investigator in interpreting instrument signals and also on the way a particular material responds to a given transducer.

The method described in this paper for measuring J_{Ic} does not require any complicated analysis or sophisticated instrumentation. The equipment needed is virtually the same as that needed for a K_{Ic} test. The actual testing will take longer since there are more specimens and more steps per specimen than in a K_{Ic} test. However, all of the steps are relatively simple and do not require judgment on the part of the investigator. The method described here is only a first attempt at establishing a uniform test method. Individual steps may be altered or more precisely defined in the future as more tests are conducted by this method.

Size Effect

The effect of specimen size on J_{Ic} does not appear to be very great for the A216 steel. Although there is a definite size effect on the J versus crack extension curves in Figs. 7 and 8, this could be due mainly to the overestimation effect shown in Figs. 5 and 6. This overestimation would certainly be specimen size dependent. Taking a J_{Ic} measurement point as described appears to eliminate this type of size effect. The real concern is that the specimen may be so small that J no longer characterizes the crack-tip field. From Table 2 it can be seen that the smaller specimens do give a slightly higher J_{Ic} value. However, this difference is small enough that any size effect cannot be distinguished from normal variations due to material difference or testing technique.

Previously, a specimen size requirement had been recommended as follows

$$a, B, b \geq \alpha J_{Ic} / \sigma_{flow} \quad (3)$$

where α was assumed to be between 25 and 50. Taking J_{Ic} to be 2000 in.·lb/in.² from these test results and α to be 25 would give a specimen

size requirement of 0.85 in. (1.70 in. for $\alpha = 50$). For the specimens used here the 1T CT and 1 by 2-in. bend bars would be the smallest specimens to meet the size requirement. The J_{Ic} value from the smaller specimen may then show a slight increase due to a size effect. Certainly, results for different materials are needed to do a more thorough evaluation of specimen size effect on J_{Ic} . It is realistic, however, to assume that there will be a specimen effect as the critical dimensions become smaller. To be safe a limit should be temporarily established. To date, all J_{Ic} results appeared to be consistent whenever α was 25 or greater. Therefore, a value of $\alpha = 25$ will be used in setting a specimen dimension size requirement.

Fracture Toughness Versus Temperature

The well-known temperature dependence of the plane-strain fracture toughness of low to intermediate strength steels leads to practical difficulties in characterizing this toughness by means of linear elastic K_{Ic} tests. Beyond the lower shelf temperature range very large sections must be tested. These tests are expensive and very often test material is unavailable in the required size. J_{Ic} tests permit the characterization of fracture toughness over any desired temperature range with relatively small inexpensive specimens. The rationale of the J_{Ic} fracture criterion results in a direct correspondence between J_{Ic} and K_{Ic} [2,3].

$$J_{Ic} = G_{Ic} = \frac{1 - \nu^2}{E} K_{Ic}^2 \quad (4)$$

To illustrate Eq 4, plane-strain J_{Ic} fracture toughness tests were performed from -150°F to $+250^\circ\text{F}$ using ASTM Grade A216-C steel. J_{Ic} values were determined from one inch thick compact tension specimens. The J_{Ic} values were converted to K_{Ic} numbers using Eq 4. These converted values are plotted in Fig. 10 along with valid K_{Ic} test results from another investigation [8]. Specimens up to 12-in. thick were used for the K_{Ic} tests.

The agreement between the results of the J_{Ic} tests and valid K_{Ic} values is considered to be very good. However, there are several points which must be discussed. For J_{Ic} tests below room temperature, results are plotted for specimens which failed by 100 percent cleavage. In this case there is no ambiguity regarding the J_{Ic} measurement point. At room temperature and 250°F , J_{Ic} values were determined by the method proposed earlier in the paper.

The most important point regarding the comparison of valid K_{Ic} values and those derived from J_{Ic} tests is the scatter and high values in the J_{Ic} data. This occurrence is logical considering the property variability of the casting steel and the relative sampling size of J_{Ic} and K_{Ic} test specimens.

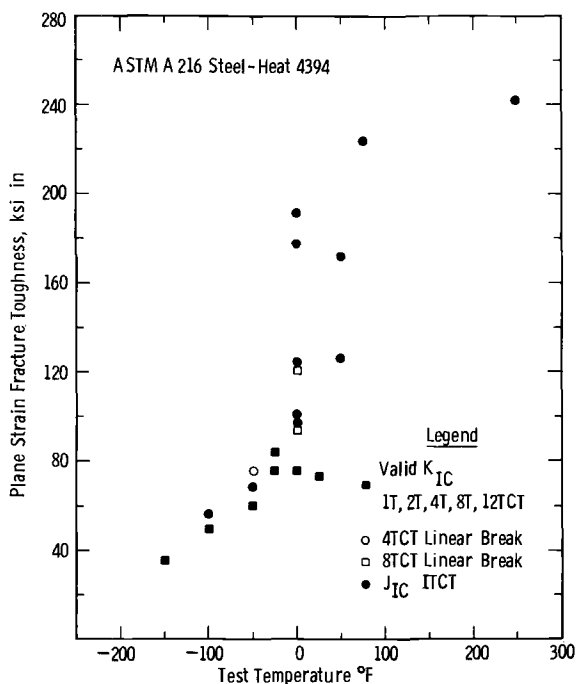


FIG. 10—Fracture toughness versus test temperature.

For example, the K_{Ic} values at 0 and 25°F were determined with 12-in.-thick specimens. The crack tip leading edge thus sampled 12 times the property controlling near tip volume of the 1-in.-thick J_{Ic} specimens. Since a weakest-link analogy is appropriate for cleavage fracture the 12-in.-thick K_{Ic} sample would be expected to fail close to the lowest value of 12 J_{Ic} tests. In general, the smaller test specimens will be more likely to be entirely composed of tough material while larger specimens will be more likely to contain a low toughness region and thus exhibit a relatively low K_{Ic} or J_{Ic} value. As shown by the data, occasionally a small sample will contain a low toughness region giving a low test value. Clearly, as the specimen size decreases, more tests must be performed to determine lower bound properties. The tendency for J_{Ic} values to lie somewhat above the K_{Ic} curve is interpreted as a Weibull type phenomena.

Tentative J_{Ic} Test Method

The following is a recommended procedure for a tentative J_{Ic} uniform test method. As mentioned before this is merely a first attempt at a procedure and represents only the current state of the art. The test method is presented in outline form so that individual steps can be easily identified. Figure 11 provides a schematic of test and analysis steps.

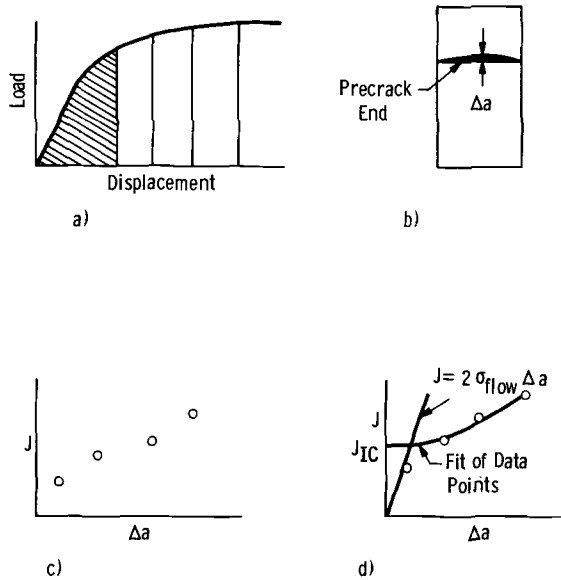


FIG. 11—Procedure for J_{IC} measurement. (a) Load specimens to various displacements, (b) measure crack extension, (c) calculate J for each specimen and plot versus Δa , and (d) construct two curves for J_{IC} measurement.

Specimens

1. A bend type specimen is needed. This includes 3- or 4-point bend bars, compact tension specimens, or WOL specimens.
2. The specimen should be deeply notched with $a/W \geq 0.6$.
3. All specimens should be precracked in fatigue with maximum loads less than half of the expected specimen limit load and $K_{max}/E < 0.002 \text{ in.}^{1/2}$.
4. Four to six specimens with identical crack lengths should be prepared.

Testing Equipment

1. Testing machine with a load monitor.
2. A load point displacement monitor.
3. An X-Y recorder for plotting load versus load point displacement.
4. A crack tip marking facility.
5. A crack extension measurement facility. (This can often be as simple as a scale and a magnifying glass.)

Testing Procedure

1. Load each specimen to different displacement values using displacement control if possible, Fig. 11a. (It is desirable to load one specimen to a point where no actual crack extension has occurred and the others to different amounts of crack extension. It may be difficult to determine this

prior to testing; however if specimens are loaded individually and each fracture surface examined before the next specimen is loaded, this can easily be done.)

2. Unload each specimen and mark the crack. (Heat tinting is an easy way to mark the crack for steel. For other materials a dye penetrant or a fatigue mark could be used.)

3. Pull the specimen apart and measure crack extension. The crack extension should be measured at its maximum point and taken to include all crack extension from the fatigue precrack to the end of the mark, Fig. 11b.

Data Analysis

1. Calculate J values from the load versus load point displacement record using $J = 2A/bB$, where A is the area under the curve up to the point of unloading (Fig. 11a), b is the uncracked ligament measured from the end of the fatigue crack, and B is specimen thickness. (Note: In measuring area under the curve do not subtract out the area due to elastic unloading. The right-hand side of the area measured should be a vertical line at the unloading displacement.)

2. Plot J versus crack extension, Fig. 11c.

3. Construct the line $J = 2\sigma_{\text{flow}}\Delta a$ (Fig. 11d). (σ_{flow} can be taken halfway between yield and ultimate stresses.)

4. Draw best fit line to the J versus crack extension points, Fig. 11d. Include only the points where actual crack extension has occurred. Where crack extension appears only as a stretch zone the point should fall along the line $J = 2\sigma_{\text{flow}}\Delta a$.

5. Mark J_{Ic} at the intersection of the lines constructed in Steps 3 and 4, Fig. 11d.

Specimen Size Analysis

1. Calculate J/σ_{flow} .

2. Compare specimen dimensions, a , B , b with J/σ_{flow} ($\alpha = \text{dimension}/J/\sigma_{\text{flow}}$).

3. α should be greater than 25 for a valid specimen size.

This procedure is recommended to anyone interested in doing J_{Ic} testing. It is likely that individual steps will have to be altered, expended or clarified. This can only be done as more test results are acquired. It is suggested that questions which arise over the use of this procedure be promptly addressed to the authors.

Conclusions

1. By evaluating J-integral test results in the form of a resistance curve a simple method for determining a J_{Ic} measurement point is defined.

J_{Ic} is taken as the intersection between a stretch zone line ($J = 2\sigma_{flow}\Delta a$) and a fitted curve to the J versus crack extension points.

2. A tentative test procedure is presented.

3. Results of J_{Ic} versus temperature are compared with previous K_{Ic} data and show good agreement.

Acknowledgment

The authors gratefully acknowledge the contributions of A. R. Petrush of the Mechanics Department and R. B. Stouffer of the Materials Testing and Evaluation Laboratory to various phases of the experimental program.

References

- [1] Rice, J. R., *Journal of Applied Mechanics, Transactions, American Society of Mechanical Engineers*, Vol. 35, June 1968, pp. 379–386.
- [2] Begley, J. A. and Landes, J. D. in *Fracture Toughness, ASTM STP 514*, American Society for Testing and Materials, 1972, pp. 1–20.
- [3] Landes, J. D. and Begley, J. A. in *Fracture Toughness, ASTM STP 514*, American Society for Testing and Materials, 1972, pp. 24–39.
- [4] Bucci, R. J., Paris, P. C., Landes, J. D., and Rice, J. D. in *Fracture Toughness, ASTM STP 514*, American Society for Testing and Materials, 1972, pp. 40–69.
- [5] Rice, J. R., Paris, P. C., and Merkle, J. G. in *Progress in Flow Growth and Fracture Toughness Testing, ASTM STP 536*, American Society for Testing and Materials, 1973, pp. 231–245.
- [6] Brown, W. F., Jr. and Srawley, J. E., *Plane Strain Crack Toughness Testing of High Strength Metallic Materials, ASTM STP 410*, American Society for Testing and Materials, 1966.
- [7] *Fracture Toughness Evaluation by R-Curve Methods, ASTM STP 527*, American Society for Testing and Materials, 1973.
- [8] Shabbits, W. O., Pryle, W. H., and Wessel, E. T., unpublished data.
- [9] Robinson, J. N. and Tetelman, A. S. in Part I of this symposium.

C. F. Shih¹

Small-Scale Yielding Analysis of Mixed Mode Plane-Strain Crack Problems

REFERENCE: Shih, C. F., "Small-Scale Yielding Analysis of Mixed Mode Plane-Strain Crack Problems," *Fracture Analysis, ASTM STP 560*, American Society for Testing and Materials, 1974, pp. 187–210.

ABSTRACT: The small-scale yielding analysis of an elastic-plastic body with a line crack under plane-strain conditions subject to combinations of Mode I and II loadings is examined. The analysis of the near-tip field follows the works of Hutchinson and Rice and Rosengren. Dominant singularity solutions governing the asymptotic behavior of the stresses and strains at the crack tip are obtained for the complete range of loadings between Mode I and II. The results of an accurate finite element technique, which imbeds the dominant singularity solutions, directly relates the near-tip behavior to the elastic stress intensity factors K_I and K_{II} . Implications of this study to mixed mode fracture mechanics is also discussed, particularly with respect to the direction of crack initiation and the relation of fracture toughness under mixed modes to that in Mode I. Details of the mixed mode plastic zone sizes and shapes are also given.

KEY WORDS: yield strength, mechanical properties, fracture properties, crack initiation, plastic properties

Strain hardening plasticity solutions for small-scale yielding crack problems in plane strain, which bring out the behavior at the crack tip in the plastic zone, have been presented by Hutchinson [1,2]² and Rice and Rosengren [3]. They restricted attention to problems in which the stress distribution was either symmetric (Mode I) or antisymmetric (Mode II) with respect to the crack tip. In this paper the pure mode analyses have been extended to include combinations of Mode I and II loadings. Comprehensive surveys of plane-strain fracture mechanics are found in Refs 4, 5, and 6.

In small-scale yielding the plastic zone is small compared to the crack length. The region in the immediate vicinity of the crack tip in the plastic zone is referred to as the near-field. At distances large compared to the plastic zone but still small compared to the crack length, the elastic singu-

¹ Research Fellow in Applied Mechanics, Division of Engineering and Applied Physics, Harvard University, Cambridge, Mass. 02138.

² The italic numbers in brackets refer to the list of references appended to this paper.

larity dominates the stress and strain distribution. The far-field of the small scale yielding problem is described by

$$\sigma_{ij} = (2\pi r)^{-1/2}[K_I \sigma_{ij}^I(\theta) + K_{II} \sigma_{ij}^{II}(\theta)] \quad (1)$$

where r and θ are polar coordinates centered at the crack tip as shown in Fig. 1. The symbols K_I and K_{II} denote the Mode I and II elastic stress intensity factors, and σ_{ij}^I and σ_{ij}^{II} are well-known dimensionless functions associated with the elastic singularity which depend only on the orientation angle θ .

One measure of the strength of the singularity is Rice's [7] path-independent J -integral. For small scale yielding J is related to the elastic stress intensity factors by

$$J = \frac{1 - \nu^2}{E} (K_I^2 + K_{II}^2) \quad (2)$$

where ν is Poisson's Ratio, and E is Young's Modulus. Thus, the J -integral may be thought of as a measure of the square of the resultant amplitude of the elastic singularity. At this point we introduce a single parameter, denoted by M^e , which characterizes the relative strengths of K_I and K_{II} in the far-field. A convenient definition is

$$\begin{aligned} M^e &= \frac{2}{\pi} \tan^{-1} \left| \lim_{r \rightarrow \infty} \frac{\sigma_{\theta\theta}(\theta = 0)}{\sigma_{r\theta}(\theta = 0)} \right| \\ &= \frac{2}{\pi} \tan^{-1} \left| \frac{K_I}{K_{II}} \right| \end{aligned} \quad (3)$$

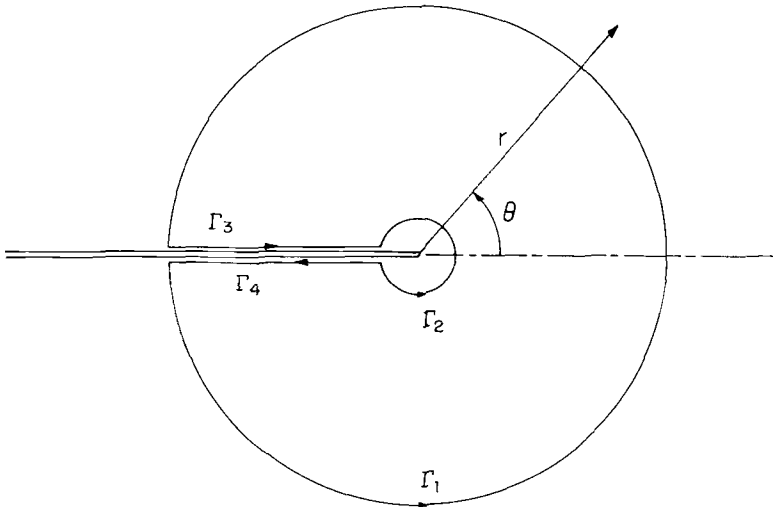


FIG. 1—Polar coordinate system centered at crack tip and integration paths.

With this definition M^e , hereby referred to as the far-field mixity parameter, ranges from 0 to 1, with $M^e = 0$ for pure Mode II and $M^e = 1$ for pure Mode I conditions at the far-field. (Note: For the case in which a crack in an infinite plate makes an angle β (in radians) to a far pure tension field, one finds from the elastic solution that $M^e = (2/\pi)\beta$.)

As in Refs 1, 2, and 3, J_2 deformation theory of plasticity is used in the near-field analysis. For the dominant singularity of the near-field the elastic strains are negligible compared to the plastic strains and only the plastic part of the stress-strain relation enters in the dominant singularity analysis. In simple tension a power hardening relation between the plastic strain and stress is assumed so that for "large" plastic strains

$$\epsilon^p \sim \alpha \left(\frac{\sigma}{\sigma_0} \right)^{n-1} \frac{\sigma}{E} \tag{4}$$

where σ_0 is the yield stress in simple tension, α may be regarded as a material constant, and n is the strain hardening coefficient. Application of the J -integral to the mixed mode small-scale yielding problem reveals that the dominant singularity governing the asymptotic behavior of the stresses, strains, and displacement at the crack tip has the form [1,2,3]

$$\begin{aligned} \sigma_{ij} &= \sigma_0 K_M^p r^{-1/(n+1)} \bar{\sigma}_{ij}(\theta, M^p), \quad \sigma_e = \sigma_0 K_M^p r^{-1/(n+1)} \bar{\sigma}_e(\theta, M^p) \\ \epsilon_{ij}^p &= \frac{\alpha \sigma_0}{E} (K_M^p)^n r^{-n/(n+1)} \bar{\epsilon}_{ij}^p(\theta, M^p), \quad u_i = \frac{\alpha \sigma_0}{E} (K_M^p)^n r^{1/(n+1)} \bar{u}_i(\theta, M^p) \end{aligned} \tag{5}$$

The dimensionless functions $\bar{\sigma}_{ij}$, $\bar{\sigma}_e$, $\bar{\epsilon}_{ij}^p$, \bar{u}_i depend only on θ and the near-field mixity parameter M^p defined below. The amplitude of the dominant singularity is K_M^p and this is given definite meaning by setting the maximum value of the θ -variation of the effective stress, $\bar{\sigma}_e = [(3/2) \bar{\sigma}_{ij} \bar{\sigma}_{ij}]^{1/2}$, to unity where $\bar{\sigma}_{ij} = \bar{\sigma}_{ij} - (\bar{\sigma}_{kk}/3)\delta_{ij}$. The superscript p emphasizes that K_M^p is the plastic stress intensity factor and the subscript M emphasizes that it applies to mixtures of Mode I and II. The near-field mixity parameter M^p is introduced in Eq 5 to identify each possible set of θ -variations of stresses and strains. One convenient way of identification is the relative composition of Mode I and II conditions directly ahead of the tip. Thus M^p is defined, in the same way as M^e in Eq 3, in terms of the tensile and shear stresses ahead of the crack tip by

$$\begin{aligned} M^p &= \frac{2}{\pi} \tan^{-1} \left| \lim_{r \rightarrow 0} \frac{\sigma_{\theta\theta}(r, \theta = 0)}{\sigma_{r\theta}(r, \theta = 0)} \right| \\ &= \frac{2}{\pi} \tan^{-1} \left| \frac{\bar{\sigma}_{\theta\theta}(\theta = 0, M^p)}{\bar{\sigma}_{r\theta}(\theta = 0, M^p)} \right| \end{aligned} \tag{6}$$

where M^p also ranges from 0 to 1, with $M^p = 0$ for pure Mode II and $M^p = 1$ for pure Mode I conditions in the near-field.

In elastic crack problems the mixed mode singularity can be expressed as a linear combination of the pure Mode I and II singularities as in Eq 1. However in the plastic range, the equations are nonlinear and hence superposition is not possible. Nevertheless, the angular distribution of stresses and strains depend on the single parameter M^p and we find from our numerical solutions to be discussed later that for each particular value of M^p there corresponds a unique angular variation of stresses and strains ranging from pure Mode I to pure Mode II. Thus, the two parameters K_{M^p} and M^p completely identify the near-field for a given value of the power hardening coefficient n (whether or not small-scale yielding applies).

In pure Mode I (or pure Mode II), the plastic stress intensity factor can be expressed directly in terms of the corresponding elastic stress intensity factor K_I (or K_{II}) using the path-independent J -integral. In mixed mode small-scale yielding, K_{M^p} can also be expressed in terms of the J -integral but the expression depends implicitly on the additional parameter M^p . That is,

$$J = \frac{1 - \nu^2}{E} (K_I^2 + K_{II}^2) = \frac{\alpha \sigma_0^2}{E} I_n(M^p) (K_{M^p})^{n+1} \quad (7)$$

where $I_n(M^p)$ is a numerical constant determined from the singularity analysis, to be given later, which depends on the strain hardening coefficient n and the near-field mixity M^p . A complete specification of the near-field in terms of K_I and K_{II} (or, equivalently, J and M^e) requires that the relationship between M^e and M^p be known.

Budiansky and Rice [8] examined several path-independent integrals recently discovered by Knowles and Sternberg [9] but, contrary to their initial hopes, these integrals did not provide this additional relationship. We also were unable to find any method to directly connect the near-field to the far-field which by-passes an analysis of the intermediate field. However, an accurate finite element approach, similar to the one used by Hilton and Hutchinson [10] was developed which has enabled us to calculate the relationship between M^e and M^p . Thus K_{M^p} and M^p are now known in terms of the elastic intensity factors K_I and K_{II} ; and the near-field can be regarded as completely determined for small-scale yielding.

In the next section the near-field will be dealt with in some detail. Solutions to the dominant singularity have been obtained for n ranging from 1 to 99. The slip line field and stress distribution for a perfectly plastic material, valid at the immediate vicinity of the tip, is given in the section on perfect plasticity solutions at near-field. In the section on the small-scale yielding problem, the relationship between M^e and M^p is obtained for essentially the complete range of the strain hardening coefficient n . Details of the mixed mode plastic zone sizes and shapes are also given. Finally, we conclude the paper with a discussion of some of the implications of this study to mixed mode fracture mechanics.

Dominant Singularity Analysis

The equations governing the dominant singularity are taken directly from Ref 1 and the reader may refer there for details. The generalized power hardening relation between the plastic strains ϵ_{ij}^p and the stresses σ_{ij} which holds asymptotically at the crack tip (which reduces to Eq 4 in simple tension) is

$$\epsilon_{ij}^p = \frac{3}{2} \alpha \left(\frac{\sigma_e}{\sigma_0} \right)^{n-1} \frac{s_{ij}}{E} \quad (8)$$

where

$$s_{ij} = \sigma_{ij} - \frac{\sigma_{kk}}{3} \delta_{ij}$$

and

$$\sigma_e^2 = \frac{3}{2} s_{ij} s_{ij}$$

All the other quantities have been defined earlier. Under plane-strain conditions when the elastic strains are negligible, $\sigma_{zz} = (\sigma_{rr} + \sigma_{\theta\theta})/2$ and the effective stress is related to the stress components by

$$\bar{\sigma}_e^2 = \frac{3}{4} (\bar{\sigma}_{rr} - \bar{\sigma}_{\theta\theta})^2 + 3\bar{\sigma}_{r\theta}^2$$

while the plastic strains consistent with Eq 5 are given by

$$\bar{\epsilon}_{rr}^p = -\bar{\epsilon}_{\theta\theta}^p = \frac{3}{4} \bar{\sigma}_e^{n-1} (\bar{\sigma}_{rr} - \bar{\sigma}_{\theta\theta})$$

$$\bar{\epsilon}_{r\theta}^p = \frac{3}{2} \bar{\sigma}_e^{n-1} \bar{\sigma}_{r\theta}$$

An outline of the solution procedure used follows. An Airy stress function is introduced and a partial differential equation governing the stress function is derived from the compatibility equation. A separated solution, Eq 5 can be obtained thereby reducing the problem to a fourth order, nonlinear differential equation. In the beginning phase of the investigation, the equations were solved by shooting methods as in Refs 1, 3 which were adequate for the pure mode analyses. However, the shooting method and its variants were inadequate for the mixed mode analyses. A more sophisticated method employing finite difference procedure with quasi-linearization [11,12] was then tried and highly accurate solutions with very rapid convergence were obtained.

The θ -variation of the stresses, strains, and the effective stress associated with the dominant singularity are shown in Figs. 2 and 3 for $n = 3$ and 13, respectively. Included in each figure are the extreme cases of Mode I and II plus two intermediate states. The four cases in Figs. 2 and 3 are arranged

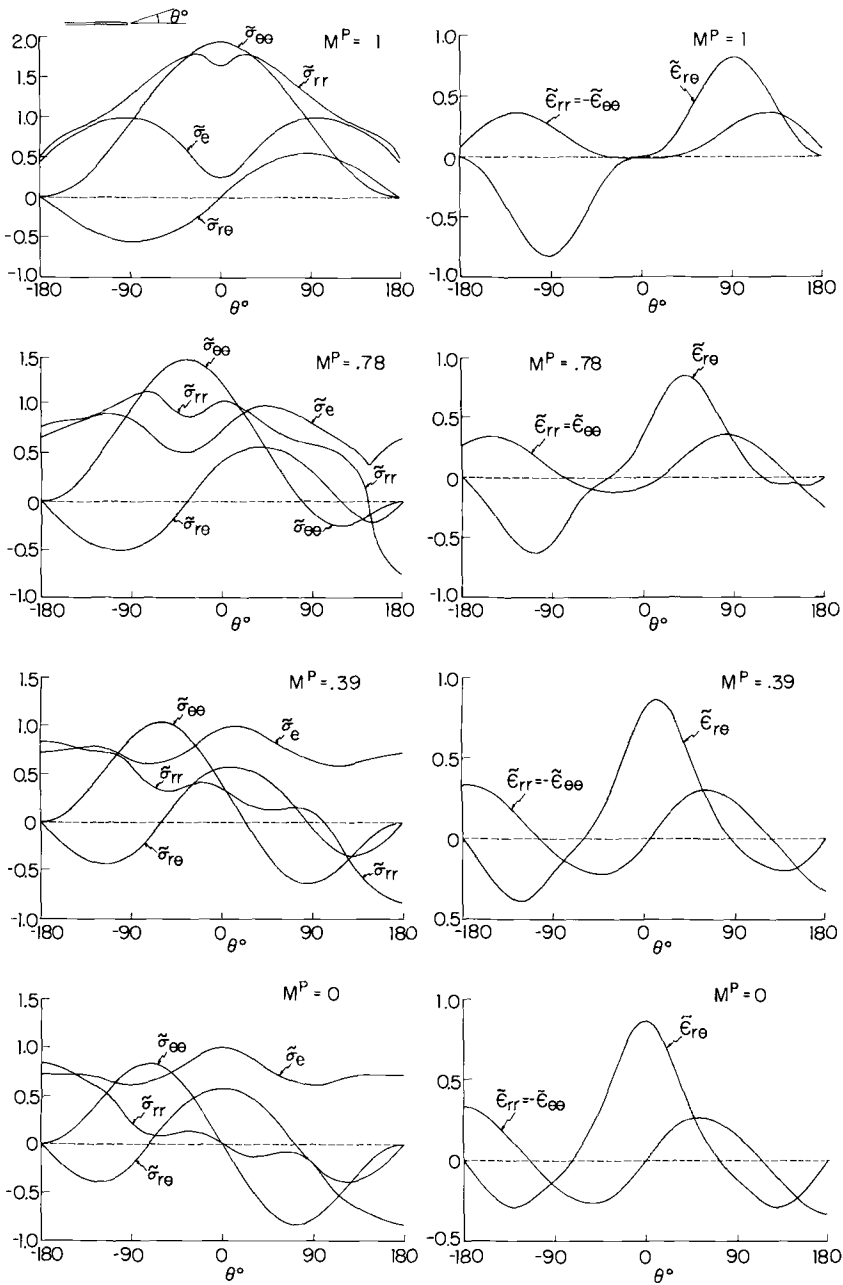


FIG. 2— θ -variations of stresses and strains at the tip of a crack for plane strain with $n = 3$.

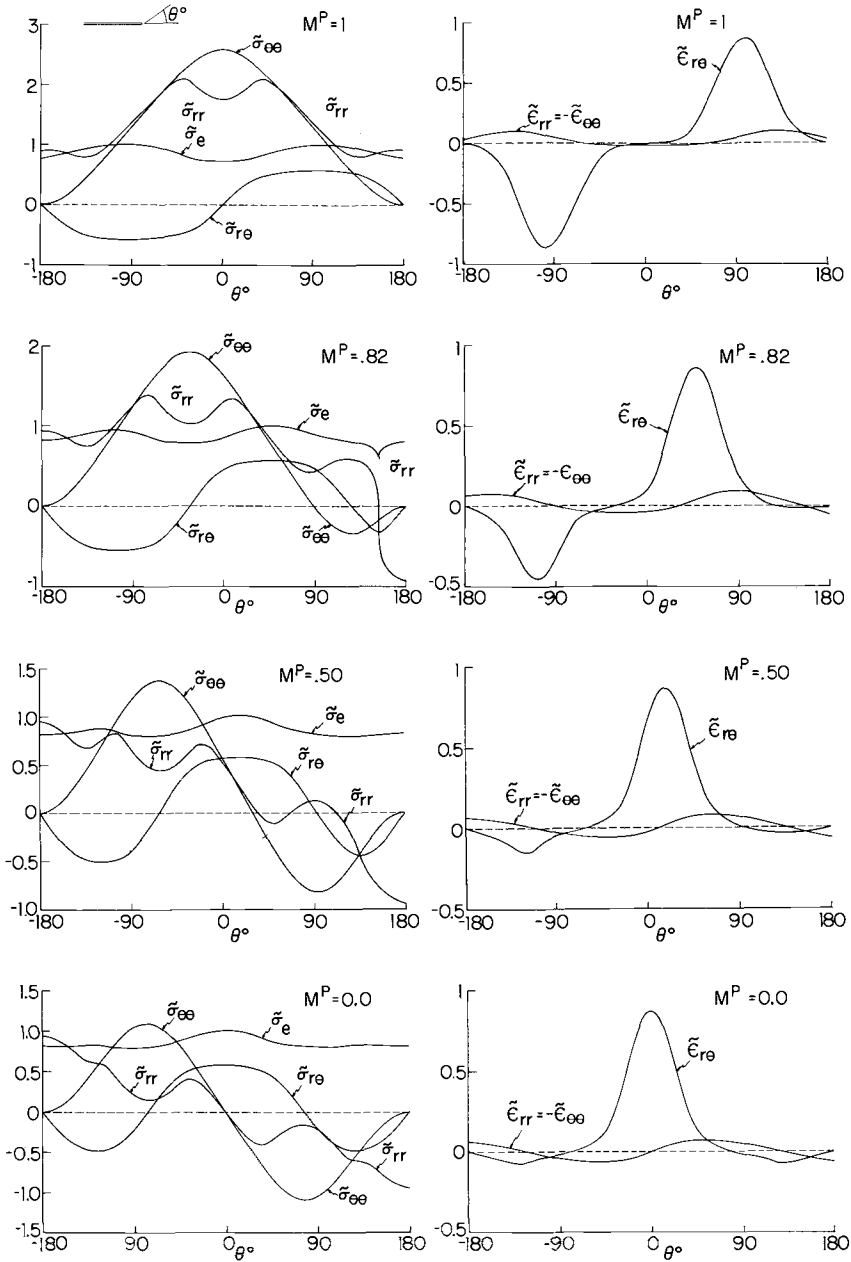


FIG. 3— θ -variations for stresses and strains at the tip of a crack for plane strain with $n = 13$.

in order of increasing asymmetry with values of M^p chosen such that the corresponding values of M^e for small-scale yielding are approximately $M^e = 1, 0.7, 0.3, 0$, respectively, as will be seen in the section on the small-scale yielding problem.

As mentioned at the beginning of the paper two parameters K_{M^p} and M^p are required to completely specify the stress and strain distribution in the vicinity of the crack tip, and that the J -integral does not provide enough information for the determination of both. Budiansky and Rice [8] examined some new path independent integrals recently discovered by Knowles and Sternberg [9] but, as already mentioned, these new integrals did not supply the additional information that would completely relate K_{M^p} and M^p to K_I and K_{II} . However, their investigation did provide an unexpected result which will explain a peculiar feature of the dominant singularity solutions as well as of the perfect plasticity solutions to be developed in the next section.

What has come to be referred to as the J -integral is actually the first component of the vector [8]

$$J_k = \int_{\Gamma_1} (W n_k - \sigma_{ij} n_j u_{i,k}) ds$$

where W is the strain energy density, Γ_1 is a curve in the x_1, x_2 plane, and n_k is the unit normal to Γ_1 . For small-scale yielding, J_1 is given by Eq 2 and J_2 is related to K_I and K_{II} by

$$J_2 = -\left(\frac{1 + \nu}{E}\right) (K_I K_{II}) \quad (9)$$

The closed contour $\Gamma = \Gamma_1 - \Gamma_2 + \Gamma_3 + \Gamma_4$ in Fig. 1 encloses no singularities, hence the integral vanishes when evaluated along Γ . The contributions due to Γ_1 and Γ_2 are bounded, and hence the contributions due to Γ_3 and Γ_4 must also be bounded. As discussed in Ref 8 this requires that the strain energy density associated with the dominant singularity Eq 5 be equal at opposite points on the faces of the crack (that is, for $\theta = \pm\pi$). Since W depends only on $(\bar{\sigma}_{rr})^2$ along the crack face, this requirement is equivalent to

$$\bar{\sigma}_{rr}(\theta = \pi) = \pm \bar{\sigma}_{rr}(\theta = -\pi) \quad (10)$$

for all values of M^p . Since $\bar{\sigma}_{rr}(\pi) = \bar{\sigma}_{rr}(-\pi)$ for Mode I and $\bar{\sigma}_{rr}(\pi) = -\bar{\sigma}_{rr}(-\pi)$ for Mode II, Eq 10 implies that at some value of M^p there must be an abrupt transition from one sign to the other.³ The numerical results strongly indicate that for any deviation from Mode I, the minus sign holds in Eq 10, that is,

$$\bar{\sigma}_{rr}(\theta = \pi) = -\bar{\sigma}_{rr}(\theta = -\pi) \quad \text{for } 0 \leq M^p < 1 \quad (11)$$

³ The possibility that the transition occurs with $\bar{\sigma}_{rr}(\pi) = \bar{\sigma}_{rr}(-\pi) = 0$ at some M^p was not observed, except for the case of $n = 1$ at $M^p = 1$.

The perfect plasticity solution of the next section also corroborates Eq 11. The transition zones in Figs. 2 and 3 are connected with Eq 11 and become more severe as M^p approaches unity. The numerical technique used here was capable of handling the zones in which there was a rapid variation of the stresses.

The J -integral evaluated along Γ_2 using the dominant singularity gives

$$J = \frac{\alpha\sigma_0^2}{E} (K_{M^p})^{n+1} I_n(M^p) \tag{12}$$

where

$$I_n = \int_{-\pi}^{\pi} \left\{ \frac{n}{n+1} \bar{\sigma}_e^{n+1} \cos \theta - [\sin \theta (\bar{\sigma}_{rr}(\bar{u}_\theta - \bar{u}_r') - \bar{\sigma}_{r\theta}(\bar{u}_r + \bar{u}_\theta')) + \frac{1}{n+1} (\bar{\sigma}_{rr}\bar{u}_r + \bar{\sigma}_{r\theta}\bar{u}_\theta) \cos \theta] \right\} d\theta \tag{13}^4$$

As already mentioned, for small-scale yielding the parameters of near-field and far-field are related by

$$J = \frac{\alpha\sigma_0^2}{E} (K_{M^p})^{n+1} I_n(M^p) = \frac{1-\nu^2}{E} (K_I^2 + K_{II}^2) \tag{14}$$

Values of $I_n(M^p)$ for n ranging from 1 to ∞ and M^p ranging from 0 to 1 are shown in Fig. 4. (The $n = \infty$ curve is obtained by extrapolation.) The values of I_n for pure Mode II ($M^p = 0$) given previously in Ref 2 are in error.

The tensile stress $\sigma_{\theta\theta}$ will be examined in some detail since it figures prominently in many fracture initiation studies. Let θ^* be the angular position at which the tensile stress $\sigma_{\theta\theta}$ attains its maximum at a fixed radius r in the near-field for any given value of M^p and the hardening exponent n ; the tensile stress at θ^* is denoted by $\sigma_{\theta\theta}^*$. In Fig. 5a, θ^* is shown as a function of M^p . From Eq 5

$$\sigma_{\theta\theta}^* = \sigma_0 K_{M^p} r^{-1/(n+1)} \bar{\sigma}_{\theta\theta}(\theta^*, M^p)$$

for any M^p . Similarly let $(\sigma_{\theta\theta}^*)_I$ be the tensile stress and K_I^p its associated plastic intensity factor for $M^p = 1$. Then the ratio of the maximum tensile stress in mixed mode to that in Mode I at the same value of r and n is

$$\frac{\sigma_{\theta\theta}^*}{(\sigma_{\theta\theta}^*)_I} = \frac{K_{M^p}}{K_I^p} \frac{\bar{\sigma}_{\theta\theta}(\theta^*, M^p)}{\bar{\sigma}_{\theta\theta}(0,1)} \tag{15}$$

To obtain a meaningful ratio, we take J to have the same value in mixed mode as in Mode I so that Eq 12 gives

$$(K_{M^p})^{n+1} I_n(M^p) = (K_I^p)^{n+1} I_n(M^p = 1)$$

⁴()' denotes differentiation with respect to θ .

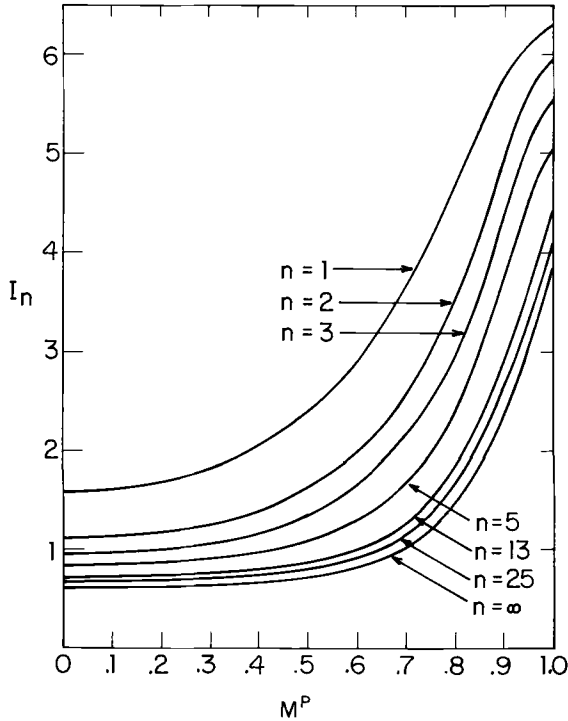


FIG. 4—Values of I_n as defined by Eq 13.

Thus, Eq 15 may be rewritten as

$$\frac{\sigma_{\theta\theta}^*}{(\sigma_{\theta\theta}^*)_I} = \left[\frac{I_n(M^p = 1)}{I_n(M^p)} \right]^{1/(n+1)} \frac{\bar{\sigma}_{\theta\theta}(\theta^*, M^p)}{\bar{\sigma}_{\theta\theta}(0, 1)} \tag{16}$$

This ratio is plotted as a function of M^p in Fig. 5b.

We end this section with the note that the dominant singularity solutions including the use of plastic intensity factors and J 's are in no way restricted by the size of the plastic zone. However, only in small-scale yielding can the J 's be related to the elastic stress intensity factors by Eqs 9 and 14.

Perfect Plasticity Solutions at Near-Field

The Mises yield criterion for perfect plasticity and plane strain, assuming negligible elastic strains (or incompressibility) is

$$\sigma_e^2 = \frac{3}{4}(\sigma_{rr} - \sigma_{\theta\theta})^2 + 3\sigma_{r\theta}^2 = \sigma_0^2 \tag{17}$$

The Prandtl slip line field and stress distribution of Mode I at the tip of a crack is well-known [2,7]. Our attempt to find a continuous stress field and its associated characteristics, centered at the crack tip, which satisfies the traction-free boundary conditions on $\theta = \pm\pi$ and the yield condition

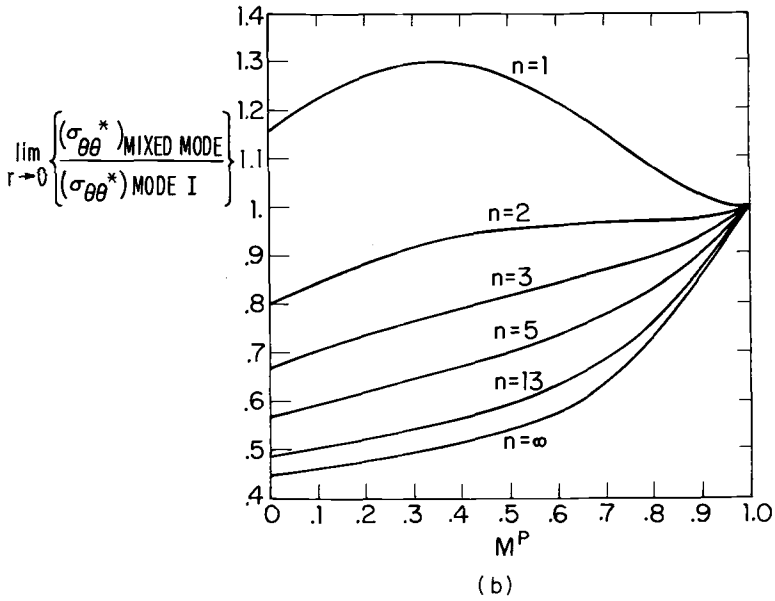
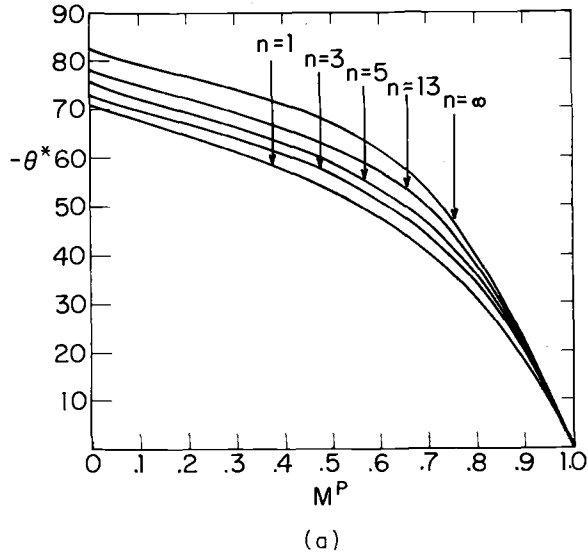


FIG. 5—(a) The position of maximum tensile stress θ^* (in degrees) as a function of M^P . (b) Ratio of the amplitude of the maximum tensile stress in mixed mode to that of Mode I as defined by Eq 16. (Both curves labeled $n = \infty$ are obtained from the perfect plasticity analysis at near-field.)

given by Eq 17 on the interval $-\pi \leq \theta \leq \pi$ and which is only slightly perturbed from the pure Mode I solution has not been successful (see Appendix). In fact, the dominant singularity solutions for low hardening materials shown in Fig. 3 point to the possibility of a discontinuity in σ_{rr} in the non-hardening limit for deviations from pure Mode I. Stress discontinuities in perfect plasticity in a plane-stress crack problem have been discussed in Ref 2 and further references on this subject may be found there.

Let OG be the radial line of discontinuity in Fig. 6a and let $\theta_{OG} = \pi - \alpha$. Continuity of traction across a radial line originating from the tip requires that $\sigma_{\theta\theta}$ and $\sigma_{r\theta}$ be continuous functions of θ . Requiring the yield condition Eq 17 to be satisfied on both sides of OG, the jump in σ_{rr} is

$$\sigma_{rr}^+ - \sigma_{rr}^- = 4 \left(\frac{\sigma_0^2}{3} - \sigma_{r\theta}^2 \right)^{1/2} \quad (18)$$

where σ_{rr}^+ and σ_{rr}^- are the two roots of Eq 17. The asymmetric slip line fields and the stress distributions may be related to the single parameter α . Two additional angles which arise in the analyses (see Fig. 6a) are γ and δ which are related to α by

$$\begin{aligned} \gamma &= -2\alpha \\ \delta &= -\alpha + \frac{\cos 2\alpha}{2} - \frac{1}{2} \end{aligned} \quad (19)$$

for $0 \leq \alpha \leq \pi/4$.

As α approaches $\pi/4$ the magnitude of the jump in σ_{rr} given by Eq 18 decreases and finally vanishes when α equals $\pi/4$. For this value of α , γ equals $-\pi/2$ and δ equals $-\pi/4 - 1/2$, and the two fan zones BOC and EOD have angular spans of $\pi/4 - 1/2$ and $\pi/4 + 1/2$, respectively. For even greater asymmetry the slip line field is completely continuous and any further shift towards the Mode II distribution causes a fan zone to develop at $\theta = 3\pi/4$ as shown in Fig. 6b. Denote the forward boundary of the fan zone by OF and let $\theta_{OF} = \pi - \alpha_F$. Then FOCDE rotates as a rigid block until it is completely symmetrical about $\theta = 0$ which corresponds exactly to Mode II (see Fig. 7).

The relationships between α_F , δ , and γ are given by

$$\begin{aligned} \gamma &= -\frac{\pi}{4} - \alpha_F \\ \delta &= -\frac{1}{2} - \alpha_F \end{aligned} \quad (20)$$

for $\pi/4 \leq \alpha_F \leq 3\pi/8 - 1/4$. The stresses may be expressed analytically throughout the transition from Mode I to II, and the details are given in the Appendix. Similar to the dominant singularity solutions for hardening

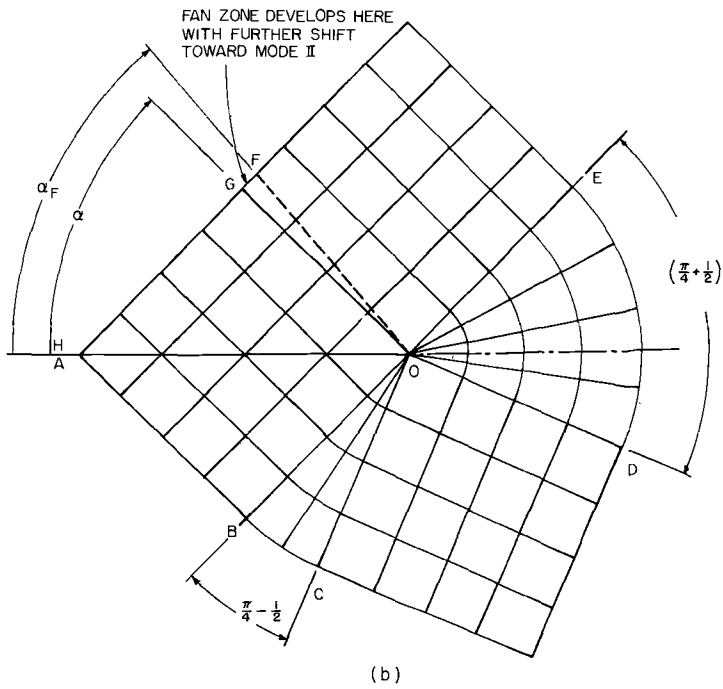
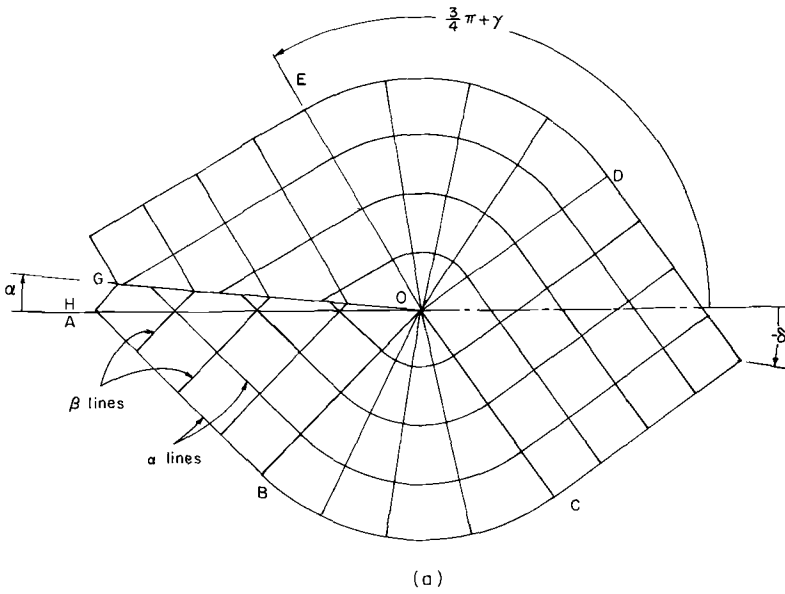


FIG. 6—Two mixed mode slip-line fields and definitions used in the analysis.

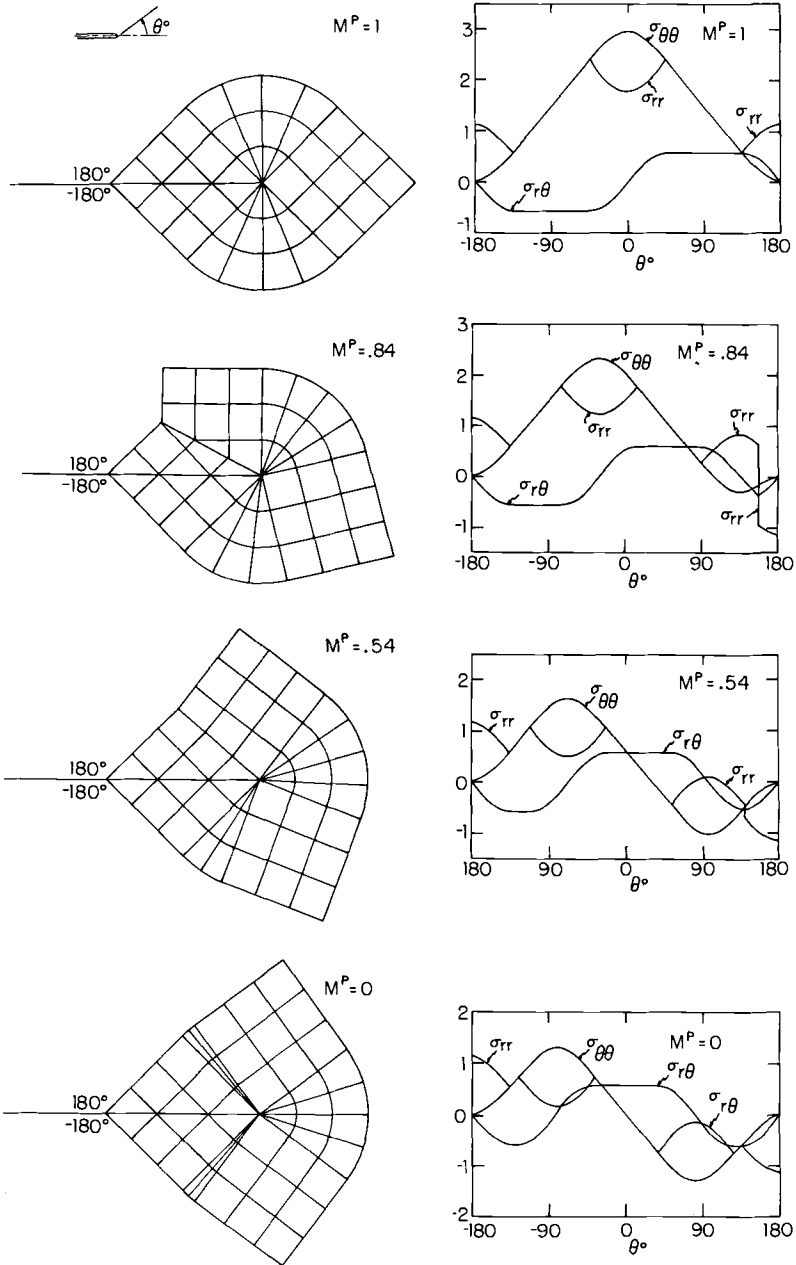


FIG. 7—Slip-line fields and stress distributions at the tip of a crack in a perfectly plastic material for plane strain. Stresses have been normalized by σ_0 .

materials, the stress distribution and its associated slip line field is uniquely characterized by M^p defined as in Eq 6. It is found that M^p may be expressed parametrically in terms of the angle δ as

$$\begin{aligned}
 M^p &= \frac{2}{\pi} \tan^{-1} \left\{ \frac{(1 + 2\pi + 2\delta) + \cos 2\delta}{-\sin 2\delta} \right\} \\
 & \qquad \qquad \qquad 0 \geq \delta \geq -\frac{\pi}{4} \\
 &= \frac{2}{\pi} \tan^{-1} \left\{ 1 + \frac{3\pi}{2} + 4\delta \right\} \\
 & \qquad \qquad \qquad -\frac{\pi}{4} \geq \delta \geq -\frac{3\pi}{8} - \frac{1}{4}
 \end{aligned} \tag{21}$$

The stress distribution and slip line field for four values of M^p are given in Fig. 7. The Mode II limit was given in Ref 2.

The maximum tensile stress occurs at $\theta = \delta$ and at this value

$$\begin{aligned}
 \sigma_{\theta\theta}^* &= \frac{\sigma_0}{\sqrt{3}} (2 + \pi + 2\delta) \\
 \sigma_{rr}^* &= \frac{\sigma_0}{\sqrt{3}} (\pi + 2\delta) \\
 \sigma_{r\theta}^* &= 0
 \end{aligned} \tag{22}$$

for the entire range of δ , $0 \geq \delta \geq -(3\pi/8) - 1/4$. From Eq 22

$$\frac{\sigma_{\theta\theta}^*}{(\sigma_{\theta\theta}^*)_I} = 1 + \frac{2\delta}{2 + \pi}$$

and appears to be the non-hardening limit of Eq 16. The position of maximum stress θ^* and the ratio $\sigma_{\theta\theta}^*/(\sigma_{\theta\theta}^*)_I$ as a function of M^p is identified by the $n = \infty$ curve in Figs. 5a and b.

The stress distribution for a low-hardening material closely approximates that given by the perfect plasticity solution as can be seen from a comparison of the $n = 13$ solution given in Fig. 3 with that of the perfect plasticity solution given in Fig. 7. This close agreement strongly suggests that the non-hardening limit of the stresses of the dominant singularity solution is the perfect plasticity solution. The strains at the tip of the crack in perfect plasticity cannot be obtained by any elementary analysis. However, it may be noted that the $1/r$ singularity in strains can occur only in the fan zone where the only non-zero component is $\epsilon_{r\theta}^p$. These features are reflected in the low strain hardening solution of Fig. 3.

The Small-Scale Yielding Problem

In this section the parameters characterizing the near-field in the plastic zone will be directly related to the elastic stress intensity factors using an accurate finite element procedure similar to the one used in Ref 10.

In the numerical calculations, an elastic-plastic material with the following uniaxial stress-strain relation is used

$$\epsilon = \begin{cases} \frac{\sigma}{E}; & \sigma \leq \sigma_0 \\ \left(\frac{\sigma}{\sigma_0}\right)^{n-1} \frac{\sigma}{E}; & \sigma > \sigma_0 \end{cases} \quad (23)$$

The J_2 deformation theory is invoked, and plastic deformation is assumed to be independent of the hydrostatic component of stress, σ_{kk} , and completely determined by the stress deviator, s_{ij} , and its invariant σ_e .

The generalized stress-strain relation can be written as

$$\sigma_{ij} = \begin{cases} \frac{\nu E}{(1+\nu)(1-2\nu)} \epsilon_{kk} \delta_{ij} + \frac{E}{(1+\nu)} \epsilon_{ij}; & \sigma_e \leq \sigma_0 \\ \frac{\nu E}{(1+\nu)(1-2\nu)} \epsilon_{kk} \delta_{ij} + \frac{E}{(1+\nu)} \epsilon_{ij} - \frac{E e_{ij}}{(1+\nu)} + \frac{2}{3} \frac{\sigma_e}{e_e} e_{ij}; & \sigma_e > \sigma_0 \end{cases} \quad (24)$$

where

$$\begin{aligned} \frac{e_e}{\sigma_e} &= \frac{1}{E} \left[\left(\frac{\sigma_e}{\sigma_0} \right)^{n-1} - \frac{1}{3} (1-2\nu) \right] \\ e_{ij} &= \epsilon_{ij} - \frac{\epsilon_{kk}}{3} \delta_{ij} \\ e_e^2 &= \frac{2}{3} e_{ij} e_{ij} \end{aligned}$$

with the other quantities as defined earlier.

A brief description of the numerical method follows; a more complete account of a similar method is treated in Ref 10. The finite element method imbeds the dominant singularity solution by the use of a singular tip element centered at the crack tip as shown in Fig. 8, whose behavior is completely described by Eq 5. The near-tip behavior, for which the dominant singularity solution (Eq 5) is asymptotically correct, can be accurately represented by the singular element if it is sufficiently small. In addition, the displacements at the nodes on the common boundary Γ_2 , of the tip element and of the elements that encircle it, are also given by Eq 5. Two rigid body constants are included to complete the description of these

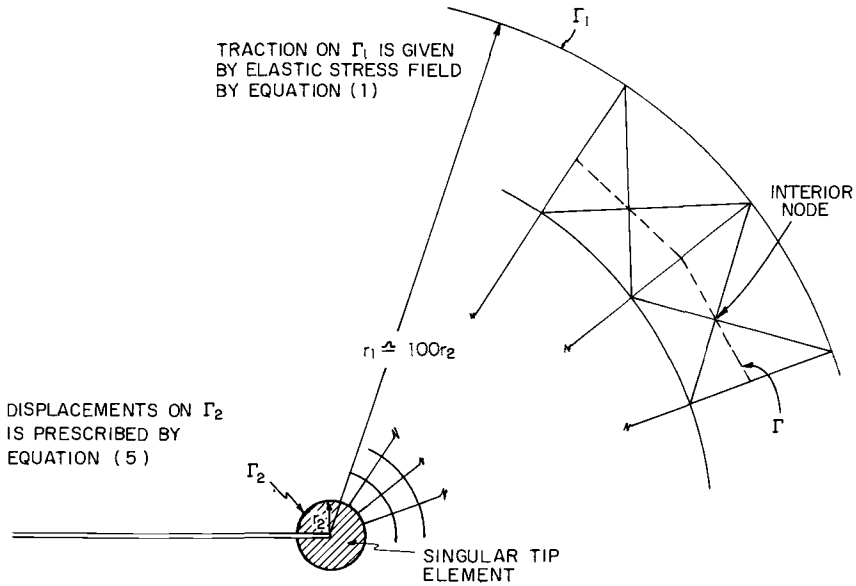


FIG. 8—The finite element mesh showing the singular tip element encircled by quadrilateral elements and the far-field traction boundary.

nodal displacements. Thus, the singular tip element and the nodes on Γ_2 contribute two unknown parameters, namely K_M^p and M^p and two rigid body motion constants to the potential energy functional. At the outer boundary Γ_1 , traction corresponding to the elastic solution (Eq 1) is prescribed. The region between Γ_1 and Γ_2 is represented by conventional elements.⁵ The outer boundary Γ_1 is taken at a radius of approximately $100 r_2$. The maximum extent of the plastic zone never exceeds $15 r_2$ for all the cases considered, and by numerical experimentation this was found to be sufficient to guarantee the accuracy stated later. The potential energy functional is minimized with respect to K_M^p , M^p , rigid body constants, and the displacements at all the nodes between Γ_1 and Γ_2 . The resulting non-linear system of equations was solved by Newton's method. Such an approach permits an accurate description of the stresses and strains throughout the entire domain and is particularly attractive since K_M^p and M^p are computed directly.

The numerical results are in good agreement with the analytical predictions where such comparisons are possible. The stress and strain intensity factors for either pure Mode I or II may be directly calculated using Eq 14. This can be done with great accuracy since I_n can be com-

⁵ The quadrilateral element is subdivided into four triangular constant strain elements; however the middle node is removed by static condensation and therefore does not enter into the final stiffness matrix.

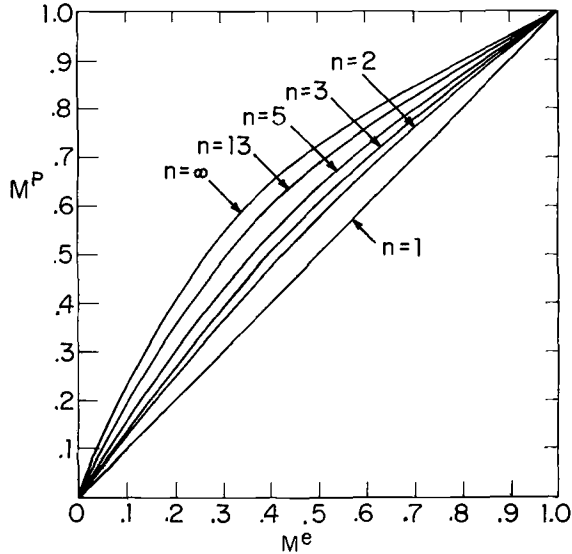


FIG. 9—Near-field mixity M^p versus far-field mixity M^e for small-scale yielding in plane strain.

puted very accurately as has been done in the pure mode analyses of Refs 1, 2, and 3. The stress intensity factor obtained directly in the finite element procedure⁶ differed from the former by an average of 1 percent over the range of n considered. Alternatively, the value of J for the singular tip element can be obtained by substituting the latter value of the stress intensity factor into Eq 12. This differed from the “prescribed” value of J given by Eq 2 by no more than 3 percent for all the cases considered. For the case of $n = 1$, that is, linear elasticity, where a direct comparison in mixed mode is possible, the computed stress intensity factors were within 1 percent of the known value for all mixtures of Mode I and II.

The relationship between M^e and M^p , the central relationship of this entire paper, is shown in Fig. 9. The $n = \infty$ curve is obtained by extrapolation.⁷

The finite element analysis was repeated at selected values of M^e and n for two additional stress-strain relationships slightly different in character from Eq 23. One of these was the Ramberg-Osgood tensile relation given by

$$\epsilon = \frac{\sigma}{E} \left[1 + \frac{3}{7} \left(\frac{\sigma}{\sigma_0} \right)^{n-1} \right] \quad (25)$$

⁶ The typical finite element mesh has 13 rings and 25 radial lines at angular intervals of 15 deg for a total of 312 quadrilateral elements.

⁷ Unless otherwise indicated all the results presented are for the stress-strain relationship as given by Eq 24 with ν set at 0.3.

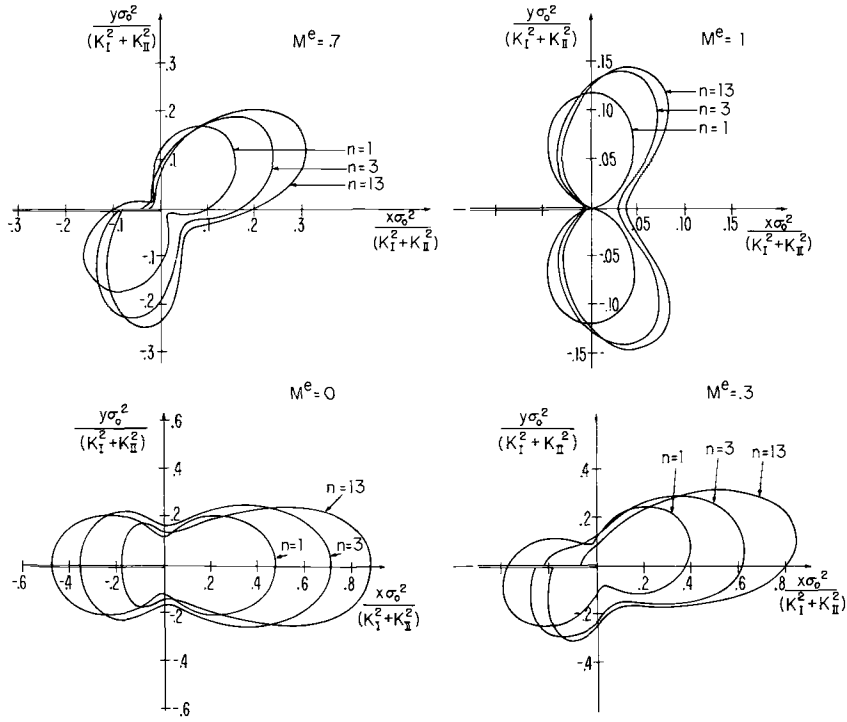


FIG. 10—Elastic-plastic boundaries for small-scale yielding in plane strain.

The second was a tensile relation which had a distinct yield stress but no discontinuity in the slope of the stress-strain relation as does Eq 23. It was given by

$$\epsilon = \begin{cases} \frac{\sigma}{E}; & \text{for } \sigma \leq \sigma_0 \\ \left(\frac{1-n}{E}\right)(\sigma - \sigma_0) + \frac{\sigma}{E} \left(\frac{\sigma}{\sigma_0}\right)^{n-1}; & \text{for } \sigma > \sigma_0 \end{cases} \quad (26)$$

The computed values of M^p for a given M^e differed only slightly from the results in Fig. 9 for the same value of n .⁸ It is concluded that the relation of M^p to M^e depends primarily on the strain hardening exponent n .⁹

The plastic zones based on Eq 23 corresponding to four values of M^e are plotted in Fig. 10, note that three different scales on the axes are used. The plots clearly show that while the plastic zone undergoes relatively

⁸ The variation in M^p is less than $1/2$ percent.

⁹ Results obtained for ν ranging from 0.1 to 0.45 for stress-strain relations given by Eqs 23 and 25 differed by $1/2$ percent at most from the $M^e - M^p$ relationship associated with $\nu = 0.3$.

minor changes with increasing n in Mode I, it makes significant advances ahead of the crack in Mode II. The plastic zones for low hardening materials are strikingly similar to the plastic zone for a perfectly plastic material in Mode I obtained by Levy et al [13] using a conceptually similar finite element technique which employed a J_2 flow theory.

Conclusions

The maximum tensile stress has been used with some success [14,15] in fracture initiation studies in mixed mode for brittle materials. In particular, the fracture initiation angle measured from combined mode experiments is fairly close to the direction at which the tensile stress, computed from the elastic result (Eq 1), attains its maximum.

In Fig. 5a, the angular position of maximum tensile stress (at a fixed radius) θ^* is plotted against M^p . Using the M^e versus M^p curves of Fig. 9, θ^* can be translated into a function of M^e for small-scale yielding as shown in Fig. 11. The angles of initial crack growth experimentally obtained by Liu [16] and Pook [17] are also included in the same figure. Most of the experimental results fall between the $n = 1$ and the $n = \infty$ curves. Sih [18] has discussed variations in fracture initiation angle based on local strain energy density considerations.

The experiments of Refs 16, 17, and 19 indicate an increase in fracture toughness, as measured by the critical value of J , for example, for deviations from pure Mode I conditions; and most experiments reveal a higher fracture toughness in Mode II than in Mode I. From Fig. 5b it is clear that a departure from Mode I conditions (that is, M^p less than unity) gives rise

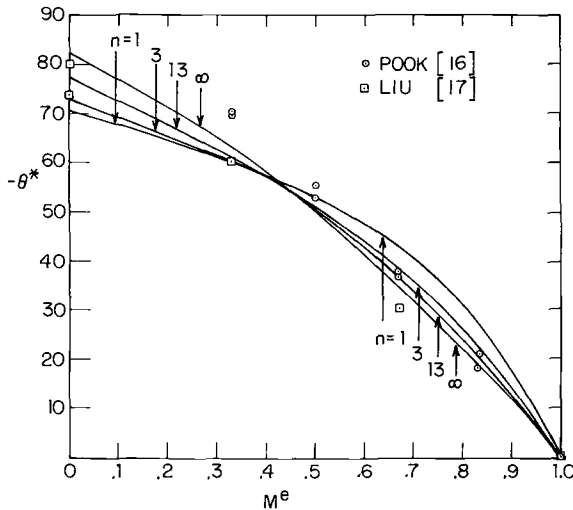


FIG. 11— θ^* (in degrees) as a function of M^e . Experimental results of Liu [16] and Pook [17] are included.

to a reduction in the peak value of the amplitude of the tensile stress component $\sigma_{\theta\theta}$ associated with the dominant singularity in the plastic zone as long as the strain hardening exponent is greater than about 3. The reduction is greater with higher values of n . Thus, these predictions concur in the possibility of increases in measured fracture toughness for deviation from pure Mode I. The elastic result (the $n = 1$ curve) indicates quite the opposite.

Acknowledgments

The author is extremely grateful to J. W. Hutchinson for suggesting the problem and for his expert guidance and encouragement throughout the entire investigation. This work was supported in part by the Air Force Office of Scientific Research under Grant AFOSR-73-2476, in part by the National Aeronautics and Space Administration under Grant NGL 22-007-012, and by the Division of Engineering and Applied Physics, Harvard University.

APPENDIX

Details of Perfect Plasticity Solutions

The Mises yield condition near the crack tip where elastic strains may be neglected is

$$\sigma_e^2 = \frac{3}{4} (\sigma_{rr} - \sigma_{\theta\theta})^2 + 3\sigma_{r\theta}^2 = \sigma_0^2 \quad (27)$$

As mentioned in the section on perfect plasticity solutions at near-field, the slip line field for Mode I is well-known (see Fig. 7). Let us examine the means of introducing slight asymmetry to the problem with the requirement that the resulting field remains close to the symmetric field. One procedure is to preserve the number of constant stress and fan regions but to change their shapes slightly. The angular span of fan zones BOC and DOE may be perturbed, but the constant stress zones must maintain their shapes. This, we shall later show, leads to an inadmissible stress field. Alternatively, additional uniform stress or fan zones or both may be introduced, but this is impossible without immediate substantial deviation from the Mode I slip line field. A discussion of the properties of uniform stress regions and fan zones is given in Prager and Hodge [20].

We proceed to discuss in detail the first procedure. Following the convention of Hill [21]

$$p + 2k\phi = C_1 \text{ along the } \alpha\text{-characteristics} \quad (28)$$

$$p - 2k\phi = C_2 \text{ along the } \beta\text{-characteristics} \quad (29)$$

where $p = -(\sigma_{rr} + \sigma_{\theta\theta})/2$, $k = \sigma_0/\sqrt{3}$, and ϕ is the anti-clockwise angular rotation of the α -line from the x -axis.

A little asymmetry is introduced by rotating the constant stress zone COD by an amount δ ; this is equivalent to perturbing the angular spans of the fan regions BOC and DOE. In region AOB

$$p = -\frac{\sigma_0}{\sqrt{3}} \quad \text{and} \quad \phi = -\frac{\pi}{4}$$

Thus from Eq 28

$$C_1 = -\frac{\sigma_0}{\sqrt{3}} \left(1 + \frac{\pi}{2}\right)$$

The α characteristics cross the fan zone BOC and extend right into the constant stress region COD. Therefore the pressure, p , in COD, is given by

$$p = -\frac{\sigma_0}{\sqrt{3}} \left(1 + \frac{\pi}{2}\right) - 2\frac{\sigma_0}{\sqrt{3}} \phi$$

However, $\phi = \pi/4 + \delta$ throughout COD, hence

$$p = -\frac{\sigma_0}{\sqrt{3}} (1 + \pi + 2\delta)$$

and from Eq 29

$$C_2 = -\frac{\sigma_0}{\sqrt{3}} \left(1 + \frac{3\pi}{2} + 4\delta\right)$$

in COD. The β characteristics originating in COD passes through the fan zone DOE into the uniform stress region EOH. The pressure p throughout EOH, according to the β characteristics from COD, is

$$p = -\frac{\sigma_0}{\sqrt{3}} (1 + 4\delta)$$

since $\phi = 3\pi/4$ everywhere in EOH. However, the traction-free conditions at OH and the requirement that Eq 27 be satisfied in EOH requires p to be $-\sigma_0/\sqrt{3}$ in EOH. Thus, the proposed slip-line field is inadmissible.

To overcome this impasse, we introduce a discontinuity in the slip-line field. It is obvious that the discontinuity must originate at one of the traction-free boundaries and then move inwards. A discontinuity that originates elsewhere will require finite changes in strain energy for any slight departure from Mode I.

The slip-line field is similar to the one just discussed, except that a discontinuity represented by the radial line OG at an angle α from the traction-free boundary is included as shown in Fig. 6a. In region AOB the constant stress state is given by

$$\sigma_{xx} = \frac{2\sigma_0}{\sqrt{3}} \quad \text{and} \quad \sigma_{yy} = \sigma_{xy} = 0$$

or

$$\sigma_{rr} = \frac{\sigma_0}{\sqrt{3}} (1 + \cos 2\theta); \quad \sigma_{\theta\theta} = \frac{\sigma_0}{\sqrt{3}} (1 - \cos 2\theta); \quad \sigma_{r\theta} = -\frac{\sigma_0}{\sqrt{3}} \sin 2\theta$$

In the fan zone BOC

$$\sigma_{rr} = \sigma_{\theta\theta} = \frac{\sigma_0}{\sqrt{3}} \left(1 + \frac{3\pi}{2} + 2\theta\right); \quad \sigma_{r\theta} = -\frac{\sigma_0}{\sqrt{3}}$$

The stress state in COD is uniform and is represented by

$$\begin{aligned}\sigma_{rr} &= \frac{\sigma_0}{\sqrt{3}} \left[(1 + \pi + 2\delta) - \sin \left(\frac{\pi}{2} + 2\delta - 2\theta \right) \right] \\ \sigma_{\theta\theta} &= \frac{\sigma_0}{\sqrt{3}} \left[(1 + \pi + 2\delta) + \sin \left(\frac{\pi}{2} + 2\delta - 2\theta \right) \right] \\ \sigma_{r\theta} &= \frac{\sigma_0}{\sqrt{3}} \cos \left(\frac{\pi}{2} + 2\delta - 2\theta \right)\end{aligned}$$

where δ is the rotation of COD about 0. In DOE the stresses are

$$\sigma_{rr} = \sigma_{\theta\theta} = \frac{\sigma_0}{\sqrt{3}} \left(1 + \frac{3\pi}{2} + 2\theta - 4\delta \right); \quad \sigma_{r\theta} = \frac{\sigma_0}{\sqrt{3}}$$

In EOG

$$\begin{aligned}\sigma_{rr} &= \frac{\sigma_0}{\sqrt{3}} [1 + 4\delta - 2\gamma + \cos(2\gamma - 2\theta)] \\ \sigma_{\theta\theta} &= \frac{\sigma_0}{\sqrt{3}} [1 + 4\delta - 2\gamma - \cos(2\gamma - 2\theta)] \\ \sigma_{r\theta} &= \frac{\sigma_0}{\sqrt{3}} \sin(2\gamma - 2\theta)\end{aligned}$$

where γ represents the angular shift of OE. Finally, in the region HOG behind the discontinuity OG, the stresses are

$$\begin{aligned}\sigma_{rr} &= -\frac{\sigma_0}{\sqrt{3}} (1 + \cos 2\theta) \\ \sigma_{\theta\theta} &= -\frac{\sigma_0}{\sqrt{3}} (1 - \cos 2\theta) \\ \sigma_{r\theta} &= \frac{\sigma_0}{\sqrt{3}} \sin 2\theta\end{aligned}$$

The parameters δ and γ may be related to α by requiring that $\sigma_{\theta\theta}$ and $\sigma_{r\theta}$ be continuous across OG. This gives

$$\begin{aligned}\gamma &= -2\alpha \\ \delta &= -\frac{1}{2} - \alpha + \frac{\cos 2\alpha}{2}\end{aligned}\tag{30}$$

As OG moves inwards the jump in σ_{rr} diminishes and finally at $\alpha = \pi/4$, the slip-line field is completely continuous. At this point

$$\gamma = -\frac{\pi}{2} \quad \text{and} \quad \delta = -\frac{1}{2} - \frac{\pi}{4}$$

Further shift to Mode II causes a fan zone FOG to develop at $\theta = 3\pi/4$ with stresses given by

$$\begin{aligned}\sigma_{rr} = \sigma_{\theta\theta} &= -\frac{\sigma_0}{\sqrt{3}} \left(1 + \frac{3\pi}{2} + 2\theta \right) \\ \sigma_{r\theta} &= -\frac{\sigma_0}{\sqrt{3}}\end{aligned}$$

Let α_F denote the position of OF the forward radial boundary of the developing fan, then

$$\begin{aligned}\gamma &= -\frac{\pi}{4} - \alpha_F \\ \delta &= -\frac{1}{2} - \alpha_F\end{aligned}\tag{31}$$

References

- [1] Hutchinson, J. W., *Journal of the Mechanics and Physics of Solids*, Vol. 16, No. 1, Jan. 1968, pp. 13–31.
- [2] Hutchinson, J. W., *Journal of the Mechanics and Physics of Solids*, Vol. 16, No. 5, Sept. 1968, pp. 337–347.
- [3] Rice, J. R. and Rosengren, G. F., *Journal of the Mechanics and Physics of Solids*, Vol. 16, No. 1, Jan. 1968, pp. 1–12.
- [4] Rice, J. R. in *Fracture*, Vol. II, H. Liebowitz, Ed., Academic Press, New York, 1968, pp. 191–311.
- [5] Irwin, G. R. and Paris, P. C. in *Fracture*, Vol. III, H. Liebowitz, Ed., Academic Press, New York, 1971, pp. 2–48.
- [6] McClintock, F. A. in *Fracture*, Vol. III, H. Liebowitz, Ed., Academic Press, New York, 1971, pp. 48–227.
- [7] Rice, J. R., *Journal of Applied Mechanics, Transactions*, American Society of Mechanical Engineers, Vol. 35, 1968, pp. 379–386.
- [8] Budiansky, B. and Rice, J. R., *Journal of Applied Mechanics, Transactions*, American Society of Mechanical Engineers, Vol. 40E, No. 1, March 1973, pp. 201–203.
- [9] Knowles, J. K. and Sternberg, E., *Archive for Rational Mechanics and Analysis*, Vol. 44, No. 3, Jan. 1972, pp. 187–211.
- [10] Hilton, P. D. and Hutchinson, J. W., *Engineering Fracture Mechanics*, Vol. 3, No. 4, 1971, pp. 435–451.
- [11] Roberts, S. M. and Shipman, J. S., *Two-Point Boundary Value Problems: Shooting Methods*, American Elsevier, New York, 1972.
- [12] Keller, H. B., *Numerical Methods for Two-Point Boundary Value Problems*, Blaisdell Publishing Company, Waltham, Mass., 1968.
- [13] Levy, N., Marcal, P. V., Ostergren, W. J., and Rice, J. R., *International Journal of Fracture Mechanics*, Vol. 7, No. 2, June 1971, pp. 143–156.
- [14] Erdogan, F. and Sih, G. C., *Journal of Basic Engineering, Transactions*, American Society of Mechanical Engineers, Vol. 85D, 1963, pp. 519–525.
- [15] Williams, J. G. and Ewing, P. D., *International Journal of Fracture Mechanics*, Vol. 8, No. 4, Dec. 1972, pp. 441–446.
- [16] Liu, A. F., “Crack Growth and Failure of Aluminum Plate Under In-Plane Shear,” presented at AIAA 11th Aerospace Sciences Meeting, Washington, D. C., Jan. 1973.
- [17] Pook, L. P., *Engineering Fracture Mechanics*, Vol. 3, No. 3, Oct. 1971, pp. 205–218.
- [18] Sih, G. C. in *Mechanics of Fracture*, G. C. Sih, Ed., Noordhoff International Publishing Leyden, The Netherlands, 1973.
- [19] Wilson, W. K., “On Combined Mode Fracture,” Westinghouse Research Report 69-1E7-FMECH-R1, Westinghouse Research Laboratories, Pittsburgh, Pa., June 1969.
- [20] Prager, W. and Hodge, P. G., *Theory of Perfectly Plastic Solids*, Wiley, New York, 1951.
- [21] Hill, R., *The Mathematical Theory of Plasticity*, Oxford University Press, London, 1950.

Unimod: An Applications Oriented Finite Element Scheme for the Analysis of Fracture Mechanics Problems

REFERENCE: Nair, Prasad and Reifsnider, K. L., "Unimod: An Applications Oriented Finite Element Scheme for the Analysis of Fracture Mechanics Problems," *Fracture Analysis, ASTM STP 560*, American Society for Testing and Materials, 1974, pp. 211-225.

ABSTRACT: A new concept in elastic-plastic analysis using finite element techniques is analyzed. The resulting procedural scheme, called Unimod, is found to be an effective method of performing stress analysis of complex elastic-plastic defect problems which cannot be handled by classical elastic fracture mechanics. Advantages of the Unimod scheme include extreme versatility, universal applicability to existing programs and conceptual as well as operational simplicity.

KEY WORDS: fracture properties, stresses, strains, stress analysis, finite element methods, fatigue (materials)

Most engineering materials develop zones of plastic deformation at the tip of a crack under load. For small-scale yielding, the elastic singular solutions are usually adequate representations of the stress and strain distributions at distances of one or two diameters of the plastic zone away from the crack tip, and beyond. However, if the remote stress reaches a value which is at least as great as one half of the net section yield stress in ductile or semi-brittle materials, it is quite likely that the elastic singular solution is not a good approximation to any part of the stress distribution. More generally, there is a rather large class of problems in which the nature of the stress (or strain) singularity at the crack tip depends on the level of applied load so that any elastic singularity having a fixed functional form is inadequate. An obvious example of the latter is the situation where local material properties vary as a function of position as would be the case in composite materials.

A variety of discrete element techniques has been developed to handle problems which are beyond the scope of linear elastic fracture mechanics

¹ Graduate research assistant and associate professor of Engineering Science and Mechanics, respectively, Virginia Polytechnic Institute and State University, Blacksburg, Va. 24061.

[1-5].² These techniques are generally highly sophisticated, however, and application to a particular problem (crack size, specimen geometry, material response characteristics, and prescribed type of loading) usually requires a fair amount of specialized effort. Also, even the simplest subsequent specimen geometry change or change of crack length requires that a new discrete element grid be established requiring considerable additional work. The choice of a grid to analyze a crack problem (or any problem involving a singularity) is, in itself, a tedious procedure and has been the subject of much study. (See, for example, Ref 6.) In many instances, the present analysis scheme, Unimod, can be used to solve these elastic-plastic problems with comparable (in some cases superior) accuracy. At the same time, changes of specimen geometry, crack size, and local material response characteristics can be handled with almost negligible effort, especially in comparison to many other numerical methods.

Unimod—The Technique

The concept of Unimod can be extracted from an intuitive argument. A crack or defect is commonly analyzed by using a finite element grid with a very fine grid size (small elements) in the vicinity of the expected singularity, or by using special singularity elements to surround the tip. However, one is limited in the fineness of the grid by truncation error and, in other cases, by the size of the resulting system of equations that must be solved in view of available computer facilities. In any case, since the elements at the crack tip always have finite size, or employ a truncated series representation, they are unable to represent a deformation singularity with complete accuracy. For the case of the common method of analysis based on the variational principle of minimum potential energy, the finite elements near a crack tip will always be too stiff. In a sense, the local stiffness of the material will always be overestimated, especially in the presence of plasticity. In such a situation, the singularity occurs in strain at the tip of the crack, while the stress distribution becomes relatively flat (although still singular if the material strain hardens). Strain hardening will control the actual value of stress near the tip, but the effective stiffness of the near-tip material is greatly reduced in the real material during plastic deformation near the strain singularity as large plastic strains develop. Since finite elements at the crack tip represent an average value of strain throughout their individual regions, that value, and the corresponding stiffness assigned to the element, will always be unrepresentative of the singular strain region. In particular, those elements will be too stiff compared to reality, and the predicted strains will be too small. The present scheme advances a simple solution to that problem, brought about by reducing the stiffness of a

² The italic numbers in brackets refer to the list of references appended to this paper.

crack tip element or elements to a negligible value by definition, thereby forcefully creating a strain amplification which is constrained only by the surrounding "normal" elements. For convenience, a value of 1 psi is found to be an adequate approximation to a zero modulus value, without causing computational problems, hence the name Unimod. It so happens that a value which is two orders of magnitude (or more) less than the elastic modulus produces essentially identical results. Actually, that fact makes Unimod an analysis scheme rather than a numerical manipulation. This process allows strain to develop at the crack tip more nearly as it does in real materials for elastic-plastic situations.

A conceptual similarity exists between Irwin's correction factor for small-scale yielding and the Unimod scheme. The former argument states, among other things, that the linear elastic stress field description is reasonably accurate for the case of small-scale yielding if the crack is assumed to be larger than reality by the amount

$$r_y = \frac{1}{2\pi} \left(\frac{K}{\sigma_y} \right)^2 \quad (1)$$

where K is the field stress amplitude (stress intensity factor) and σ_y is the material yield strength [7]. In other words, a certain volume (or strip) of material ahead of the crack tip is assumed to have negligible stiffness in order to determine the correct stress distribution with an elastic analysis for a mildly elastic-plastic case. Unimod can be thought of as a carry-over of that concept to finite element analysis. In fact, we will see in the discussion section that r_y as determined by elastic parameters, is, in many cases, an excellent estimate of the distance ahead of the crack which should be reduced to unit modulus if good agreement with experimental results is to be obtained. Hence, Eq 1 can frequently be used to determine how many elements ahead of the crack should be relaxed to unit stiffness for any grid to be used for such an investigation.

The results in the present report were obtained using the grid system shown in Fig. 1 where Nodes 1 to 33 define the crack axis which is an axis of symmetry for Mode I loading. The crack was effected by releasing Nodes 1 to 8 and 1 to 10 to model a single-edge-notched plate. For the experimental results used for comparison, the elements near the crack represented material elements 30 mils by 30 mils. As will be shown in the section on results, the results were extremely insensitive to any value of an element modulus below about 10^4 psi when that element (or several such elements) was embedded at the singularity in a matrix of normal elements. Fortunately, then, one need not attempt to determine a specific value for the stiffness of the singularity element. There is no loss of generality by reducing it to unity.

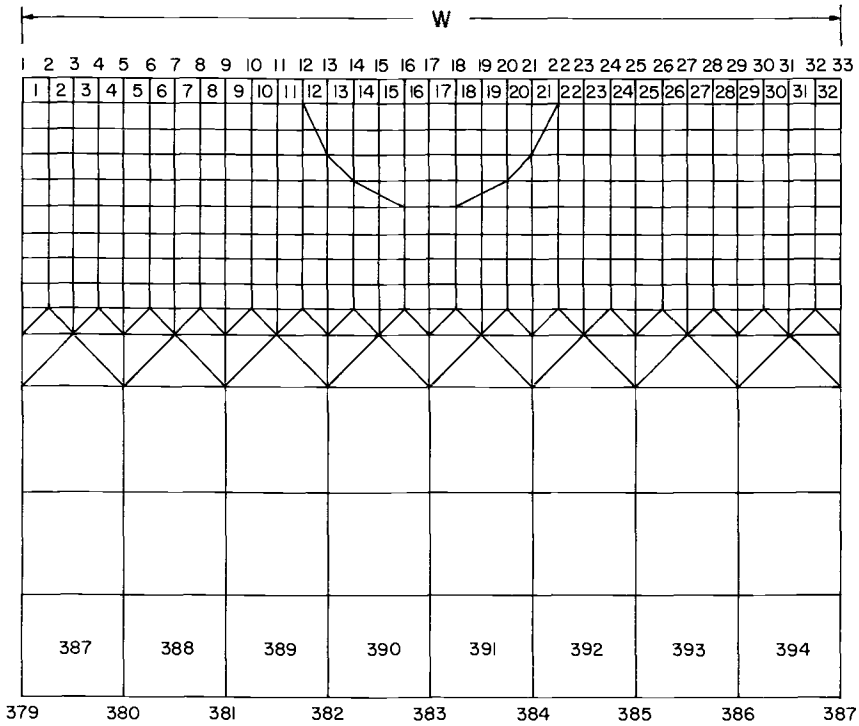


FIG. 1—Finite element grid for the geometry modeled.

Results Using Unimod

The technique of relaxing the modulus of elasticity has been carried out using E. L. Wilson’s “Axisymmetric Solids Finite Element Program” [8]. Plane stress conditions were assumed. Two strain hardening materials were considered, namely, 6061-T6 AL with a strain hardening ratio, $E_{plastic}/E_{elastic} = 0.04$ and 90-10 Brass with $E_{plastic}/E_{elastic} = 0.16$. A case of $E_{plastic} \simeq 0.0$ for AL was also examined to study the effect of change in grid size on stored strain energy.

In the various figures described below, plots of stress and strain are made against distance along the crack axis, normalized by the crack length measured from the crack tip. Unimod I(8) is understood to mean that the elastic modulus of Element Number 8 (a crack tip element) has been reduced to the extent indicated. Unimod I(9), Unimod I(10) and Unimod I(11) have similar meanings. Unimod II(8 and 9) and Unimod II(10 and 11) have two elements, 8 and 9 and 10 and 11, respectively, with reduced modulus. The amount to which the modulus is reduced is indicated in the figures as $E = 10$, $E = 10^2$, or $E = 10^3$. The number of iterations carried out by the finite element analysis is denoted by “5 iterations,” etc. All data will

be compared with previous established results as reported by Underwood et al, hereafter referred to as "the WVT report" [9,10]. The constitutive bilinear idealizations used in the present analysis are compared to the actual stress-strain curves of the materials used in the WVT report in Fig. 2.

In Fig. 3, the remote applied stress is 15.13 ksi. Figure 3 shows the plastic strain distribution and clearly illustrates the manner in which the Unimod technique develops a more accurate high strain region close to the crack tip. Our normal program (with no modulus reduction) is seen to be unsatisfactory near the crack tip as it fails to rise quickly enough to pick up the singular strains. Calculated values from the WVT report are somewhat better than our normal program. However, the WVT reports' calculated values also rise much too slowly very near the crack tip. The WVT reports' measured plastic strains are very close to the Unimod data. Unimod I(8), Unimod I(9), and Unimod II(8 and 9) appear to be more representative of true plastic strains than both the WVT calculated values and our normal program. The lack of experimental measurements of plastic strains right up to the crack tip prevents complete comparisons. Corresponding stress

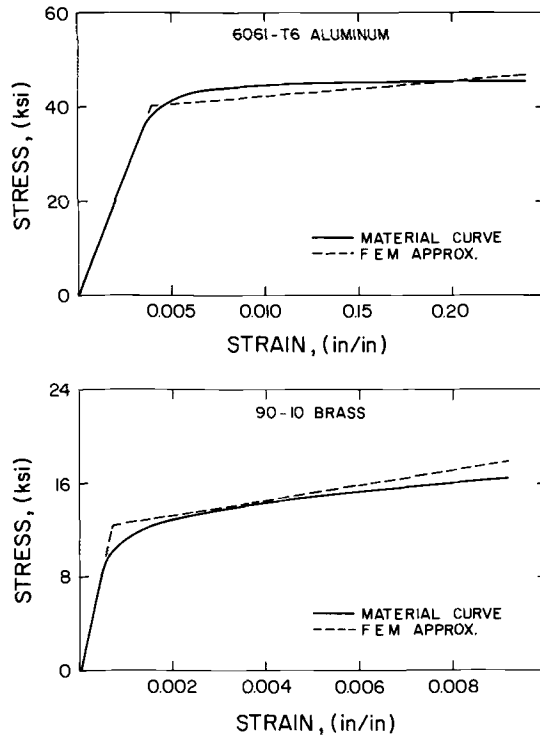


FIG. 2—Approximations of material stress-strain response used for finite element method (FEM).

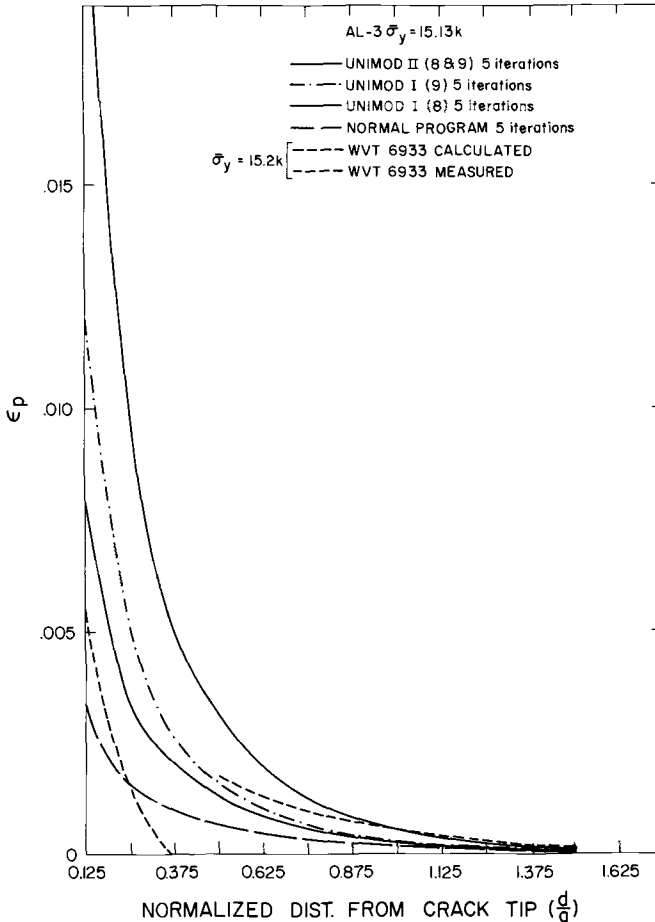


FIG. 3—Plastic strain distributions versus distance ahead of crack tip for 6061-T6 AL-3. $\bar{\sigma}_y = 15.13$ ksi.

distributions were found to be marginally different; the Unimod analyses indicated higher stresses close to the crack tip. It should be emphasized that the “normal program” data and that produced by Unimod II(8 and 9) were produced by the same computer program. The only change that was made was that Elements 8 and 9 near the crack tip were required to have an elastic modulus of unity in the second case. The grid used was rectangular, with characteristic dimensions of about 0.03 in. near the crack tip (see Fig. 1).

With increasing remote load, the inadequacy of the normal program becomes more apparent, as shown in Fig. 4. Here the remote stress is 20 ksi, that is, about half the yield stress. There is also a marked underestimation of the plastic strains by the WVT (calculated) data. An interesting

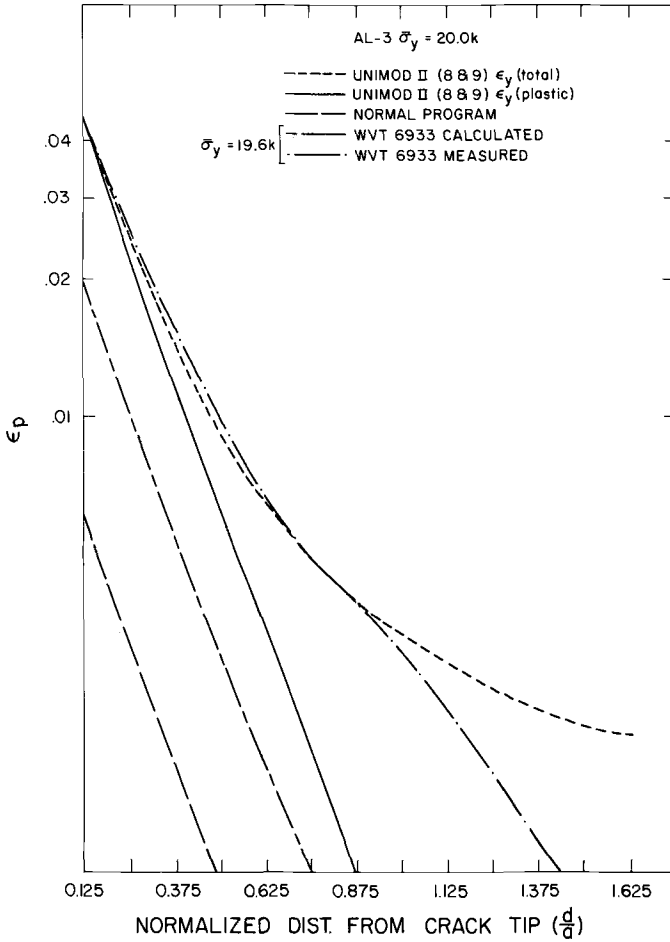


FIG. 4—Plastic strain distributions versus distance ahead of crack tip for 6061-T6 AL-3. $\bar{\sigma}_y = 20.0$ ksi.

feature of Fig. 4 is the nature of the good fit between Unimod II(8 and 9) for total strains and the WVT (measured) unloaded strains. In cases of high remote loading ($\sigma_y \simeq \sigma_{yield}/2$), the plastic zone apparently prevents some relaxation of the elastic singular stresses near the elastic-plastic boundary. Plastic strains calculated by the Unimod II(8 and 9) scheme, and the measured strains match well nearer the crack tip. Again, the stress distributions were found to be comparable to each other.

In Figs. 5 through 7, a different strain-hardening material, 90-10 Brass, is analyzed. For a remote stress of $\bar{\sigma}_y = 7.5$ ksi, Fig. 5 clearly differentiates the high strain region developed by Unimod II and the normal program. Here the yield stress is much lower than that of aluminum; consequently, $\bar{\sigma}_y = 7.5$ ksi is greater than half the yield stress. As expected, the Unimod

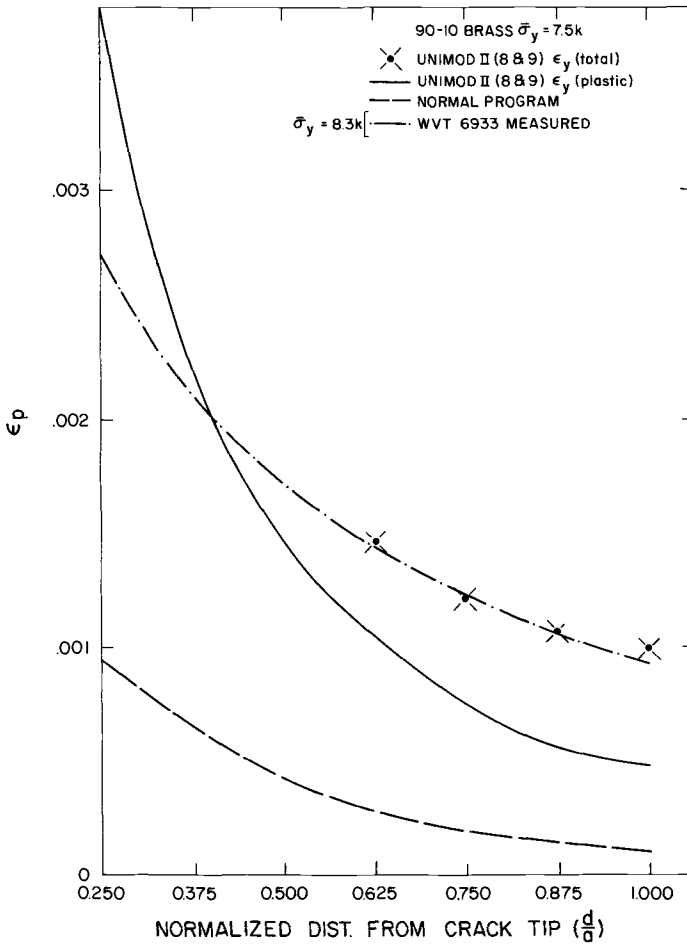


FIG. 5—Plastic strain distributions versus distance ahead of crack tip for 90-10 Brass. $\bar{\sigma}_y = 7.5$ ksi.

II(8 and 9) analysis comes closer to the available measured data. As noted previously, the total strains calculated by the Unimod II analysis more accurately match the elastic singular region of the measured values. Strain distributions for an increased loading ($\bar{\sigma}_y = 8.5$ ksi) are shown in Fig. 6. In this case, the Unimod II results appear to overestimate the strains. The effect of changing the value of the local elastic modulus was also studied in this figure. It was found that there was no apparent change in the strain (or stress) distributions when the elastic modulus of the Unimod elements was varied by three orders of magnitude, namely, $E = 10$, 10^2 , and 10^3 psi. In other words, it did not matter how small the elastic modulus at the crack tip was chosen to be as long as it was several orders of magni-

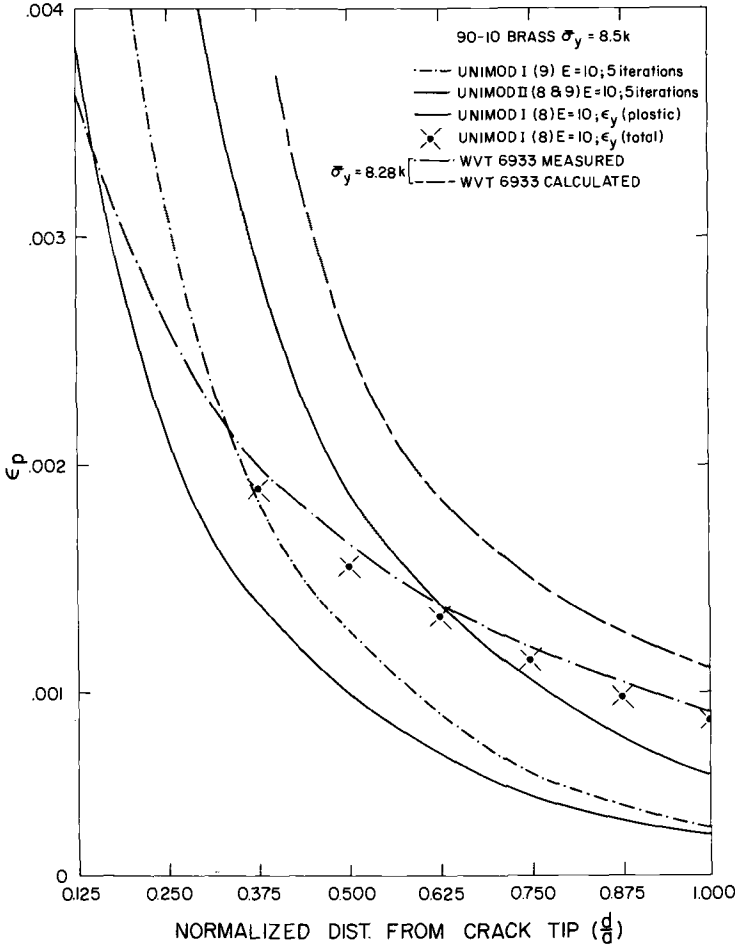


FIG. 6—Plastic strain distributions versus distance ahead of crack tip for 90-10 Brass. $\bar{\sigma}_y = 8.5$ ksi.

tude less than the normal elastic modulus. This fact adds greatly to the versatility and generality of the Unimod technique.

Figure 7 is a normalized stress representation for 90-10 Brass for $\bar{\sigma}_y = 8.5$ ksi. Unimod analysis stresses are somewhat higher than the normal program stresses near the crack tip. Both the stress (and strain) distributions converge away from the crack tip. This fact is also demonstrated by Fig. 3.

In general, it was found that, with increasing remote load, Unimod II produced the best results for strain distributions at a singularity in the present case; at the same time, the corresponding stresses appeared to be reasonable. At lower remote loads either Unimod I(8) or Unimod I(9) was

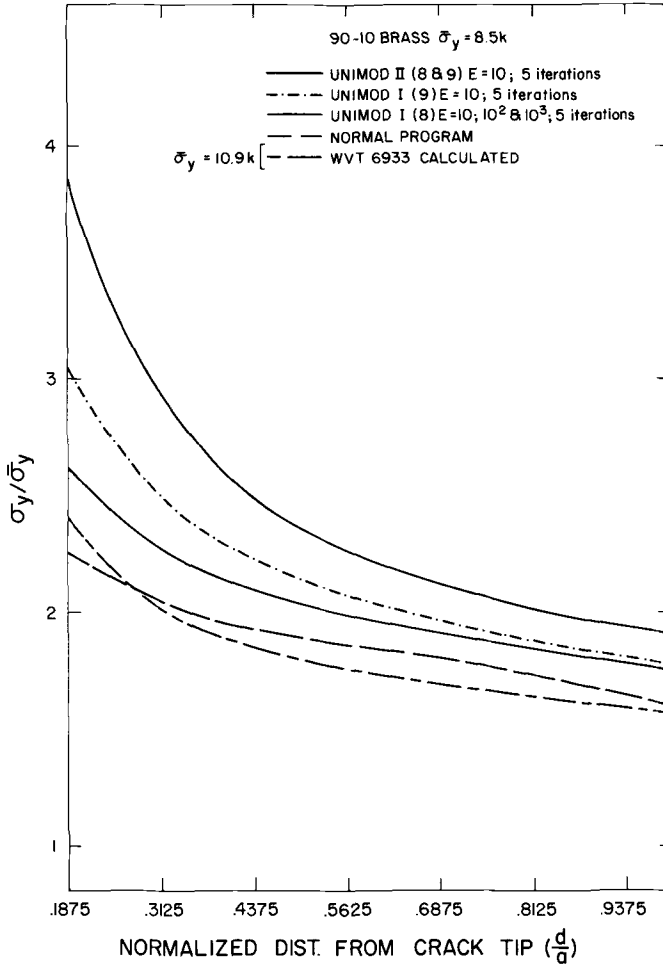


FIG. 7—Normalized stress distributions versus distance ahead of crack tip for 90-10 Brass. $\bar{\sigma}_y = 8.5$ ksi.

satisfactory. It is necessary, however, to establish a method of optimizing the choice of elements to be assigned reduced stiffness for problems when no experimental data is available to support a post-analysis evaluation. Two such methods, described in the following, are suggested by the authors.

A fairly widely accepted criterion for the choice of an optimum finite element grid, in general, is the uniformity of the strain energy values for each element throughout the grid system [11-13]. For singularity cases, this idea can be extended so that an optimum grid is one in which the average energy of the elements in the singular region is as near as possible to that of elements remote from the singularity in the uniform stress region. This technique is illustrated by Fig. 8 and can be used as a quantitative

method for the determination of the optimum number of relaxed elements. Figure 8 shows that the Unimod II analysis should be optimum for this case of high remote (applied) stress which is borne out by comparison with experimental data. (See Fig. 4, for example.) It so happens that the average energy per element for the Unimod II scheme is nearly identical to the remote average in this case. This criterion is a sensitive one as can be determined by the large differences between mean energies for Unimod II, Unimod I, and the normal program.

A more direct optimization scheme is afforded by analogy to the Irwin correction factor for small-scale yielding, as discussed in the beginning of this paper. If that analogy holds, r_y should predict the distance ahead of the crack that should be assigned negligible stiffness. For our edge crack specimen

$$r_y = \frac{a}{2} \left[C \frac{\sigma_\infty}{\sigma_y} \right]^2 \tag{2}$$

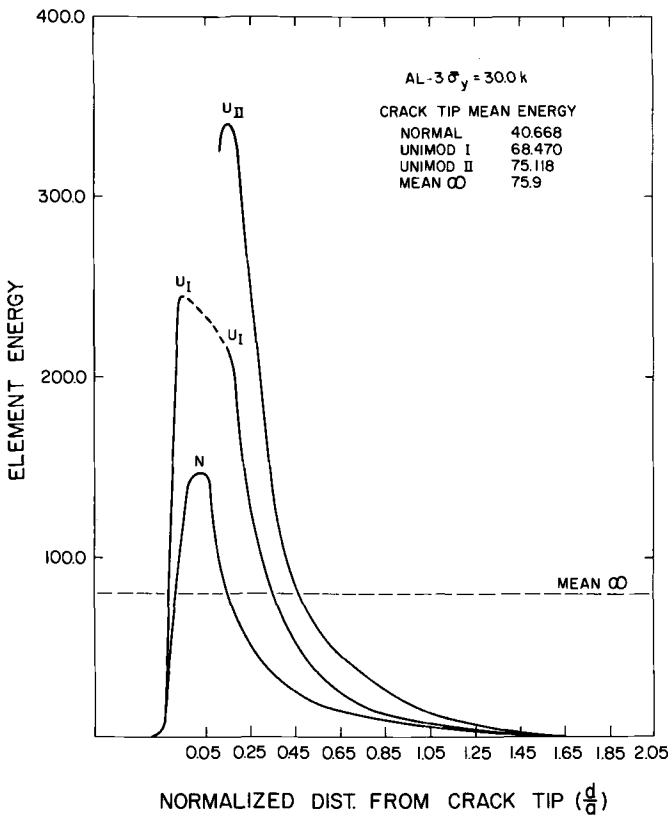


FIG. 8—Strain energy per element as a function of a distance from the crack tip along the crack axis, with corresponding average values in the singular and remote regions.

where C is a function of the ratio of crack length (a) to specimen width (w), and σ_∞ is the applied remote stress. For the present case of aluminum with $\sigma_\infty = 20.0$ ksi, $\sigma_y = 39.8$ ksi, $C = 1.29$ for $a/w = 0.3$, and $a = 0.3$ in. for unit width, $r_y = 0.063$ in. For the present grid, two elements would have a width of 0.0625 in. so that this technique would predict that Unimod II results would be very good for this case. Figure 4 shows that this is, in fact, so. For the present case of aluminum with $\sigma_\infty = 15.13$ ksi, $\sigma_y = 39.8$ ksi, $C = 1.29$ for $a/w = 0.3$ for unit width, $r_y = 0.036$ in. The method then predicts that Unimod I should be used with the present grid for most accurate results. Figure 3 verifies this prediction with experimental evidence. Similar results are obtained for the brass analyzed. This simple and direct method worked very well, in general, for our present analysis. However, results obtained using r_y are most satisfactory for nearly-perfect plastic materials and small-scale yielding.

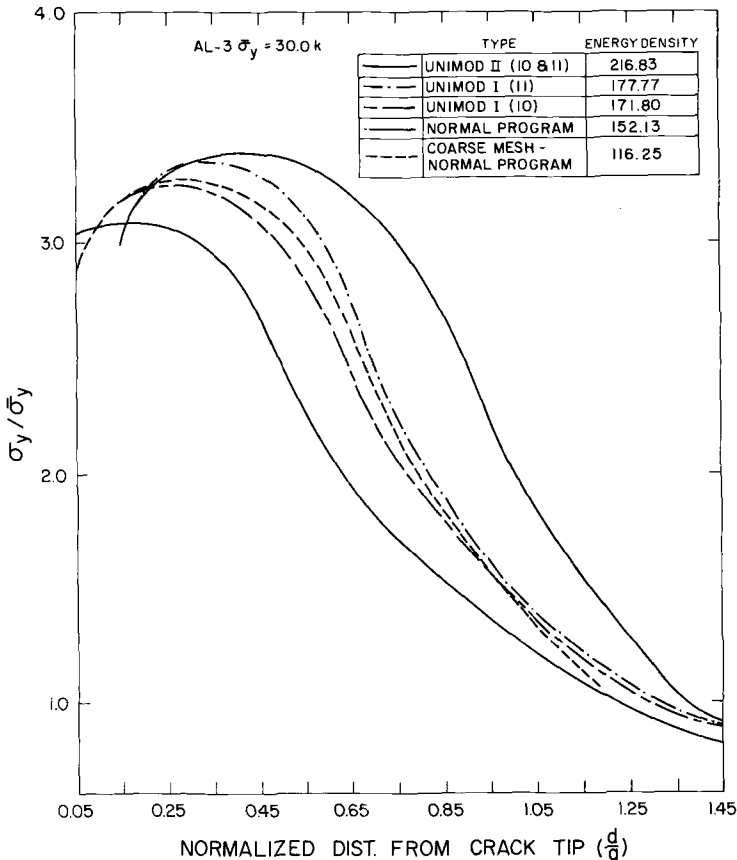


FIG. 9—Normalized stress distributions versus distance ahead of crack tip for 7076 AL. $\bar{\sigma}_y = 30.0$ ksi.

Comparisons with change in grid size are studied in Figs. 9 and 10. 7076 AL was modeled with $E_{\text{plastic}}/E_{\text{elastic}} \approx 0.0$ and a remote load of 30.0 ksi was applied. Figure 9 is a stress plot, and shows that the various curves tend to converge away from the crack tip. In the top of the figure is inset the stored strain energy values for the various types of analyses. The coarser the mesh, the lesser the stored potential energy. The changes in grid size are analogous to the various Unimod analyses. This aspect of the relationship can be verified by the respective stored potential energies in each case. Figure 10 shows a smaller plastic zone for the coarser grid size. As before, the high strain region is well developed by the Unimod analyses for this material with no strain hardening.

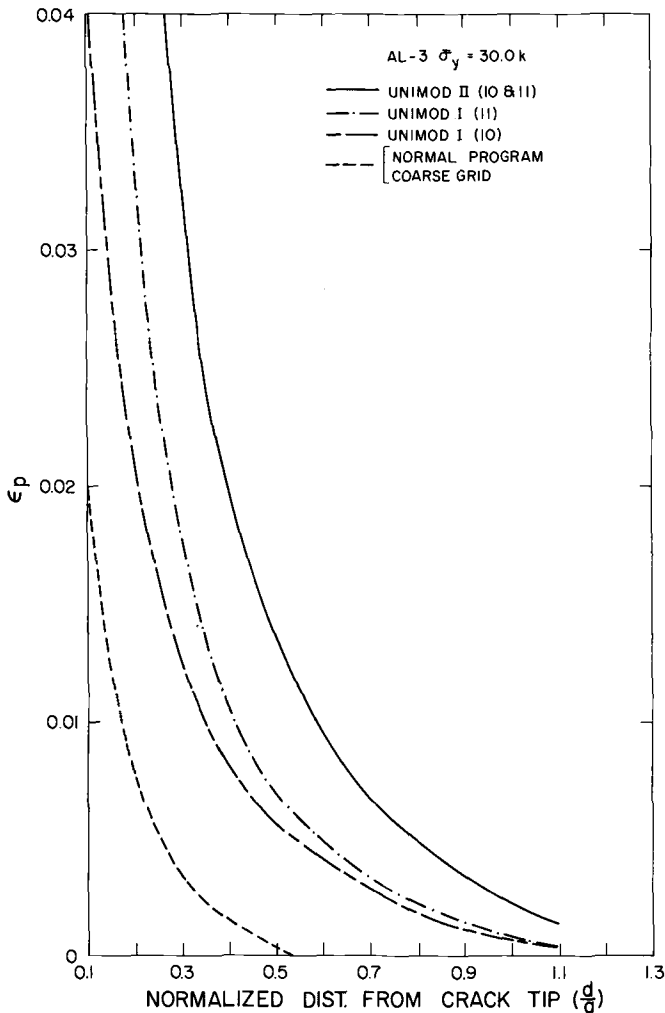


FIG. 10—Plastic strain distributions versus distance ahead of crack tip for 7076 AL. $\bar{\sigma}_y = 30.0 \text{ ksi}$.

Discussion and Conclusions

The data just reported (as well as a larger body of data in Ref 14) indicate that a simple singularity element can be obtained by reducing the elastic-plastic modulus of the element to unity. Some advantages of the method are the following.

1. It is completely general, that is, it can be used for any finite element program.

2. It is simple. It does not require major additions to a standard finite element program in order to develop a useful analysis of a crack or other singular defect.

3. It is extremely versatile. The most obvious point in support of this fact is made by noting that no special grid or specimen geometry is associated with the method. A crack, for example, can be inserted, removed, lengthened, or moved about from place to place using the *same* (reasonably fine) grid, a significant advantage to the fracture analyst or engineer. Moreover, changes of geometry do not affect it.

4. It is a flexible method. As shown by the present data, the method can be used for materials with widely varying strain-hardening characteristics. No special adaptation would be necessary to apply the technique to nonuniform materials.

The limitations of the Unimod technique should also be noted. To the extent that the choice of the number of elements near the crack tip to be relaxed to unit stiffness is discretionary, that decision represents a limitation on the accuracy of the method. However, this matter has been addressed from the standpoint of element strain energy values and relaxed length determinations based on the Irwin correction factor quite successfully in the present case. The degree to which this limitation can be overcome can be determined only by the success or failure of future applications. It should be noted that choosing the number of elements to be relaxed is an optimization process exactly analogous to choosing a specific discrete element grid. Changing the number of relaxed elements, however, is far simpler than changing the element grid.

A second limitation is created by the relaxation process itself in that the data generated by the relaxed elements themselves are not necessarily representative, at least so far as we are able to interpret it at this time. This is an important limitation since crack tip information needed for some fracture criteria is lost. However, since the other data in the neighborhood of the tip is improved, criteria such as the J-integral could be used with improved accuracy.

Finally, it should be emphasized that Unimod does not, in general, produce data with the same accuracy as many of the highly sophisticated specialized singularity programs in use today. However, the authors have

found it to be a very useful alternative to such methods which we use in more demanding circumstances. It is also believed that there is an urgent need for relatively simple, general methods of analysis which can be used by engineers to solve practical fracture mechanics problems which are beyond the scope of linear elastic fracture mechanics. Unimod is a step in that direction.

Acknowledgments

This research was carried out under the sponsorship of the Department of Defense, Contract No. DAA-F07-69-C-0444 monitored by Benet Laboratories, Watervliet Arsenal, Watervliet, N. Y. Their support and encouragement is gratefully acknowledged. The authors would also like to thank G. W. Swift for his valuable and tolerant assistance in various aspects of the computer manipulations.

References

- [1] Hilton, P. D. and Hutchinson, J., *Journal of Engineering Fracture Mechanics*, Vol. 3, 1971, pp. 435-451.
- [2] Swedlow, J. L., Williams, M. L., and Yang, W. H., *Proceedings*, First International Conference on Fracture, Vol. 1, 1965, pp. 259-282.
- [3] Rice, J. R. and Tracey, D. M., "Computational Fracture Mechanics," *Proceedings*, International Symposium on Numerical and Computer Methods in Structural Mechanics, Urbana, Illinois, Sept. 1971.
- [4] Hibbit, H. D., Marcal, P. V., and Rice, J. R., *International Journal of Solids and Structures*, Vol. 6, 1970, pp. 1069-1086.
- [5] Griffis, C. A., "Finite Element Analysis of Notched Tensile Specimens in Plane Stress," NRL Report 7278, Sept. 1971.
- [6] Carroll, W. E., "An Optimum Idealization in Discrete Element Analysis," Doctoral Dissertation, Dept. of Engineering Science & Mechanics, Va. Polytechnic Institute and State University, 1971.
- [7] McClintock, F. A. and Irwin, G. R., *Fracture Toughness Testing and Its Applications*, *ASTM STP 381*, American Society for Testing and Materials, 1964, pp. 85-113.
- [8] Wilson, E. L., "Finite Element Analysis of Two Dimensional Structures," Ph.D. Dissertation, University of California, Berkeley, 1963.
- [9] Underwood, J. H., Swedlow, J. L., and Kendall, D. P., "Experimental and Analytical Strains in an Edge-Cracked Sheet," Benet R. & E. Laboratory, Technical Report WVT-6933, Sept. 1969, Watervliet, N. Y.
- [10] Underwood, J. H., Swedlow, J. L., and Kendall, D. P., *Engineering Fracture Mechanics*, Vol. 2, 1971, pp. 183-196.
- [11] Oliviera, E. R. Arantes, "Optimization of Finite Element Solutions," *Proceedings*, 3rd Conference on Matrix Methods in Structural Mechanics, Wright-Patterson Air Force Base, Ohio, 1971.
- [12] Turcke, D. J. and McNiece, G. M., "A Variational Approach to Grid Optimization in the Finite Element Method," *International Conference on Variational Methods in Engineering*, University of Southampton, U. K., Sept. 1972.
- [13] McNiece, G. M. and Marcal, P. V., "Optimization of Finite Element Grids Based on Minimum Potential Energy," *Journal of Engineering for Industry, Transactions*, American Society of Mechanical Engineers, June 1972.
- [14] Reifsnider, K. and Nair, P., "Unimod: An Applications-Oriented Finite Element Scheme for Fracture Mechanics Analysis," VPI-E-73-18, College of Engineering, Virginia Polytechnic Institute and State University, Blacksburg, Va., April 1973.

Application of the J-Integral to Obtain Some Similarity Relations*

REFERENCE: Chang, S. J. and Witt, F. J., "Application of the J-Integral to Obtain Some Similarity Relations," *Fracture Analysis, ASTM STP 560*, American Society for Testing and Materials, 1974, pp. 226-239.

ABSTRACT: Experimental evidence seems to suggest that, for two elastic-plastic bodies which are geometrically similar to each other but with the same thickness and subjected to similar loadings, the ratio of their total energy inputs until the time of crack initiation is approximately equal to the ratio of their linear dimensions, independent of the amount of work hardening to be associated with the material. This result, as well as a set of other similarity conditions, is examined analytically in the present work from the J-integral criterion. It is shown that the similarity result in energy is exactly correct for rigidly plastic material as a consequence of Ilyushin's principle in plasticity. For the elastic-plastic material, if the two similar specimens are not extremely different in size, it can be justified for regions both close to and far from the crack tip. Under this condition, the ratio of their total energy inputs until the time of crack initiation will not be significantly influenced by the contributions from their transition regions and this similarity relation in energy may be a close approximation.

KEY WORDS: fracture properties, plastic deformation, plastic properties, Ilyushin's principle, elastic-plastic deformation, crack initiation

It is often desirable to predict the fracture condition for a larger specimen from the testing result of a smaller but geometrically similar specimen subjected to similar loading. For two linear and brittle elastic bodies which are geometrically similar to each other except of the same thickness, it is easy to show that for plane-strain conditions, the ratio of their energy inputs until the time of fracture is proportional to the ratio of their linear dimensions. The thickness of the two specimens has to be chosen adequately so that both of them satisfy the condition of plane-strain fracture. Experimental evidence [1,2]³ seems to suggest that this similarity condition

* Research sponsored by the U. S. Atomic Energy Commission under contract with Union Carbide Corporation.

¹ Mathematics Research Staff, Oak Ridge Laboratory, Oak Ridge, Tenn. 37830.

² Formerly, Director, Heavy Section Steel Technology Program; now with Westinghouse Electric Corporation, Madison, Pa. 15663.

³ The italic numbers in brackets refer to the list of references appended to this paper.

of energies just described for the linear elastic case may still be a good approximation for specimens tested in their elastic-plastic range under the condition of plane-strain fracture. It is interesting since this result is independent of the amount of work hardening to be associated with the material. If this result can be reasonably justified, it may offer a convenient and simple rule in fracture tests involving elastic-plastic behavior.

Recently, the J -integral [3] has been proposed by Begley and Landes [4,5] as a fracture criterion for elastic-plastic materials in which large-scale plasticity may be involved. To calculate the energy input up to the time of failure, and consequently the critical J value, the point of failure is defined to be that where the crack initiates. It is to be noted that for elastic-plastic fracture the computation of energy as required by the computation of the critical J value is fairly sensitive to how the point of fracture is defined. In some cases of elastic-plastic fracture, crack initiation does not generally coincide with maximum load or unstable growth. This question is even more important if the two specimens are different in size. It appears to be influenced by the geometry and size of the specimen as well as the material behavior of the body. This question seems to remain unresolved and is under investigation [6].

From the J -integral criterion, the similarity condition in energy as just described is shown to be a direct consequence from the condition that along each pair of the contours of integration for the J -integrals the ratio of the respective stress components can be assumed as a constant value. This assumption is then examined for different cases. It is obviously valid for linear elastic case. It is shown to be true as a result of Ilyushin's principle [7] for rigidly plastic materials which can be described by pure power law. Furthermore, the pure power law material is shown to be the only rigidly plastic material for which our assumption is correct at any point within the body. For the case of elastic-plastic fracture, the solutions for stress fields in an elastic-plastic body are influenced substantially by the size of the plastic zone. At fracture, the relative sizes of the plastic zones for geometrically similar specimens are generally not equal. It is not likely that our assumption can be correct exactly everywhere for the elastic-plastic case. However, by confining our analysis to specific regions within the elastic-plastic body, the assumption is justified for regions close to the crack tip from the singular solution of Rice and Rosengren [8] and of Hutchinson [9,10]. If the two specimens are not extremely different in size and both are elastic-plastic, there exists some evidence, such as the antiplane problem treated by Rice [11], that this assumption is approximately correct for a region either close to the crack tip or near the boundary. Under this condition, the ratio of their total energy inputs until the time of crack initiation may not be significantly influenced by the transition region, and this similarity relation in energy may be a close approximation. It is understood that we do not attempt to argue the extreme cases such as

to compare a fully plastic body with a geometrically similar but much larger specimen which behaves in a fully elastic manner. An interesting investigation along this line was also made recently by Merkle [12].

Some Preliminary Relations

In the analysis we assume that the material is nonlinear elastic so that the strain energy function exists and is a well-defined quantity. We are interested in deriving the fracture initiation conditions between two geometrically similar specimens but with the same thickness under similar loading conditions by the method of the J-integral [3]. At present we limit our analysis to the two-dimensional plane-strain condition and to the case of flat fracture. The J-integral in its two-dimensional form is

$$J = \int_{\Gamma} W dx_2 - T_i \frac{\partial u_i}{\partial x_1} ds \quad (1)$$

where W denotes the strain energy density, T_i is the traction vector, and u_i is the displacement vector. In Eq 1 the crack is assumed to be parallel to the x_1 -direction and Γ is any contour of integration enclosing the crack tip and terminating on the straight edges of the crack.

We shall restrict ourselves by assuming the material to be the Ramberg-Osgood type whose stress-strain relation is the well-known form

$$E\epsilon_{ij} = (1 + \nu) s_{ij} + \frac{1 - 2\nu}{3} \sigma_{kk} \delta_{ij} + \frac{3}{2} \alpha \frac{1}{\sigma_y^{n-1}} \sigma_e^{n-1} s_{ij} \quad (2)$$

By choosing this particular type of material, we shall treat the elastic-plastic solid as nonlinear elastic under the assumption of the deformation theory of plasticity as was done by Rice and Rosengren [8] and Hutchinson [9]. We have to, of course, assume that at any point within the contour of integration the material does not exhibit unloading.

In Eq 2 s_{ij} is the stress deviator

$$s_{ij} = \sigma_{ij} - \frac{1}{3} \sigma_{kk} \delta_{ij} \quad (3)$$

σ_y is the yield stress, and σ_e is the effective stress defined by

$$\sigma_e^2 = \frac{3}{2} s_{ij} s_{ij} \quad (4)$$

For $\sigma_e = \sigma_y$ the Mises yield condition is recovered. E , ν , n , and α in Eq 2 are Young's modulus, Poisson's ratio, the work hardening coefficient, and a material constant, respectively. It is convenient to separate Eq 2 into two parts: the first two terms of Eq 2 being denoted as the elastic strain $E\epsilon_{ij}^e$ and the last term as the plastic strain $E\epsilon_{ij}^p$.

The strain energy function based on Eq 2 is defined to be

$$w = \int \sigma_{ij} d\epsilon_{ij} = \sigma_{ij}\epsilon_{ij} - \int \epsilon_{ij} d\sigma_{ij} \tag{5}$$

which can be calculated as

$$w = \frac{1}{2E} [(1 + \nu) \sigma_{ij}\sigma_{ij} + \nu\sigma_{kk}^2] + \frac{n}{n + 1} \frac{\alpha}{E\sigma_y^{n-1}} \sigma_e^{n+1} \tag{6}$$

The first term denotes the elastic work w_e and the second denotes the plastic work w_p .

The Similarity Conditions

In this section, we shall analyze the fracture conditions for two-dimensional geometrically similar specimens subjected to similar loadings. That is, two geometrically similar bodies are of identical material behavior but with the same thickness. Hereafter, the thickness of the specimen is assumed to be chosen appropriately so that the plane-strain condition is satisfied. The analysis is based on the J-integral criterion. To evaluate the J-integral, we shall choose the contours of the integration to be located at the same relative positions within the two specimens. Suppose that the ratio of the linear dimensions of the two specimens is denoted by a constant, k_g . The ratio of the total lengths of the contours is obviously the same constant. The material behavior is not specified at the present moment.

We shall make an assumption that at any corresponding points along any pair of contours the ratio of their stress components is a constant value

$$k_s = \frac{\sigma_{ij}}{\sigma'_{ij}} \tag{7}$$

where a prime is used to denote the quantities for the second specimen. The validity of this assumption depends on the constitutive behavior of the material, the geometry of the specimen, and the boundary loading of the body. By using the condition that at the moment of crack initiation the J values for both specimens assume the same material constant, we shall derive a set of similarity conditions from the assumption made in Eq 7 and the property of the material.

The validity of the similarity conditions depends on whether the assumption (Eq 7) can be justified for the specific material and for the geometry of the problem. In the following sections, we shall discuss how the assumption shown in Eq 7 can be justified. For the linear elastic case, the ratio k_s is easily shown to be a constant value within the entire specimen. It is interesting to see in the next section that Eq 7 is true exactly for the rigidly plastic material with the property of work hardening. It is unlikely that

Eq 7 can be valid exactly for the case of elastic-plastic behavior. In this case the influence of plastic zone has to be taken into account. As we shall discuss later, if the two specimens are not quite different in size and both of them are elastic-plastic, Eq 7 tends to be a good approximation in regions both close to the boundary and close to the crack tip. Equation 7 is not to be applied as an approximation to the cases that the two specimens are extremely different in sizes so that their plastic zone sizes are severely out of proportion.

In the following analysis, both of the bodies are assumed to be elastic-plastic. On the application of the J-integral criterion, one observation may be made about the experimental measurement of the critical J , which is denoted by J_{Ic} for plane strain case. J_{Ic} value was determined by Begley and Landes from the measurement of crack initiation, which in their cases coincides with the maximum load. In some cases of elastic-plastic fracture the crack initiation and the unstable growth do not always coincide to each other. It appears to be influenced by the geometry and size of the specimen as well as the material behavior of the body. The question seems to be unresolved. An investigation was made recently by Corten [6].

Consider the case in which the J-integral is evaluated within the plastic region, so that the effect due to the elastic strain is negligible as compared with that due to the plastic strain. The first term of the strain energy function in Eq 6 is negligible and, consequently, the J-integral in Eq 1 should assume a form with the effect of plastic strain only. The ratio k_s as expressed in terms of the strain components is

$$k_s = \frac{\sigma_{ij}}{\sigma_{ij}'} = \left(\frac{\epsilon_{ij}}{\epsilon_{ij}'} \right)^{1/n} \quad (8)$$

Substituting Eqs 6 and 8 into Eq 1, we obtain

$$J = \int_{\Gamma} \left(w dx_2 - T_i \frac{\partial u_i}{\partial x_1} ds \right) = k_s^{n+1} k_{\theta} J' \quad (9)$$

Since the two specimens are made of identical material, we have

$$J_{Ic} = J_{Ic}' = k_s^{n+1} k_{\theta} J_{Ic}' \quad (10)$$

which leads to a simple relation

$$k_s = \left(\frac{1}{k_{\theta}} \right)^{1/(n+1)} \quad (11)$$

Consequently, the ratio of the critical energies per unit area is

$$k_w = \frac{w}{w'} = k_{\theta}^{-1} \quad (12)$$

and the ratio of the critical strains is

$$k_e = \frac{\epsilon_{ij}}{\epsilon_{ij}'} = \left(\frac{1}{k_\theta} \right)^{1-1/(n+1)} \tag{13}$$

A set of similarity relations is therefore obtained.

Since n is the work hardening coefficient of the material, the material will tend to become perfectly plastic for increasing n . If we assume that the second specimen is smaller, $k_\theta > 1$, then the fracture stress for this specimen will be larger, $k_s < 1$, as it should be. However, with fixed k_θ but increasing n , k_s will approach the limit, 1. Obviously, it indicates that for perfectly plastic material the fracture stresses for both specimens remain the same. For critical fracture strain, Eq 13 shows that, for increasing n , k_e tends to k_θ^{-1} ; this provides a measure on the critical condition which is more sensitive than their fracture stresses, which are almost equal.

Consider the case that the contour of integration is located completely within the elastic region. The result should be a set of relations which correspond to that for the linear elastic case. In Eq 6, the second term due to the plastic strain is negligible and

$$k_s = \frac{\sigma_{ij}}{\sigma_{ij}'} = \frac{\epsilon_{ij}}{\epsilon_{ij}'} \tag{14}$$

After substituting Eqs 6 and 14 into the J-integral, we obtain a set of linear elastic conditions

$$k_s = \frac{1}{\sqrt{k_\theta}} \tag{15}$$

$$k_{v'} = \frac{1}{k_\theta} \tag{16}$$

and

$$k_e = \frac{1}{\sqrt{k_\theta}} \tag{17}$$

which correspond to the ratios for the fracture stresses, the fracture energies, and the fracture strains.

The more interesting part, however, seems to be the result of the energy ratio shown both in Eq 12 and in Eq 16. It is invariably proportional to $1/k_\theta$, irrespective of the work hardening parameter n . For some time this result has appeared repeatedly from experimental results where plane-strain condition exists as discussed by Witt [1,2]. The equivalent energy concept originated from these results.

Ilyushin's Principle for Rigidly Plastic Material

Ilyushin's principle [7] states that for rigidly plastic material which follows the pure power law in shear, if the boundary traction is increased

by the factor q , the stress field within the solid body will be increased by the same factor and the strain will be increased by the factor q^n , where n is the work hardening coefficient of the material in shear. From this principle, our assumption stated by Eq 7 is easily shown to be satisfied throughout the solid body and, therefore, the similarity relations just derived are exactly correct for rigidly plastic material. Furthermore, for a rigidly plastic solid, the pure power law material is the only material which has the property of increase of the stress field in exact proportion to increase of the boundary traction. Consequently, for elastic-plastic material it is not likely that we can use the assumption (Eq 7) to derive exactly the similarity relation of the fracture energies. We may obtain the approximate similarity relations by checking the appropriateness of the assumption in different regions of the specimen. This will be illustrated in the following sections.

If the material is incompressible and its behavior in shear follows a pure power law relation

$$e_{ij} = A\sigma_e^{n-1}s_{ij} \quad (18)$$

where e_{ij} and s_{ij} are the deviatorial strain and stress, respectively, and A is a material constant, then, for a constant q , $q^n e_{ij}$ and $q\sigma_{ij}$ will satisfy the same constitutive equations as well as the condition of incompressibility. Suppose σ_{ij} is the solution of a problem with its strain components e_{ij} . Since $q^n e_{ij}$ and $q\sigma_{ij}$ will satisfy the equations of equilibrium, they are also the solution of a problem of the same geometry. However, in this problem the boundary traction is equal to the previous boundary traction multiplied by the factor q .

Equation 18 implies the relation between the effective stress σ_e and the effective strain ϵ_e

$$\epsilon_e = A\sigma_e^n \quad (19)$$

We shall see in the following that for Ilyushin's principle to be true Eq 19 is the only possible relation between the effective stress σ_e and the effective strain ϵ_e for an incompressible material. Let σ_{ij}^* be the solution of the problem with ϵ_{ij}^* as its corresponding strain components. For any constant q of the new set of stress components

$$\sigma_{ij} = q\sigma_{ij}^* \quad (20)$$

will satisfy the equations of equilibrium. Similarly,

$$\epsilon_{ij} = p\epsilon_{ij}^* \quad (21)$$

where p is another constant, will satisfy the equations of compatibility. Since σ_{ij}^* is the solution of the problem it must satisfy constitutive equations of the form

$$e_{ij}^* = \frac{\Phi(\sigma_e^*)}{\sigma_e^*} s_{ij}^* \quad (22)$$

and the condition of incompressibility. Equation 22 implies

$$\epsilon_e^* = \Phi(\sigma_e^*) \tag{23}$$

If σ_{ij} is also a solution, then it must have

$$\epsilon_e = \Phi(\sigma_e) \tag{24}$$

Combining Eqs 20, 21, 23, and 24, we obtain a condition for the function Φ as

$$p(q) \Phi(\sigma_e^*) = \Phi(q\sigma_e^*) \tag{25}$$

In this equation, q and σ_e^* can be viewed as two independent variables. The functional form of Φ can be determined by the following procedure. By differentiating Eq 25 by q and σ_e^* and dividing the two resulting equations, we obtain

$$\frac{p'(q)}{p(q)} \frac{\Phi(\sigma_e^*)}{\Phi'(\sigma_e^*)} = \frac{\sigma_e^*}{q} \tag{26}$$

or

$$q \frac{p'(q)}{p(q)} = \sigma_e^* \frac{\Phi'(\sigma_e^*)}{\Phi(\sigma_e^*)} = n \tag{27}$$

Equation 27 must be equal to a constant n because both q and σ_e^* can be varied independently. Integration of Eq 27 yields

$$\Phi(\sigma_e) = A\sigma_e^n \tag{28}$$

and

$$p(q) = Bq^n \tag{29}$$

where $B = 1$ in view of Eq 25. Hence, the only relation between the effective stress and the effective strain is a pure power law and $p = q^n$ is the necessary relation between the stress and the strain. Thus, it is easy to conclude that the increase of the stress within the body will be in exact proportion of the boundary traction only if the material follows the pure power law in shear. In particular, material which has a linear range in shear followed by a nonlinear property and the elastic-plastic material are excluded from this class.

Singular Solution Near the Crack Tip

The similarity results obtained in the preceding section depend mainly on our assumption in Eq 7 that k_s is a constant value along the corresponding contours, since, otherwise, we shall not be able to factor out the ratio k_θ from the integral sign. This assumption, unfortunately, is not easily shown for nonlinear materials. At present, we are able to show that it is approximately correct for the region close to the crack tip where the singular solution of Rice and Rosengren [8] and Hutchinson [9] applies.

In fact, this singular solution near the crack tip is a general result for the specimen of Ramberg-Osgood material. The solution is not restricted to the case of small-scale yielding and is equally valid for the case when the yielding zone is of considerable size. For small-scale yielding, the nonlinear stress intensity factor can be determined easily from the linear elastic solution. The physical meaning of the stress intensity factor, K , is shown in the stress components near the crack tip as expressed by Eqs 33, 34, and 35. In addition, for the large-scale yielding the nonlinear stress intensity factor can be determined as follows. Similar to Hutchinson's result for the two-dimensional plane stress case, the stress intensity factor for this case is

$$K = \left(\frac{1}{\alpha}\right)^{1/(n+1)} \left(\frac{J}{I}\right)^{1/(n+1)} \quad (30)$$

where J is the J value of the material in nondimensionalized form, and I is a constant which depends only on the work hardening coefficient n . With this value of K , the stress components near the crack tip can be expressed in terms of the stress function

$$\varphi = Kr^s \tilde{\varphi}(\theta) \quad (31)$$

where both r and $(\tilde{\varphi}\theta)$ are nondimensional quantities, not affected by the size of the specimen. In Eq 31

$$s = \frac{2n + 1}{n + 1} \quad (32)$$

The stress components are

$$\sigma_r = Kr^{s-2} \left(s\tilde{\varphi} + \frac{d^2\tilde{\varphi}}{d\theta^2} \right) \sigma_y \quad (33)$$

$$\sigma_\theta = Kr^{s-2} s(s-1) \tilde{\varphi} \sigma_y \quad (34)$$

$$\sigma_{r\theta} = Kr^{s-2} (1-s) \frac{d\tilde{\varphi}}{d\theta} \sigma_y \quad (35)$$

where σ_y is the yielding stress. Obviously, the assumption made in Eq 7 is satisfied by the set of stress components just listed.

Elastic-Plastic Problems

In this section we shall discuss the applicability of Eq 7 to an elastic-plastic body. This question is related to but more stringent than the question of proportional loading. It can be seen that if the condition of proportional loading is satisfied at some point within the body, then the different stress components at this point will be related to each other by fixed ratios which are not influenced by the increasing boundary loading. In this case, there can be only one proportionality constant k_s , which was defined by Eq 7, for all stress components at this particular point. For Eq 7, not only

should there be proportional loading so that there is a single k_s for each point but also the constant should be independent of the position along the path of integration for the J-integral.

In many cases [13] the condition of proportional loading has been shown to be a very close approximation. Frequently, appreciable deviation comes from the region near the moving elastic-plastic boundary owing to the increase of the boundary loading. Hence the possible deviation of assumption (Eq 7) comes from this region at least.

An interesting result was obtained in one problem [13]; the condition of proportional loading was satisfied exactly in a region of the body as soon as the elastic-plastic boundary had passed through the region. In general this condition cannot be satisfied. Thus there may not be a single constant k_s there. As shown before the region close to the crack tip, the Eq 7 is approximately correct. This implies that the condition of proportional loading is also satisfied there. We shall show by an example in this section that Eq 7 is also satisfied for regions far from the crack tip.

A general strain-plane method for the problem of elastic-plastic bodies subjected to longitudinal shear on their boundary was devised by Rice [11]. In particular, a crack problem of this kind was solved by this method. From this example we are able to demonstrate that our Eq 7 is valid both far from and close to the crack tip. Consequently, our similarity relations are valid in both of these areas, in this particular problem. If the two specimens are not extremely different in size such that the plastic zones are not severely out of proportion, Eq 7 is anticipated to be a close approximation in these two regions with sufficient areas. The total energy of fracture may not be significantly influenced by the contribution from the area near the elastic-plastic boundary. The ratio of the total fracture energies for the two geometrically similar specimens each with unit thickness may be approximately proportional to the ratio of their linear dimensions. The solution of Rice is generally for an elastic-plastic body under large-scale yieldings but the boundary traction is restricted to longitudinal shear. It should be noted that in the previous sections our assumption is actually proved for those cases, but in the present section we can only demonstrate that it is consistent with this example.

To solve the elastic-plastic problems under longitudinal shear, Rice converts the only nonvanishing shear strains ϵ_1 and ϵ_2 independent variables, whereas the physical coordinates x_1 and x_2 become dependent variables. The far field solution is transformed to the region close to the origin in the strain plane. An advantage of this method is to reduce the nonlinear problem into a linear one, so that the method of separation of the variables can be employed. The solution is represented by a series form which is used to match the elastic solution across the elastic-plastic boundary. A drawback of this method in solid mechanics is that it has to be limited to the longitudinal shear problem or to other problems with a high degree of

symmetry, since, otherwise, the number of strain components exceeds the number which can be handled conveniently.

For an arbitrary stress-strain relation, which relates the principal stress and the principal strain

$$\sigma = f(\epsilon) \quad (36)$$

the equation of equilibrium can be expressed as

$$\frac{\partial x_1}{\partial \sigma_1} + \frac{\partial x_2}{\partial \sigma_2} = 0 \quad (37)$$

if σ_1 and σ_2 are used as the independent variables. Similarly, the equation of compatibility can be expressed as

$$\frac{\partial x_1}{\partial \epsilon_1} - \frac{\partial x_2}{\partial \epsilon_2} = 0 \quad (38)$$

where ϵ_1 and ϵ_2 are the independent variables. In Eq 37 σ_1 and σ_2 are their corresponding strain components. Now Eq 38 is satisfied if we introduce a function ψ by

$$x_1 = \frac{\partial \psi}{\partial \epsilon_2} \quad (39)$$

$$x_2 = \frac{\partial \psi}{\partial \epsilon_1} \quad (40)$$

Substituting

$$\frac{\partial x_1}{\partial \sigma_1} = \frac{\partial \epsilon_1}{\partial \sigma_1} \frac{\partial x_1}{\partial \epsilon_1} + \frac{\partial \epsilon_2}{\partial \sigma_1} \frac{\partial x_1}{\partial \epsilon_2} \quad (41)$$

$$\frac{\partial x_2}{\partial \sigma_2} = \frac{\partial \epsilon_1}{\partial \sigma_2} \frac{\partial x_2}{\partial \epsilon_1} + \frac{\partial \epsilon_2}{\partial \sigma_2} \frac{\partial x_2}{\partial \epsilon_2} \quad (42)$$

into Eq 37, we obtain the governing equation of ψ as

$$\frac{\partial \epsilon_1}{\partial \sigma_1} \frac{\partial^2 \psi}{\partial \epsilon_1^2} + \left(\frac{\partial \epsilon_1}{\partial \sigma_2} + \frac{\partial \epsilon_2}{\partial \sigma_1} \right) \frac{\partial^2 \psi}{\partial \epsilon_1 \partial \epsilon_2} + \frac{\partial \epsilon_2}{\partial \sigma_2} \frac{\partial^2 \psi}{\partial \epsilon_2^2} = 0 \quad (43)$$

which is linear in ψ .

If Eq 43 is expressed in polar coordinates by

$$\epsilon e^{i\varphi} = \epsilon_2 - i\epsilon_1 \quad (44)$$

$$\sigma e^{i\varphi} = \sigma_2 - i\sigma_1 \quad (45)$$

where i is the unit imaginary number, then we obtain

$$\frac{\sigma(\epsilon)}{\epsilon \sigma'(\epsilon)} \frac{\partial^2 \psi}{\partial \epsilon^2} + \frac{1}{\epsilon} \frac{\partial \psi}{\partial \epsilon} + \frac{1}{\epsilon^2} \frac{\partial^2 \psi}{\partial \varphi^2} = 0 \quad (46)$$

In the elastic region, Eq 46 reduces to the Laplace equation. Let

$$\zeta = \frac{\epsilon}{\epsilon_0} e^{i\varphi} = \frac{\epsilon_2 - i\epsilon_1}{\epsilon_0} \tag{47}$$

where ϵ_0 is the yielding strain at the elastic-plastic boundary. In the elastic region, $|\zeta| < 1$, which is close to the boundary,

$$\zeta \rightarrow s = \frac{\sigma_\infty}{\sigma_0} = \frac{\epsilon_\infty}{\epsilon_0} \tag{48}$$

where σ_∞ is the longitudinal shear applied at the boundary and ϵ_∞ is the corresponding strain. It is interesting to see that the far field solution is transformed to a region which is close to the origin in the strain plane. The boundary of the specimen is transformed to a “crack” in the strain plane. In this region the solution is elastic. Near the “crack tip” of the transformed specimen, a singular solution is obtained as

$$\frac{-x_1 + ix_2}{a} = \frac{s}{\sqrt{\zeta^2 - s^2}} (f(s) - 1) \tag{49}$$

where a is the crack length. Obviously ζ is close to s if $(-x_1 + ix_2)/a$ tends to a large value. For two geometrically similar specimens we easily see that for some relative position

$$\frac{(\zeta_1/s_1)^2 - 1}{(\zeta_2/s_2)^2 - 1} = \left[\frac{f(s_1) - 1}{f(s_2) - 1} \right]^2 \tag{50}$$

which can be reduced to a more convenient form

$$\left(\frac{\zeta_1}{\zeta_2} \right)^2 \left(\frac{s_2}{s_1} \right)^2 = 1 + \left[\left(\frac{f(s_1) - 1}{f(s_2) - 1} \right)^2 - 1 \right] \left[1 - \left(\frac{s_2}{\zeta_2} \right)^2 \right] \tag{51}$$

Since $1 - (s_2/\zeta_2)^2$ is a small number, we conclude that assumption (Eq 7) is approximately true with a deviation which is indicated by the second term on the right-hand side of Eq 51. Furthermore, if the two specimens are not extremely different in size and s is appreciably smaller than one, then a rough estimate, according to Rice’s result, shows for $\lambda = 1$ that $1 - f(s) \approx 1 + (\pi/4) B_0 C_1 s^2$. For $1/n = 0.3$, $B_0 C_1 \approx 0.54$. Hence, the number in the first square bracket of Eq 51 is smaller than one and is able to contribute to the approximation shown in Eq 7. This helps to extend the region of validity of Eq 7 from the boundary of the specimen. As mentioned by Rice, $f(s) = 0$ for a completely elastic specimen. For this case

$$\frac{\zeta_1}{\zeta_2} = \frac{s_1}{s_2} \tag{52}$$

which is independent of s_2/ζ_2 , as expected.

For either small-scale or large-scale yielding, the function ψ as defined by Eqs 39 and 40 near the crack tip assumes a form

$$\psi = D_1 \left(\frac{\epsilon}{\epsilon_0} \right)^{-1/n} \sin \varphi \quad (53)$$

where D_1 is a constant and n is the work hardening coefficient of the elastic-plastic material. Thus

$$x_1 = -D_1 \frac{1}{\epsilon} \left(\frac{\epsilon}{\epsilon_0} \right)^{-1/n} \left(\cos^2 \varphi - \frac{1}{n} \sin^2 \varphi \right) \quad (54)$$

$$x_2 = D_1 \frac{1}{\epsilon} \left(\frac{\epsilon}{\epsilon_0} \right)^{-1/n} \left(\frac{1}{n} + 1 \right) \sin \varphi \cos \varphi \quad (55)$$

The constant D_1 is linearly dependent on the linear dimension of the specimen. Therefore at the same relative position of two geometrically similar specimens, the preceding equations show that our Eq 7 is satisfied. It is seen that if the region is not very small, then Eq 53 for ψ will contain different powers of ϵ .

Discussion

It is interesting to see that from Ilyushin's principle the similarity relations are rigorously valid for a rigidly plastic material with the property of work hardening. Hence, the ratio of total fracture energies for two geometrically similar specimens each with unit thickness is proportional to the ratio of their linear dimensions. This is the basis of the equivalent energy method provided that the plane-strain assumption is satisfied.

From the singular solution of Rice and Rosengren and of Hutchinson, we have shown the validity of the similarity relation in fracture energy for regions close to the crack tip. In fact the independence of this similarity relation on the work hardening coefficient is not surprising, as can be seen from their result that the structure of the energy density is invariably proportional to $1/r$ where r is the distance from the point to the crack tip, irrespective of the nonlinearity of the material. This similarity relation can also be regarded as an immediate consequence from Neuber's result [14] that for any nonlinear material the product of the stress concentration factor and the strain concentration fact is invariably proportional to the square of the product of their Hookian counterparts.

Our similarity relation on the total fracture energy depends heavily on whether the contribution due to the region near the elastic-plastic boundary will significantly influence the assumption made in Eq 7. It will be interesting to investigate the question quantitatively. We shall make some calculation for this purpose later.

On the demonstration of our result by Rice's solution, it is understood that his method is limited to the antiplane problems. Consequently, our

result is also dictated by the same limitation. We shall investigate later any possible generalization to the inplane case similar to the case discussed by Gowda and Topper [18]. It may also be interesting to investigate the effect of large deformation [16].

Acknowledgment

We are indebted to J. R. Rice of Brown University for his helpful suggestions, to J. G. Merkle of Oak Ridge National Laboratory, and H. T. Corten of the University of Illinois for valuable discussions,

References

- [1] Witt, F. J. and Mager, R. T., *Nuclear Engineering and Design*, Vol. 17, 1971, pp. 91–102.
- [2] Witt, F. W., *Nuclear Engineering and Design*, Vol. 20, 1972, pp. 237–249.
- [3] Rice, J. R., *Journal of Applied Mechanics*, Vol. 25, 1968, pp. 379–386.
- [4] Begley, J. A. and Landes, J. D. in *Fracture Toughness, ASTM STP 514*, American Society for Testing and Materials, 1972, pp. 1–20.
- [5] Landes, J. D. and Begley, J. A. in *Fracture Toughness, ASTM STP 514*, American Society for Testing and Materials, 1972, pp. 24–39.
- [6] Corten, H. T., private communication, and Zaverl, F., Jr., “Influence of Specimen Dimension on J_c Fracture Toughness Test,” Master’s thesis, Dept. of Theoretical and Applied Mechanics, University of Illinois, Urbana, 1974.
- [7] Ilyushin, A. A., *Applied Mathematics and Mechanics*, Vol. 10, 1946, pp. 347–356.
- [8] Rice, J. R. and Rosengren, G. F., *Journal of the Mechanics and Physics of Solids*, Vol. 16, 1968, pp. 1–12.
- [9] Hutchinson, J. W., *Journal of the Mechanics and Physics of Solids*, Vol. 16, 1968, pp. 13–31.
- [10] Hutchinson, J. W., *Journal of the Mechanics and Physics of Solids*, Vol. 16, 1968, pp. 337–347.
- [11] Rice, J. R., *Journal of Applied Mechanics*, Vol. 34, 1967, pp. 287–298.
- [12] Merkle, J. G. in *Progress in Flaw Growth and Fracture Toughness Testing, ASTM STP 536*, American Society for Testing and Materials, 1973, pp. 264–280.
- [13] Budiansky, B., *Applied Mathematics and Mechanics*, Vol. 35, 1971, pp. 40–48.
- [14] Neuber, H., *Journal of Applied Mechanics*, Vol. 28, 1961, pp. 544–550.
- [15] Gowda, C. V. Byre and Topper, T. H., *Journal of Applied Mechanics*, Vol. 37, 1970, pp. 77–84.
- [16] Chang, S. J., *Journal of Applied Mathematics and Physics*, Vol. 23, 1972, pp. 149–152.

C. B. Buchalet¹

Fracture Mechanics Evaluation of the Integrity of an Inlet Nozzle of a Pressurized Water Reactor Vessel Following a Postulated Loss of Coolant

REFERENCE: Buchalet, C. B., "Fracture Mechanics Evaluation of the Integrity on an Inlet Nozzle of a Pressurized Water Reactor Vessel Following a Postulated Loss of Coolant," *Fracture Analysis, ASTM STP 560*, American Society for Testing and Materials, 1974, pp. 240-255.

ABSTRACT: A fracture mechanics analysis was performed to evaluate the effects of a postulated loss of coolant on an inlet nozzle of a pressurized water reactor vessel.

Following rupture of one of the reactor main coolant pipes, ambient temperature water is introduced in the reactor vessel, through the primary inlet nozzles by the safety injection system (in the analysis, the temperature of the water was conservatively assumed to be equal to 32°F). Prior to the transient, the vessel is at high temperature (550°F) and the cold water injection produces a thermal shock resulting in high thermal stresses in the vessel's wall. A continuous circumferential surface crack is assumed to be present at the inside surface of one of the primary inlet nozzles at the time the transient occurs. The postulated crack is subjected to thermal stresses calculated using a finite element technique.

The stress intensity factor relative to the continuous crack under the actual stress profile normal to the section of the crack was calculated at discrete time intervals during the transient, and compared to the fracture toughness of the material, for different values of the crack depth. The critical crack depths are obtained when the stress intensity factor equals the fracture toughness.

Various locations of the nozzle were evaluated. The critical region is at the nozzle reinforcement where a 2-in.-deep crack would become unstable 200 s after the beginning of the transient. However, such a crack is readily detectable by current preservice and inservice inspection techniques, and thus the analysis demonstrates that the integrity of the reactor vessel nozzles would be maintained following a postulated loss of coolant accident.

KEY WORDS: fracture properties, nuclear reactors, thermal shock, structural design, stress analysis, cracks, fatigue (materials)

One of the major areas receiving attention in the nuclear industry today is emergency core cooling. The postulated rupture of one of the reactor

¹ Senior Engineer, Westinghouse Electric Corporation, Nuclear Energy Systems, Pittsburgh, Pa. 15230.

main coolant pipes would result in a rapid drop of the system's pressure due to the loss of the coolant. In order to maintain the core submerged by cooling fluid, a safety injection system (SIS) is initiated. At the instant the pipe ruptures, the SIS introduces water into the reactor vessel, at a temperature which could be as low as 32°F. Prior to the transient, the reactor is at its normal operating conditions and at high temperature (~550°F). Thus, the cold water rapidly injected into the reactor vessel will result in high thermal stresses in the vessel's wall.

The present analysis is directed toward predicting the crack stability limits in a pressurized water reactor vessel during cold water injection through the emergency core cooling system (ECCS), following a postulated loss of coolant accident (LOCA).

Although not subjected to neutron bombardment, regions other than the reactor beltline are of concern during the cold water injection, due to stress concentrations associated with geometrical discontinuities. One of these regions is the reactor vessel inlet nozzle (primary inlet nozzle), through which the cold water is injected.

A fracture mechanics analysis of the reactor vessel primary inlet nozzle during cold water injection is presented in this paper for the case of a typical three loop Westinghouse plant.

Method of Analysis

The overall basis for applying fracture mechanics technology is interdisciplinary and requires information and data in three areas: (1) material properties, (2) stresses existing in the structure, and (3) defects in the structure. First, attention is given to the defects in the structure and the stress intensity factor expressions related to these defects.

Flaw Shape and Stress Intensity Factor Expression

The basic assumption employed in linear elastic fracture mechanics (LEFM) is that a crack or crack-like defect exists in the structure. The essence of the approach is to relate the stress field developed in the vicinity of the crack tip to the applied stress on the structure, the material properties, and the size of defect necessary to cause failure (critical crack size).

Surface defects were considered in the analysis because they are more severe than embedded defects of the same size. It is generally agreed that cracks or crack-like surface defects that may be present in reactor vessels are more likely to have a semi-elliptical shape than to be continuous. However, at present, stress intensity factor solutions for semi-elliptical flaws can only consider uniform tension and bending stresses. In the present analysis, during the early states of the transient, the stress profiles through the wall exhibit a very steep gradient near the inside surface and an almost uniform compressive stress through the major part of the wall

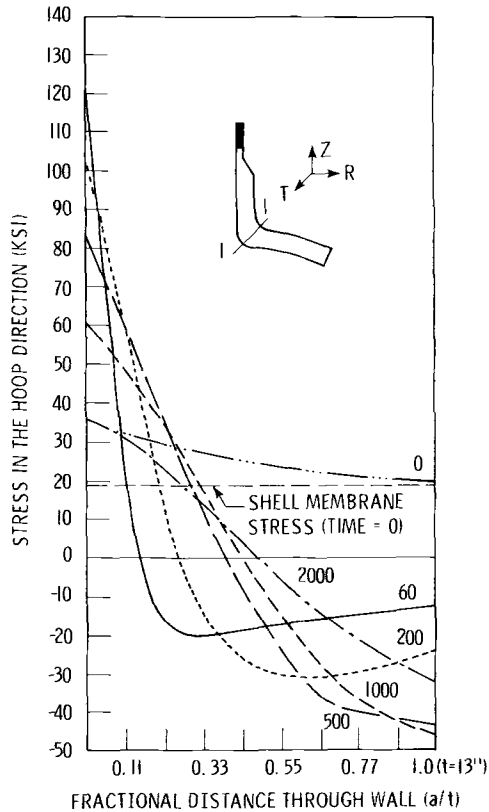


FIG. 1—Primary inlet nozzle stress profiles in Section 1-1 during a postulated loss of coolant accident.

(see Fig. 1). In this particular case, the approximation of the actual stress profile by a linear stress profile would be too conservative. For this reason, the actual stress profile and a continuous crack (circumferential) were considered in the analysis.

For shallow surface cracks, the conservatism introduced by considering a continuous flaw instead of a semi-elliptical flaw is small when the ratio of the depth-to-length of the flaw becomes less than 0.1. For this value of the ratio, there is less than 10 percent difference between the results for a semi-elliptical flaw and a continuous flaw.

The fracture toughness of the material varies through the wall due to the temperature gradient developed through the thickness during the transient. Thus, for a shallow semi-elliptical flaw, the critical location (where instability occurs) is not necessarily at the maximum depth of the crack, but could be somewhere closer to the inside surface of the wall because of the lower toughness of that region. Therefore, an initial semi-elliptical flaw

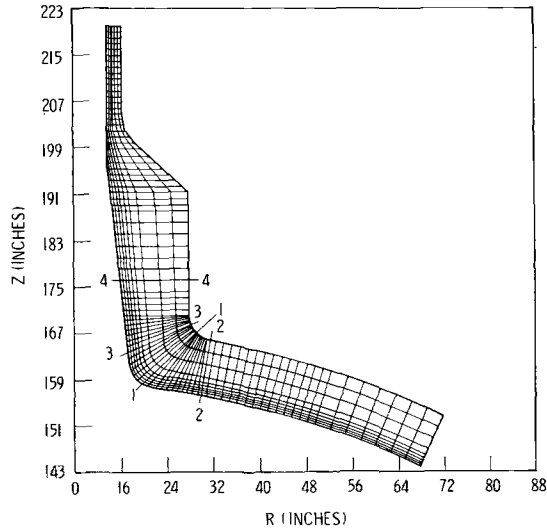


FIG. 2—Inlet nozzle model.

with a given depth-to-length ratio may grow in length prior to propagating through the thickness, thereby approaching a continuous flaw. For these reasons the conservative model of a continuous surface flaw was used in the present analysis.

The reason for considering a circumferential crack rather than a longitudinal crack (corner crack) is that the analysis of a longitudinal crack would require a three-dimensional analysis. However, comparison of stress intensity factor solutions for circumferential and longitudinal flaws in a cylinder indicates that, under the same nominal stress profile, there is almost no difference between the two solutions for crack depths up to 20 percent of the wall thickness. In the nozzle, the hoop and axial stresses produced by the thermal shock are almost equal and the wall thickness in Section 1-1 of the nozzle (see Fig. 2) is equal to 13 in. Thus, for crack depths up to about 2.5 in., the solution relative to the circumferential crack represents correctly the longitudinal flaw solution.

The stress intensity factor for a continuous surface crack in a plate can be obtained from the stress intensity factor solution relative to a through crack in an infinite body. The stress intensity factor for a continuous, through-the-thickness crack in an infinite body subjected to an arbitrary nominal stress field $\sigma(x)$ is given by Eq 1 [1].²

$$K_I = \frac{1}{\sqrt{\pi a}} \int_a^a \sigma(x) \left(\frac{a+x}{a-x} \right)^{1/2} dx \quad (1)$$

² The italic numbers in brackets refer to the list of references appended to this paper.

where a is half the crack length. The applied stress, σ , can be written in a polynomial form

$$\sigma(x) = A_0 + A_1x + A_2x^2 + A_3x^3 \quad (2)$$

Correcting for free surface and finite thickness, [2] Eq 1 becomes after integration

$$K_I = 1.9851 A_0 a^{1/2} F_1 + 1.2638 A_1 a^{3/2} F_2 + 0.9926 A_2 a^{5/2} F_3 + 0.8425 A_3 a^{7/2} F_4 \quad (3)$$

where a is the crack depth. F_1 , F_2 , F_3 , and F_4 are the finite thickness correction factors relative to $\sigma = 1$, $\sigma = x$, $\sigma = x^2$, and $\sigma = x^3$, respectively. These factors are presented in Fig. 3.

Equation 3 is valid for a flat plate where the movement of the back wall is totally prevented. If the plate is free of any constraint, Eq 3 cannot be applied for crack depths greater than 20 percent of the wall thickness, because the bending effect due to introducing the crack becomes important. In the nozzle geometry, the bowing of the back wall is not totally prevented and Eq 3 is not appropriate. For this reason, the solution relative to circumferential cracks in the nozzle is approximated by a solution derived for a circumferential crack located at the inside surface of a large hollow cylinder

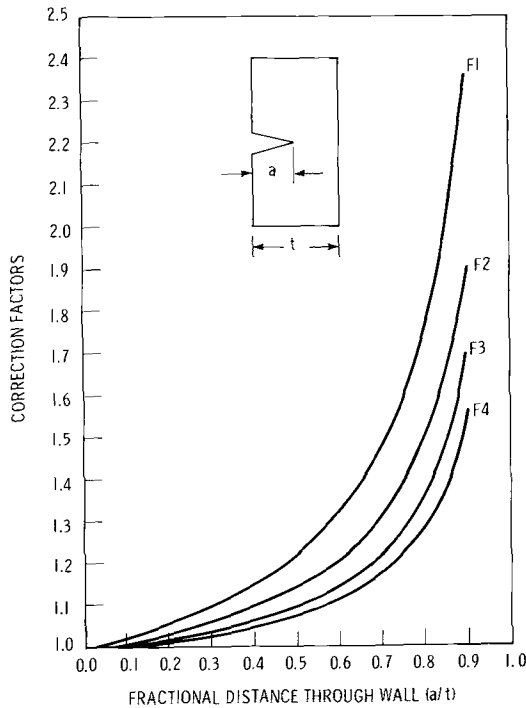


FIG. 3—Finite thickness correction factors for a plate.

and subjected to a stress profile as defined in Eq 2. This solution was obtained by using Eq 3 for crack depths up to 20 percent of the wall thickness and finite element results [2] for crack depths greater than 20 percent of the wall thickness. This approximation is conservative because the inside radius of the nozzle is smaller (~ 17 in.) than the radius of the cylinder (78 in.) for which the stress intensity expression was derived and therefore, the actual stress intensity factor is smaller than the stress intensity factor for the cylinder. The stress intensity factor used is as follows

$$K_I = 1.9851a^{1/2}A_0F_1^{(C)} + 1.2638a^{3/2}A_1F_2^{(C)} + 0.9926a^{5/2}A_2F_3^{(C)} + 0.8425a^{7/2}A_3F_4^{(C)} \quad (4)$$

where a is the crack depth. $F_1^{(C)}$, $F_2^{(C)}$, $F_3^{(C)}$, and $F_4^{(C)}$ are the cylinder back wall magnification factors relative to $\sigma = 1$, $\sigma = x$, $\sigma = x^2$, and $\sigma = x^3$, respectively. These factors are plotted in Fig. 4.

In the present analysis, the stress intensity factor, K_I , was calculated by the computer code TSHOCK [3] using Eq 4.

Stress Analysis

Because of the complex geometry of the nozzle, a finite element technique was required to calculate the temperatures and stresses resulting

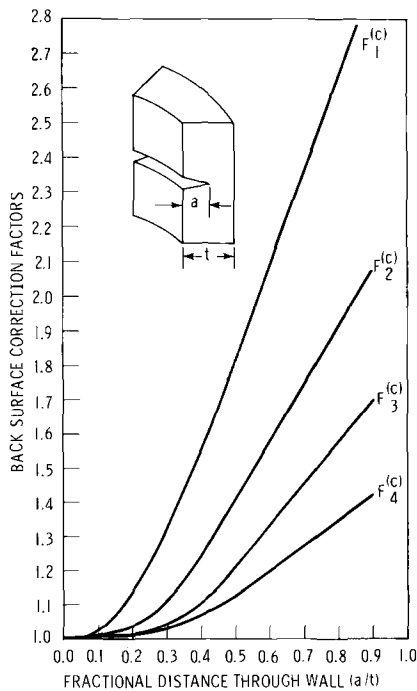


FIG. 4—Back surface correction factors for a cylinder.

from the postulated LOCA. The computer codes TFEATS [4] and ANSYS [5] were used for this analysis. In order to avoid the analysis of a three-dimensional problem, the nozzle region was transformed into an axisymmetric geometry, approximating the reactor vessel cylinder by a sphere having a mean radius two times greater than the mean radius of the cylinder. The stiffness of the actual geometry, thus, is well represented.

The two-dimensional region being examined is divided into elements, either triangles or quadrilaterals, connected at a finite number of points. The connection points are called nodal points. If the force-displacement relationship for each of these discrete structural elements is known (the element "stiffness" matrix), then, the force displacement relationship for the entire structure can be assembled using standard matrix methods [6].

The general form of the stiffness matrix for each element is

$$[k] \{u\} = \{f\} \quad (5)$$

where

$[k]$ = element stiffness matrix,

$\{u\}$ = vector of the element nodal displacements, and

$\{f\}$ = vector of the element nodal forces.

For the total structure

$$[K] \{U\} = \{F\} \quad (6)$$

where

$[K] = \sum_{i=1}^n [k] =$ total structure stiffness matrix,

$\{U\}$ = vector of all the nodal displacements in the structure, and

$\{F\}$ = vector of all the corresponding nodal forces, thermal forces, and pressure forces.

If sufficient boundary conditions are specified on $\{U\}$ to guarantee a unique solution, Eq 6 can be solved to obtain the nodal point displacements at each node in the structure. From these displacements, the force and stress within each structural element can be calculated.

The boundary conditions are the applied forces and pressure, the reactor coolant temperature, and the heat transfer coefficients. It is assumed that during the first few seconds, nucleate boiling occurs at the interface between the coolant and the vessel wall. For the few seconds (10) that it was assumed nucleate boiling occurs, a high heat transfer coefficient of 10 000 Btu/h·ft²·°F was used in the calculations. Following this initial phase of the transient, the heat in the component wall was assumed to be removed by forced convection. The forced convection heat transfer coefficients were calculated using the Dittus-Boelter equation

$$H = 0.023 f \frac{k}{D} \text{Re}^{0.8} \text{Pr}^{0.4} \quad (7)$$

where

f = safety coefficient = 1.3,

k = thermal conductivity of the fluid (Btu/h·ft·°F),

D = hydraulic diameter (ft),

$Re = \frac{\rho V D}{\mu}$ = Reynolds number,

ρ = density of the fluid (lb/ft³),

V = fluid velocity (ft/h),

μ = fluid viscosity (lb/h·ft),

$Pr = \frac{C_p \mu}{k}$ = Prandtl number, and

C_p = specific heat (Btu/lb·°F).

Table 1 presents the physical and mechanical properties of the A508 Class 2 forging steel used in the stress analysis.

TABLE 1—Inlet nozzle material properties (A508 Class 2).

Temperature (°F)	Density (lb/in. ³)	Specific Heat (Btu/lb·°F)	Conductivity (Btu/hr·in.·°F)	Young's Modulus (psi)	Poisson's Ratio	Thermal Expansion Coefficient (in./in.·°F)
+30	0.284	0.111	2.232	29.2×10^6	0.297	6.0×10^{-6}
+600	0.278	0.146	1.944	25.6×10^6	0.313	7.2×10^{-6}

Fracture Toughness

The fracture mechanics material parameter of specific interest for this analysis is the inherent fracture toughness, K_{Ic} , of the material. Generally, the reactor vessel primary inlet nozzle is fabricated from ASME SA508 Class 2 forging steel. The 508 Class 2 forging material has approximately the same toughness as A533-B plate steel for which a large amount of K_{Ic} data is available [7]. Westinghouse has constructed a reference curve K_{Ic} versus temperature. This curve is a lower bound of experimental data obtained on A533-B Class 1 material in both longitudinal and transverse directions and on A508 Class 2 material. The reference curve, presented in Fig. 5, is indexed to an RT_{NDT} ³ equal to 10°F. All the RT_{NDT} values obtained on A508 Class 2 forging material were less than 10°F. The upper shelf value (250 ksi√in.) in the curve of Fig. 5 is based upon data obtained

³ RT_{NDT} is defined according to the ASME Code, Section III, Para. NB-2300. At $RT_{NDT} + 60^\circ\text{F}$, the Charpy V Notch energy is equal to 50 ft·lb and the lateral expansion equals 35 mils.

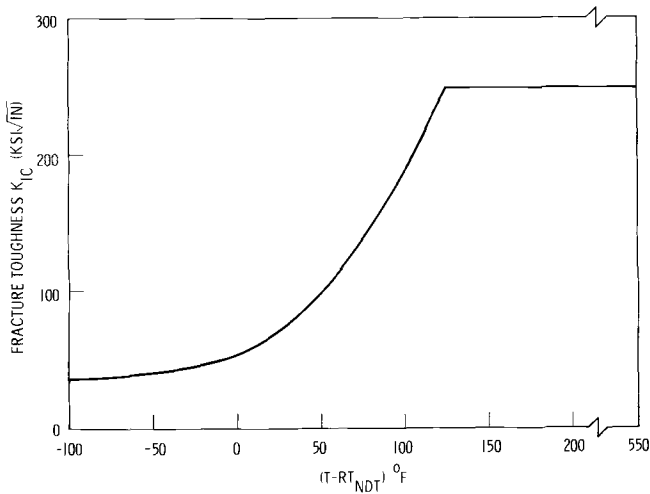


FIG. 5—Fracture toughness reference curve.

on A533-B specimens oriented in the transverse direction utilizing the equivalent energy method proposed by Witt [8].

Analysis and Results

The temperature and pressure transients resulting from a postulated LOCA are shown in Fig. 6. During the first phase of the transient, the actuation of the accumulators results in a rapid drop of the coolant temperature, from 555 to 70°F (assumed minimum temperature for the water in the accumulators). The second phase of the transient begins when the accumulators are empty. The safety injection water is then pumped from the refueling water storage tank (RWST). The assumed minimum temperature for the water in the RWST is 32°F.

Using the transients given in Fig. 6, temperature and stresses in the reactor vessel inlet nozzle were calculated using the TFEATS computer code. Figure 2 shows the geometry and finite element model used in the analysis. The elements are narrower near the inside surface where the temperature and stress gradients are steep. The values of the heat transfer coefficients used in the analysis are given in Fig. 7.

Figure 2 shows the various sections that have been analyzed. As an example, the stress profiles through Section I-I, as a function of time during the transient, are plotted in Fig. 1. High peak stresses develop near the inside surface of the wall. The stress profiles do not differ very much from one section to the other during the first 100 s following the beginning of the transient. During this period of time, the geometry and the value of the heat transfer coefficient have little influence on the stresses building

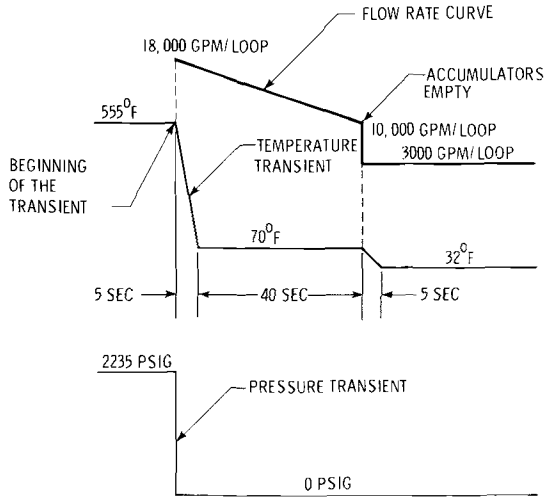


FIG. 6—Pressure and temperature transients for the primary inlet nozzle during a postulated loss of coolant accident.

up in the wall. In fact, the peak stress in the wall approaches the theoretical value of thermal stress under complete restraint

$$\sigma_{\max} = \frac{E\alpha\Delta T}{1 - \nu} \quad (8)$$

where

- E = Young's modulus of the material,
- α = thermal expansion coefficient,
- ΔT = temperature step, and
- ν = Poisson's ratio.

Table 2 shows a comparison of the peak elastically calculated stresses for the inside element in the various sections as calculated by Eq 8 and by the finite element model. After the first 100 s, geometry and heat transfer coefficients have a significant influence on the stress profiles.

TABLE 2—Comparison of peak stresses calculated by Eq 8 and by finite element method.

Section	$E\alpha\Delta T/(1 - \nu)$ (psi)	Finite Element Calculation (psi)
1-1	110 000	103 000
2-2	116 000	111 000
3-3	147 000	131 000
4-4	114 000	114 000

TIME (SECONDS)	PIPE REGION I (BTU/HR-FT ² -°F)	CORNER REGION II (BTU/HR/FT ² -°F)	SHELL REGION III (BTU/HR/FT ² -°F)
0-10	10,000	10,000	10,000
> 10	1,140	4,000	2,000

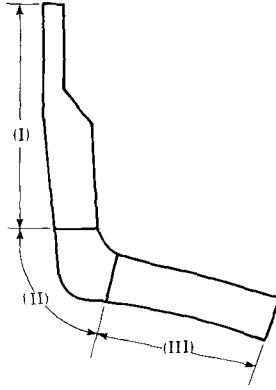


FIG. 7—Heat transfer coefficients for the primary inlet nozzle during a postulated loss of coolant accident.

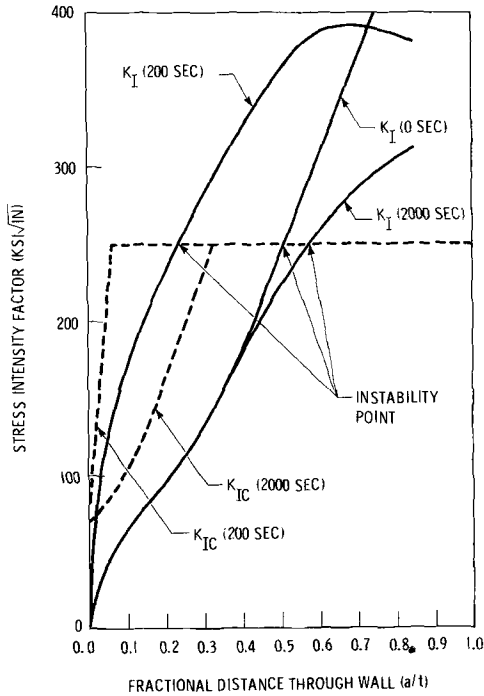


FIG. 8—Stress intensity factor and fracture toughness in Section 1-1 as a function of time during a postulated loss of coolant accident.

Using the stress profiles at several discrete time intervals, the stress intensity factor (K_I) profiles were calculated at the various nozzle sections, as a function of crack depth with the computer code TSHOCK.

The application of linear elastic fracture mechanics theory requires that, in the calculation of the stress intensity factor K_I , the stress used be the nominal stress existing in the section of the crack, without the presence of the crack. Thus, as long as the introduction of the mechanical discontinuity representing the crack has no influence on the nominal stress field, the stress profiles can be calculated without introducing the crack in the structure. In the present situation, the crack is parallel to the thermal flux and therefore does not disturb it. In this case, the stress profiles used in the calculation of the stress intensity factor can be determined in the structure without the presence of the crack.

Figure 8 presents the stress intensity factor K_I in Section 1-1, as a function of time during the postulated LOCA. Also plotted in Fig. 8 is the fracture toughness K_{Ic} . In Fig. 8, the critical crack depths are obtained at the intersections between the stress intensity factor curves and the fracture toughness curves corresponding to the same time during the transient.

The critical crack depths at the various locations in the nozzle are plotted as a function of time in Fig. 9. The minimum critical crack depth is in Section 4.4 and reaches 2 in. 200 s after the beginning of the transient. A

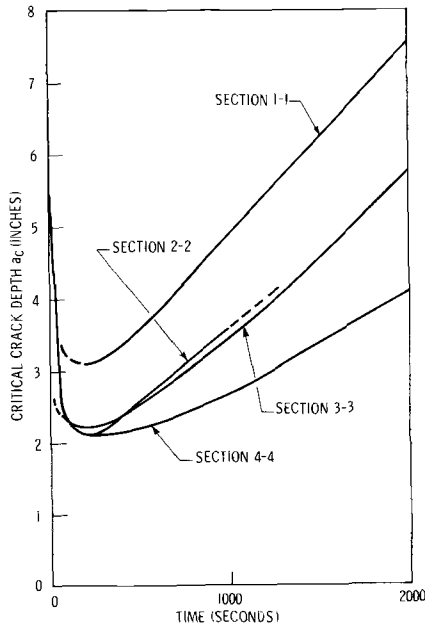


FIG. 9—Critical crack depths as a function of time during a postulated loss of coolant accident at four locations of the primary inlet nozzle.

crack having a depth equal to or larger than 2 in. is readily detectable by current preservice inspection techniques.

Conclusions

A fracture mechanics analysis was performed to evaluate the effects of the thermal shock undergone by a pressurized water reactor vessel inlet nozzle during a postulated loss of coolant accident. The temperature and stress profiles in the nozzle wall were calculated and used to determine the stress intensity factor and fracture toughness profiles at discrete time intervals during the transient. Critical crack depths were then obtained at various locations of the nozzle when the stress intensity factor equals the fracture toughness of the material.

Continuous inside surface cracks would be critical during a postulated loss of coolant accident if their depths equal or exceed 2 in. Such cracks are readily detectable by current nondestructive inspection techniques. Thus, the integrity of the reactor vessel primary inlet nozzles would be maintained in the event of a loss of coolant accident.

References

- [1] Sih, G., Paris, P., and Erdogan, F., *Transactions, American Society of Mechanical Engineers*, Vol. 84, Series E, 1962, pp. 306–312.
- [2] Ehrenpreis, S. N., Riccardella, P. C., and Mager, T. R., "Fracture Mechanics Analysis of the Integrity of the Reactor Vessel Following a Postulated Loss-of-Coolant Accident," presented at the 1970 Annual Meeting, American Society of Mechanical Engineers, Dec. 1970, unpublished.
- [3] Riccardella, P. C., "T-SHOCK, Stress Intensity Factors in Reactor Vessels, FORTRAN IV, CDC 7600," Westinghouse NES Proprietary.
- [4] Swanson, J. A., "FEATS, A Computer Program for Finite Element Thermal Stress Analysis of Plane of Axisymmetric Solids," WANL-TME-1888, Dec. 1969.
- [5] Swanson, J. A., *ANSYS, Engineering Analysis System User's Manual*, Swanson Analysis Systems, Inc., Elizabeth, Pa., Jan. 1971.
- [6] Zienkiewicz, O. C. and Cheung, Y. K., *The Finite Element Method in Structural and Continuum Mechanics*, McGraw-Hill Co., New York, 1967.
- [7] Mager, T. R. and Thomas, F. O., "Heavy Section Steel Technology Program Technical Report No. 5, Evaluation by Linear Elastic Fracture Mechanics of Radiation Damage to Pressure Vessel Steels," WCAP-7328, Nov. 1969.
- [8] Buchalet, C. and Mager, T. R. in *Progress in Flaw Growth and Fracture Toughness Testing, ASTM STP 536*, American Society for Testing and Materials, 1973, pp. 281–296.

DISCUSSION

*J. H. Underwood*¹ (written discussion)—The author should be complemented for considering the bending constraint of a finite specimen as a separate and important effect on the K_I calibration. Often the back surface of finite specimens is considered to affect K_I in the same basic manner as does the front surface. However, whereas the presence of the front surface produces no basic change in loading conditions and causes in the order of a 10 percent change in K_I , the presence of the back surface involves a change from a semi-infinite to a finite geometry. The accompanying change from infinite to finite resistance to gross specimen bending often becomes the dominant factor in determining K_I for edge-notched finite geometries.

Two aspects of Buchalet's work can be compared with some recent work in the literature and discussed in relation to bending constraint effects. They are (1) his K_I expressions for an internal, circumferential notch in hollow cylinders under axial tension; and (2) his representation of a long, shallow surface flaw by using a continuous flaw.

Swedlow and Ritter² have considered circumferentially notched cylinders from a different point of view, that is, crack front curvature effects. Their results can nevertheless be compared with those under discussion. The form of Buchalet's K_I expressions (Eqs 3 and 4) is a good basis of comparison.

$$K_I = 1.12 \sqrt{\pi} \sigma \sqrt{a} \cdot F \quad (9)$$

His K_I expressions reduce to the form of Eq 9 for the situation of a uniform axial stress, σ , applied to a cylinder with an internal, circumferential notch of depth, a . His correction factor, F , is a function of the notch-depth to wall-thickness ratio, a/t . Buchalet presents correction factors for two loading conditions (see Figs. 3 and 4): a flat plate where the movement of the back wall is "totally prevented," which can also apply to a cylinder with a large amount of bending constraint; and a large cylinder with a small amount of bending constraint due to a large radius to wall-thickness ratio, r/t . These correction factors are listed in Table 3 along with factors of the same form from Swedlow and Ritter's work and from the Gross et al³ analysis of a single-edge-notched plate.

¹ Metallurgist, Materials Engineering Division, Benet Weapons Laboratories, Watervliet, N. Y. 12189.

² Swedlow, J. L. and Ritter, M. H. in *Stress Analysis and Growth of Cracks, Part 1, ASTM STP 513*, American Society for Testing and Materials, 1972, pp. 79-89.

³ Gross, B., Srawley, J. E., and Brown, W. F., "Stress Intensity Factors for a Single-Edge-Notch Tension Specimen by Boundary Collocation of a Stress Function," Technical Note D-2395, NASA, Aug. 1964.

TABLE 3—Comparison of notched cylinder stress intensity factors
 $F = K/1.12 \sigma \sqrt{\pi a}$.

Reference Geometry	Buchalet		Swedlow and Ritter		Gross et al
	Constrained Plate	Large Cylinder	Small Cylinder	Large Cylinder	SEN Plate
	F_1	$F_1^{(c)}$	$F_2, r/t = 2$	$F_8, r/t = 8$	F_G
$a/t = 0$	1.00	1.00	1.00	1.00	1.00
0.1	1.02	1.03	1.01	1.04	1.06
0.2	1.05	1.14	1.02	1.16	1.22
0.3	1.09	1.33	1.06	1.32	1.48
0.4	1.15	1.56	1.11	1.58	1.88
0.5	1.22	1.82	1.20	1.88	2.51

Swedlow and Ritter's small cylinder results for $r/t = 2$ agree well with Buchalet's constrained plate data: Swedlow and Ritter's large cylinder results for $r/t = 8$ agree well with Buchalet's large cylinder data. In both cases this good agreement is more than an accident. The agreement between F_1 and F_2 tends to confirm Buchalet's suggestion that the K_I of a constrained plate can be used to approximate the K_I of a cylinder with significant bending constraint. The constraint on the cylinder can be attributed to the low value of r/t , but it produces about the same K_I as in a plate with external constraint. The second area of agreement just mentioned, between $F_1^{(c)}$ and F_8 , indicates that for large values of r/t , that is, $r/t > 8$, cylinders behave as thin-walled cylinders and display a uniformly small amount of bending constraint. Finally, a comparison of the large (namely, thin-walled) cylinder results with the SEN plate results shows a further decrease in bending constraint as evidenced by the higher K_I for a SEN plate. This further decrease in constraint may be associated with the change from the doubly connected nature of the cylinder to the simply loaded plate.

Regarding Buchalet's assumption that a continuous flaw is a reasonable and less than 10 percent conservative representation of a shallow, semi-elliptical surface flaw, the comparison in Table 4 may be of interest (also includes findings of Rice and Levy⁴ and Shah and Kobayashi⁵). The table lists the same parameter, F , described in Eq 8 for continuous and surface flaws in finite thickness plates. Note that a less than 10 percent difference between continuous flaws and $a/2c = 0.1$ surface flaws is indicated for values of a/t near zero. However, for flaw depths of only $0.2t$, the difference is up to 30 percent. Although both surface flaw analyses are approximate,

⁴ Rice, J. R. and Levy, N., *Journal of Applied Mechanics, Transactions, American Society of Mechanical Engineers*, Vol. 39, March 1972, pp. 185-194.

⁵ Shah, R. C. and Kobayashi, A. S. in *The Surface Crack: Physical Problems and Computational Solutions*, American Society of Mechanical Engineers, 1972, pp. 79-124.

TABLE 4—Comparison of shallow flaw stress intensity factors
in plates $F = K/1.12 \sigma \sqrt{\pi a}$.

Reference Geometry	Gross et al Continuous Flaw $a/2c = 0$	Rice and Levy Surface Flaw $a/2c = 0.1$	Shah and Kcbayashi Surface Flaw $a/2c = 0.1$
$a/t = 0$	1.00	...	0.93
0.1	1.06	0.91	0.93
0.2	1.22	0.94	0.94
0.3	1.48	1.01	0.94

the fact that both indicate a significantly lower K_I for quite shallow flaws should not be ignored. This lower K_I for surface flaws could be explained by the bending constraint supplied by the uncracked material beyond the $2c$ extent of the surface flaw as opposed to the lack of such bending constraint in the case of the continuous flaw.

In defense of Buchalet's assumption, the significant difference between continuous and surface flaws in plates just mentioned might not be present in hollow cylinders due to their doubly connected nature.

